



ALMA MATER STUDIORUM
UNIVERSITÀ DI BOLOGNA

DOTTORATO DI RICERCA IN
FISICA

Ciclo 36

Settore Concorsuale: 02/A1 FISICA SPERIMENTALE DELLE INTERAZIONI
FONDAMENTALI

Settore Scientifico Disciplinare: FIS/01 FISICA SPERIMENTALE

Exploring Dark Energy and Modified Gravity with *Euclid*-CMB Cross-Correlation

Presentata da: Angelo Giuseppe Ferrari

Coordinatore Dottorato

Alessandro Gabrielli

Supervisore

Prof.ssa Nicoletta Mauri

Co-supervisori

Dott. Fabio Finelli

Dott. Massimiliano Lattanzi

Esame finale anno 2024

Abstract

In this thesis we study the synergy between observations of the cosmic microwave background (CMB) and the large scale structure of the Universe, in the context of the ESA mission *Euclid*. The *Euclid* mission aims at building the largest galaxy catalogue to date, observing galaxies in about a third of the sky, and providing high quality data for the study of dark energy, dark matter and gravity. In this context we first discuss modified gravity theories that can be targeted by *Euclid* and provide original cosmological constraints with existing datasets on a subset of scalar-tensor theories of gravity, discussing also their implications for the Hubble tension. We then forecast for *Euclid* capabilities in further constraining this class of models in combination with CMB experiments. In the forecasts we initially focus on the combination of CMB lensing with *Euclid* observables showing its relevance for extended cosmological models, and finally we provide forecasts for the full CMB-*Euclid* joint analysis. This study shows the striking complementarity of these datasets, which breaks degeneracies between cosmological parameters, guaranteeing the largest constraining power, both on the standard cosmological parameters and on the parameters of the extended models, such as the sum of the neutrino masses or the modified gravity parameters. In order to provide these constraints and fulfill the forecasts it is necessary to build an end-to-end pipeline for the joint analysis of *Euclid* and CMB data, we explore this topic as well by presenting the results of the validation and implementation of the likelihood module for the cross-correlation observables. In particular we delve into the details of the likelihood for the detection of the integrated Sachs-Wolfe effect through the correlation of the CMB temperature field and galaxy number counts; and also discuss the implementation of CMB lensing in the official *Euclid* likelihood code.

Contents

Introduction	1
1 Basics of modern cosmology	3
1.1 General Relativity	3
1.2 Friedmann-Lemaître-Robertson-Walker metric	4
1.3 Kinematics of the Friedmann models: redshift, distances, and horizons	5
1.4 Dynamics of the Friedmann models	6
1.5 The Hot Big-Bang model	8
1.5.1 Problems of the hot Big-Bang model and inflation	9
1.6 The inhomogenous Universe	10
1.6.1 Metric perturbations	11
1.6.2 Gauges	12
1.6.3 Einstein equations	13
1.6.4 Boltzmann equations	14
1.6.5 Initial conditions	17
1.7 Cosmological observations	20
1.7.1 Cosmic microwave background	20
1.7.2 Type Ia Supernovae (SNIa)	24
1.7.3 Galaxies as a probe of the matter distribution of the Universe	25
1.8 Summary of the standard model of cosmology	31
2 Current and novel constraints on modified gravity	33
2.1 Horndeski action and its special cases	33
2.2 Equations of motion in a FLRW universe	36
2.3 Stability conditions	38
2.4 Screening	38
2.5 Current constraints on modified gravity and STTs	40
2.5.1 Constraints from gravitational waves	42
2.5.2 Constraints from big-bang nucleosynthesis	42
2.5.3 Constraints from Solar System and laboratory observations	42
2.6 Cosmological constraints	44
2.6.1 IG, NMC and EMG in the standard branch	44
2.6.2 IG, NMC and EMG in the phantom branch	46
2.6.3 Nonminimally coupled Galileon	60
3 <i>Euclid</i> and cross-correlation of its probes with CMB	77
3.1 The <i>Euclid</i> mission	77
3.1.1 The satellite	78
3.1.2 The instruments: VIS and NISP	79
3.1.3 The Science Ground Segment	83
3.1.4 The <i>Euclid</i> Consortium	84
3.2 <i>Euclid</i> main probes	84

3.2.1	<i>Euclid</i> spectroscopic galaxy clustering	85
3.2.2	<i>Euclid</i> photometric probes	86
3.2.3	Combination of spectroscopic and photometric probes	90
3.3	CMB cross-correlation	92
3.3.1	Cross-correlation with the late-ISW effect	95
3.3.2	CMB lensing and its cross-correlation	97
3.3.3	Signal-to-noise for CMB-cross correlations	99
4	<i>Euclid</i>-CMB cross-correlation likelihood	103
4.1	Validation of the ISW-galaxy cross-correlation likelihood	104
4.1.1	Likelihood and specifications	105
4.1.2	Validation of the theoretical prediction	105
4.2	CMB lensing mock pipeline	110
4.2.1	CMB lensing in CLOE	110
4.2.2	Quadratic estimators of the CMB Lensing power spectrum	111
4.2.3	Mock CMB lensing data vector and likelihood corrections	114
4.3	Discussion and future perspectives	117
5	<i>Euclid</i>-CMB cross-correlation forecasts in extended models	119
5.1	Fisher forecast formalism	119
5.2	Specifications for <i>Euclid</i> and CMB experiments	121
5.2.1	<i>Euclid</i>	121
5.2.2	CMB surveys	122
5.3	Models	124
5.4	Results	125
5.4.1	Baseline results with IST:F-like specifications	125
5.4.2	Impact of number bins	126
5.4.3	Impact of shot-noise	128
5.4.4	Baseline results with Flagship 2 specifications	130
5.4.5	Full CMB- <i>Euclid</i> joint analysis	133
5.5	Discussion and future directions	139
	Conclusions	141
	A Statistical methods for data analysis in Cosmology	145
A.1	Parameter inference	145
A.1.1	Credible intervals	148
A.2	Model comparison	148
	B Linearly perturbed equations in scalar-tensor theories	151
B.1	Einstein equations	151
B.2	Scalar field equation	153
	Bibliography	155

Introduction

The cosmological concordance model is the so-called Λ cold dark matter (Λ CDM) model. This model has established itself in the last thirty years or so, and provides a good fit to many cosmological observations [1]. It assumes the cosmological principle (homogeneity and isotropy on large scales) and its basic ingredients are: Einstein’s theory of General Relativity as theory of gravity, the standard model of particle physics, a cosmological constant (Λ) and a cold dark matter (CDM) component. The cosmological constant, provides an explanation to the recent acceleration of the expansion of the Universe in the Λ CDM model and it is described as a perfect fluid with negative pressure; this new component is called dark energy. Dark matter does not interact (or does it very weakly) electromagnetically and its existence had been postulated on the basis of observational evidences [2] and is supported by both astrophysical probes, as galaxy rotational curves and cluster mergers, and cosmological probes such as the cosmic microwave background (CMB). The prefix “cold” means that such matter was non-relativistic when, in the early Universe, it decoupled from radiation (as opposed to the “hot” dark matter) and current observations of structure formation suggest that the great majority of dark matter has to be “cold”.

The nature of dark energy and dark matter is still unknown and must lie outside the standard model of particle physics. The study of different possibilities and alternatives for these dark components is one of the most active field of cosmology and particle physics. Beyond the simple Λ CDM model, also on the basis of a discrepancy between observations and theoretical predictions for the vacuum energy, many alternatives have been proposed, such as dynamical dark energy models or modified gravity theories in which a scalar field drives the accelerated expansion solving some of the cosmological constant fine tuning problems.

In this decade, it will be possible to study and constrain these extensions of the standard model with unprecedented precision as we will see the blossoming of cosmological observations of the Large Scale Structure (LSS) of the Universe, that will help disclosing the nature of dark energy and dark matter. Among these observations, the Euclid mission¹, which will build a catalog of more than a billion galaxies and whose data will be accompanied by other ground based experiments such as Vera Rubin observatory²; and SKAO³, stands out, thanks to its power in constraining dark matter, dark energy, modified gravity and neutrino masses. Therefore, in the near future, observations of the LSS of the Universe will complement CMB observations, which, up to now, dominated and shaped the field of precision cosmology, and will continue to contribute with ongoing surveys such as ACT⁴, SPT-3G⁵, or upcoming ones like the Simons Observatory⁶, liteBIRD⁷ and CMB Stage 4⁸.

¹https://www.esa.int/Science_Exploration/Space_Science/Euclid

²<https://rubinobservatory.org/>

³<https://www.skao.int/>

⁴<https://lambda.gsfc.nasa.gov/product/act/index.html>

⁵<https://astro.fnal.gov/science/cnbr/spt-3g/>

⁶<https://simonsobservatory.org/>

⁷<https://www.isas.jaxa.jp/en/missions/spacecraft/future/litebird.html>

⁸<https://cmb-s4.org/>

Introduction

In this context, the synergy between LSS and CMB is crucial, and since they are not independent (the fluctuations we see in the CMB are the seeds for the formation of LSS), it is possible to cross-correlate them: this is called CMB-LSS cross correlation (CMBXC). The main advantages of CMBXC are its ability to break degeneracies between model parameters (cosmological or astrophysical) and to decrease the uncorrelated systematic uncertainties of each probe, thus offering a robustness test. Moreover, the cross-correlation between LSS and the CMB temperature data can probe scales where CMB is dominated by cosmic variance; in particular, at these scales it can single out a peculiar signature of dark energy: the late integrated Sachs Wolfe (ISW) effect [3, 4]. At the same time, the cross-correlation of LSS with CMB lensing, due to its sensitivity to the amplitude of matter fluctuations σ_8 , the matter density Ω_m and the sum of neutrino masses [5], is of uttermost importance to improve the constraints of the LSS probes. Thus, LSS-CMB, and in particular the *Euclid*-CMB cross-correlation will be fundamental for the study of dark energy, dark matter and neutrinos.

In this thesis, we first investigate some modified gravity models with current CMB and LSS data, we then describe the *Euclid* mission and the preparation for upcoming CMBXC data analysis, and conclude the thesis by providing forecasts on the capabilities of *Euclid* combined with CMB of constraining modified gravity models and the sum of the neutrino masses.

In detail, the thesis is structured as follows

- (I) In chapter 1 we introduce the basic concepts of modern cosmology and the current cosmological concordance model, providing an overview of the cosmological probes relevant for this work.
- (II) Chapter 2 is a general overview of modified gravity and Horndeski theories, followed by the current constraints on these models. We close the chapter providing original cosmological constraints on scalar-tensor theories of gravity and discussing their implications for the open problems of cosmology.
- (III) Chapter 3 offers an overview of the *Euclid* mission, its scientific objectives and the main observables: galaxy clustering and weak lensing. We also introduce the cross-correlation between *Euclid* photometric probes and CMB observables.
- (IV) In Chapter 4 we presents the methodology and results of the validation and tests of the likelihood for *Euclid*-CMB cross correlation, aimed at building an end-to-end pipeline for the upcoming data analysis.
- (V) Finally, in chapter 5 we discuss the capability of the photometric *Euclid* survey to constrain extended cosmological models when combined with current and future CMB anisotropy datasets.

In this thesis we employ the metric signature $(-, +, +, +)$ and natural units $c = \hbar = 1$; an overdot denotes a derivative with respect to cosmic time while a prime stands for derivative with respect to conformal time. The convention for tensor indices is the following: greek letters for spacetime indices ($\mu, \nu, \dots = 0, 1, 2, 3$), and latin letters for spatial indices ($i, j, \dots = 1, 2, 3$).

In many plots presented in this work, the goal is to show qualitative behaviours comparisons, thus, the exact values of the cosmological parameters are not relevant. If not specified, they are fixed at the *Planck* analysis best-fit [1].

Chapter 1

Basics of modern cosmology

1.1 General Relativity

Since gravity is the dominant force on cosmological scales, the theory of gravity is the basis of every cosmological model. General relativity (GR) [6] is the best theory of gravity we have at present as it has been corroborated by multiple experiments and observations since its inception [7]. The central pillar of GR is the equivalence principle of gravitation and inertia, i.e., in a sufficiently small neighborhood of any spacetime point in an arbitrary gravitational field, the laws of physics reduce to those of special relativity and it is not possible, by means of local experiments, to detect the presence of a gravitational field [8]. Thus, within GR, gravity is not described by a field defined on spacetime, but it becomes instead a property of spacetime itself; in particular it is a manifestation of the curvature of spacetime. In this context, events are points in the 4-dimensional spacetime manifold, and once chosen a coordinate system, an event can be uniquely identified by its coordinates $x_\mu = (x_0, x_1, x_1, x_3)$. The spacetime interval between two events x_μ and $x_\mu + dx_\mu$ is

$$ds^2 = g_{\mu\nu}(x)dx^\mu dx^\nu, \quad (1.1)$$

where $g_{\mu\nu}$ is the 2-rank symmetric metric tensor, which defines distances and lengths of vectors on the manifold. The metric tensor is the fundamental object that contains all the information about spacetime curvature. In essence, within GR, spacetime can be curved by matter and the motion of matter itself is described in the curved spacetime. Two equations are therefore necessary: one to describe the motion of matter in a curved spacetime and a second one to model how the gravitational field, i.e. spacetime curvature, responds to the presence of matter. Free test particles move along paths of shortest possible distance, meaning that they minimize the integral $\int ds$ between two fixed endpoints. These trajectories $x_\mu(\lambda)$ (parametrized by an affine parameter λ) are called geodesics and satisfy the following equation

$$\frac{d^2 x^\mu}{d\lambda^2} + \Gamma_{\rho\sigma}^\mu \frac{dx^\rho}{d\lambda} \frac{dx^\sigma}{d\lambda} = 0, \quad (1.2)$$

where $\Gamma_{\rho\sigma}^\mu$ is the Christoffel symbol:

$$\Gamma_{\mu\nu}^\rho = \frac{1}{2}g^{\rho\sigma} \left(\frac{\partial g_{\mu\sigma}}{\partial x^\nu} + \frac{\partial g_{\nu\sigma}}{\partial x^\mu} - \frac{\partial g_{\mu\nu}}{\partial x^\sigma} \right). \quad (1.3)$$

The geodesic equation thus describes how matter responds to gravity, while the way matter curves spacetime generating gravity is encapsulated in Einstein's field equation which relates the geometry of spacetime with the total energy-momentum tensor (EMT):

$$G_{\mu\nu} = R_{\mu\nu} - \frac{1}{2}g_{\mu\nu}R = 8\pi GT_{\mu\nu}. \quad (1.4)$$

1. Basics of modern cosmology

$G_{\mu\nu}$ is the Einstein tensor, $R_{\mu\nu}$ and $R \equiv g^{\mu\nu}R_{\mu\nu}$ are called, respectively, the Ricci tensor and Ricci scalar. They are contractions of the Riemann curvature tensor

$$R^\lambda{}_{\mu\rho\nu} = \Gamma^\lambda{}_{\mu\nu,\rho} - \Gamma^\lambda{}_{\mu\rho,\nu} + \Gamma^\lambda{}_{\alpha\rho}\Gamma^\alpha{}_{\mu\nu} - \Gamma^\lambda{}_{\alpha\nu}\Gamma^\alpha{}_{\mu\rho}, \quad (1.5)$$

which depends on the metric and its derivatives. G is Newton's constant and $T_{\mu\nu}$ is the EMT.

Due to the form of the Riemann tensor (1.5), the Einstein tensor satisfies the Bianchi identities, $\nabla_\nu G^{\mu\nu} = 0$, and through Eq. (1.4) it leads to the conservation law for the EMT: $\nabla_\nu T^{\mu\nu} = 0$.

1.2 Friedmann-Lemaître-Robertson-Walker metric

In cosmology, Eq. (1.4) has to be solved for the entire matter distribution of the Universe. To simplify this task we make use of the cosmological principle which states that the Universe is homogeneous and isotropic on large scales. The assumption of homogeneity and isotropy of 3-space selects a preferred class of observers: those for whom the Universe appears isotropic, the so-called comoving observers. Using a coordinate system (t, x^i) associated with comoving observers we can express the metric that solves Eq. (1.4) under these assumptions as:

$$ds^2 = -dt^2 + a^2(t) \left[\frac{dr^2}{1 - Kr^2} + r^2(d\theta^2 + \sin^2\theta d\varphi^2) \right], \quad (1.6)$$

where t is the proper time of comoving observers and (r, θ, φ) are the usual spherical coordinates of 3-space. The curvature parameter K can take three possible values: $K = 0, +1, -1$, corresponding, respectively, to flat, spherical (closed) and hyperbolic (open) spatial hypersurfaces. Finally, $a(t)$ is the scale factor and it uniquely determines the temporal evolution of the metric once the curvature parameter has been fixed.

The metric (1.6) has been obtained using only symmetry arguments, with no reference to the source of gravity $T_{\mu\nu}$ or the Einstein field equations. In order to determine the form of $a(t)$ and the value of K it is necessary to specify the matter content in the Einstein's equations: homogeneity and isotropy require the EMT to take the perfect fluid form [9]

$$T^{\mu\nu} = p g^{\mu\nu} + (\rho + p) u^\mu u^\nu, \quad (1.7)$$

where ρ and $p \equiv w\rho$ are, respectively, the total density and total pressure of the fluid, and $u^\mu = dx^\mu/\sqrt{-ds^2}$ is the 4-velocity. whereas the EMT (1.7) is that of a perfect fluid and we use the notation ρ and p to denote its density and pressure, there is no requirement for the source to be an actual ideal fluid. In particular, the pressure p is not required to be positive, as it would be in an ideal fluid.

1.3 Kinematics of the Friedmann models: redshift, distances, and horizons

Due to the expansion of the Universe, the wavelength of light emitted by distant objects gets stretched out by a factor proportional to the scale factor. We thus observe at time t_0 ¹ a longer wavelength, λ_0 , than the emitted one λ at the time t . This phenomenon is called cosmological redshift, with the redshift, z , defined as

$$1 + z \equiv \frac{\lambda_0}{\lambda_1} = \frac{a(t_0)}{a(t_1)} \equiv \frac{a_0}{a(t_1)}. \quad (1.8)$$

For nearby sources, $a(t)$ can be expanded around t_0 : $a(t) = a(t_0)[1 + (t - t_0)H_0 + \dots]$, where H_0 is the Hubble constant

$$H_0 \equiv \left(\frac{\dot{a}(t)}{a(t)} \right)_{t=t_0} = 100 h \text{ km s}^{-1} \text{ Mpc}^{-1}. \quad (1.9)$$

The concept of distance in a FLRW universe can be defined in several ways and to do so it is useful to redefine the radial coordinate $d\chi \equiv dr/(1 - Kr^2)$ to rewrite the FLRW metric as

$$ds^2 = -dt^2 + a^2(t) \left[d\chi^2 + f_K^2(\chi) d\Omega^2 \right], \quad (1.10)$$

where

$$f_K(\chi) \equiv \frac{1}{\sqrt{|K|}} \begin{cases} \sinh(\sqrt{|K|}\chi) & K < 0 \\ \sqrt{|K|}\chi & K = 0 \\ \sin(\sqrt{|K|}\chi) & K > 0. \end{cases} \quad (1.11)$$

This quantity is the *metric distance* $d_m \equiv f_K(\chi)$. The distance related to the radial coordinate is the *comoving distance*, which, between us and a galaxy at redshift z is

$$\chi(z) = \int_{t_1}^{t_0} \frac{dt}{a(t)} = \int_0^z \frac{dz}{H(z)}, \quad (1.12)$$

and for a flat universe coincides with the metric distance. It is not observable, what is observable is the *physical distance*, also called *proper distance*, which is the comoving distance multiplied by the scale factor: $d_{\text{pr}} = a(t)\chi$. At small redshifts, the physical distance is simply $t_0 - t$, thus, from Eq. (1.8), it follows that redshift increases linearly with distance, $z \simeq H_0 d$. This is the *Hubble law*, introduced by Hubble [10] in the form $v_{\text{gal}} = Hd$, where v_{gal} is the recessional velocity of a galaxy at a physical distance d .

Another definition of interest in cosmology is the *angular diameter distance* d_A , which measures the distance of an object with observed angular size in the sky $\delta\theta$ and of known physical extension D ,

$$d_A = \frac{D}{\delta\theta}, \quad (1.13)$$

¹The subscript 0 means today unless otherwise specified.

1. Basics of modern cosmology

which, in a flat universe simply reduces to $d_A = \chi/(1+z)$.

Finally, we introduce the *luminosity distance* d_L connecting the intrinsic Luminosity L of a source at a given comoving distance χ and redshift z , with its observed flux F :

$$F = \frac{L}{4\pi d_m^2(1+z)^2} \equiv \frac{L}{4\pi d_L^2}, \quad (1.14)$$

from which we can identify

$$d_L = d_m(1+z), \quad (1.15)$$

and obtain the relationship between the luminosity and the angular diameter distance as

$$d_A = \frac{d_L}{(1+z)^2}. \quad (1.16)$$

If the Universe has a finite age light can only travel a finite distance from its beginning, the maximum comoving distance travelled by a photon since the Big Bang is called *particle horizon* χ_p , it is given by

$$\chi_p = \int_{t_i}^{t_0} \frac{dt}{a(t)} = \int_{\ln a_i}^{\ln a} (aH)^{-1} d \ln a, \quad (1.17)$$

where $(aH)^{-1}$ is the so called *Hubble radius*. The Hubble radius is often referred to as the horizon cause the two are of the same order of magnitude in standard cosmologies: $\chi_p \sim (aH)^{-1}$, but they are conceptually different. Indeed, the Hubble radius is the distance travelled by a photon in a Hubble time H^{-1} while the particle horizon is the maximum distance a photon can travel since the Big Bang.

There exist another horizon, the *event horizon* which is defined as

$$\chi_e \equiv \int_{t_0}^{t_f} \frac{dt}{a(t)} = \int_{a_0}^{a_f} \frac{da}{H(a)a^2}, \quad (1.18)$$

where t_f is the final moment of the Universe, if the expansion goes on forever $t_f \rightarrow +\infty$. The event horizon represent the largest comoving distance from which light emitted now can ever reach the observer in the future.

1.4 Dynamics of the Friedmann models

Inserting the FLRW metric (1.6) and the EMT (1.7) into the Einstein's field equations (1.4) we obtain the Friedmann equations, that can be solved to determine the time evolution of the scale factor $a(t)$,

$$\left(\frac{\dot{a}}{a}\right)^2 \equiv H^2 = \frac{8\pi G}{3}\rho - \frac{K}{a^2} \quad (1.19)$$

$$\ddot{a} = -\frac{4\pi G}{3}(\rho + 3p)a. \quad (1.20)$$

1.4. Dynamics of the Friedmann models

Eq. (1.20) implies that the Universe expansion decelerates ($\ddot{a} < 0$) if $\rho + 3p > 0$. This inequality, called the *strong energy* condition, can be rewritten as $w > -\frac{1}{3}$. A deceleration in the expansion of the Universe is in contrast with observations which show that the expansion is accelerating. Since ordinary matter and radiation satisfy the strong energy condition there has to be in the Universe an additional component with negative pressure ($w < -1/3$) to explain the current accelerated expansion; this component is known as dark energy (DE), and it can be described parameterized in different ways. In the standard model of cosmology, called Λ -cold-dark-matter (Λ CDM) model, the cosmological constant, corresponding to a component with $w = -1$, plays the role of DE.

Note that Hubble law states $H > 0$, implying from Eq. (1.20) that $a(t)$ is a growing function of time ($\dot{a} > 0$ at all times). Thus, there exist a time in the past where $a(t) = 0$ and density and pressure become infinite, this is the Big-Bang singularity and it cannot be avoided in the Friedmann models.

A third equation can be obtained considering the 0-th component of the local conservation of the EMT: $\dot{\rho} + 3H(\rho + p) = 0$, which, using the equation of state $p = w\rho$, can be integrated to give

$$\rho(t) = \rho_0(t) \left(\frac{a}{a_0} \right)^{-3(1+w)}. \quad (1.21)$$

Eqs. (1.19) to (1.21) are not independent, given two of them is sufficient to derive the third equation. Once a parameter of state w is specified Eq. (1.21) give the evolution of density as a function of the scale factor. We list below the different components of the Universe whose behaviour can be parametrized by w .

Cold matter: pressureless matter, $w_m = 0$, with negligible kinetic energy. It is composed by all non relativistic massive particles like nuclei and electrons of ordinary matter, usually called baryonic matter, and by cold dark matter (CDM), a type of matter which interacts only gravitationally and whose particle nature is still unclear. It follows from the equation of state and Eq. (1.21) that as the Universe expand the matter density scales as $\rho_m \propto a^{-3}$.

Radiation: composed by ultra relativistic particles like photons or, in the early Universe, neutrinos, its equation of state is $w_r = 1/3$ and its energy density scales as $\rho_r \propto a^{-4}$. The reason for the extra factor a^{-1} with respect to matter is cosmological redshift, which is proportional to a^{-1} .

Cosmological constant: it is characterized by a constant energy density

$$\rho_\Lambda = \frac{\Lambda}{8\pi G} \propto a^0, \quad (1.22)$$

and therefore the equation of state is $w_\Lambda = -1$. Since the energy density of the cosmological constant does not dilute, this term becomes dominant with respect to the other components as the Universe expands. This component can be naturally interpreted as the energy of vacuum but its small inferred value compared to typical scales in particle physics [11] has led to the quest for alternative models.

1. Basics of modern cosmology

Curvature: We can define an effective curvature energy density that enters Eq. (1.19) as

$$\rho_K = -\frac{3K}{8\pi G}a^{-2}, \quad (1.23)$$

and has, consequently, equation of state $w_K = -1/3$.

It is useful to define dimensionless density parameters:

$$\Omega_{i,0} \equiv \frac{\rho_{i,0}}{\rho_{crit,0}} = \frac{8\pi G}{H_0^2}\rho_i; \quad (1.24)$$

where the critical density ρ_{crit} is the density of a flat Universe and the subscript $i = r, m, \Lambda$ for radiation, non-relativistic matter and cosmological constant identifies the different components of the Universe. Splitting the matter contribution in its components, the subscript c identifies cold dark matter while b stands for baryons. The sum of the density parameters $\Omega_{tot} = \sum_i \Omega_i$ can either be larger than unity, corresponding to a closed universe, smaller than 1, which corresponds to an open universe, or exactly 1, as in a flat universe.

With these definitions, dropping the subscript 0 in the density parameters and following the convention $a_0 = 1$, Eq. (1.19) can be rewritten in the following way:

$$\frac{H^2}{H_0^2} = \Omega_r a^{-4} + \Omega_m a^{-3} + \Omega_k a^{-2} + \Omega_\Lambda. \quad (1.25)$$

Since the scale factor increases with time, radiation, which initially dominates the matter content of Universe, is diluted faster than matter, and at a certain point in time, called matter-radiation equality, the two components contribute equally: $\rho_r(z_{eq}) = \rho_m(z_{eq})$. After equality we enter the so called matter epoch, but, since the matter density dilutes as a^{-3} while the cosmological constant contribution is constant, we reach equality between these two components and the expansion of the Universe starts to accelerate as the cosmological constant dominates.

The official values for the density parameters obtained by the *Planck* collaboration [12] are $\Omega_K = 0.0007 \pm 0.0019$ [1], $\Omega_m = \Omega_c + \Omega_b = 0.3111 \pm 0.0056$, and $\Omega_\Lambda = 0.6889 \pm 0.0056$. The relativistic contribution coming from the cosmic microwave background and the cosmic neutrinos background is $\Omega_r \simeq 9.4 \times 10^{-5}$.

The description of Universe in terms of these components is known as the Λ CDM model.

1.5 The Hot Big-Bang model

As we have seen the early Universe was dominated by relativistic degrees of freedom, we can subdivide this epoch of radiation domination into the following stages:

- Quark era: $T > T_{QH} \simeq 200 - 300$ MeV. The temperature is too high to allow hadronization: matter is in the form of free quarks in a quark gluon-plasma. At the end of this epoch ($T = T_{QH}$), quarks and antiquarks bind together to form hadrons.

1.5. The Hot Big-Bang model

- Hadron era: $T_{QH} > T > T_\pi \simeq 130 \text{ MeV}$. Hadrons dominate until pions and antipions annihilate at $T = T_\pi$.
- Lepton era: $T_\pi > T > T_e \simeq 0.5 \text{ MeV}$. Leptons dominate the energy content until positrons-electrons annihilate at T_e . Primordial nucleosynthesis occurs during this era and before the end of this epoch neutrinos decouple from the cosmological fluid at $T \simeq 1 \text{ MeV}$.
- Plasma era: $T_e > T > T_{eq} \simeq 1 \text{ eV}$. The Universe is composed by photons, baryonic matter (protons, electrons and helium nuclei), CDM and neutrinos, both decoupled from the photon-baryon fluid.

After matter-radiation equivalence the photon-baryon fluid is still tightly coupled thanks to efficient Thomson scattering, as temperature decreases electrons are captured by protons and neutral hydrogen forms for the first time. This process, known as recombination leads to a drop in free electrons and consequently Thomson scattering becomes inefficient, leading to the decoupling of photons and baryons at redshift $z \simeq 1100$. The photons freely propagating since then constitute the cosmic microwave background (CMB).

In addition to the prediction of the existence of the CMB as relic radiation [13], the Hot Big Bang model also naturally predicts the abundances of light chemical elements produced during Big-Bang Nucleosynthesis (BBN) [14] and the expansion of the Universe.

1.5.1 Problems of the hot Big-Bang model and inflation

The hot Big-Bang theory has undoubtedly been successful but it is plagued by some problems. We highlight here two of them².

- The flatness problem: Observations are consistent with a flat universe: $\Omega_K = 0.0007 \pm 0.0019$ [1]. To account for the observed degree of flatness today, the initial density parameter must have deviated from unity by no more than one part in 10^{56} , giving rise to a fine tuning problem.
- The horizon problem: the observation of an homogeneous CMB monopole on the entire sky, i.e. scales much larger than the Hubble radius at the time when the CMB was formed, is puzzling. The angular size of regions that were in causal contact at the time of decoupling is only a small fraction of the sky, approximately $\theta_{\text{hor}} \simeq 1.6^\circ$ [9] and no physical influence could have smoothed out initial inhomogeneities bringing these regions to the same temperature. This is known as the Horizon problem.

The most compelling solution to these problems is cosmic inflation, which postulates an exponential expansion stage in a cold and quantum era before the thermal epoch of the standard Big Bang cosmology. During this phase the scale factor increased by a factor

²Historically, the missing observation of hot relics such as magnetic monopoles or the gravitino, predicted by Great Unified or supergravity theories, was one of the main reason to introduce inflation. We don't discuss this problem here, focusing on the issues of the hot Big-Bang model and not of those of speculative theories.

1. Basics of modern cosmology

$e^{\mathcal{N}}$, where \mathcal{N} is the number of e-folds. If $|\Omega_K| = \mathcal{O}(1)$ at the beginning of inflation, then at the end it would be of order $e^{-2\mathcal{N}}$. This implies that if inflation lasts long enough, meaning that $\mathcal{N} > 62$ [9], then the flatness problem is solved.

Concerning the horizon problem: the exponential expansion would stretch tiny causally connected patches to cosmic sizes, providing enough time to homogenize our observable Universe. Quantitatively, the proper horizon, defined as the scale factor times the particle horizon, at the time of last scattering t_L is

$$d_H(t_L) \equiv a(t_L) \int_{t_*}^{t_L} \frac{dt}{a(t)} = \frac{a(t_L)}{a_I H_I} (e^{\mathcal{N}} - 1) \quad (1.26)$$

where t_* and t_I are the time of beginning and end of inflation; H_I is the Hubble parameter during inflation and the number of e-folding is given by $\mathcal{N} = H_I(t_I - t_*)$. The condition that the proper horizon at the time of last scattering is larger than the angular diameter distance of the last scattering surface: $d_H(t_L) > d_A(t_L)$, requires $\mathcal{N} > 62$, exactly like the flatness problem.

Without going into the mathematical details, the simplest way to achieve inflation is by considering a fluid with negative pressure by means of a scalar field $\varphi(t)$ called the inflaton. At some early time the scalar field takes a value such that its potential $V(\varphi)$ is very large but quite flat, in this way the field slowly rolls down the potential and the Hubble parameter decreases very slowly, allowing a nearly exponential expansion of the Universe before the field configuration changes significantly. At the end of inflation the inflaton field oscillates around the minimum of the potential and decays into other particles. This period is called preheating and it is the first stage of reheating which connects the cold and quantum inflation phase to the thermal hot Big-Bang cosmology.

1.6 The inhomogenous Universe

So far we have considered an homogenous and isotropic universe and the metric (1.6) and the EMT (1.7) are consequences of this assumption. However, the presence of gravitational bound structures such as galaxies and clusters shows that the matter distribution in our Universe is not homogeneous and isotropic. The amplitude of the fluctuations in the energy-density of the Universe were 10^5 smaller than the background at the time of last scattering ($z \simeq 10^3$); these small fluctuations generated in the early Universe are amplified by gravitational instability leading to the formation of cosmic structures. The study of the anisotropies and inhomogeneities is central in modern cosmology as it is necessary for the comparison between predictions and observables which allows to test cosmological models and constrain the parameters describing our Universe.

For these reasons in this section we introduce first order perturbation theory. Density perturbations are considered random Gaussian field so that their Fourier modes are decoupled at linear level. The convention for the Fourier transform is:

$$A(\tau, \mathbf{x}) = \int \frac{d\mathbf{k}}{(2\pi)^3} A(\tau, \mathbf{k}) e^{i\mathbf{k} \cdot \mathbf{x}}, \quad A(\tau, \mathbf{k}) = \int d\mathbf{x} A(\tau, \mathbf{x}) e^{-i\mathbf{k} \cdot \mathbf{x}}, \quad (1.27)$$

1.6. The inhomogenous Universe

and the power spectrum $P_A(\tau, \mathbf{k})$ of a function A is then

$$\langle A(\tau, \mathbf{k})A^*(\tau, \mathbf{k}') \rangle = (2\pi)^3 P_A(\tau, k) \delta_D^{(3)}(\mathbf{k} - \mathbf{k}'). \quad (1.28)$$

We follow the notation and conventions of [15] and draw heavily from [16]. We consider, for simplicity, flat ($K = 0$) FLRW metric expressed in conformal time $d\tau = a(t) dt$, and raise and lower spatial indices with the Kronecker delta throughout this section.

1.6.1 Metric perturbations

To account for inhomogeneities we consider linear perturbations $\delta g_{\mu\nu}(\tau, \mathbf{x})$ around the background FLRW metric $\bar{g}_{\mu\nu}(\tau)$: $g_{\mu\nu}(\tau, \mathbf{x}) = \bar{g}_{\mu\nu}(\tau) + \delta g_{\mu\nu}(\tau, \mathbf{x})$, so that we can write the perturbed metric in a general way [17]

$$ds^2 = a^2(\tau) \left[-(1 + 2A)d\tau^2 + 2B_i dx^i d\tau + (\delta_{ij} + h_{ij}) \right], \quad (1.29)$$

where A , B_i and h_{ij} are functions of space-time. The metric perturbations can be decomposed into 3 categories according to their transformation properties with respect to a local 3-rotation on hypersurfaces of constant time: scalar (δg_{00}), vector (δg_{0i}) and tensor (δg_{ij}) perturbations, this is called scalar-vector-tensor (SVT) decomposition. The vector mode δg_{0i} can be written, thanks to the Helmholtz decomposition theorem, as the gradient of a scalar field plus a vector field with null divergence: $B_i = \partial_i B + \hat{B}_i$, with $\partial^i \hat{B}_i = 0$. In a similar manner, the tensor perturbation can be decomposed as:

$$h_{ij} = 2C\delta_{ij} + 2\partial_{(i}\partial_{j)}E + 2\partial_{(i}\hat{E}_{j)} + 2\hat{E}_{ij}; \quad (1.30)$$

with

$$\partial_{(i}\partial_{j)}E \equiv \left(\partial_i\partial_j - \frac{1}{3}\delta_{ij}\nabla^2 \right) E, \quad (1.31)$$

$$\partial_{(i}\hat{E}_{j)} \equiv \frac{1}{2} \left(\partial_i\hat{E}_j + \partial_j\hat{E}_i \right). \quad (1.32)$$

The hatted objects are divergenceless: $\partial^i \hat{E}_i = 0 = \partial^i \hat{E}_{ij}$; moreover \hat{E}_{ij} is also traceless. This latter term encodes the tensorial degrees of freedom of the FLRW metric. The decomposition (1.30) consists of a scalar part (the first two term on the right hand side), a vector part (third term), and a tensor part corresponding to the fourth term \hat{E}_{ij} . We have therefore separated the 10 degrees of freedom of the metric into 4 scalar, 4 vector and 2 tensor degrees of freedom. The importance of the SVT decomposition lays in the fact the equations for scalars vectors and tensors do not mix at linear order and the perturbations evolve independently [18].

Physically, the scalar perturbations are induced by energy density inhomogeneities and they exhibit gravitational instability leading to the formation of structure in the Universe; they will be the focus of the remaining of the section for these reasons. Vector perturbations arise from the rotational motion of the fluid and in standard cosmologies they decay very quickly with the expansion of the Universe, while tensor modes, instead, physically represents gravitational waves propagating on the background FLRW metric.

1.6.2 Gauges

In a FLRW universe, only one time slicing is compatible with the assumption of homogeneity, while, in a perturbed universe there are infinite time slicings such that on each slice, all quantities remain close to their average values. The fluctuation of a variable at a given spacetime point is the difference between its actual value and the average value in that point, e. g., for energy density $\delta\rho(\tau, \mathbf{x}) = \rho(\tau, \mathbf{x}) - \bar{\rho}(\tau)$. The average $\bar{\rho}(\tau)$ depends on the choice of the time slicing, while true value $\rho(\tau, \mathbf{x})$ is unambiguously defined, therefore choosing a different slicing the quantity $\rho(\tau, \mathbf{x})$ is compared with an average computed on a different hypersurface and thus $\delta\rho(\tau, \mathbf{x})$ would take a different value, meaning that the fluctuations is dependent on the choice of the equal-time hypersurface. A gauge is a choice of time slicing and gauge transformations are induced by the coordinate transformation

$$x^\mu \rightarrow \tilde{x}^\mu = x^\mu + d^\mu(x^\nu), \quad (1.33)$$

where d^μ has to be small in every point to ensure that the perturbations are still linear after the coordinate transformation.

The solutions to the equations of motion for the perturbed quantities would contain some spurious “gauge modes” that have no impact on the observables, they just reflect the gauge freedom of changing coordinate system without affecting the physical results.

There are two ways to deal with gauge issues: implement a gauge-invariant formalism or fixing the gauge.

Gauge independent formalism: introduce combinations of the metric perturbations that are invariant under the transformation (1.33) and solve gauge-invariant equations for these variables. The most common quantities of this kind are the so called Bardeen potentials [19]

$$\Psi_B \equiv A + \mathcal{H}(B - E') + (B - E')', \quad (1.34)$$

$$\Phi_B \equiv -C - \mathcal{H}(B - E') + \frac{1}{3}\nabla^2 E. \quad (1.35)$$

where $\mathcal{H} \equiv a'/a$ is the conformal Hubble parameter.

Gauge fixing: one can simply fix the gauge and carry on the computations in the preferred gauge as observable quantities are independent of this choice [16]. Furthermore, the choice of the gauge could be relevant for numerical integration of the equations of motion or simplify the physical interpretation of the solutions. Two gauges relevant for this thesis:

- *The synchronous gauge*, whose name stems from the fact that it selects a set of “fundamental” comoving observers for which the conformal time coordinate increases at the same rate, is defined by the conditions $A_s = B_s = 0$. With this choice the metric (1.29) is $ds^2 = a^2(\tau) [-d\tau^2 + (\delta_{ij} + h_{ij})]$. The connection with the notation of Ref. [15] is: $2C \equiv h/3$, $2E \equiv \mu$, $\hat{E}_i \equiv A_i$ and $2\hat{E}_{ij} \equiv h_{ij}^T$. We define h_{ij} as a

1.6. The inhomogenous Universe

Fourier integral

$$h_{ij}(\tau, \mathbf{x}) = \int \frac{d\mathbf{k}}{(2\pi)^3} e^{i\mathbf{k}\cdot\mathbf{x}} \left[\hat{k}_i \hat{k}_j h(\tau, \mathbf{k}) + \left(\hat{k}_i \hat{k}_j - \frac{1}{3} \delta_{ij} \right) 6\eta(\tau, \mathbf{k}) \right], \quad \mathbf{k} = k \hat{k}. \quad (1.36)$$

The synchronous gauge is not uniquely fixed by the above conditions because the choice of the initial hypersurface and its coordinate assignments are arbitrary [15]. This residual gauge freedom manifests in fictitious gauge modes appearing in the solutions of the Einstein equations, and it is commonly fixed by working in the CDM rest frame. This gauge is useful for the simple form of the equations and the stability for in the numerical integration of the perturbed Einstein-Boltzmann equations.

- *The Newtonian (or longitudinal) gauge* defined by $B_1 = E_1 = 0$. It is customary to identify $A \equiv \psi_N$ and $C \equiv -\phi_N$, in such a way that the metric takes the form

$$ds^2 = a(\tau) \left[-(1 + 2\psi_N) d\tau^2 + (1 - 2\phi_N) \delta_{ij} dx^i dx^j \right]. \quad (1.37)$$

In the weak field limit of the Einstein field equation ψ_N represents the Newtonian gravitational potential.

1.6.3 Einstein equations

We can write the Einstein equations by splitting the EMT and the Einstein tensor into a background and a perturbed part

$$\delta G^\mu{}_\nu = 8\pi G \delta T^\mu{}_\nu. \quad (1.38)$$

The right hand side of Eq. (1.38) contains the perturbed EMT, whose components are

$$T^0{}_0 = -(\bar{\rho} + \delta\rho), \quad (1.39)$$

$$T^0{}_i = (\bar{\rho} + \bar{p})v_i = -T^i{}_0, \quad (1.40)$$

$$T^i{}_j = (\bar{p} + \delta p)\delta^i_j + \Sigma^i_j, \quad (1.41)$$

in which $\delta\rho$ and δp are, respectively, the density and pressure perturbations, $v^i = dx^i/d\tau$ is the coordinate velocity of the fluid and $\Sigma^i_j = T^i_j - \delta^i_j T^k_k/3$. As in Ref. [15] we define

$$\delta \equiv \delta\rho/\rho \quad (1.42)$$

$$\theta \equiv ik^j v_j, \quad (1.43)$$

$$(\bar{\rho} + \bar{p})\sigma \equiv - \left(\hat{k}_i \hat{k}_j - \frac{1}{3} \delta_{ij} \right) \Sigma^i_j. \quad (1.44)$$

1. Basics of modern cosmology

Thus, the time-time, longitudinal time-space, trace space-space and traceless space-space Einstein equations are [15]

$$k^2\eta - \frac{1}{2}\mathcal{H}h' = -4\pi Ga^2 \sum_i \delta\rho_i^{(S)}, \quad (1.45)$$

$$k^2\eta' = 4\pi Ga^2 \sum_i (\bar{\rho}_i + \bar{p}_i)\theta_i^{(S)}, \quad (1.46)$$

$$h'' + 2\mathcal{H}h' - 2k^2\eta = -24\pi Ga^2 \sum_i \delta p_i^{(S)}, \quad (1.47)$$

$$h'' + 6\eta'' + 2\mathcal{H}(h' + 6\eta') - 2k^2\eta = -24\pi Ga^2 \sum_i (\bar{\rho}_i + \bar{p}_i)\sigma_i^{(S)}, \quad (1.48)$$

in the synchronous gauge, while, in the Newtonian gauge they take the following form

$$k^2\phi_N + 3\mathcal{H}(\phi'_N + \mathcal{H}\psi_N) = -4\pi Ga^2 \sum_i \delta\rho_i^{(N)}, \quad (1.49)$$

$$k^2(\phi'_N + \mathcal{H}\psi_N) = 4\pi Ga^2 \sum_i (\bar{\rho}_i + \bar{p}_i)\theta_i^{(N)}, \quad (1.50)$$

$$\phi''_N + \mathcal{H}(\psi_N + 2\phi_N)' + \left(2\frac{a''}{a} - \mathcal{H}^2\right) + \frac{k^2}{3}(\phi_N - \psi_N) = 4\pi Ga^2 \sum_i \delta p_i^{(N)}, \quad (1.51)$$

$$k^2(\phi_N - \psi_N) = 12\pi Ga^2 \sum_i (\bar{\rho}_i + \bar{p}_i)\sigma_i^{(N)}, \quad (1.52)$$

where the index i runs over all species contributing to the content of the Universe.

To close the system of equations it is necessary to add the equations describing the time evolution of density and velocity perturbations to the Einstein's equations. These are the so called Boltzmann equations and are the topic of the next section.

1.6.4 Boltzmann equations

The Boltzmann equations take into account the interactions between different species, we derive them for photons, massless neutrinos, CDM and baryons in the synchronous gauge, for their expression in the Newtonian gauge see Ref. [15].

Consider the phase space described by three spatial coordinates x_i and their conjugate momenta P_i . The conjugate momentum is the spatial part of the 4-momentum and in the synchronous gauge it is related to the proper momentum, $p^i = p_i$ (measured by an observer at a fixed spatial coordinate), by $P_i = a(\delta_{ij} + h_{ij}/2)p^j$. The phase space distribution $f = f(x^i, q, n_j, \tau)$ evolves as

$$\frac{df}{d\tau} = C[f], \quad (1.53)$$

where $q_j \equiv ap_j \equiv qn_j$ in which q is its magnitude and n_j its direction. The collision term on the right hand side takes into account all possible interactions and differs from species to species.

1.6. The inhomogenous Universe

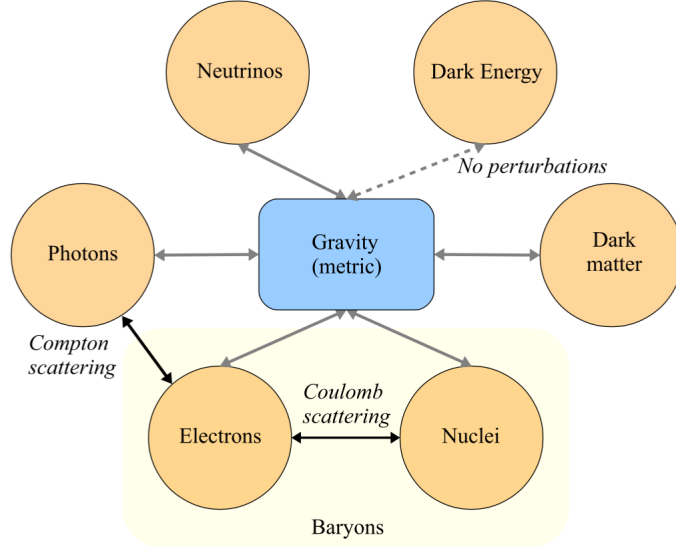


Figure 1.1: Representation of the ways the different components of the Universe interact, these interactions are described by the Einstein-Boltzmann equations. Some species do not interact directly but they are all connected through their interactions with gravity. Figure taken from [18].

The phase-space distribution can be expanded around its zeroth-order

$$f(x^i, q, n_j, \tau) = f_0(q) \left[1 + \Psi(x^i, q, n_j, \tau) \right], \quad (1.54)$$

where, the zeroth-order is the Fermi-Dirac (Bose-Einstein) distribution for fermions (bosons).

The components of the EMT given in Eqs. (1.42) to (1.44) can be written in terms of the perturbation Ψ . Moreover, writing the total derivative of Eq. (1.53) in terms of partial derivatives and using the geodesic equation to get the expression for $dq/d\tau$, the Boltzmann equation in k -space in the synchronous gauge becomes

$$\frac{\partial \Psi}{\partial \tau} + i \frac{q}{\epsilon} (\mathbf{k} \cdot \hat{n}) \Psi + \frac{d \ln f_0}{d \ln q} \left[\eta' - \frac{h' + 6\eta'}{2} (\hat{k} \cdot \hat{n})^2 \right] = \frac{1}{f_0} \left(\frac{\partial f}{\partial \tau} \right)_C. \quad (1.55)$$

where $\hat{n} = \mathbf{q}/|\mathbf{q}|$, and $\epsilon = (q^2 + a^2 m^2)^{1/2} = -P_0$. This equation is valid for all the components of the cosmological fluid, what changes depending on the species considered is the collision term on the right hand side.

Neutrinos

For the sake of simplicity only massless neutrinos are considered here, for them $q = \epsilon$ and the collisional term can be neglected. To reduce the number of variables we integrate out the q -dependence from Eq. (1.55) and expand the angular dependence of the perturbation Ψ in a series of Legendre polynomials $P_\ell(\hat{k} \cdot \hat{n})$:

$$F_\nu(\mathbf{k}, \hat{n}, \tau) \equiv \frac{\int q^3 dq f_0(q) \Psi}{\int q^3 dq f_0(q)} \equiv \sum_{\ell=0}^{\infty} (-i)^\ell (2\ell + 1) F_{\nu\ell}(\mathbf{k}, \tau) P_\ell(\hat{k} \cdot \hat{n}). \quad (1.56)$$

1. Basics of modern cosmology

Integrating Eq. (1.55) over $q^3 dq f_0(q)$ and dividing it by $\int q^3 dq f_0(q)$, the Boltzmann equation becomes

$$\frac{\partial F_\nu}{\partial \tau} + ik\mu F_\nu = -\frac{2}{3}h' - \frac{4}{3}(h' + 6\eta')P_2(\mu), \quad (1.57)$$

where $\mu = \hat{k} \cdot \hat{n}$. By using the Legendre expansion (1.56) we obtain for the perturbations δ_ν, θ_ν and σ_ν defined in Eqs. (1.42) to (1.44):

$$\delta'_\nu = -\frac{4}{3}\theta_\nu - \frac{2}{3}h', \quad \theta_\nu = k^2 \left(\frac{1}{4}\delta_\nu - \sigma_\nu \right), \quad (1.58)$$

$$F'_{\nu 2} = 2\sigma'_\nu = \frac{8}{15}\theta_\nu - \frac{3}{5}kF_{\nu 3} + \frac{4}{15}(h' + 6\eta'), \quad (1.59)$$

$$F'_{\nu \ell} = \frac{k}{2\ell + 1} [lF_{\nu(\ell-1)} - (\ell + 1)F_{\nu(\ell+1)}], \quad \ell \geq 3. \quad (1.60)$$

Starting from the Boltzmann equation we have obtained an infinite hierarchy of equations for the multiple moments of the distribution function. The hierarchy is usually truncated at some ℓ_{\max} ; most of the codes that numerically solve the Boltzmann hierarchy apply the truncation scheme proposed in Ref. [15], which is designed to minimize artificial reflection of power from ℓ_{\max} back to lower multipoles [20].

Photons

Photons can be treated similarly to massless neutrinos, but in this case the collisional terms cannot be neglected because, before recombination photons are tightly coupled with baryons via Thomson scattering, and even after recombination there is some residual energy transfer between the two species. Additionally, photons are linearly polarized in the plane perpendicular to their propagation direction \hat{n} . This is due to the fact that Thomson scattering produces linear polarization of the scattered radiation when the incident radiation field has a quadrupole moment [18]. Before recombination photons and baryons are tightly coupled and no quadrupole can be formed, near the end of recombination, due to rarer interactions between photons and electrons, a quadrupole moment forms and causes the polarization of the CMB [21].

It is common to consider the sum of phase space densities in the two polarization states for each k and \hat{n} , $F_\gamma(\mathbf{k}, \hat{n}, \tau)$, defined as in equation (1.56), and the difference $G_\gamma(\mathbf{k}, \hat{n}, \tau)$. Their explicit expressions together with the collision factor can be found in Ref. [15], while the Boltzmann equations are:

$$\delta'_\gamma = -\frac{4}{3}\theta_\gamma - \frac{2}{3}h', \quad (1.61)$$

$$\theta'_\gamma = k^2 \left(\frac{1}{4}\delta_\gamma - \sigma_\gamma \right) + a n_e \sigma_T (\theta_b - \theta_\gamma), \quad (1.62)$$

$$\sigma'_\gamma = \frac{4}{15}\theta_\gamma - \frac{3k}{10}F_{\gamma 3} + \frac{2}{15}(h' + 6\eta') - \frac{a n_e}{20}\sigma_T(18\sigma_\gamma - G_{\gamma 0} - G_{\gamma 2}), \quad (1.63)$$

$$F'_{\gamma \ell} = \frac{k}{2\ell + 1} [lF_{\gamma(\ell-1)} - (\ell + 1)F_{\gamma(\ell+1)}] - a n_e \sigma_T F_{\gamma \ell}, \quad \ell \geq 3, \quad (1.64)$$

1.6. The inhomogenous Universe

where the subscripts b and γ refer to baryons and photons respectively, $\sigma_T = 0.6652 \times 10^{-24} \text{ cm}^{-2}$ is the Thomson cross-section and n_e is the proper mean density of the electrons. The term $an_e\sigma_T(\theta_b - \theta_\gamma)$ in Eq. (1.62) describes the interaction with baryons which transfers momentum and energy between the two components. The hierarchy for photons is truncated in the same manner as for massless neutrinos.

Cold dark matter

CDM is described as a pressureless perfect fluid $\omega = \omega' = 0$ with zero anisotropic pressure $\sigma_c = 0$, interacting with other species only through gravity, thus the collisional term is zero. Since in the synchronous gauge we work in the rest frame of CDM $\theta_c = 0$, the only equation for CDM is $\delta'_c = -h'/2$.

Baryons

Baryons are also described as perfect fluids but are tightly coupled to photons by Thomson scattering, and the Boltzman equations are [15]

$$\delta'_b = -\theta_b - \frac{1}{2}h', \quad (1.65)$$

$$\theta'_b = -\mathcal{H}\theta_b + c_s^2 k^2 \delta_b + \frac{4\bar{\rho}_\gamma}{3\bar{\rho}_b} a n_e \sigma_T (\theta_\gamma - \theta_b), \quad (1.66)$$

where $c_s^2 = \delta p / \delta \rho$ is the baryon sound speed squared.

Tight coupling approximation

At early times, the scattering rate for photon-baryon interaction $\Gamma_{\gamma b} \equiv 1/t_{\gamma b} \simeq n_e \sigma_T$ is larger than the Hubble rate $\Gamma_H \equiv 1/t_H \simeq (a\tau)^{-1}$, therefore any deviation of $\theta_\gamma - \theta_b$ from zero rapidly decays away. Deep in the radiation era we can then set $\theta_b = \theta_\gamma = \theta_{\gamma b}$, i.e. a tight coupling between baryons and photons. Combining (1.62) and (1.66) in such a way that the scattering terms cancel we get [22]:

$$\left(\frac{4}{3}\Omega_\gamma - \Omega_b\right) \theta'_{\gamma b} = -\Omega_b \mathcal{H} \theta_{\gamma b} + \frac{1}{3}\Omega_\gamma k^2 \delta_\gamma, \quad (1.67)$$

and neglecting the scattering terms in the equations for the density contrasts they become

$$\delta'_b = -\theta_{\gamma b} - \frac{1}{2}h', \quad \delta'_\gamma = -\frac{4}{3}\theta_{\gamma b} - \frac{2}{3}h'. \quad (1.68)$$

1.6.5 Initial conditions

In order to solve the Einstein-Boltzmann system of differential equations it is necessary set the initial conditions for the metric and density perturbation. Initial conditions are linked to the spectra of primordial perturbations produced by inflation and we will focus only on adiabatic initial perturbations since they are predicted by the simplest

1. Basics of modern cosmology

inflationary models [23] and this hypothesis is also supported by the small amount of isocurvatures allowed by CMB data [24]. These initial values for the cosmological fluctuations are usually set deep in the radiation era but after the neutrinos decoupling.

In the radiation era $a \sim \tau$ and $\mathcal{H} \sim \tau^{-1}$ and we consider scales which are outside the horizon³: $k\tau \ll 1$.

Adiabatic perturbations

In the matter and radiation plasma before the equivalence the entropy per matter particle is given by $\Gamma = T^3/n_m$ with n_m the number density of matter particles. The entropy perturbation is then defined as

$$\mathcal{S} \equiv \frac{\delta\Gamma}{\Gamma} = 3\frac{\delta T}{T} - \delta_m = \frac{3}{4}\delta_r - \delta_m, \quad (1.69)$$

where $\rho_r \propto T^4$ has been used in the last equality. The requirement for the entropy perturbation to vanish is

$$\delta_\gamma \simeq \delta_\nu \simeq \frac{4}{3}\delta_c \simeq \frac{4}{3}\delta_b. \quad (1.70)$$

Fluctuations satisfying the above equations are called adiabatic or iso-entropic. They perturbations are characterized by the fact that the fractional perturbations in number density are the same for both radiation and non-relativistic matter. This global perturbation to the total energy density leads through the Einstein equations to a perturbation to the local geometry of the Universe. Matter perturbations that do not contribute to the curvature perturbation at the leading order are possible and they are called isocurvature (or entropy) perturbations. As already anticipated, isocurvatures are strongly constrained by CMB data [24].

For these reasons, the initial conditions are commonly set to be adiabatic, they take the following form in the synchronous gauge [15, 22]:

$$h = C(k\tau)^2, \quad \eta = 2C - \frac{5 + 4R_\nu}{6(15 + 4R_\nu)}C(k\tau)^2, \quad (1.71)$$

$$\delta_\gamma = -\frac{2}{3}C(k\tau)^2, \quad \delta_c = \delta_b = \frac{3}{4}\delta_\nu = \frac{3}{4}\delta_\gamma, \quad (1.72)$$

$$\theta_c = 0, \quad \theta_\gamma = \theta_b = -\frac{1}{18}C(k^4\tau^3), \quad \theta_\nu = \frac{23 + 4R_\nu}{15 + 4R_\nu}\theta_\gamma, \quad (1.73)$$

$$\sigma_\nu = \frac{4C}{3(15 + 4R_\nu)}(k\tau)^2, \quad (1.74)$$

where $R_\nu = \rho_\nu/(\rho_\nu + \rho_\gamma)$ is the neutrino fraction and C is connected to the primordial power spectrum of fluctuations.

³ k is a superhorizon scale if $k\tau < 1$ while it is a subhorizon mode when $k\tau > 1$.

The curvature perturbation

Adiabatic perturbations give rise to constant curvature fluctuations. The gauge-invariant comoving curvature perturbation can be defined in terms of the Bardeen potentials as [25]

$$\mathcal{R} = -\Psi_B - \frac{2}{3(1+\omega)\mathcal{H}}(\Psi'_B + \mathcal{H}\Phi_B), \quad (1.75)$$

and it obeys the following evolution equation [25]:

$$\mathcal{R}' = \frac{2}{3(1+\omega)\mathcal{H}} k^2 \left[c_s^2 \Phi_B + \frac{1}{3}(\Phi_B - \Psi_B) \right] + 3\mathcal{H} c_s^2 \mathcal{S}. \quad (1.76)$$

From the equation above it's clear that the on superhorizon scales ($k \ll \mathcal{H}$) the curvature perturbation remain constant if the fluctuation is adiabatic ($\mathcal{S} = 0$). For this reason adiabatic perturbations are also called curvature perturbations.

Conventionally the primordial power spectrum is usually given for the comoving curvature perturbation \mathcal{R} whose form, predicted by inflation, is

$$P_{\mathcal{R}}(k) = \frac{2\pi^2}{k^3} A_s \left(\frac{k}{k_\star} \right)^{n_s-1}, \quad (1.77)$$

where k_\star is called the pivot scale and it is usually chosen to be $k_\star = 0.05 \text{ Mpc}^{-1}$, A_s is the amplitude of the primordial power spectrum and n_s its spectral tilt. The last two are free parameters of the model and they have to be fitted to the data when analyzing a cosmological dataset. For $n_s = 1 (\simeq 1)$ the power spectrum is said to be scale invariant (nearly scale invariant), in the sense that the dimensionless power spectrum $\Delta_{\mathcal{R}} \equiv k^3 P_{\mathcal{R}}(k)/(2\pi^2)$ is scale invariant.

Thus, once the initial conditions are given and the primordial power spectrum has been given or computed from an inflationary model, it is possible to solve the Einstein-Boltzmann equations for the cosmological perturbations and relate in this way the initial conditions from inflation to the late-time observables. In fact, the power spectrum of a given variable at a given time can be connected to the primordial power spectrum in the following way

$$P_A(\tau, k) = \mathcal{T}_A^2(\tau, k) P_{\mathcal{R}}(k) \equiv \left[\frac{A(\tau, \mathbf{k})}{\mathcal{R}(\mathbf{k})} \right]^2 P_{\mathcal{R}}(k), \quad (1.78)$$

where \mathcal{T} is called transfer function and there is no time dependence for \mathcal{R} since it can be evaluated at a time early enough such that $k \ll \mathcal{H}$. It is customary to normalize $\mathcal{R}(\mathbf{k}) = 1$. The transfer function is only a function of k , not \mathbf{k} , since the equations of motions for all perturbations do not depend on the direction of the wave vector in order to respect isotropy.

The task of solving the Einstein-Boltzmann equation to obtain the transfer functions is usually carried out numerically using dedicated codes called Einstein-Boltzmann codes, the most widespread ones are CLASS⁴ [20, 26] and CAMB⁵ [27].

⁴https://lesgourg.github.io/class_public/class.html

⁵<https://camb.info/>

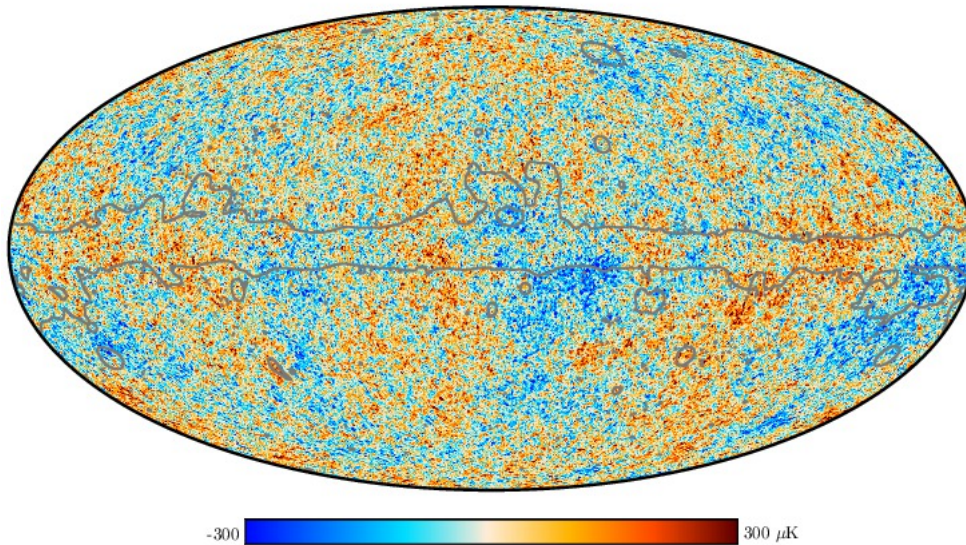


Figure 1.2: Full sky *Planck* CMB temperature map. Figure taken from [12].

1.7 Cosmological observations

In this section we outline some of the most important observational probes used in cosmology to test physical models of the Universe, presenting also some the key observational campaigns (past or present) relative to each probe. This overview is not comprehensive of all the probes employed in modern cosmology and relative experiments, moreover for the observables relevant for the *Euclid* mission⁶ we will give a more thorough treatment when needed, in the following chapters.

1.7.1 Cosmic microwave background

After recombination, which happened at $z_{\text{rec}} \simeq 1100$, photons and baryons decouple and radiation is free to propagate as the Universe becomes transparent to light. This stream of photons constitutes the CMB. The CMB has a black-body spectrum with a temperature of $T_{\text{CMB}} = 2.72548 \pm 0.00057$ [28]. It is observed to be isotropic on the sky, with temperature anisotropies of the order $\Theta \equiv \delta T/T \sim 10^{-5}$, these are the imprints of the primordial density fluctuations. The most accurate map of the CMB anisotropies in temperature is shown in Fig. 1.2 and comes from the *Planck* mission [12].

It is possible to compress the information encoded in the CMB anisotropies maps into the angular power spectrum expanding the temperature anisotropy $\Theta(\theta, \varphi)$ on the sky in terms of spherical harmonics:

$$\Theta(\theta, \varphi) = \sum_{\ell=1}^{\infty} \sum_{m=-\ell}^{\ell} a_{\ell m} Y_{\ell m}(\theta, \varphi), \quad (1.79)$$

⁶https://www.esa.int/Science_Exploration/Space_Science/Euclid

1.7. Cosmological observations

where the multipole ℓ is related to an angular scale $\theta \sim 2\pi/\ell$, while the index m describes angular orientation. The multipole coefficients $a_{\ell m}$ represents deviation from the average temperature and therefore their expectation value is null, $\langle a_{\ell m} \rangle = 0$, but they have a nonzero variance. This variance, for Gaussian fluctuations, can be fully described by the angular power spectrum

$$\langle a_{\ell' m'}^* a_{\ell m} \rangle = \delta_{\ell\ell'} \delta_{mm'} C_\ell^{\text{TT}}, \quad (1.80)$$

with $\langle \rangle$ representing the ensemble average. We cannot average over an ensemble of different realizations of the sky as we are limited to only one Universe, so ideally, if we could measure the temperature over the full sky without any noise, the observed power spectrum would be a quantity averaged over m

$$C_\ell^{\text{obs}} = \frac{1}{2\ell + 1} \sum_{m=-\ell}^{m=\ell} |a_{\ell m}|^2. \quad (1.81)$$

This introduces a limitation, known as *cosmic variance*, on how accurately the CMB angular power spectrum can be known, due to the fact that we can average only over a finite number $(2\ell + 1)$ of independent modes for each multiple ℓ . For a given C_ℓ , the error associated to cosmic variance is [9]

$$\Delta C_\ell = \sqrt{\frac{2}{2\ell + 1}} C_\ell. \quad (1.82)$$

CMB temperature anisotropies can be divided into primary and secondary anisotropies. The primary anisotropies were already present at the time of decoupling while the secondary ones originated during the propagation of the photons from the last scattering surface to us, they thus provide information about structure formation.

Primary anisotropies are the result of different processes happening at different scales. On super-Hubble scales the photons are only subject to the gravitational interaction. Due to the presence of inhomogeneities in the gravitational potential, the photons originating in overdense regions have to climb out of a potential well, losing energy for gravitational redshift. The opposite happens to a photon rolling down a potential hill. This mechanism causes a variation in the temperature contrast $\Theta = \psi_N = \Psi_B$, where ψ_N is the gravitational potential defined in Eq. (1.37). This effect is compensated partially by a gravitational time delay: a photon originating in an overdense region is scattered at a slightly earlier time and thus at a higher temperature compared to a photon from a region of average or below average density. This contributes as $\Theta = -2\psi_N/3$, and the resulting net effect is $\Theta = \psi_N/3$, which is known as *Sachs-Wolfe effect* [29]. Since on large scales we have $2\psi_N = -\delta$, the hot (cold) spots in the CMB corresponds to underdense (overdense) regions.

On sub-Hubble scales there are acoustic oscillations, called baryon acoustic oscillations (BAO), due to the fact that the baryon-photon fluid falls in the potential wells created by the dark matter perturbations and gets compressed in the process, leading to an increase in the radiation pressure which counteracts the compression, and resulting in an oscillating behaviour of the fluid. In the density peaks of these sound waves, the baryon-photon fluid is adiabatically compressed and thus hotter than the average, viceversa for

1. Basics of modern cosmology

the bottoms. Both contribute to the CMB power spectrum because it is quadratic in the perturbations and therefore we expect peaks corresponding to the scales that were in the extrema of their oscillations at z_{dec} , even peaks for rarefaction and odd peaks for compression. We can see in the top panel of Fig. 1.3 these acoustic peaks. The first peak, at $\ell \simeq 220$, corresponds to the angular scale of the horizon at recombination ($\theta \simeq 1.6^\circ$), and it can give us an estimate of the total density parameter.

At the smallest scales ($\ell > 1000$) the dominating process is the so-called *Silk damping*: the perfect fluid approximation for the photon-baryon fluid is not valid at these scales due to the finite mean free path of photons, and the two components are effectively decoupled. Under a certain characteristic size called the Silk scale, the temperature fluctuations are therefore erased by the diffusion of photons and primary CMB anisotropies are damped on the smallest angular scales (less than few arcmins).

Secondary anisotropies consists of several effects, some of the most relevant are:

- Integrated Sachs-Wolfe effect (ISW): in a matter dominated universe the Bardeen potentials are constant and photons enter and leave a potential well with their frequency being unaffected: the blue shift that the photons acquire by falling into a gravitational potential is exactly cancelled by the redshift induced by climbing out of it. This is no longer true in a universe with a significant contribution coming from dark energy or radiation: in this scenario the gravitational potentials vary with time shifting the frequency of the photons. The contribution to the temperature fluctuations induced by the change of the gravitational potential due to the residual radiation after decoupling is called *early* ISW effect. Instead, in the late Universe, when we enter the dark energy dominated era, the gravitational potentials start to decay causing a further contribution to the temperature fluctuations. This is known as the *late* ISW (LISW) effect and we will discuss in the following how it can be probed by studying the cross correlation between *Euclid* and CMB data.
- The thermal Sunyaev–Zeldovich effect: CMB photons passing through clusters of galaxies or other regions of dense and hot gas are inverse Compton scattered by the hot electrons causing a localized spectral distortion of the black body.
- Gravitational lensing: the photons of the CMB are deflected by the gravitational fields of the large scale structure (LSS) of matter and we observe them coming from a slightly different direction. The lensing of the CMB smooths the acoustic peaks in the temperature power spectrum and generates a peculiar signal in the polarization of the CMB on small scales. CMB lensing also induces a nonzero four point correlation function which can be used to reconstruct the lensing potential ϕ and its power spectrum $C_\ell^{\phi\phi}$ [5]. The details of the CMB lensing power spectrum and its reconstruction will be addressed in sections 3.3.2 and 4.2.

In the CMB there is more information than the one contained in its temperature fluctuations. Indeed, because of the Thomson scattering between baryons and photons before recombination, the CMB is also linearly polarized. This polarization is described by using combinations of the Stokes parameters Q and U commonly used to characterize the polarization of a radiation field. These non-local combinations of Q and U are called E and B modes [30]. E-mode polarization (as Θ) is produced by all type of

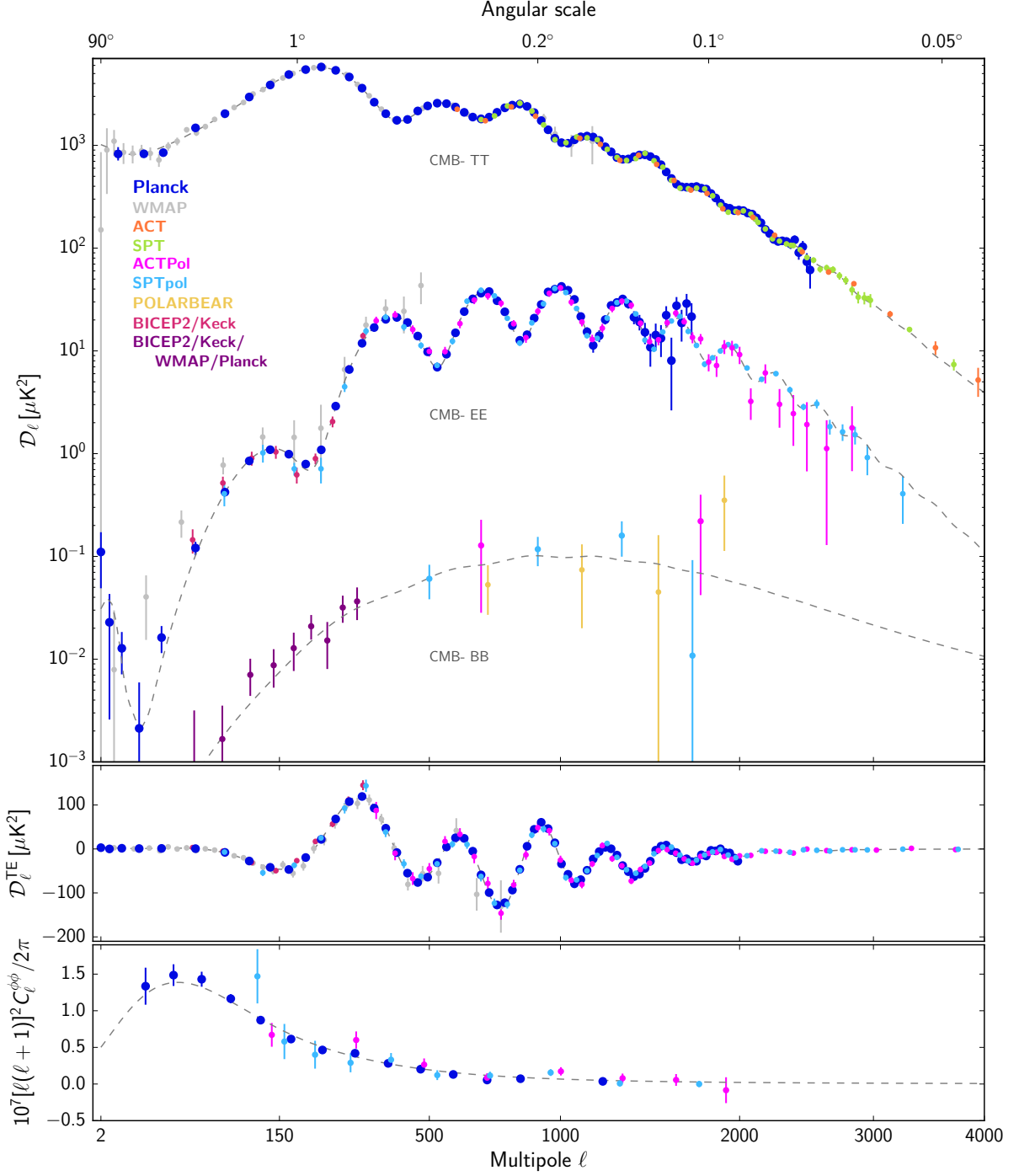


Figure 1.3: Compilation of CMB angular power spectrum measurements. The upper panel shows the power spectra of the temperature and E-mode and B-mode polarization signals, the next panel the cross-correlation spectrum between T and E, while the lower panel shows the lensing deflection power spectrum. The quantity D_ℓ is defined by $D_\ell \equiv \ell(\ell + 1)C_\ell/(2\pi)$. Different colours correspond to different experiments, each retaining its original binning. For *Planck*, ACTPol, and SPTpol, the EE points with large error bars are not plotted to avoid clutter. The dashed line is the best-fit Λ CDM model to the *Planck* temperature, polarization, and lensing data. Figure Taken from [12].

1. Basics of modern cosmology

perturbations - scalar, vector, tensor - whereas B-mode polarization only by vector and tensor perturbations. Θ and E-modes are correlated, while the ΘB and EB correlations are nonzero only in presence of parity violating processes in the generation of the initial fluctuations. Primordial B-mode polarization (generated by primordial gravitational waves or primordial magnetic fields) is obscured by the parasitic gravitational lensing signal, which causes the blurring of E-mode polarization from scalar perturbations along the line of sight. In analogy to the temperature field angular power spectrum, the power spectra for the E and B modes are

$$\langle E_{\ell'm'}^* E_{\ell m} \rangle = \delta_{\ell'm'} \delta_{\ell m} C_{\ell}^{EE}, \quad (1.83)$$

$$\langle a_{\ell'm'}^* E_{\ell m} \rangle = \delta_{\ell'm'} \delta_{\ell m} C_{\ell}^{TE}, \quad (1.84)$$

$$\langle B_{\ell'm'}^* B_{\ell m} \rangle = \delta_{\ell'm'} \delta_{\ell m} C_{\ell}^{BB}. \quad (1.85)$$

In general, the link between the primordial power spectrum (1.77) and the CMB angular power spectra is given by

$$C_{\ell}^{XY} = \frac{2}{\pi} \int_0^{\infty} dk k^2 P_{\mathcal{R}}(k) \mathcal{T}_{\ell}^X(k) \mathcal{T}_{\ell}^Y(k), \quad (1.86)$$

where $\mathcal{T}_{\ell}(k)$ are the corresponding transfer functions.

A summary of the current measurements of temperature, E-mode polarization spectra and their cross correlation, together with the CMB lensing power spectrum measured by several CMB experiments is shown in Fig. 1.3. The dashed line in the figure is the Λ CDM best-fit model to the *Planck* 2018 likelihood.

In chapter 2 we will make use of CMB data in temperature, polarization, and lensing from *Planck* Data Release 3 and relative likelihoods [31, 32]. We refer to this dataset as P18 in the following.

1.7.2 Type Ia Supernovae (SNIa)

A type Ia supernovae originates from the explosion of a white dwarf that have surpassed the Chandrasekhar mass [33] through accretion of matter from a companion in a binary system [34]. All SNIa have almost identical intrinsic luminosity and their absolute magnitude is known (after calibration). For this reason and due to the fact that they can be observed at high redshifts thanks to their immense luminosity they can be used as indicators of the luminosity distance. In particular, SNIa observations measure the distance modulus μ , which is the difference between the observed and absolute magnitude of a source [35]:

$$\mu = 5 \log_{10} (d_L / 10 \text{ pc}), \quad (1.87)$$

where d_L is the luminosity distance defined in Eq. (1.14). This quantity is sensitive to Ω_m and Ω_{Λ} and for this reason the study of the SNe Ia luminosity distances led to the discovery of the accelerated expansion of the Universe [36, 37], providing the first evidence of dark energy. If calibrated, i.e. their absolute magnitude is inferred by measuring independently the distance of a sample of SNe, they can also provide a competitive measurement of the Hubble constant. Thanks to improvements in calibrations of SNe using

1.7. Cosmological observations

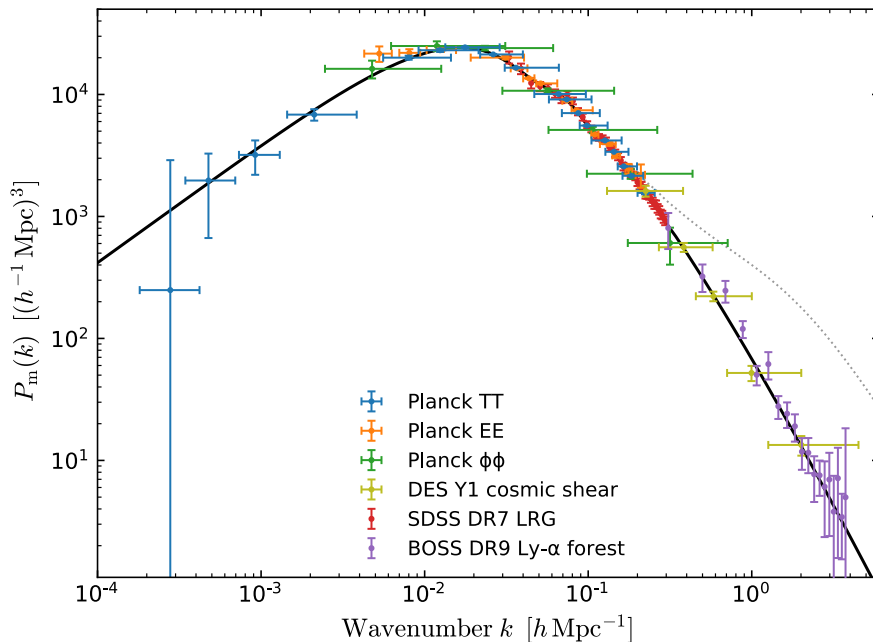


Figure 1.4: Linear matter power spectrum $P(k, z = 0)$ inferred from different cosmological probes and the Λ CDM model prediction. The dotted line represents the effect of nonlinear clustering. Figure taken from [12].

Cepheids variables and together with the expansion of catalogs, the direct measurement of the Hubble constant with SNIa is now [38]

$$H_0 = 73.04 \pm 1.04 \text{ km s}^{-1} \text{ Mpc}^{-1}. \quad (1.88)$$

This measurement is in 5σ tension with the inference in the Λ CDM model using *Planck* CMB data, which gives $H_0 = 67.36 \pm 0.54 \text{ km s}^{-1} \text{ Mpc}^{-1}$. This difference between the two estimates is known as the Hubble tension and it is one of the most discussed issues in cosmology at the moment.

In the following chapter we will use the Pantheon catalog of SNIa [39]⁷ and refer to it as SN; this dataset is comprised of 1048 measurements of the luminosity distances at redshifts $0.01 < z < 2.3$. In conjunction to this catalog we will consider a prior on the SNe peak absolute magnitude M_B [40] [hereafter $p(M)$] of $M_B = -19.2435 \pm 0.0373 \text{ mag}$, or analogously, a Gaussian prior on the Hubble constant from Eq. (1.88) [hereafter $p(H_0)$].

1.7.3 Galaxies as a probe of the matter distribution of the Universe

The distribution of matter in the Universe can be modeled using the matter power spectrum, $P_{\delta\delta}(k, z)$, which, following the conventions of Eqs. (1.77) and (1.78), is

$$P_{\delta\delta}(k, z) = 2\pi^2 A_s k^{-3} \left(\frac{k}{k_\star} \right)^{n_s-1} \left[\frac{\delta(\mathbf{k}, z)}{\mathcal{R}(\mathbf{k})} \right]^2, \quad (1.89)$$

⁷<https://github.com/dscolnic/Pantheon>

1. Basics of modern cosmology

where, the function $\delta(\mathbf{k}, z) = (\delta\rho_c + \delta_b)/(\rho_c + \rho_b)$ is the matter density contrast at a given scale and redshift. Its late-time evolution in the Λ CDM model can be written as [18]

$$\delta(\mathbf{k}, z) = \delta(\mathbf{k}, \tilde{z}) \frac{D(z)}{D(\tilde{z})}, \quad (1.90)$$

where \tilde{z} is an arbitrary redshift corresponding to the beginning of matter domination, while $D(z)$ is the so-called growth factor, usually normalized to unity today.

Fig. 1.4 shows the matter power spectrum inferred from different cosmological probes and the Λ CDM prediction, which fits the data quite well, as the black continuous line, while the dotted line shows the impact of nonlinear clustering at $z = 0$. Nonlinear clustering is relevant when the density contrast is $\delta \geq 1$; in this regime, the formalism we detailed in section 1.6 is no longer valid. The breakdown of linear perturbation theory is more relevant on small scales and the onset of the nonlinear regime corresponds to a scale $k_{NL} \simeq 0.25 h \text{Mpc}^{-1}$ today. There are several prescription developed to take into account nonlinearities, the two most used ones, obtained by fitting of cosmological simulations, are `halofit` [41–43] and `HMcode` [44, 45].

The shape of the matter power spectrum depends on the evolution of the perturbations, which in turn depend on gravity; it presents a turnover at a scale of $k_{\text{eq}} \simeq 2 \times 10^{-2} h \text{Mpc}^{-1}$ corresponding to the scale that enters the Hubble radius at matter-radiation equality. The growth of structure on smaller scales, that entered the horizon during the radiation era, is suppressed, this is the reason why the matter power spectrum is a decreasing function of k for $k > k_{\text{eq}}$.

The key question is how we can infer the matter distribution from observations of astronomical objects, mainly galaxies. There are several probes that make use of galaxies to study the matter distribution of the Universe among which I will briefly introduce here galaxy clustering, BAO, and weak lensing (WL) citing current observation, while giving a more thorough description of these probes in the context of the *Euclid* mission in chapter 3.

Galaxy clustering

Galaxy clustering refers to the three dimensional distribution of galaxies in the Universe, obtained by measuring their angular coordinates on the sky and their redshifts. Since the statistical distributions of galaxies depends on the cosmological model, measuring their positions provides valuable information to validate/invalidate models and constrain their parameters. By measuring the positions of galaxies we are not directly probing the matter distribution of the Universe, which is mostly dark matter, but we can use galaxies as a tracer of the underlying matter distribution. For this reason we need a modelling for the relation between the galaxy and matter distribution, the so called galaxy bias. In the linear regime, the galaxy overdensity can be related to the total matter overdensity by a scale independent galaxy bias $b(z)$ as

$$\delta_g = b(z)\delta. \quad (1.91)$$

Although introduced here in general for galaxies, different biases link the matter density contrast to other matter tracers, such as different types of galaxies or clusters of galaxies.

1.7. Cosmological observations

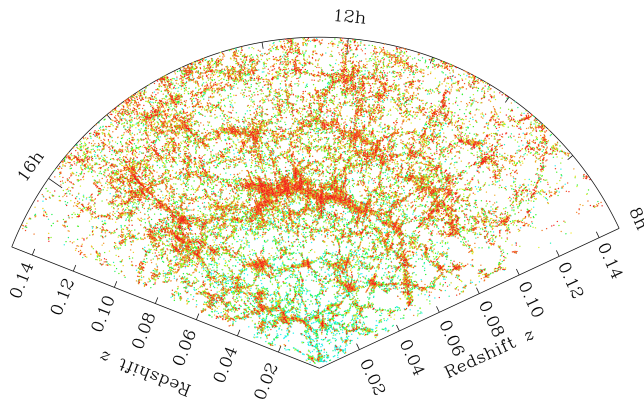


Figure 1.5: Sloan Digital Sky Survey (SDSS) galaxy map: A slice of the universe showing the large-scale structure of galaxies in the northern sky, with us situated at the bottom center. Each dot is a galaxy and the color corresponds to the color of the galaxy (red dots represent redder galaxies) the green-red color of that galaxy (Credit: M. Blanton and Sloan Digital Sky Survey).

The bias can depend on the scale k .

Additionally, the positions of galaxies are estimated from the measurement of their redshifts, which depends on two effects: the redshift due to the cosmological expansion and the redshift (or blueshift) due to peculiar motions. Therefore, the positions of galaxies appear squashed in redshift space, due to the additional Doppler shift caused by peculiar velocities, in addition to the redshift caused by the Hubble flow. We distinguish between redshift space, where galaxy positions are estimated by their redshift, and real space, which corresponds to the actual position of galaxies; the relationship between the redshift space galaxy power spectrum P_{gg} and the real-space matter power spectrum $P_{\delta\delta}$ is

$$P_{gg}(k, \mu_k, z) = [b(z) + f(z)\mu_k^2]^2 P_{\delta\delta}(k, z), \quad (1.92)$$

where $b(z)$ is the galaxy bias previously introduced and the last term in the square bracket describes the RSD at linear level [46]. There, $\mu_k \equiv \hat{k} \cdot \hat{n}$ is the cosine of the angle between the line of sight and the wavevector \mathbf{k} , and $f(z)$ is the linear growth rate defined by $f \equiv d \ln D(a) / d \ln a$.

The observational campaigns that measure galaxy clustering are called galaxy redshift survey surveys and they are classified in two main categories: spectroscopic and photometric surveys, depending on how the redshifts of the galaxies are obtained. In spectroscopic surveys, the spectra of the source is measured and then compared with a source of the same kind with known emission or absorption lines, looking for characteristic features. In photometric surveys the light coming from a galaxy passes through several filters and it is therefore observed in different wavelength bands, this allows to convert the images into low resolution spectra and the redshift is obtained with a fit to a template spectral energy distribution (SED) of a galaxy. The main advantage of photometry is its speed: in a photometric survey it is possible to collect a larger amount of redshifts in the same amount of time, compared to an analogous spectroscopic survey, which, although more precise, will have a smaller sample. The drawbacks of photometric surveys are the systematics errors, which can be difficult to evaluate and extremely

1. Basics of modern cosmology

pernicious if not treated properly.

The first systematic galaxy redshift survey was the *Center for Astrophysics (CfA) redshift Survey* [47], which started in 1977 and measured the redshifts of more than 14 000 galaxies up to about $z \simeq 0.05$. Examples of more modern galaxy surveys are the *Sloan Digital Sky Survey (SDSS)*⁸ and the *Dark Energy Survey (DES)*⁹. SDSS is comprised by a series of photometric and spectroscopic surveys which are ongoing since the year 2000. The last data release of SDSS-IV, containing more than 1.5 million galaxies, was in 2020 [48]. Fig. 1.5 shows the map of galaxies constructed by SDSS in the northern sky up to redshift $\simeq 0.14$, where each point represents a galaxy.

DES, instead, is a photometric survey, which covered an area of 5000 square degrees on the sky and observed more than 300 million galaxies. They have provided results obtained from the photometric survey alone in [49] but the most stringent constraints come from the combination with WL measurements [50]. This combination of DES data is consistent with the *Planck* analysis of CMB data. Also SDSS results on the determination of the Hubble constant agree with the *Planck* value [48].

Baryon acoustic oscillations

The peaks and troughs observed in the CMB temperature angular power spectrum (Fig. 1.3) originate from the acoustic oscillations in the baryon-photon fluid described in section 1.7.1. These oscillations affect the baryons; in fact, after decoupling from the photons, at around $z_d \simeq 1020$, a time called baryon drag, the sound waves remain imprinted in the baryon distribution and, through gravitational interactions, in the dark matter distribution as well. Thus, dark matter will tend to cluster more on this scale and galaxies will be more likely to form in correspondence of this BAO scale, which is determined by the comoving sound horizon at baryon drag r_d . This preferred scale, expected to be observed in the baryon distribution in the Universe appears in observations as a preferred angular separation of galaxies in the transverse direction, and a preferred redshift separation of galaxies along the line of sight.

BAO were first observed by the Two-degree-Field Galaxy Redshift Survey as oscillations in the power spectrum of galaxies [57], and by the SDSS [51] as an uptick in the 2-point correlation function (excess probability of finding two galaxy at a certain distance with respect to a random distribution), in correspondence of the BAO scale. The latter result is shown in the left panel of Fig. 1.6.

The fact that galaxies have a preferred clustering scale can be used to probe the expansion of the Universe, in fact BAOs measurements in the transverse direction constrain the acoustic scale ratio $D_V(z)/r_d$, where r_d is measured by CMB data to be about 147 Mpc, while the distance D_V is

$$D_V(z) = \left(D_A^2(z) \frac{cz}{H(z)} \right)^{1/3}. \quad (1.93)$$

The BAO measurements in the radial direction, instead, constrain the product $H(z)r_d$ and since r_d is precisely measured from *Planck* data, the BAO measurement corresponds

⁸<https://www.sdss.org/>, <https://www.sdss4.org/>, <https://classic.sdss.org/home.php>

⁹<https://www.darkenergysurvey.org/>

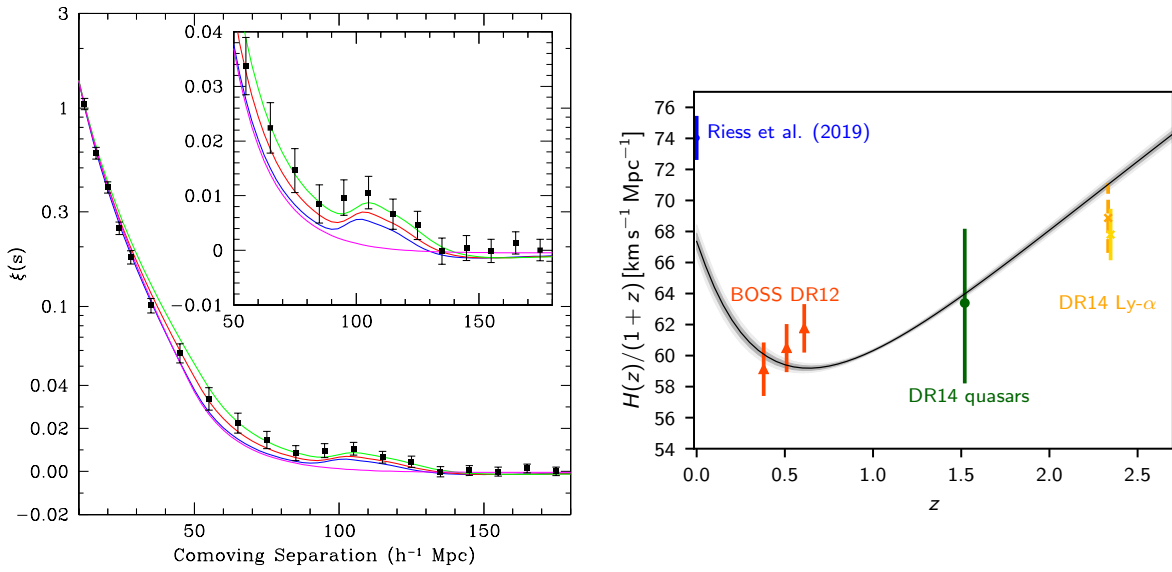


Figure 1.6: **Left:** two point correlation function of galaxies. The data points come from SDSS and the solid lines correspond to predictions of different cosmological models; the magenta corresponds to a ΛCDM model with no baryons, showing the statistical significance of the peak. Taken from [51]. **Right:** comoving Hubble parameter as a function of redshift. The data points corresponds to measurements coming from BAO [52–55] and, at $z = 0$, from Supernovae [56]. The narrow grey bands are the *Planck* 68% and 95% confidence level ranges in ΛCDM . The plot shows the onset of acceleration around $z = 0.6$. Taken from [1].

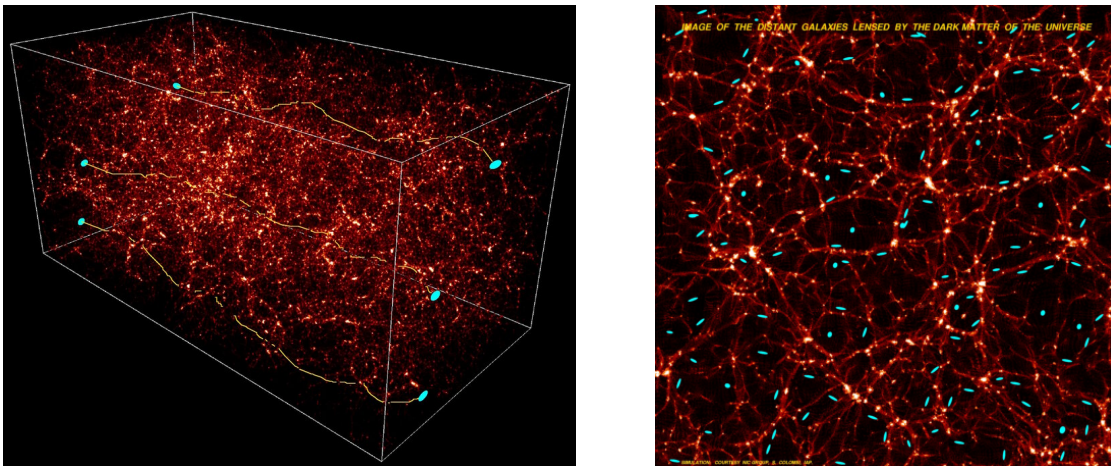


Figure 1.7: **Left:** Illustration of the deflection of the light rays of three distant galaxies as they cross the Universe (Copyright CNRS/IAP/Colombi/Mellier). **Right:** effect of the propagation of light through the LSS of the Universe on the observed shapes of galaxies.

to a measurement of the Hubble parameter (right panel of Fig. 1.6).

In chapter 2 we will use BAO data from BOSS DR12 [52]; low- z BAO measurements from SDSS DR7 and 6dF [58, 59]; Lyman-alpha forest BAO measurements from eBOSS DR14, and a combination of those [54, 55, 60]. Hereafter we call this combination of datasets simply BAO. We will also consider the full shape (hereafter FS) of BOSS DR12 power spectrum measurements [61, 62].

Weak lensing

Another important approach to study the matter distribution of the Universe is to observe the shape of galaxies. General relativity predicts gravitational lensing, i.e., that light coming from an astronomical source is deflected by intervening matter along the line of sight; when the deflection is large the effect is called strong lensing. To map the matter in the Universe, it is more relevant to study the opposite regime, called weak-lensing: on traversing the inhomogeneous matter distribution in the Universe, light rays from distant galaxies are weakly deflected and distorted, causing a subtle change in the shape of observed galaxies. This effect is known as *cosmic shear* and it is illustrated in Fig. 1.7. Therefore, in principle, by measuring the shapes of images, the gravitational field of the large scale structure of the Universe can be mapped, and, consequently we can infer the matter distribution. Cosmic shear is a very small effect: it typically causes a distortion in the image of a source much smaller than the intrinsic ellipticity of galaxies. However, it is still possible to measure cosmic shear by statistically averaging all these small distortions [63]; in fact, the distortion in the shape of close galaxies is alike since their light rays are crossing similar gravitational fields, and since there are no preferred directions in the intrinsic random orientation of galaxies it is thus possible to measure the distortion which has a preferred direction.

The shear field is the results of the projection of the three-dimensional gravitational field along the line-of-sight, in fact, we can write a mapping between the lensed (image)

1.8. Summary of the standard model of cosmology

coordinates $\boldsymbol{\theta}$ to the unlensed (source) coordinates $\boldsymbol{\beta}$ as an integral along the line of sight:

$$A_{ij} \equiv \frac{\partial \beta_i}{\partial \theta_j} - \delta_{ij} = -2 \int_0^{\chi_s} d\chi f_K(\chi) \frac{f_K(\chi_s - \chi)}{f_K(\chi_s)} \partial_i \partial_j \phi_N(\mathbf{x}(\boldsymbol{\theta}, \chi)) \quad (1.94)$$

where i, j represent the directions on the sky and χ_s is the comoving distance to the source, $\phi_N = \Phi_B$ is the gravitational potential defined in Eq. (1.37), equal to the Bardeen potential (1.35), and f_K was defined in Eq. (1.11). The matrix A_{ij} is usually parametrized as

$$A_{ij} = \begin{pmatrix} 1 - k - \gamma_1 & -\gamma_2 \\ -\gamma_2 & 1 - k + \gamma_1 \end{pmatrix}, \quad (1.95)$$

where k , which encodes the magnification of the image, is called *convergence*, and γ_1 , and γ_2 are the components of the shear, as they describes the distortion in the shapes of the images.

The first measurements of cosmic shear were reported in the year 2000 by several groups almost simultaneously [64–66], since then several refined measurements followed. As anticipated earlier in the context of galaxy redshift surveys, DES provides, in addition to galaxy clustering measurements, cosmic shear observation and cross correlation with galaxy clustering. Cross correlating galaxy clustering with cosmic shear is not only useful to obtain tighter constrains but also to break degeneracies between parameters and to reduce systematics as they differ for each probe.

1.8 Summary of the standard model of cosmology

Parameter	Value
ω_b	0.02242 ± 0.00014
ω_c	0.11933 ± 0.00091
H_0 [km s ⁻¹ Mpc ⁻¹]	67.66 ± 0.42
τ_{reio}	0.0561 ± 0.0071
$\ln(10^{10} A_s)$	3.047 ± 0.014
n_s	0.9665 ± 0.0038

Table 1.1: Constraints from [1] on the Λ CDM parameters at 68% CL considering the combination **P18+BAO**.

The standard cosmological model, also known as the Λ CDM model or concordance model, explains successfully the current cosmological observations described in section 1.7. This model assumes flat spatial sections ($\Omega_k = 0.001 \pm 0.002$ [1]), postulates all dark matter to be cold and that the current acceleration in the expansion of the Universe is due to a cosmological constant Λ . In the Λ CDM model, primordial fluctuations are Gaussian and described by the power law (1.77), with by an amplitude A_s and a spectral index n_s .

1. Basics of modern cosmology

Λ CDM fits most of the current cosmological observations with only six free parameters:

- Ω_b , the baryon energy density today,
- Ω_m , the total matter energy density today, or Ω_c , the cold dark matter energy density today,
- H_0 the Hubble constant,
- τ , the Thomson scattering optical depth at reionization,
- A_s , the amplitude of the primordial power spectrum,
- n_s the scalar spectral index of the primordial power spectrum.

It is often common to consider the following parameters $\omega_i = \Omega_i h^2$ ($i = m, b, c$) instead of directly using the density parameters, moreover, when considering galaxy clustering, the parameter σ_8 is used in place of A_s as it is more easily accessible to galaxy surveys. This parameter represents the amplitude of mass fluctuations smoothed on a scale of $8 h^{-1} \text{Mpc}$

$$\sigma_8^2 = \int \frac{dk}{k} \frac{k^3 P_{\text{lin}}(k)}{2\pi^2} |W_{\text{TH}}(kR_8)|^2, \quad (1.96)$$

where W_{TH} is a top-hat filter in Fourier space. Since A_s enters linearly in the power spectrum it is linearly related to σ_8^2 , which can then be considered as the normalization of the power spectrum. The values of the Λ CDM parameters inferred by the *Planck* collaboration using a combination of CMB and BAO data are reported in Table 1.1.

This set of parameters can be extended to study alternative models or to probe deviations from the standard model. One example is the CPL parameterization [67, 68] where the equation of state of dark energy is time dependent:

$$w_{\text{DE}}(z) = w_0 + w_a \frac{z}{1+z}, \quad (1.97)$$

consequently the model takes the name $w_0 w_a$ CDM. Other common extensions are to fit the sum of the neutrino masses to the data or the so called μ, Σ parameterization of modified gravity. Other alternatives are models built upon an underlying theory of gravity different from GR, these models often try to explain dark energy by different means than a cosmological constant and they will be the topic of chapter 2. Models where DM is composed by a mixture of cold and warm/hot dark matter are also systematically studied by the community.

There are several motivations to study extended cosmological models, the most obvious one is to compare them to the standard model in how well they can fit the data. Another one is to provide a better explanation to the nature of dark matter and dark energy. A final one is to potentially help alleviating the tensions on some Λ CDM parameters coming from different cosmological observations [69–71].

Chapter 2

Current and novel constraints on modified gravity

Einstein’s theory of General Relativity, upon which the standard cosmological model is built, has had remarkable experimental success and its extensions and modifications cannot be completely justified by experimental reasons. Motivations to look beyond GR arise naturally in the context of fundamental physics and cosmology, in fact, the nature of DE and DM is still uncertain and modifications to the laws of gravity on cosmological scales provide a possible explanation. For these reasons, a plethora of new proposals has emerged, ranging from parametrizations to probe deviations from GR [7, 72] to extensions of GR.

Scalar-tensor theories (STTs) of gravity are one of many such proposal, the first theory of this kind was originally conceived by Jordan [73] and later by Brans and Dicke [74], formalizing Dirac’s idea of a time-dependent Newton’s constant [75]. The gravitational constant is in fact a function of a time-dependent scalar degree of freedom in STTs. More formally, STTs are characterized, in addition to the metric tensor, by the presence a scalar field nonminimally coupled to the Ricci scalar R but not coupled with matter at the Lagrangian level, guaranteeing in this way that the weak equivalence principle is satisfied [76]. Therefore, the local value of the gravitational field is determined only by the distribution of matter in the Universe, incorporating in this way Mach’s principle, which states that the global distribution of matter should determine local gravitation. This is a distinctive characteristic of STTs: the cosmological distribution of matter affects local gravitational experiments and consequently the strong equivalence principle does not hold anymore [76].

In this chapter we provide a brief overview of a general class of STTs: Horndeski theories [77], and then focus on a subset of theories with a minimal set of extra parameters compared to Λ CDM, continuing the work of [78].

In sections 2.6.2 and 2.6.3 we present novel cosmological constraints on STTs, based on the research works in [79, 80].

Some of the models described in this chapter are also relevant in the context of the forecasts for the *Euclid* mission presented in chapter 5,

2.1 Horndeski action and its special cases

One of the conditions for a STT to be viable is that the scalar field does not induce an Ostrogradsky instability [81] associated with an Hamiltonian unbounded from below. To avoid this kind of instabilities it is sufficient to have at most second-order time derivatives in the equations of motion (EOM) for the scalar field (Klein-Gordon (KG) equation). Gregory Horndeski constructed in 1974 the most general STT with second order EOM [77], but its relevance for cosmology has been appreciated only recently

2. Current and novel constraints on modified gravity

with the rediscovery in the context of Galileons [82–84], which have been proved to be equivalent to Horndeski theories in Ref. [85]. The action of the theory is

$$\mathcal{S}_H = \int d^4x \sqrt{|g|} (\mathcal{L}_H + \mathcal{L}_M), \quad (2.1)$$

where $|g|$ is the absolute value of the determinant of the metric tensor $g_{\mu\nu}$, \mathcal{L}_M is the matter Lagrangian which does not depend on the scalar field and it is minimally coupled with the metric $g_{\mu\nu}$. The gravitational Lagrangian \mathcal{L}_H is given by

$$\begin{aligned} \mathcal{L}_H = & G_2(\sigma, X) + G_3(\sigma, X)\square\sigma + G_4(\sigma, X)R + G_{4,X}(\sigma, X)[(\square\sigma)^2 - (\nabla_\mu\nabla_\nu\sigma)(\nabla^\mu\nabla^\nu\sigma)] \\ & - \frac{1}{6}G_{5,X}(\sigma, X) \left[(\square\sigma)^3 - 3(\square\sigma)(\nabla_\mu\nabla_\nu\sigma)(\nabla^\mu\nabla^\nu\sigma) + 2(\nabla^\mu\nabla_\alpha\sigma)(\nabla^\alpha\nabla_\beta\sigma)(\nabla^\beta\nabla_\mu\sigma) \right] \\ & + G_5(\sigma, X)G_{\mu\nu}\nabla^\mu\nabla^\nu\sigma. \end{aligned} \quad (2.2)$$

Here, R and $G_{\mu\nu}$ are, respectively, the Ricci scalar and the Einstein tensor introduced in Eq. (1.4), σ is the scalar field and $X \equiv -\nabla_\mu\sigma\nabla^\mu\sigma/2 = -\partial_\mu\sigma\partial^\mu\sigma/2 = -(\partial\sigma)^2/2$ its kinetic term, while $\square \equiv \nabla^\mu\nabla_\mu$ is the covariant d'Alembert operator. The functions $G_{2,3,4,5}$ depend on the field σ and the kinetic term X , with $G_{i,\sigma}, G_{i,X}$ indicating the derivative of the i th G function with respect to the scalar field and the kinetic term. The Lagrangian (2.2) encompasses several models, some of them listed below.

General relativity GR itself is a subclass of Horndeski theory with the G functions given by $G_4 = M_{Pl}^2/2$ and $G_2 = G_3 = G_5 = 0$, where $M_{Pl} = 1/\sqrt{8\pi G}$ is the reduced Planck mass.

Quintessence and k-essence K-essence [86–89] corresponds to $G_2 = G_2(\sigma, X)$, $G_3 = G_5 = 0$, $G_4 = M_{Pl}^2/2$, while Quintessence [90, 91] is a subset of K-essence with $G_2 = X - V(\sigma)$ where $V(\sigma)$ is the potential of σ .

Brans-Dicke (BD) and induced gravity (IG) Brans-Dicke theory [73, 74] is often discussed by using a different symbol for the scalar field: ϕ , we follow this convention here. The theory is given by

$$G_2(\phi, \chi) = 2\frac{\omega_{BD}}{\phi}\chi, \quad G_3 = 0, \quad G_4(\phi) = \phi, \quad G_5 = 0, \quad (2.3)$$

where $\chi \equiv -\nabla_\mu\phi\nabla^\mu\phi/2$. GR is recovered in the limit $\omega_{BD} \rightarrow \infty$, and this parameter is constrained to be $\omega_{BD} > 40000$ by the Cassini probe [92]. Therefore, BD is viable in the limit of large ω_{BD} , but this fine-tuning, necessary to satisfy the experimental bounds, makes the model unappealing. To accommodate for the accelerated expansion of the Universe, BD has to be endowed with a potential $V(\phi)$ for the scalar field, which enters the G_2 in Eq. (2.3).

The BD model can be recast into an equivalent form known as *induced gravity* (IG) [93–95], the two theories are in fact connected by the field redefinition $\phi = \xi\sigma^2/2$, with

2.1. Horndeski action and its special cases

$\xi = Z/(4\omega_{\text{BD}}) > 0$, and $Z = \pm 1$ being the sign of the kinetic term. The IG action is therefore

$$\mathcal{S}_{\text{IG}} = \int d^4x \sqrt{-g} \left(\frac{1}{2} \xi \sigma^2 R - \frac{Z}{2} (\partial\sigma)^2 - V(\sigma) + \mathcal{L}_{\text{M}} \right), \quad (2.4)$$

Here, the GR limit corresponds to $\xi \rightarrow 0$. The cosmological implications of IG for $Z = 1$ have been extensively studied in [96–100] and will be discussed in section 2.6.

General nonminimally coupled (NMC) theories A generalization of IG and BD is obtained by extending the coupling function to the Ricci scalar to be an arbitrary function of the field $F(\sigma)$ [101]

$$\mathcal{S}_{\text{NMC}} = \int d^4x \sqrt{-g} \left(\frac{F(\sigma)}{2} R - \frac{Z}{2} (\partial\sigma)^2 - V(\sigma) + \mathcal{L}_{\text{M}} \right). \quad (2.5)$$

These theories have been studied initially in [102–108] and more recently, cosmological constraints have been obtained on NMC theories depending on the form of the coupling $F(\sigma)$ and the potential $V(\sigma)$. To set the nomenclature we list below some of the models encompassed by the action (2.5).

- IG itself is a special case of NMC with $F(\sigma) = \xi\sigma^2$.
- Effectively massless NMC, characterized by $F(\sigma) = N_{\text{Pl}}^2 + \xi\sigma^2$, $V(\sigma) \propto F^2(\sigma)$ and $Z = +1$, studied in [109, 110], and also in [111], where an additional parameter Δ is introduced to allow for an imbalance between the effective gravitational constant G_{eff} between two test masses, and Newton’s constant G_{N} , as $G_{\text{eff}}(z=0) = G_{\text{N}}(1 + \Delta)^2$, while $N_{\text{Pl}} = M_{\text{Pl}}$ is kept fixed. The case with $\xi = 1/6$ is the conformally coupled (CC) model, while the subclass with ξ as a free parameter is called NMC+ (NMC−) when $\xi > 0$ ($\xi < 0$).
- Early modified gravity (EMG), characterized by $F(\sigma) = M_{\text{Pl}}^2 + \xi\sigma^2$, and a generalized potential $V_{\text{EMG}}(\sigma) = \Lambda + \lambda\sigma^4/4$, always with $Z = +1$, studied in [112].

We present in section 2.6.2 novel constraints on IG, the effectively massless NMC and EMG in the so-called phantom branch ($Z = -1$), and provide Fisher forecasts for the joint analysis of data from the *Euclid* mission and several CMB experiments in chapter 5, for these models in the standard branch ($Z = +1$).

Kinetic braidings and its extensions: BDG and IGG The most general subclass of Horndeski theories consistent with the tensor propagation speed c_t equal to the speed of light is given by [113]

$$\mathcal{S} = \int d^4x \sqrt{|g|} [G_4(\sigma)R + G_2(\sigma, X) + G_3(\sigma, X)\square\sigma + \mathcal{L}_{\text{M}}]. \quad (2.6)$$

The so-called kinetic braiding [114, 115] corresponds to the minimally coupled case, i.e., $G_4 = M_{\text{Pl}}^2/2$; this can be generalized by introducing a nonminimal coupling. In particular, we consider the following G functions

$$G_2 = ZX - V(\sigma) + 4\zeta(\sigma)X^2, \quad G_3 = -2g(\sigma)X, \quad G_4 = F(\sigma)/2, \quad (2.7)$$

2. Current and novel constraints on modified gravity

We discuss novel constraints on these models in section 2.6.3.

I have presented the models that are relevant for this thesis, but the Horndeski action encompasses many others, such as $f(R)$ gravity [116–118], Gauss-Bonnet couplings [119–122], $f(\mathcal{G})$ gravity [123, 124] and others, for a complete review see [113, 125]. We also want to point out that the effective field theories (EFTs) of dark energy [126, 127] can be remapped to Horndeski theories and are therefore equivalent.

2.2 Equations of motion in a FLRW universe

We present the EOM for the action (2.6) with the G functions Eq. (2.7), because this is the most general theory we will study in the following and all the special cases we consider can be obtained by specializing the equations to the model under study. For example, once the EOM for (2.7) have been obtained, to get the IG equations one has to set $F(\sigma) = \xi\sigma^2$ and $g(\sigma) = \zeta(\sigma) = 0$.

By varying the action with respect to the metric we obtain the modified Einstein field equation

$$G_{\mu\nu} = \frac{1}{F(\sigma)} \left[T_{\mu\nu}^{(M)} + T_{\mu\nu}^{(G)} + Z(\partial_\mu\sigma\partial_\nu\sigma - \frac{1}{2}g_{\mu\nu}\partial^\rho\sigma\partial_\rho\sigma) - g_{\mu\nu}V(\sigma) + (\nabla_\mu\nabla_\nu - g_{\mu\nu}\square)F(\sigma) \right], \quad (2.8)$$

where $T_{\mu\nu}^{(M)} = -\frac{2}{\sqrt{|g|}}\frac{\delta(\sqrt{|g|}\mathcal{L}_M)}{\delta g^{\mu\nu}}$ is the energy-momentum tensor of matter and $T_{\mu\nu}^{(G)}$ is the ‘‘Galileon energy momentum tensor’’, defined as

$$T_{\mu\nu}^{(G)} = -2\left\{ g(\sigma)\nabla_\mu\sigma\nabla_\nu\sigma\square\sigma - \nabla_{(\mu}\sigma\nabla_{\nu)}[g(\sigma)(\partial\sigma)^2] + \frac{1}{2}g_{\mu\nu}\nabla_\alpha\sigma\nabla^\alpha[g(\sigma)(\partial\sigma)^2] - \frac{\zeta(\sigma)}{2}g_{\mu\nu}(\partial\sigma)^4 + 2\zeta(\sigma)\nabla_\mu\sigma\nabla_\nu\sigma(\partial\sigma)^2 \right\}, \quad (2.9)$$

with $\nabla_{(\mu}\sigma\nabla_{\nu)} \equiv \frac{1}{2}(\nabla_\mu\sigma\nabla_\nu + \nabla_\nu\sigma\nabla_\mu)$.

The KG equation for the scalar field is obtained by varying the action (2.6) with respect to the field, giving

$$\square\sigma[Z - 4\zeta(\partial\sigma)^2] - 2g\{(\square\sigma)^2 - \nabla^\mu\nabla^\nu\sigma\nabla_\mu\nabla_\nu\sigma - \nabla^\mu\sigma\nabla^\nu\sigma R_{\mu\nu}\} - 3\zeta_{,\sigma}(\partial\sigma)^4 + 4g_{,\sigma}\nabla^\mu\sigma\nabla^\nu\sigma\nabla_\mu\nabla_\nu\sigma + g_{,\sigma\sigma}(\partial\sigma)^4 - 4\zeta(\sigma)\nabla_\mu[(\partial\sigma)^2]\nabla^\mu\sigma + \frac{1}{2}F_{,\sigma}R - V_{,\sigma} = 0. \quad (2.10)$$

Considering a spatially flat FLRW universe: $ds^2 = -dt^2 + a^2(t)dx^2$, the covariant Einstein field equations (2.8) reduce to:

$$3FH^2 = \rho + \frac{1}{2}Z\dot{\sigma}^2 - 3H\dot{F} + V(\sigma) + \dot{\sigma}^3[6g(\sigma)H - \dot{g}(\sigma) + 3\zeta(\sigma)\dot{\sigma}] \equiv \rho + \rho_\sigma, \quad (2.11)$$

$$\begin{aligned} -2F\dot{H} &= \rho + p + Z\dot{\sigma}^2 + \ddot{F} - H\dot{F} + \dot{\sigma}^2[(6gH - 2g_{,\sigma}\dot{\sigma})\dot{\sigma} + 4\zeta\dot{\sigma}^2 - 2g\ddot{\sigma}] \\ &\equiv \rho + p + \rho_\sigma + p_\sigma, \end{aligned} \quad (2.12)$$

2.2. Equations of motion in a FLRW universe

where:

$$\rho_\sigma = \frac{Z}{2}\dot{\sigma}^2 - 3H\dot{F} + V(\sigma) + \dot{\sigma}^3[6g(\sigma)H - \dot{g}(\sigma) + 3\zeta(\sigma)\dot{\sigma}], \quad (2.13)$$

$$p_\sigma = \frac{Z}{2}\dot{\sigma}^2 - V(\sigma) + \ddot{F} + 2H\dot{F} - \dot{\sigma}^4(g_{,\sigma} - \zeta) - 2g\dot{\sigma}^2\ddot{\sigma}. \quad (2.14)$$

The scalar field equation (2.10) in the FLRW metric takes the following form:

$$\begin{aligned} \ddot{\sigma}(Z + 12gH\dot{\sigma} - 4(g_{,\sigma} - 3\zeta)\dot{\sigma}^2) - 3F_{,\sigma}(2H^2 + \dot{H}) + V_{,\sigma} + 3ZH\dot{\sigma} \\ + 6g(3H^2 + \dot{H})\dot{\sigma}^2 + 12H\zeta\dot{\sigma}^3 - (g_{,\sigma\sigma} - 3\zeta_{,\sigma})\dot{\sigma}^4 = 0. \end{aligned} \quad (2.15)$$

Due to the nonminimal coupling $F(\sigma)R$ in the Lagrangian, the Newton's constant in the Friedmann equations is replaced by a time varying cosmological gravitational constant $G_{\text{cosm}} = (8\pi F)^{-1}$, which depends on the value of the scalar field σ . This means that in STTs the gravitational effects are encoded not only in the curvature of spacetime but also in the interaction with the scalar field. We wish to stress the fact that the coupling constant G_{cosm} is not the one measured between test masses. The effective gravitational constant G_{eff} , which can be measured locally, is obtained in the weak field limit of the theory, and for the model (2.6) is given by [128, 129]

$$G_{\text{eff}} = \frac{1}{16\pi G_4} \left[\frac{4G_{4,\sigma}^2 + G_4(G_{2,X} - 2G_{3,\sigma})}{3G_{4,\sigma}^2 + G_4(G_{2,X} - 2G_{3,\sigma})} \right]. \quad (2.16)$$

The above expression for G_{eff} is valid only for theories where screening mechanism are not relevant [128] (see section 2.4).

We define the density parameters for radiation (r), pressureless matter (m) and the scalar field (σ) following the notation of Ref. [96]:

$$\tilde{\Omega}_i = \frac{\rho_i}{3FH^2} \equiv \frac{\rho_i}{\rho_{\text{crit}}} \quad (i = r, m, \sigma). \quad (2.17)$$

It is also useful to define the dark energy density and pressure parameters in a framework that mimics Einstein gravity at the present time, this is done by rewriting the Friedmann equations as [96, 101, 130]

$$3F_0H^2 = \rho + \rho_{\text{DE}}, \quad -2F_0\dot{H} = \rho + p + \rho_{\text{DE}} + p_{\text{DE}}, \quad (2.18)$$

which leads to

$$\rho_{\text{DE}} = \frac{F_0}{F}\rho_\sigma + \rho \left(\frac{F_0}{F} - 1 \right); \quad p_{\text{DE}} = \frac{F_0}{F}p_\sigma + p \left(\frac{F_0}{F} - 1 \right). \quad (2.19)$$

Thus, in this framework we can define the effective parameter of state for DE as $w_{\text{DE}} \equiv p_{\text{DE}}/\rho_{\text{DE}}$ and the density parameters mimicking radiation, matter and DE in Einstein gravity are

$$\Omega_i = \frac{\rho_i}{3F_0H^2} \quad (i = r, m, \text{DE}). \quad (2.20)$$

Note that the definitions in Eqs. (2.17) and (2.20) coincide at the present time $z = 0$: $\tilde{\Omega}_{0,i} = \Omega_{0,i}$.

2.3 Stability conditions

We present in this section the stability conditions both in the scalar and tensor sector.

Scalar-tensor theories can suffer from instabilities if the kinetic term in the Lagrangian is nonstandard, i.e., $Z = -1$ (phantom branch), and $G_3 = 0$. In order to be viable a STT has to satisfy certain stability conditions that guarantee that scalar field is not a ghost and the propagation of its perturbation respects causality. More precisely, Laplacian instabilities arise if the square of the speed of sound becomes negative, while ghost instabilities take place when the sign of the kinetic term is negative in the second-order action for scalar perturbations. The theory given by the action (2.6) is healthy, meaning it does not incur in these instabilities if the following conditions are satisfied [131, 132]

$$q_s \equiv 4G_4 \{ G_{2X} + 2G_{3\sigma} + \dot{\sigma} [(G_{2XX} + G_{3X\sigma})\dot{\sigma} - 6G_{3XH}] \} + 3(2G_{4\sigma} + G_{3X}\dot{\sigma}^2)^2 > 0, \quad (2.21)$$

$$c_s^2 \equiv \left[4G_{2X}G_4 + 8G_{3\sigma}G_4 + (6G_{4\sigma}^2 - G_{3X}\dot{\sigma}^2)(2G_{4\sigma}^2 + G_{3X}\dot{\sigma}^2) - 8G_4(G_{3X}\ddot{\sigma} + 2G_{3XH}\dot{\sigma} + G_{3X\sigma}\dot{\sigma}^2) \right] / q_s > 0. \quad (2.22)$$

Eqs. (2.21) and (2.22) show that even in IG in the phantom branch with $0 < \xi < 1/6$ ($\omega_{\text{BD}} < -3/2$) – a region in parameter space that would contain a ghost – the instability can be avoided if we add a Galileon term $G_3(\sigma, X)\square\sigma$ in the Lagrangian.

Considering the tensor sector, it is possible to identify the conditions for the absence of ghost and Laplacian instabilities by expanding the Horndeski action Eq. (2.2) up to second order in tensor perturbation. The conditions are for the cosmological Planck mass and the tensor speed of sound squared to be positive:

$$q_t \equiv 2G_4 - 2\dot{\sigma}G_{4,X} + \dot{\sigma}^2G_{5,\sigma} - H\dot{\sigma}^3G_{5,X} > 0, \quad (2.23)$$

$$c_t^2 = \frac{1}{q_t} (2G_4 - \ddot{\sigma}G_{5,\sigma} - \dot{\sigma}^2\ddot{\sigma}G_{5,X}) > 0. \quad (2.24)$$

For the action (2.6) they simply reduce to $G_4(\sigma) > 0$. This constraint is automatically satisfied by our choice of parameters since we consider $G_4(\sigma) = F(\sigma)/2$ with the dependence of F on the scalar field as $\xi\sigma^2$ and $\xi > 0$.

Moreover, we note that the speed of gravitational waves given by Eq. (2.24) can be different from the speed of light ($c = 1$), while it is always equal to unity in the models (2.6) we consider.

2.4 Screening

STTs modify the gravitational interaction on cosmological scales, but the scalar degree of freedom can also leave imprints on scales unaffected by the cosmological expansion, such as the Solar System, where deviations from GR are strongly constrained. Therefore, a modified gravity (MG) theory should either have small deviations from GR in local

2.4. Screening

regions of the Universe or be equipped with a mechanism that suppresses the effect of the scalar field in high density regions, while leaving its cosmological repercussions unaltered. In STTs, there are several types of this kind of mechanisms, called *screening mechanisms*, such as the chameleon effect [133, 134], the symmetron [135, 136] and k-Mouflage models [137]. The mechanism relevant for this thesis, as it is typical of the cubic Galileon Lagrangian $\mathcal{L} = X\Box\sigma$ considered here, is the so-called *Vainshtein screening* [138], for which we illustrate the basics results in a cosmological background.

Vainshtein screening

The Vainshtein screening is a mechanism that operates in theories with a self-interaction of the form $X\Box\sigma$: this Galileon term leads to the decoupling of the scalar field from matter and the remaining degrees of freedom within a radius r_V , known as the *Vainshtein radius*. Inside the Vainshtein radius ($r < r_V$), the theory of gravity is indistinguishable from GR: *the behavior of the gravitational potentials is Newtonian and the post-Newtonian parameters are those of GR, while the gravitational constant on small scales is given by the cosmological gravitational constant $G_N = G_{\text{cosm}} = 1/(16\pi G_4)$* [139]. For the Sun, the Vainshtein radius can be of the order of 100 pc, this guarantees that the effect of modifications of gravity cannot be observed in the scales of star systems or galaxies.

It was shown in Refs. [139, 140] that the Vainshtein mechanism cannot suppress the time variation of the gravitational constant, which is due to the cosmological background evolution of the scalar field: the mechanism is not able to set the coupling constant of gravity (the gravitational constant or equivalently σ_0). *It is only the cosmological evolution of the scalar field that determines the value of the coupling constant of GR observed on small scales today.*

The Vainshtein radius in a cosmological background, for a spherical celestial object of mass δM , is [139]

$$r_V = (\mathcal{B}\mathcal{C}\mu/H^2)^{1/3}, \quad (2.25)$$

where $\mu = \delta M/(16\pi G_4)$, \mathcal{B} and \mathcal{C} are functions of the Hordenski functions G_i , and their explicit forms are written at the end of the section. If the product $\mathcal{B}\mathcal{C}$ is of order 1, then the Vainshtein radius can be written, taking $H_0 = 70 \text{ km s}^{-1} \text{ Mpc}^{-1}$, as

$$r_V = \left(\frac{\mu}{H^2}\right)^{1/3} \simeq 100 \left(\frac{H_0}{H}\right)^{2/3} \left(\frac{\delta M}{M_\odot}\right)^{1/3}, \quad (2.26)$$

giving for the Sun, at present time $r_{V\odot} \simeq 100 \text{ pc}$. After having solved for the background evolution of the Universe, we will evaluate Eq. (2.25) directly, showing that the assumption $\mathcal{B}\mathcal{C} = \mathcal{O}(1)$, useful for the estimate above, is valid in the late Universe.

\mathcal{B} and \mathcal{C} functions For a theory given by Eq. (2.6), \mathcal{B} , \mathcal{C} and the functions that define them, are

$$\mathcal{B} \equiv \frac{4\beta_0}{\alpha_0 + 2\alpha_1\alpha_2 + \alpha_2^2}, \quad (2.27)$$

2. Current and novel constraints on modified gravity

$$\mathcal{C} \equiv \frac{\alpha_1 + \alpha_2}{\alpha_0 + 2\alpha_1\alpha_2 + \alpha_2^2}, \quad (2.28)$$

where

$$\alpha_i(t) \equiv \frac{A_i}{\mathcal{G}_T}, \quad \beta_0(t) \equiv \frac{B_0}{\mathcal{G}_T}, \quad (2.29)$$

with

$$\beta_0 \equiv \frac{\alpha_1}{2} + \alpha_2 (\neq 0), \quad (2.30)$$

and

$$\mathcal{F}_T \equiv 2G_4 \equiv \mathcal{G}_T, \quad \mathcal{E} \equiv 2XG_{2X} - G_2 - 6X\dot{\sigma}HG_{3X} + 2XG_{3\sigma} - 6H^2G_4 - 6H\dot{\sigma}G_{4\sigma}, \quad (2.31)$$

$$\begin{aligned} \mathcal{P} \equiv & G_2 + 2X(G_{3\sigma} + \ddot{\sigma}G_{3X}) + 2(3H^2 + 2\dot{H})G_4 \\ & + 2(\ddot{\sigma} + 2H\dot{\sigma})G_{4\sigma} + 4XG_{4\sigma\sigma}, \end{aligned} \quad (2.32)$$

$$\Theta \equiv \dot{\sigma}XG_{3X} + 2HG_4 + \dot{\sigma}G_{4\sigma}, \quad (2.33)$$

$$A_0 \equiv \frac{\dot{\Theta}}{H^2} + \frac{\Theta}{H} - \mathcal{G}_T - 2\frac{\dot{\mathcal{G}}_T}{H} - \frac{\mathcal{E} + \mathcal{P}}{2H^2}, \quad A_1 \equiv \frac{1}{H}\dot{\mathcal{G}}_T + \mathcal{G}_T - \mathcal{F}_T, \quad (2.34)$$

$$A_2 \equiv \mathcal{G}_T - \frac{\Theta}{H}; \quad B_0 \equiv -\frac{X}{H}\dot{\sigma}G_{3X}. \quad (2.35)$$

2.5 Current constraints on modified gravity and STTs

The current status of observations and tests of gravity is illustrated in Fig. 2.1, taken from Ref. [141]. Gravity is parameterized by a gravitational potential $\mathcal{E} \equiv GM/r$ and the curvature of space $\xi \equiv GM/r^3$. M and r are, respectively, the mass and radius of a spherical object. The strong gravity regime (large ξ) has been extensively tested with Solar System and binary pulsar observations, while, as the figure shows, the weak gravity regime (small ξ) is mostly unexplored, with only cosmological observations being relevant at those scales.

In the previous section we saw that many MG theories are equipped with a screening mechanism which hides the modifications to gravity at small scales and/or dense environments, rendering impossible to discriminate between models in those regimes. Therefore, cosmological observations play a crucial role in our understanding of gravity as it is only on those scales that the modifications to GR emerge in many alternative theories.

In this section I provide a brief overview of some of the most relevant constraints on MG: the measurement of the speed of gravitational waves, big-bang nucleosynthesis, local (Solar System and laboratory) experiments and cosmological observations.

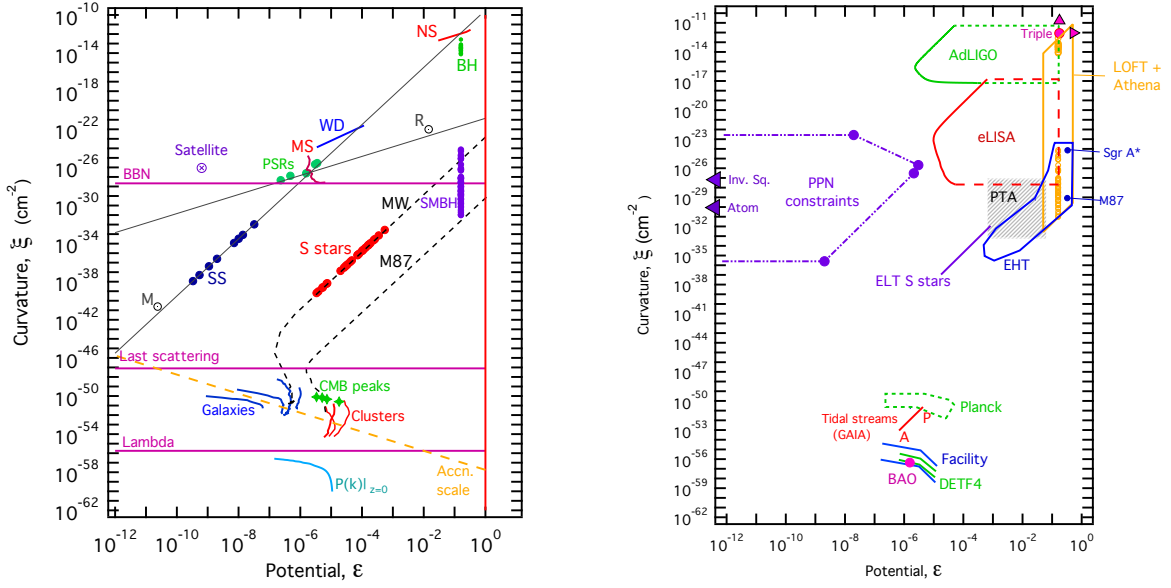


Figure 2.1: **Left:** Gravitational field’s parameter space. The horizontal lines represent the curvature of the Universe at BBN and at last scattering, while the other one is the curvature associated with the cosmological constant. The acronyms are MS: main sequence stars, WD: white dwarfs, NS: neutron stars, BH: stellar mass black holes, SMBH supermassive black holes, PSRs: binary pulsars, MW: Milky Way, SS=Solar System planets. **Right:** Experimental version of the gravitational field’s parameter space. The abbreviations are PPN: Parameterized Post-Newtonian regime, Inv.Sq.: laboratory tests of inverse square law of gravitation, Atom: atom interferometry experiments, EHT: Event Horizon Telescope, ELT: Extremely Large Telescope, DETF4: hypothetical “stage 4” experiment according to the classification of [142], Facility: future large radio telescope such as the Square Kilometer Array Observatory (SKAO). Both figures taken from Ref. [141].

2.5.1 Constraints from gravitational waves

In the general Horndenski theories (2.2) the speed of propagation of gravitational waves is given by Eq. (2.24) and it can differ from the speed of light ($c = 1$) [113], this feature of the theory has allowed to rule out several terms of the Horndenski Lagrangian when the observation of the neutron star merger GW170817 and its electromagnetic counterpart GW170817A [143–145] has demonstrated that gravitational waves travel at the speed of light with a precision of $-3.5 \times 10^{-15} \leq c_t - 1 < 7 \times 10^{-16}$. This observation alone has invalidated theories that would otherwise be viable if tested only with cosmological datasets: any possible dependence of G_4 on the kinetic term has been tightly constrained, and likewise all the terms depending on G_5 in (2.2) [113, 146, 147] (see also [148] for a different take on the issue).

2.5.2 Constraints from big-bang nucleosynthesis

The abundances of light elements produced during BBN depends on the expansion of the Universe which in turn depends on the gravitational constant. Theories where this constant is time-dependent modify therefore the abundances of light elements with respect to the standard predictions of GR. The variation of the gravitational constant from the time of BBN to today has been measured, using BBN data, first in Refs. [149, 150] where they found $G_{\text{BBN}}/G_0 = 1.01_{-0.16}^{+0.20}$ at 68% CL, and recently in [151] which presented the strongest constraint: $G_{\text{BBN}}/G_0 = 0.99_{-0.05}^{+0.06}$.

2.5.3 Constraints from Solar System and laboratory observations

Deviations from GR are strongly constrained by Solar System tests. These deviations are often parameterized in the so-called post-Newtonian (PN) formalism, which completely characterizes the weak field limit of the theory. In NMC models only the parameters γ_{PN} and β_{PN} can differ from the GR value of 1; thus the line element can be expanded as function of these two parameters and the gravitational potential Φ as

$$ds^2 = - (1 + 2\Phi - 2\beta_{\text{PN}}\Phi^2) dt^2 + (1 - 2\gamma_{\text{PN}}\Phi) dx_i dx^i. \quad (2.36)$$

Measuring or putting bounds on γ_{PN} and β_{PN} therefore means constraining the parameters of STTs such as ω_{BD} .

Solar System bounds

The post-Newtonian parameter γ_{PN} has been constrained from measurement of Shapiro time delay [152]: a radar signal sent across the Solar System past the Sun and returned to Earth after being reflected by some object (a planet or a satellite) is subject to a time delay [7]

$$\delta t \simeq \frac{1}{2}(1 + \gamma_{\text{PN}}) \left[240 - 20 \ln \left(\frac{d^2}{r} \right) \right] \mu\text{s}, \quad (2.37)$$

2.5. Current constraints on modified gravity and STTs

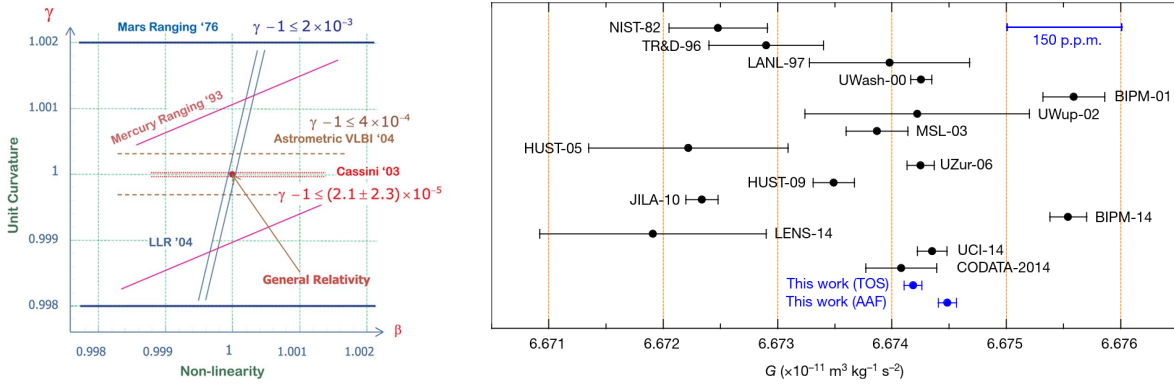


Figure 2.2: **Left:** Current constraints on the post-Newtonian parameters, from [142]. **Right:** Measurements of the gravitational constant in different experiments, from [155]. This work (TOS) and (AAF) refer to the methods used in [155] to measure G and stand for measurements using torsion pendulum experiments with the time-of-swing method and the angular-acceleration-feedback method

where d is closest distance of the light ray from the Sun and r is the distance from the Sun (in astronomical units) of the planet or satellite on which the signal has bounced. The best measurement of this kind was performed in 2003 by the Cassini spacecraft while on its way to Saturn, giving $\gamma_{\text{PN}} - 1 = (2.1 \pm 2.3) \times 10^{-5}$. This constraint can be converted into bounds on STTs without a screening mechanism such as BD (IG) which predict $\gamma_{\text{PN}} \leq 1$, the resulting limit is $\omega_{\text{BD}} > 40000$ ($\xi < 6.25 \times 10^{-6}$).

It is also possible to constrain STTs from the observed bound on the second PN parameter β_{PN} which can be obtained from observations of the shift in the perihelion of the orbit of Mercury. The measurement depends on a combination of γ_{PN} and β_{PN} , and once the Cassini constraint on the first PN parameter is assumed one obtains $\beta_{\text{PN}} - 1 = (4.1 \pm 7.8) \times 10^{-5}$ [7].

Laboratory experiments

The effective gravitational constant measured between test masses in Cavendish-like experiments is given by Eq. (2.16), therefore precise measurements translate in constraints on STTs and they can also probe screening mechanisms and the presence of Galileon fields [153]. Very precise torsion balances and atom interferometry are among the modern techniques used for the measurement of G [154]. The 2018 CODATA recommended value is $6.67430(15) \times 10^{-11} \text{ m}^3 \text{ kg}^{-1} \text{ s}^{-2}$, but as it can be seen from the right panel of Fig. 2.2 different experiments are in tension and their estimates differ on the 4th digit after the comma. In particular, the two most precise measurements, obtained using two independent methods, are, in units of $10^{-11} \text{ m}^3 \text{ kg}^{-1} \text{ s}^{-2}$ [155], $6.674184(78)$ and $6.674484(78)$, which results in a 2.7σ difference.

2.6 Cosmological constraints

In this section we first present a selection of constraints obtained using cosmological datasets on some of the simplest STTs of gravity such as IG, NMC, EMG with a standard sign of the kinetic term ($Z = 1$). This is not an exhaustive summary: there are various attempts at constraining subclasses of the Lagrangian (2.2), both considering a particular form of the G functions or using parametrizations of the Horndenski action. See e.g. [156–161]. We then discuss novel constraints on STTs both with standard and nonstandard ($Z = -1$) sign of the kinetic term, in sections 2.6.2 and 2.6.3.

The results and the plots for the cosmological dynamics and the observables in these sections are produced using a modified version of CLASSig [98]. To obtain the results, we have carried out a Markov chain Monte Carlo analysis (hereafter MCMC, see appendix A) using the publicly available sampling code MontePython-v3¹ [162, 163] connected to the aforementioned version of CLASSig. For the sampling, we use the Metropolis-Hastings algorithm with a Gelman-Rubin [164] convergence criterion $R - 1 < 0.01$, and the reported mean values and uncertainties on the parameters, together with the contour plots have been obtained using GetDist² [165]. We consider combinations of the datasets and likelihoods presented in chapter 1 (P18, BAO, FS, SN, p(M) or p(H_0)), sampling on the standard parameters, i.e. ω_b , ω_c , H_0 , τ , $\ln(10^{10} A_s)$, n_s , and the modified gravity parameters, assuming two massless neutrinos with $N_{\text{ur}} = 2.0328$, and a massive one with minimum mass $m_\nu = 0.06$ eV. The primordial ^4He mass fraction Y_p in the analysis is fixed according to the prediction of PArthENoPE [166, 167] and taking into account the relation between the baryon fraction ω_b and the varying gravitational constant which modifies the expansion rate of the Universe during BBN.

We report the difference in the model χ^2 with respect to ΛCDM : $\Delta\chi^2 \equiv \chi^2 - \chi_{\Lambda\text{CDM}}^2 \equiv -2 \ln \mathcal{L} - 2 \ln \mathcal{L}_{\Lambda\text{CDM}}$, where \mathcal{L} is the likelihood function defined in appendix A. Thus, negative values of $\Delta\chi^2$ indicate an improvement in the fit compared to ΛCDM . The minimum χ^2 is computed following the minimization method of Ref. [168]. Additionally, we quote the Akaike information criterion (AIC) [169] of the extended model \mathcal{M} relative to that of ΛCDM : $\Delta\text{AIC} = \Delta\chi^2 + 2(p_{\mathcal{M}} - p_{\Lambda\text{CDM}})$, where $p_{\mathcal{M}}$ is the number of free parameters of the model.

2.6.1 IG, NMC and EMG in the standard branch

Constraints on IG

The tightest constraints on IG (2.4) were obtained in [110] using a combination of *Planck* CMB data and BAO data, which provide $\xi < 0.00055$ at 95% CL, corresponding to an estimate of the post-Newtonian parameter $|\gamma_{\text{PN}} - 1| < 0.0022$ at 95% CL; they also provide a limit on the time variation of the gravitational constant from the radiation era to today in this class of models: $\delta G_{\text{cosm}}/G_{\text{cosm}}(z = 0) > -0.016$ (95% CL).

¹https://github.com/brinckmann/montepython_public

²<https://getdist.readthedocs.io/en/latest/>

2.6. Cosmological constraints

Constraints on NMC

For an effectively massless NMC (2.5) with $Z = +1$, P18+BAO give [110] $N_{\text{Pl}} < 1.000018 M_{\text{Pl}}$ at 95% CL for the CC model, instead when ξ is allowed to vary, the results are $N_{\text{Pl}} > 0.64 M_{\text{Pl}}$ and $\xi < 0.046$ for NMC+; and $N_{\text{Pl}} < 1.05 M_{\text{Pl}}$, $\xi > -0.042$ for NMC-. The derived constraints on the time variation of the Gravitational constant and the PN parameters, for the CC case are, at 95% CL

$$\frac{\delta G_{\text{cosm}}}{G_{\text{cosm}}(z=0)} > -0.017, \quad \gamma_{\text{PN}} > 0.999982, \quad \beta_{\text{PN}} < 1.000001. \quad (2.38)$$

Note that, while in IG $\gamma_{\text{PN}} \lesssim \mathcal{O}(10^{-3})$, the above bounds on the PN parameters γ_{PN} and β_{PN} are tighter than the analogous Solar System measurements given in section 2.5.3.

With the inclusion of a prior on the value of $H_0 = (74.03 \pm 1.42) \text{ km s}^{-1} \text{ Mpc}^{-1}$ the inferred value of the Hubble constant is $H_0 = (70.1 \pm 0.8) \text{ km s}^{-1} \text{ Mpc}^{-1}$ at 68% CL for IG, and $H_0 = (69.64_{-0.73}^{+0.65}) \text{ km s}^{-1} \text{ Mpc}^{-1}$ at 68% CL for CC. This is due to the fact that there is a degeneracy between H_0 and ξ which can accommodate for a larger H_0 with respect to ΛCDM . The Hubble tension is reduced to a significance of 2.7σ (3.2σ) for P18 in IG (CC). All these results are stable when switching to a flat potential $V(\sigma) = \Lambda$.

Cosmological bounds on the gravitational constant

In Ref. [111] a variant of the effectively massless NMC model in the standard branch with an new parameter Δ is considered. This allows for an imbalance between the effective gravitational constant G_{eff} between two test masses, and Newton's constant G_{N} : $G_{\text{eff}}(z=0) = G_{\text{N}}(1 + \Delta)^2$, while $N_{\text{Pl}} = M_{\text{Pl}}$ is kept fixed. The models studied are IG, CC and NMC in general. We report the results of Ref. [111] obtained for a combination of CMB, BAO and a prior on H_0 from Ref. [170].

For IG, at 68% and 95% CL respectively, $\Delta = -0.026 \pm 0.024$ and $10^3 \xi = 0.74_{-0.54}^{+0.52}$, corresponding to a 2.5σ detection of the coupling ξ . The constraints on the ratio of the effective gravitational constant correspond to $G_{\text{eff}}/G_{\text{N}} = 0.949 \pm 0.048$ at 68% CL.

The CC case is tightly constrained: $10^{-5} \Delta = 2.01_{-0.97}^{+0.86}$ and $G_{\text{eff}}/G_{\text{N}} = 1.000040_{-0.000019}^{+0.000017}$ at 68% CL.

The results for NMC+ (NMC-) are $\Delta = -0.0072_{-0.0020}^{+0.0053}$ (< 0.030) at 68% (95%) CL; while, the constraints on the ratio of the effective gravitational constant correspond to $G_{\text{eff}}/G_{\text{N}} = 0.986_{-0.0041}^{+0.011}$ (< 1.06) at 68% (95%) CL.

Moreover, for IG, NMC+, NMC- respectively, the inferred value of H_0 is 70.04 ± 0.83 , 69.76 ± 0.80 and $69.97_{-0.97}^{+0.82} \text{ km s}^{-1} \text{ Mpc}^{-1}$, reducing therefore the Hubble tension.

Constraints on early modified gravity

Early modified gravity, defined in section 2.1, was studied and constrained with cosmological datasets in Ref. [171] for $Z = +1$. In this model, the scalar field, grows around recombination and then undergoes a series of damped oscillations reaching $\sigma = 0$. For this reason, late-times modification of gravity are suppressed and the model passes the laboratory and Solar System tests of gravity.

2. Current and novel constraints on modified gravity

They perform the data analysis with a variety of cosmological datasets, showing a substantial reduction of the Hubble tension to 1.7σ , when considering CMB, BAO, SN, and FS, obtaining $H_0 = 71.00_{-0.79}^{+0.87} \text{ km s}^{-1} \text{ Mpc}^{-1}$ at 68 % CL. For this dataset the limits on the nonminimal coupling constant and the first post-Newtonian parameter are, respectively, $\xi < 0.42$ at 95% CL and $\gamma_{\text{PN}} - 1 > -1.7 \times 10^{-9}$ at 95% CL.

We have highlighted the main cosmological constraints on the simplest STTs of gravity, and in chapter 5 we will present forecasts showing how these constraints can be tightened when considering the data of the *Euclid* mission in combination with CMB experiments.

2.6.2 IG, NMC and EMG in the phantom branch

In this section we study the cosmological dynamics and provide constraints on IG, NMC+, NMC-, EMG in the phantom branch ($Z = -1$); the results presented are based on the research work in [79]. IG and NMC are studied with a potential $V(\sigma) = \lambda F^2(\sigma)/4$, while, for EMG, the potential is $V = \Lambda + \lambda\sigma^4/4$. In contrast to the standard branch, in EMG phantom λ is negative in order to produce damped oscillations in the evolution of the scalar field.

The equations of motion for the background evolution in a FLRW universe are given by Eqs. (2.11), (2.12) and (2.15) with $g(\sigma) = \zeta(\sigma) = 0$, joint with a choice of the nonminimal coupling function $F(\sigma)$ and the potential $V(\sigma)$ corresponding to the model considered. Analogously, the linearly perturbed Einstein and scalar field equations can be obtained from the ones given in full generality in appendix B.

In these models, the effective gravitational constant (2.16) for the force between two test masses is

$$G_{\text{eff}} = \frac{1}{8\pi F} \frac{ZF + 2F_{,\sigma}^2}{ZF + \frac{3}{2}F_{,\sigma}^2}, \quad (2.39)$$

while the post-Newtonian parameters evaluated at present time are

$$\gamma_{\text{PN}} = 1 - \frac{F_{,\sigma}^2}{ZF + 2F_{,\sigma}^2}, \quad \beta_{\text{PN}} = 1 + \frac{1}{4} \frac{FF_{,\sigma}}{2ZF + 3F_{,\sigma}^2} \frac{d\gamma_{\text{PN}}}{d\sigma}. \quad (2.40)$$

From the equations above we can see that constraints on the nonminimal coupling function F and its derivative $F_{,\sigma}$ translate into bounds on the PN parameters; while these parameters are strongly constrained by Solar System tests as we've seen in section 2.5.3, they are weakly constrained by current cosmological data, but combinations of future cosmological surveys could be competitive with Solar System measurements [111, 172, 173].

The stability conditions of the theory, given in general by Eqs. (2.21) and (2.22), simply reduce to

$$G_{\text{eff}} > 0, \quad \frac{ZF}{F_{,\sigma}^2} > -\frac{3}{2}, \quad (2.41)$$

where the last inequality is equivalent to the requirement of positivity of the kinetic energy of the scalar field in the Einstein frame [174]. For $Z = -1$ Eqs. (2.41) reduce

2.6. Cosmological constraints

to $-3/2 < -FF_{,\sigma}^2 < 0$ and $F > 0$. In principle, these requirements restrict the allowed parameter space for the parameters entering in $F(\sigma)$, nonetheless, in the following we will also include models whose parameters violates the stability conditions and test them in an agnostic way.

Phantom induced gravity

In phantom IG we impose the boundary condition on the value of the effective gravitational constant today to be equal to the Newton's constant measured on Earth: $G_{\text{eff}}(z=0) = G_{\text{N}}$, in this way we fix the current value of the scalar field.

Due to the evolution of the scalar field and consequent time dependence of the gravitational constant, STTs modify the expansion rate of the Universe. In a model with a nonminimal coupling $F(\sigma)$, this modification is

$$\frac{H(\xi \neq 0)}{H(\xi = 0)} \approx \sqrt{\frac{M_{\text{Pl}}^2}{F(\sigma)}}. \quad (2.42)$$

Decreasing the Planck mass $F(\sigma) < M_{\text{Pl}}^2$ with respect to the GR value increases the expansion rate at a given time, reducing therefore the comoving sound horizon at recombination

$$r_s = \int_{z_{\text{rec}}}^{\infty} dz' \frac{c_s(z')}{H(z')}, \quad (2.43)$$

where z_{rec} is the redshift of recombination and c_s is the speed of sound in the photon-baryon fluid.

In left panel of Fig. 2.3 we show that the nonminimal coupling function F increases in the standard branch (solid lines) while it is a decreasing function of redshift in the phantom branch (dashed lines). The different behaviour of F in the two branches is connected to a different late-time evolution of the Hubble parameter through Eq. (2.42): H is larger than in Λ CDM in the standard branch, and smaller in the phantom branch, as it can be seen from the right panel of Fig. 2.3. This also induces modifications on all the distances that depends on H , such as the comoving angular diameter distance

$$D_{\text{M}}(z) = \int_0^z \frac{dz'}{H(z')}, \quad (2.44)$$

but does not cancel out on the observed angular size of the sound horizon at the last-scattering surface θ_*

$$\theta_* = \frac{r_s}{D_{\text{M}}(z_*)}, \quad (2.45)$$

resulting in a shift of the acoustic peaks of the CMB, connected to the evolution of the coupling F [110, 175, 176]. In Fig. 2.4, we show how this shift of the acoustic peaks of the CMB temperature anisotropies angular power spectrum is related to the evolution of F , equivalent to a time evolution of the Planck mass: in the standard branch the peaks are shifted to the right while they move to the left in the phantom one. The standard Λ CDM model fits CMB data quite well, therefore these shifts need to be compensated

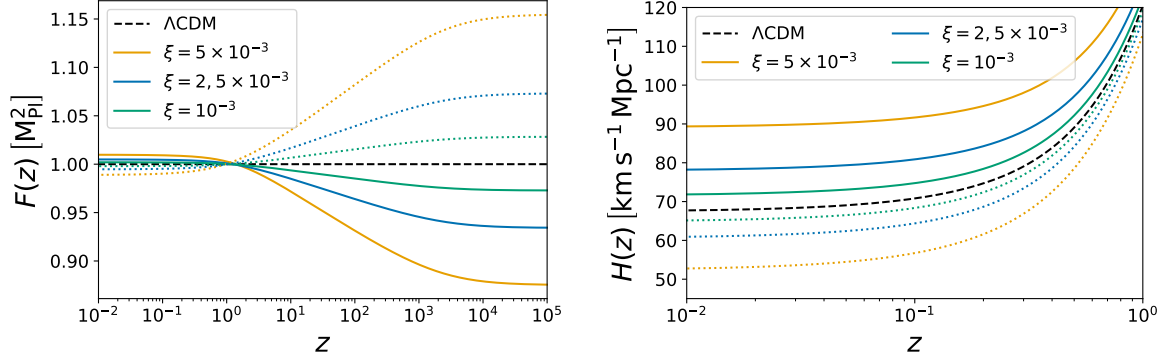


Figure 2.3: Left: time evolution of the nonminimal coupling function $F = \xi\sigma^2$ to the Ricci scalar. Right: redshift evolution of the Hubble parameter. Different values of the coupling parameter ξ are considered in the standard (solid lines) and phantom branch (dashed lines) for IG ($F = \xi\sigma^2$, $V = \lambda F^2/4$).

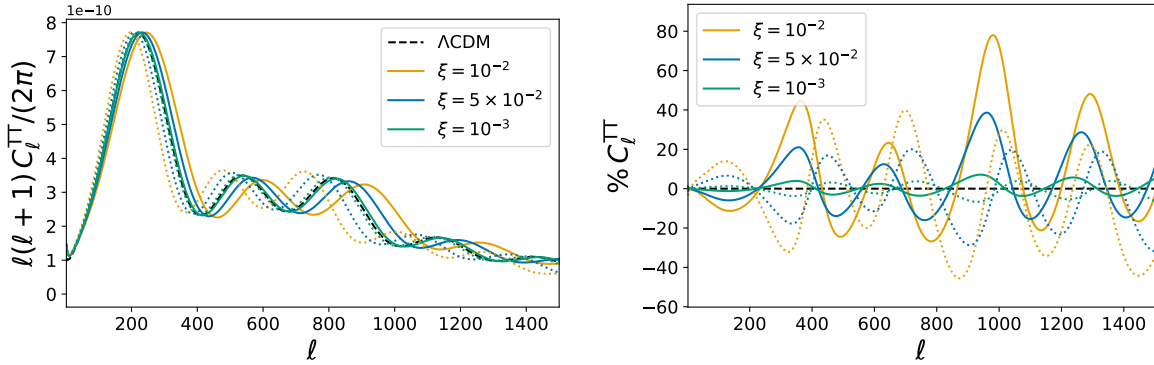


Figure 2.4: Left: CMB temperature anisotropies power spectrum. Right: relative differences with respect to the Λ CDM. Different values of the coupling parameter ξ are considered in the standard branch (solid lines) and in the phantom one (dashed lines) for IG ($F = \xi\sigma^2$, $V = \lambda F^2/4$).

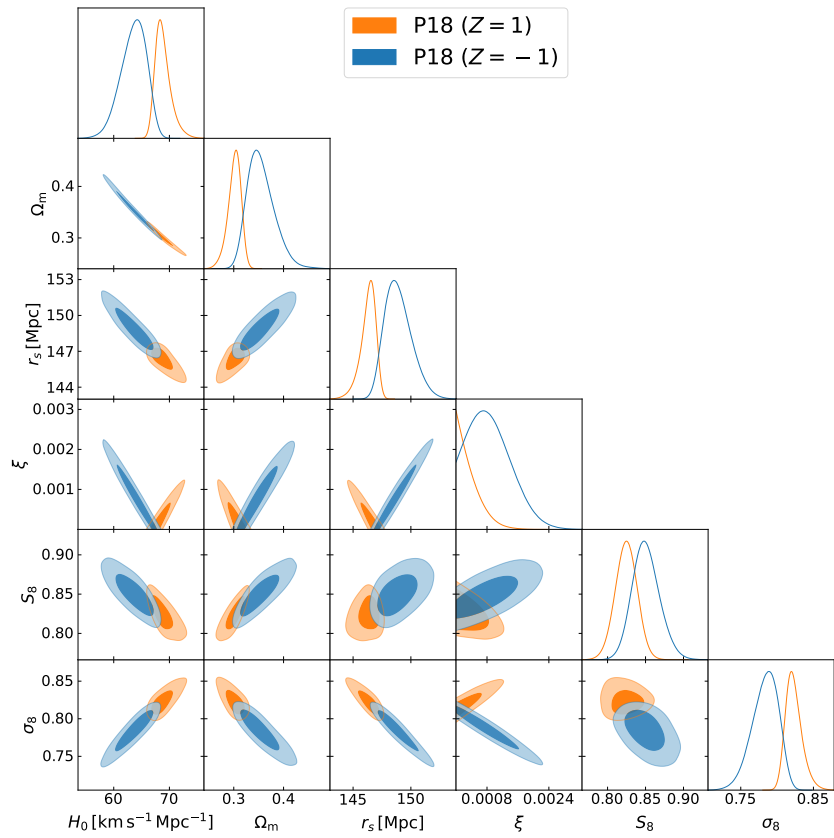


Figure 2.5: Marginalized joint 68% and 95% CL regions 2D parameter space using P18 data alone for IG ($F = \xi\sigma^2$, $V = \lambda F^2/4$) in the standard branch ($Z = 1$) in orange and in the phantom one ($Z = -1$) in blue.

2. Current and novel constraints on modified gravity

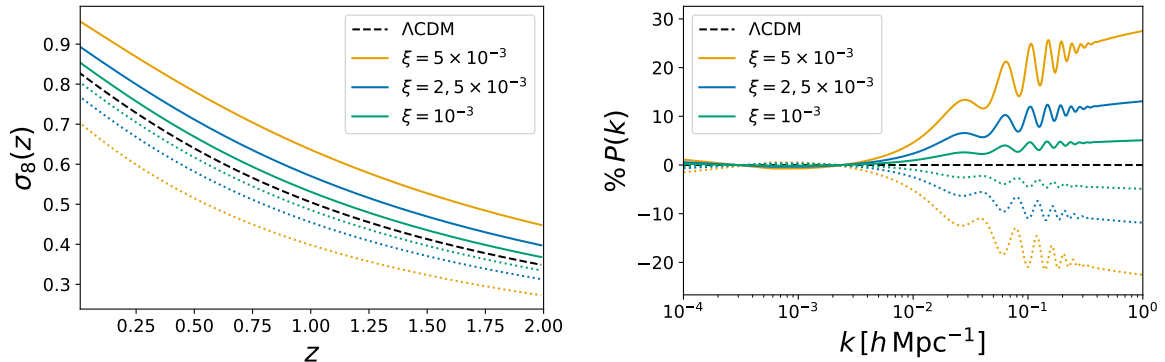


Figure 2.6: **Left:** redshift evolution of σ_8 . **Right:** relative differences of the linear matter power spectrum at $z = 0$ with respect to Λ CDM. Different values of the nonminimal coupling parameter ξ are considered in the standard branch (solid lines) and in the phantom one (dashed lines) for IG ($F = \xi\sigma^2$, $V = \lambda F^2/4$).

by some other parameters that change with respect to Λ CDM: the two branches prefer larger or smaller values of the total matter density Ω_m while keeping constant the CDM fraction. This can be seen from Fig. 2.5 where we present constraints, obtained using only CMB data, on IG in the phantom branch compared to the standard case. In the figure, in the plane ξ - H_0 the degeneracy changes orientation going from one case to the other according to Eq. (2.42). The main result we want to emphasize from this CMB-only analysis is that in the phantom branch the allowed values of the coupling ξ are larger, while the inferred value of the Hubble constant is lower, without reducing the H_0 tension. This study highlights the correspondence between the kinetic term and spatial curvature: the standard (phantom) kinetic term shifts the position to the right (left) as it happens in a universe with negative (positive) spatial curvature.

In the phantom branch, σ_8 is smaller when compared to its value both in the standard branch and in the Λ CDM model as we show in Fig. 2.6. This result can be understood considering the late-time solution of the perturbation equation for the matter density contrast in the linear regime, on sub-horizon scales

$$\delta_m'' + \left(\frac{3}{a} + \frac{H'}{H} \right) \delta_m' - \frac{G_{\text{eff}}}{2GH^2} \frac{\rho_m}{a^2} \delta_m \simeq 0, \quad (2.46)$$

with primes denoting derivatives with respect to the scale factor a . Making use of the Friedmann equations and the fact that in the matter era the field evolves as $\sigma \sim a^{2Z\xi}$ [96], it is possible to rewrite Eq. (2.46) as

$$\delta_m'' + \frac{3}{2a} \left(1 - \frac{4Z\xi}{3} \right) \delta_m' - \frac{3}{2a^2} \left(1 + \frac{16Z\xi}{3} \right) \delta_m \simeq 0. \quad (2.47)$$

The leading order solution of Eq. (2.47) in the weak coupling regime ($\xi \ll 1$), which is the range allowed from observations, is $\delta_m \sim a^{1+4Z\xi}$, this implies a slower (faster) growth of structures compared to Λ CDM for $Z < 0$ ($Z > 0$) during matter domination.

The results of our MCMC analysis for several combinations of datasets are shown in Fig. 2.7 and section 2.6.2, where the constraints on all the parameters can be found.

2.6. Cosmological constraints

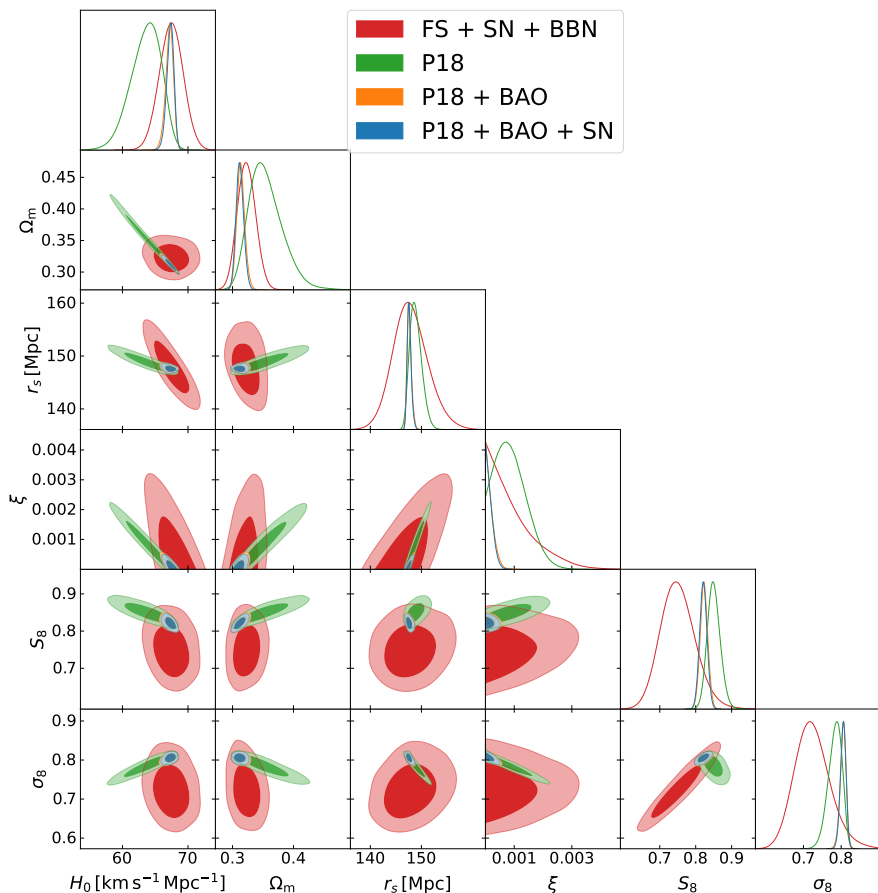


Figure 2.7: Marginalized joint 68% and 95% CL regions 2D parameter space using the CMB-independent combination FS+SN (red), P18 (green), the combination P18+BAO (orange), and the combination P18+BAO+SN (blue) for IG ($F = \xi\sigma^2$, $V = \lambda F^2/4$) in the phantom branch ($Z = -1$).

The less constraining analysis is the one without CMB information, comprising only of a combination of FS with SN and a Gaussian prior on ω_b motivated by BBN; in this case, but also for the CMB-only analysis, larger value of ξ are allowed thanks to changes in the density parameters and in the scalar spectral index. Focusing on the coupling parameter to the Ricci curvature: the upper limit on ξ at 95% CL is < 0.0024 for FS+SN, < 0.0018 for P18, < 0.00046 for P18+BAO, and < 0.00040 for P18+BAO+SN. For the Hubble constant H_0 [$\text{km s}^{-1} \text{Mpc}^{-1}$], the marginalized means and uncertainties at 68% CL are to 67.4 ± 1.8 for FS+SN, $63.6^{+2.7}_{-1.9}$ for P18, $67.17^{+0.64}_{-0.50}$ for P18+BAO, $67.29^{+0.60}_{-0.47}$ for P18+BAO+SN; in all cases lower than the corresponding results found in the standard branch (see section 2.6 and Refs. [110, 177]). Adding a prior on H_0 , the upper bound on ξ becomes much tighter: $\xi < 0.00016$ at 95% CL, while the Hubble constant increases only marginally: 68.34 ± 0.41 at 68% CL.

The results of our analysis on today's value of σ_8 are, at 68% CL, 0.717 ± 0.049 for FS+SN, $0.784^{+0.021}_{-0.015}$ for P18, $0.799^{+0.010}_{-0.009}$ for P18+FS, and 0.8059 ± 0.0058 for P18+FS+SN. However, the quantity commonly used to quantify the tension between *Planck* and weak lensing of galaxies measurements is the combination $S_8 \equiv \sigma_8 \sqrt{\Omega_m/0.3}$, for which we find

2. Current and novel constraints on modified gravity

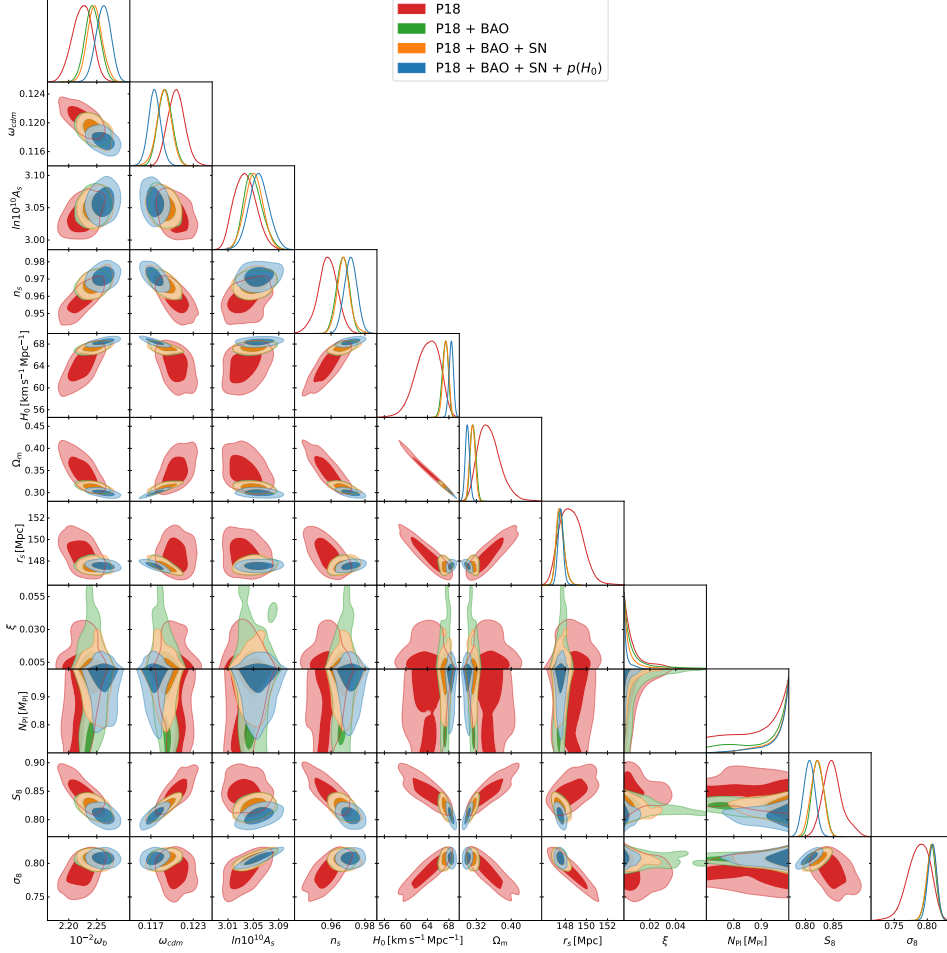


Figure 2.8: Marginalized joint 68% and 95% CL regions 2D parameter space using the P18 (green), the combination P18+BAO (orange), and the combination P18+BAO+SN (blue) for NMC+ ($F = N_{\text{Pl}}^2 + \xi\sigma^2$, $V = \lambda F^2/4$) in the phantom branch ($Z = -1$).

0.744 ± 0.050 for FS+SN, $0.850_{-0.019}^{+0.016}$ for P18, $0.831_{-0.012}^{+0.011}$ for P18+FS, and 0.825 ± 0.012 for P18+FS+SN at 68% CL, resulting to be larger than in the standard branch as shown in Fig. 2.5.

The constraints found for IG are at odds with the region of parameter space free from ghosts, which corresponds to $\xi > 1/6$. In general, this condition for ξ can be relaxed if one considers the more general Lagrangian (2.6) for which the stability conditions are given by Eqs. (2.21) and (2.22), allowing, in principle, for values $\xi < 1/6$ while maintaining the theory free of ghost and Laplacian instabilities [175, 178, 179].

Phantom nonminimal coupling

For NMC+ and NMC- in the phantom branch, we vary in our MCMC analysis the dimensionless parameter $\Delta\tilde{N}_{\text{Pl}} \equiv N_{\text{Pl}}/M_{\text{Pl}} - 1$ and ξ in addition to the six Λ CDM standard parameters.

The results for all the datasets considered are presented in Fig. 2.8 and Table 2.2 for

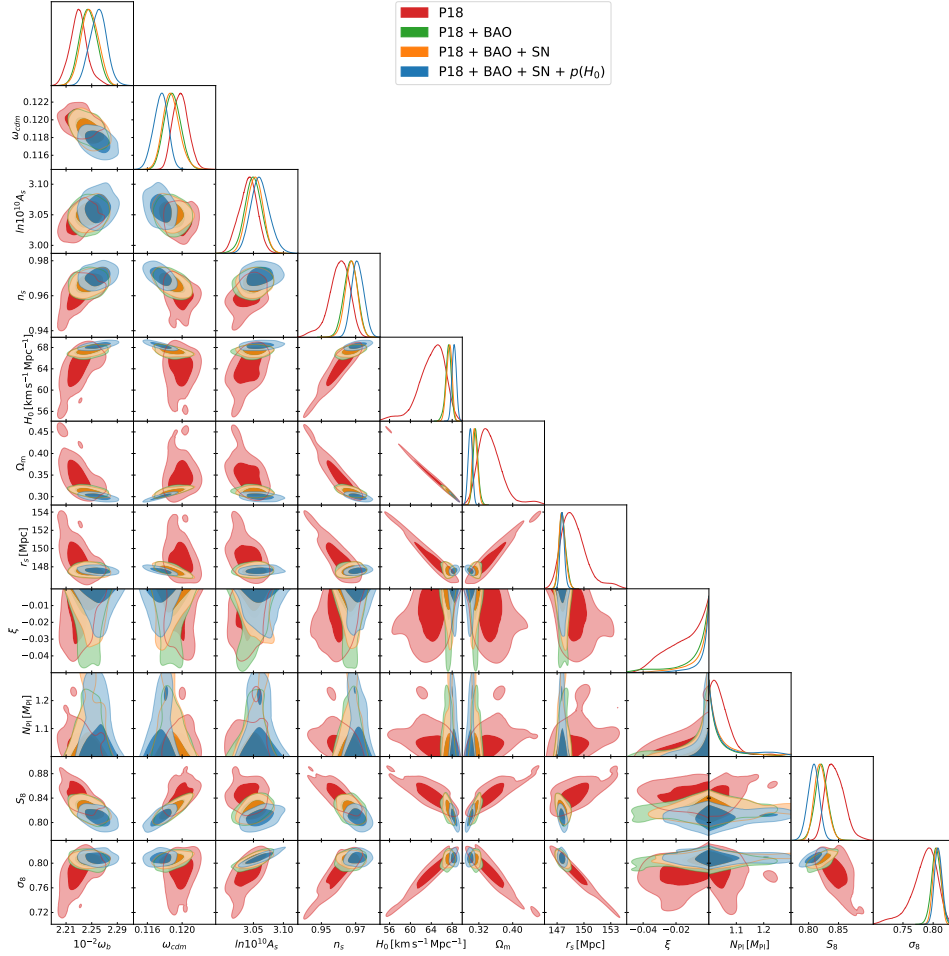


Figure 2.9: Marginalized joint 68% and 95% CL regions 2D parameter space using using the P18 (red), the combination P18+BAO (green), the combination P18+BAO+SN (orange), and the combination P18+BAO+SN+p(H_0) (blue) for NMC- ($F = N_{p1}^2 + \xi\sigma^2$, $V = \lambda F^2/4$) in the phantom branch ($Z = -1$).

2. Current and novel constraints on modified gravity

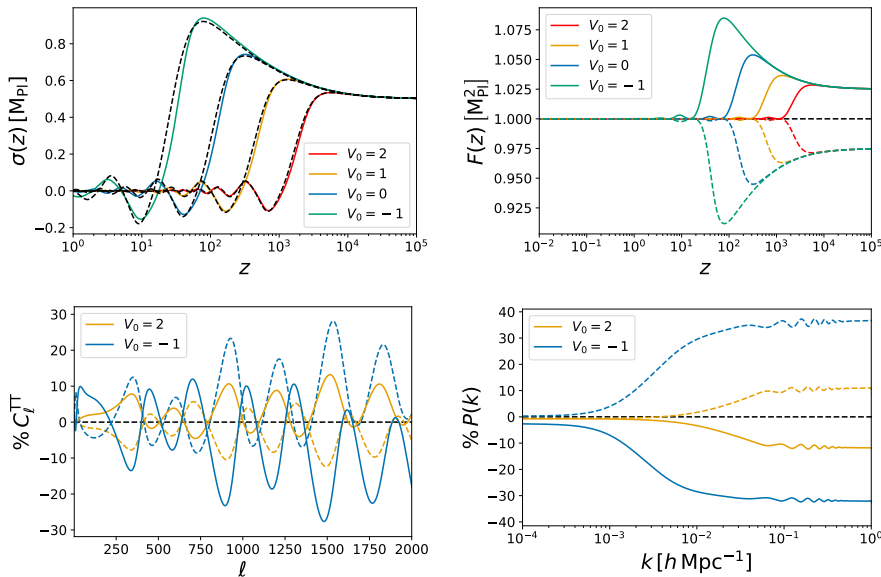


Figure 2.10: Redshift evolution of the scalar field σ (upper left panel) and of the nonminimal coupling function $F(\sigma)$ (upper right panel). Relative differences with respect to Λ CDM in the CMB temperature anisotropies power spectrum (bottom left panel) and in the linear matter power spectrum at $z = 0$ (bottom right panel). Different values of the amplitude of the potential V_0 are considered for $|\xi| = 0.1$ in the standard branch (solid lines) and in the phantom one (dashed lines) for EMG ($F = M_{\text{Pl}}^2 + \xi\sigma^2$, $V = \Lambda + \lambda\sigma^4/4$).

NMC+ and in Fig. 2.9 and Table 2.3 for NMC+. For all the datasets combinations the constraints on the cosmological parameters are consistent with the results of IG. The marginalized bounds at 95% CL on the coupling constants of NMC+ (NMC-) are $\xi < 0.0015$ (> -0.039) and $N_{\text{Pl}} > 0.91$ (< 1.18) for P18+BAO, and to $\xi < 0.0019$ (> -0.027) and $N_{\text{Pl}} > 0.83$ (< 1.21).

As it was already pointed out for the standard branch in Refs. [109, 110], there is a strong degeneracy between the parameters N_{Pl} and ξ for $F(\sigma) = N_{\text{Pl}}^2 + \xi\sigma^2$. This is due to the fact that cosmological observables are affected by contributions of the order $\mathcal{O}(\xi\sigma^2/N_{\text{Pl}}^2)$, therefore, the effects of a large value of $|\xi|$ can be compensated by increasing $|\tilde{N}_{\text{Pl}} - 1|$ and vice versa.

Phantom early modified gravity

For EMG in the phantom branch, in addition to the six standard parameters we sample on ξ and V_0 where $\lambda \equiv -10^{2V_0}/M_{\text{Pl}}^4$. The scalar field goes through damped oscillations and decays around the local maximum of the potential, $\sigma = 0$. For this reason, we do not need to impose the boundary condition $G_{\text{eff}} = G_{\text{N}}$ since it is satisfied for any initial value of scalar field σ_{ini} , which is now an additional free parameter of the theory.

In the top left panel of Fig. 2.10, we show that the background evolution of the scalar field is similar in the two branches, standard and phantom: the field is at rest in the radiation dominated era and around recombination it starts to grow sourced by non-relativistic matter. Later, it is driven into coherent damped oscillations from the

2.6. Cosmological constraints

quartic potential. Instead, the nonminimal coupling function F , shown in the top right panel, evolves differently in the two branches: before the field starts to oscillate it is an increasing function of time for $Z = 1$, while it decreases in the phantom branch. This is due to the different sign of the coupling ξ in the two branches and it affects also the spectra portrayed in the bottom panels of Fig. 2.10. In the phantom branch the acoustic peaks of the CMB temperature anisotropies angular power spectrum are shifted to the right with respect to the Λ CDM model when the scalar field starts to move after recombination ($V_0 = -1$) and they shift to the left if the scalar field starts to decay before recombination ($V_0 = 2$); the opposite happens in the case with standard kinetic term.

Concerning the linear matter spectrum, in the bottom right panel of Fig. 2.10 we show the relative differences with respect to Λ CDM, the figure portrays an enhancement in small scale power in the phantom branch and an opposite suppression in power in the standard case, independently of the value of V_0 , underlining the importance of the combination of early-time probes with late-time observations to experimentally discriminate between the two branches and break the degeneracies between the additional parameters.

We present the results for the combinations of datasets P18+BAO+SN and P18+BAO+SN+p(H_0) in Fig. 2.11 and Table 2.4; since ξ is not constrained by data we show the constraints on the combination $\xi\sigma_{\text{ini}}^2 [M_{\text{Pl}}^2]$ (connected to the additional effect on the expansion rate (2.42) before recombination). The marginalized upper limit on $\xi\sigma_{\text{ini}}^2$ at 95% CL corresponds to > -0.0026 for P18+BAO+SN and to $\xi\sigma_{\text{ini}}^2 = -0.006 \pm 0.005$ when adding p(H_0). Analogously, for the initial value of the scalar field we obtain, at 95% CL, $\sigma_{\text{ini}} [M_{\text{Pl}}] < 0.45$ for P18+BAO+SN, and $0.35^{+0.17}_{-0.15}$ for P18+BAO+SN+p(H_0). The amplitude of the self-interaction term V_0 is not well constrained either: an upper bound at 95% CL, corresponding to $V_0 < 0.81$, is obtained only in the case with the Gaussian prior on H_0 . Concerning the Hubble constant, the marginalized means and uncertainties at 68% CL correspond to $68.44^{+0.62}_{-0.79}$ for P18+BAO+SN, and $70.18^{+0.59}_{-0.68}$ for P18+BAO+SN+p(H_0); while, for S_8 we find $S_8 = 0.827 \pm 0.011$ for P18+BAO+SN, and $S_8 = 0.822 \pm 0.010$ for P18+BAO+SN+p(H_0). The constraints on all the parameters are reported in Table 2.4.

Summary of the results

We have studied the cosmological dynamics and inferred the cosmological constraints for MG models with a nonminimally coupled scalar field with a non standard sign of the kinetic term, dubbed phantom branch. This study extends the parameter space considered previously in Ref. [98, 99, 110–112, 173], and allows a comparison with other works on Brans-Dicke theory with $-3/2 < \omega_{\text{BD}} < \infty$ [176].

For an effectively massless scalar σ , like the one we considered in IG and NMC, the change of sign of the kinetic term modifies the evolution of σ , which is at rest during the radiation era, and goes as $\sigma \sim a^{2Z\xi}$ during the matter-dominated epoch.

We have further shown the effect of the sign of the kinetic term on cosmological observables such as the CMB temperature anisotropies angular power spectrum and the matter power spectrum, and we obtained the marginalized constraints for different combination of cosmological datasets by allowing the coupling to the Ricci scalar and

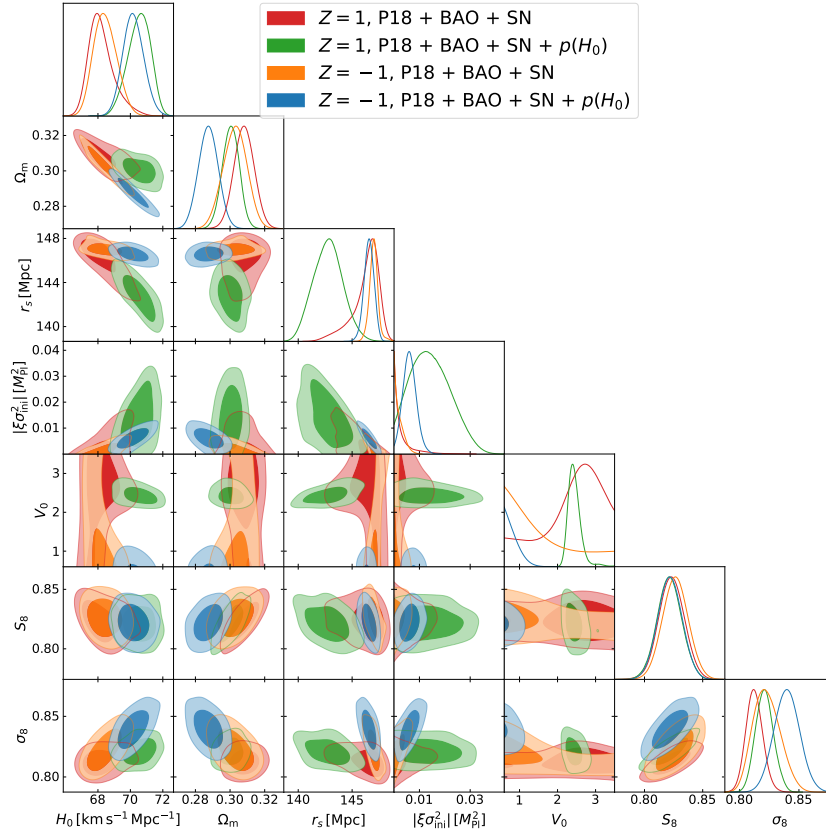


Figure 2.11: Marginalized joint 68% and 95% CL regions 2D parameter space using P18+BAO+SN (orange) and the combination P18+BAO+SN+p(H_0) (blue) for EMG ($F = M_{\text{pl}}^2 + \xi\sigma^2$, $V = \Lambda + \lambda\sigma^4/4$) in the phantom branch ($Z = -1$).

2.6. Cosmological constraints

the rest of the cosmological and nuisance parameters to vary in an MCMC analysis. Combining P18 with BAO and SN we constrain the coupling parameters at 95% CL to $\xi < 0.00040$ for $F(\sigma) = \xi\sigma^2$ and for $F(\sigma) = N_{\text{Pl}}^2 + \xi\sigma^2$ to $\xi < 0.0019$ (> -0.027) and $N_{\text{Pl}} > 0.83$ (< 1.21).

In the standard branch, nonminimally coupled STTs with early-time deviation from GR usually lead to higher inferred values for the Hubble constant H_0 and for σ_8 , together with a lower value of the matter density parameter Ω_m [110, 175, 176]; in their phantom construction instead, the modified evolution of the scalar field, connected to a different time evolution of the effective gravitational constant, inverts the degeneracy between these parameters and the coupling ones. For this reason, we obtain a lower values for σ_8 and H_0 compared to the standard branch.

We have also considered the phantom version of EMG. In this scenario the evolution of the scalar field is very similar to the standard case, with the quartic potential leading the scalar field into damped oscillations, finally decaying at $\sigma = 0$; but different signatures appear on the cosmological observables. Compared to Λ CDM, the acoustic peaks of the CMB are shifted to the right for a standard kinetic term when the scalar field moves before recombination ($V_0 = 2$) and in the phantom branch if the scalar field starts to decay after recombination ($V_0 = -1$), vice versa they shift to the left. Matter perturbations on sub-horizon scales are enhanced with respect to Λ CDM in the phantom branch and suppressed in the standard scenario, independently of the value of amplitude of the potential V_0 .

The values of the coupling parameters statistically preferred lay outside the region in parameter space free from ghosts and Laplacian instabilities. The possibility to alleviate the current tensions between different cosmological observations in STTs that satisfy the stability conditions in the phantom branch is discussed in section 2.6.3.

2. Current and novel constraints on modified gravity

Tables

Tables summarizing the results presented in this section for IG, NMC and EMG.

	P18	P18 + BAO	P18 + BAO + SN
ω_b	0.02223 ± 0.00017	0.02244 ± 0.00013	0.02245 ± 0.00013
ω_c	0.1204 ± 0.0012	0.11896 ± 0.00099	0.11882 ± 0.00096
H_0 [km s ⁻¹ Mpc ⁻¹]	$63.6^{+2.7}_{-1.9}$	$67.17^{+0.65}_{-0.48}$	$67.29^{+0.60}_{-0.47}$
τ	0.0523 ± 0.0071	$0.0584^{+0.0070}_{-0.0083}$	$0.0584^{+0.0068}_{-0.0076}$
$\ln(10^{10} A_s)$	3.037 ± 0.015	$3.051^{+0.014}_{-0.016}$	3.051 ± 0.014
n_s	$0.9574^{+0.0067}_{-0.0057}$	0.9668 ± 0.0038	0.9671 ± 0.0036
ξ	< 0.0018 (95% CL)	< 0.00046 (95% CL)	< 0.00040 (95% CL)
Ω_m	$0.354^{+0.020}_{-0.032}$	$0.3135^{+0.0059}_{-0.0068}$	$0.3120^{+0.0056}_{-0.0065}$
S_8	$0.850^{+0.016}_{-0.019}$	0.823 ± 0.011	0.821 ± 0.010
r_s [Mpc]	$148.89^{+0.8}_{-1.4}$	$147.62^{+0.31}_{-0.50}$	$147.62^{+0.29}_{-0.44}$
γ_{PN}	> 0.9928 (95% CL)	> 0.9982 (95% CL)	> 0.9984 (95% CL)
$\Delta\chi^2$	-2.8	0	-0.5

Table 2.1: Constraints on the main and derived parameters of the **IG** model (at 68% CL if not otherwise stated) considering P18 in combination with BAO and BAO+SN.

	P18	P18 + BAO	P18 + BAO + SN
ω_b	$0.02224^{+0.00018}_{-0.00016}$	0.02246 ± 0.00013	$0.02246^{+0.00011}_{-0.00014}$
ω_c	0.1206 ± 0.0012	$0.1190^{+0.0014}_{-0.0011}$	0.1189 ± 0.0010
H_0 [km s ⁻¹ Mpc ⁻¹]	$64.1^{+2.6}_{-1.7}$	67.28 ± 0.59	67.42 ± 0.52
τ	0.0514 ± 0.0081	0.0590 ± 0.0052	0.0583 ± 0.0071
$\ln(10^{10} A_s)$	$3.037^{+0.015}_{-0.023}$	$3.0517^{+0.0074}_{-0.015}$	3.051 ± 0.014
n_s	$0.9580^{+0.0058}_{-0.0047}$	0.9673 ± 0.0042	0.9674 ± 0.0039
ξ	< 0.030 (95% CL)	< 0.015 (95% CL)	< 0.019 (95% CL)
N_{Pl} [M_{Pl}]	–	> 0.91 (95% CL)	> 0.83 (95% CL)
Ω_m	$0.349^{+0.017}_{-0.030}$	$0.3121^{+0.0068}_{-0.0056}$	0.3110 ± 0.0061
S_8	$0.849^{+0.013}_{-0.019}$	$0.823^{+0.014}_{-0.009}$	$0.821^{+0.012}_{-0.011}$
r_s [Mpc]	$148.56^{+0.90}_{-1.3}$	$147.54^{+0.30}_{-0.48}$	$147.52^{+0.27}_{-0.44}$
γ_{PN}	> 0.9941 (95% CL)	> 0.9986 (95% CL)	> 0.9987 (95% CL)
β_{PN}	> 0.999965 (95% CL)	> 0.999994 (95% CL)	> 0.999994 (95% CL)
$\Delta\chi^2$	-1.5	0	-0.5

Table 2.2: Constraints on the main and derived parameters (at 68% CL if not otherwise stated) considering P18 in combination with BAO and BAO+SN for the **NMC+** model.

	P18	P18 + BAO	P18 + BAO + SN
ω_b	0.02230 ± 0.00014	0.02245 ± 0.00013	0.02247 ± 0.00013
ω_c	$0.11982^{+0.00068}_{-0.0011}$	0.11891 ± 0.00094	$0.11875^{+0.00078}_{-0.0010}$
H_0 [km s ⁻¹ Mpc ⁻¹]	$64.1^{+3.1}_{-2.1}$	$67.26^{+0.59}_{-0.45}$	$67.44^{+0.57}_{-0.45}$
τ	$0.0548^{+0.0072}_{-0.0059}$	$0.0573^{+0.0061}_{-0.0074}$	0.0590 ± 0.0068
$\ln(10^{10} A_s)$	$3.041^{+0.017}_{-0.013}$	3.049 ± 0.014	$3.052^{+0.014}_{-0.012}$
n_s	$0.9604^{+0.0067}_{-0.0045}$	$0.9669^{+0.0043}_{-0.0035}$	0.9675 ± 0.0036
ξ	> -0.036 (95% CL)	> -0.039 (95% CL)	> -0.027 (95% CL)
$N_{\text{Pl}} [M_{\text{Pl}}]$	< 1.13 (95% CL)	< 1.18 (95% CL)	< 1.21 (95% CL)
Ω_m	$0.348^{+0.021}_{-0.033}$	$0.3125^{+0.0052}_{-0.0065}$	$0.3106^{+0.0050}_{-0.0068}$
S_8	$0.844^{+0.011}_{-0.018}$	0.821 ± 0.011	$0.8204^{+0.0091}_{-0.012}$
r_s [Mpc]	$148.91^{+0.77}_{-1.6}$	$147.60^{+0.28}_{-0.43}$	$147.57^{+0.30}_{-0.40}$
γ_{PN}	> 0.988 (95% CL)	> 0.998 (95% CL)	> 0.998 (95% CL)
β_{PN}	< 1.00018 (95% CL)	< 1.000022 (95% CL)	< 1.000017 (95% CL)
$\Delta\chi^2$	-2.8	0	-0.3

Table 2.3: Constraints on the main and derived parameters (at 68% CL if not otherwise stated) considering P18 in combination with BAO and BAO+SN for the **NMC-** model.

	P18 + BAO + SN	P18 + BAO + SN + p(H_0)
ω_b	0.02246 ± 0.00014	0.02255 ± 0.00014
ω_c	0.1194 ± 0.0010	0.11900 ± 0.00099
H_0 [km s ⁻¹ Mpc ⁻¹]	$68.44^{+0.62}_{-0.79}$	$70.18^{+0.59}_{-0.68}$
τ	0.0536 ± 0.0080	$0.0503^{+0.0085}_{-0.0073}$
$\ln(10^{10} A_s)$	3.043 ± 0.016	$3.035^{+0.017}_{-0.015}$
n_s	$0.9671^{+0.0036}_{-0.0042}$	0.9687 ± 0.0038
$\xi\sigma_{\text{ini}}^2 [M_{\text{Pl}}^2]$	> -0.0057 (95% CL)	$-0.0062^{+0.0028}_{-0.0023}$
V_0	–	< 0.81 (95% CL)
$\sigma_{\text{ini}} [M_{\text{Pl}}]$	< 0.446 (95% CL)	$0.348^{+0.062}_{-0.097}$
Ω_m	0.3028 ± 0.0068	0.2875 ± 0.0056
S_8	0.827 ± 0.011	0.822 ± 0.010
r_s [Mpc]	147.00 ± 0.40	146.56 ± 0.46
$\Delta\chi^2$	-0.3	-14.9

Table 2.4: Constraints on the main and derived parameters (at 68% CL if not otherwise stated) considering P18 in combination with BAO+SN and BAO+SN+p(H_0) for the **EMG** model.

2.6.3 Nonminimally coupled Galileon

In this section, I study the cosmological dynamics and provide constraints on nonminimally coupled Galileon models; the results presented are based on the research work in [80], which also capitalizes on the development of an Einstein-Boltzmann code dedicated to this class of theories started in my master thesis [78].

In addition to the modified dynamics, the Galileon term provides a screening mechanism to potentially reconcile the models with general relativity predictions inside a Vainshtein radius, by fixing the PN parameters to their GR value. This is necessary because, without screening, the value $\xi = 5 \times 10^{-5}$ considered here, would not respect the solar system constraints on the PN parameters discussed in section 2.5.3.

The class of models considered in this section falls within the Horndeski theories (and can be remapped to an EFT formalism) allowed by the measurement of the gravitational waves propagation speed without fine tunings; in particular, we consider the action (2.6) with the G functions (2.7):

$$G_2 = ZX - V(\sigma) + 4\zeta(\sigma)X^2, \quad G_3 = -2g(\sigma)X, \quad G_4 = F(\sigma)/2. \quad (2.48)$$

This Lagrangian, with coupling function $F(\sigma) = \xi\sigma^2$ is equivalent to the extension of the Brans-Dicke model with a Galileon term. In fact with the field redefinition described in section 2.1, $\phi = \xi\sigma^2/2$, with $\xi = Z/(4\omega_{\text{BD}}) > 0$, and $Z = \pm 1$, the G functions become

$$G_2 = 2\frac{\omega_{\text{BD}}}{\phi}\chi - V(\phi), \quad G_3 = -2f(\phi)\chi, \quad G_4 = \phi, \quad (2.49)$$

where $\chi \equiv -\nabla_\mu\phi\nabla^\mu\phi/2$ and the relationship between the functions g, ζ and f is $g(\sigma) = \xi\sigma^3f(\sigma)$; $\zeta(\sigma) = \sigma^{-1}g(\sigma)$. Therefore, also following the nomenclature of Ref. [180], the model defined by Eq. (2.48) with $F(\sigma) = \xi\sigma^2$, is the *Brans-Dicke Galileon* (BDG), while we refer to the model with $G_2 = ZX - V(\sigma)$, always with $F(\sigma) = \xi\sigma^2$, as the *induced gravity Galileon* (IGG), since it is the extension of IG with a Galileon term $G_3 = -2g(\sigma)X$. We have shown that even if BD and IG are equivalent up to a field redefinition, their extensions with Galileon terms are not. In particular, IGG corresponds to BDG with, formally, $\zeta = 0$, but it is not simply a special case of BDG when $\zeta = 0$: in BDG the functions g and ζ are not independent and setting $\zeta = 0$ would mean setting $g = 0$ as well.

We study two different flavours of BDG and IGG, relating to the sign of the kinetic term Z :

- Standard branch: canonical sign for the kinetic term ($Z = 1$). In this branch we study both IGG and BDG (IGGst and BDGst) with $V(\sigma) = \lambda_n\sigma^n$, $g(\sigma) = \alpha_m\sigma^m$, for several combinations of n and m . In this scenario the potential dominates the background evolution of the Universe at late-times and provides the acceleration of the expansion of the Universe, while the G_3 enters as a small correction to the standard IG theory.
- Phantom branch: noncanonical sign for the kinetic term ($Z = -1$) and $\xi < 1/6$ ($\omega_{\text{BD}} < -3/2$). In this branch we consider only BDG with $g(\sigma) = \alpha\sigma^{-1}$, either with or without a potential. If there is no potential the burden to provide cosmic

2.6. Cosmological constraints

acceleration, a healthy theory and effective screening on small scales, is on the G_3 term. Reinserting the potential into the theory, both the Galileon term and the cosmological constant contribute to the late-time dynamics giving rise to the acceleration of the expansion of Universe.

Note that our analysis allows to study the proposal by Silva and Koyama [178] to drive the late-time acceleration of the Universe without an effective cosmological constant, but only with the G_3 term.

The equations of motion for the background evolution in a FLRW universe are given by Eqs. (2.11), (2.12) and (2.15), with $F(\sigma) = \xi\sigma^2$ and a choice for the functions $V(\sigma)$, $g(\sigma)$ and $\zeta(\sigma)$, corresponding to the model considered. The linearly perturbed Einstein and scalar field equations for this model can be found in appendix B.

IGG in the standard branch ($Z = 1$)

In the standard branch, in the region in parameter space that produces a reasonable cosmological background evolution, BDG and IGG are nearly indistinguishable [78], for this reason we restrict ourselves to IGG for $Z = 1$.

Considering a monomial potential $V(\sigma) = \lambda_n\sigma^n$ and $g(\sigma) = \alpha_m\sigma^m$, the IGG model presents exact late-time solutions with accelerated expansion in the absence of matter, with scale factor $a(t) \propto t^p$, the exponents n and m related by $m = 1 - n$, and

$$p = \frac{2(-2 + n + 4\beta - 4\xi + n^2\xi)}{(24\beta - 16\xi + 20n\xi - 8n^2\xi + n^3\xi)}, \quad (2.50)$$

$$\sigma(t) = c_0 t^{-2/(n-2)}, \quad (2.51)$$

where β , defined by $\alpha \equiv \beta c_0^{n-2}$, is a reparametrization of α , useful to show that in the limit of $\alpha \rightarrow 0$ ($\beta \rightarrow 0$) we recover the analogous solution found in IG in Ref. [181]. For $n = 4$ and $n = 2$, there are de Sitter solutions $a(t) \propto e^{Ht}$ with constant Hubble parameter $H > 0$. For $n = 4$, the solution found for IG [181]: $\sigma = \pm H\sqrt{3\xi/\lambda_4}$ is trivially still valid in IGG for every possible form of $g(\sigma)$, as this term does not contribute under the ansatz $\sigma = \text{constant}$. For $n = 2$, when $g(\sigma) \propto \sigma^{-1}$, there are solutions of the form $\sigma \propto e^{Ht\delta}$, with $\delta \equiv \delta(\alpha, \xi, H)$. Its explicit form is

$$\delta = -1, \quad \text{or} \quad \delta = \frac{-1 - 4\xi \pm \sqrt{(1 + 4\xi)^2 + 48H^2\xi\alpha}}{12H^2\alpha}. \quad (2.52)$$

In the limit $\alpha \rightarrow 0$ these solutions reduce to the ones discussed in Ref. [182]: $\delta = -1$ or $\delta = 2\xi/(1 + 4\xi)$.

In the following, we restrict to $n = m = 0$, since the numerical results are qualitatively similar for any choice of n and m ; and, instead of α , we use the rescaled, adimensional quantity $\tilde{\alpha} = \alpha \times (\text{Mpc} [\text{GeV}]^{-1})^{-2} \times (M_{\text{Pl}} [\text{GeV}])^{1+m}$.

The redshift evolution of the scalar field is shown in the left panel of Fig. 2.12, for a constant potential $V(\sigma) = \lambda_0 \equiv \Lambda$ and $g(\sigma) = \alpha$, compared to the analogous IG model with $\xi = 5 \times 10^{-5}$. It can be seen that the departure from IG is significant for larger α , i.e. stronger gravity at early times. Deep in the radiation era the field is nearly at rest but then it grows steeply (the larger α the steeper the growth) reaching the value

2. Current and novel constraints on modified gravity

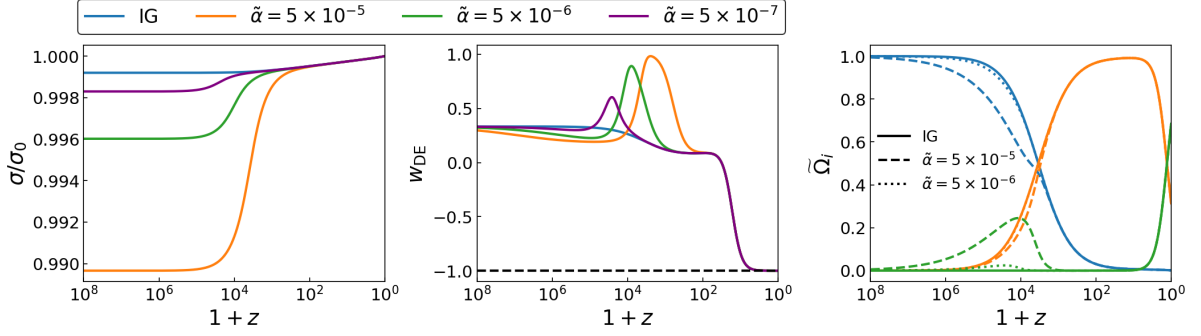


Figure 2.12: Time evolution of the scalar field (left panel), the equation of state parameter for dark energy (central panel) and the density parameters (right panel) in IGG standard ($Z = 1$) with $\xi = 5 \times 10^{-5}$, constant $V(\sigma) = \Lambda$ and $g(\sigma) = \alpha$, for different values of $\tilde{\alpha}$.

expected in IG in the matter era and evolving until today in the same way as it does in IG.

The value of the field at $z = 0$ is fixed by requiring that the effective gravitational coupling given by Eq. (2.16) coincide with the measured value of the Newton's constant G_N . For $m = 0$, the Galileon term does not contribute to Eq. (2.16), as it enters only through its derivative with respect to the σ , while, for $m \neq 0$ the contribution is negligible due to the redshift evolution of the scalar field in the matter era. Thus, we use the IG approximation, $8\pi G_{\text{eff}}(z = 0) = (1 + 8\xi) / [\xi\sigma_0^2(1 + 6\xi)]$, to fix the present value of the scalar field $\sigma(z = 0) \equiv \sigma_0$.

In the right plot of Fig. 2.12 we show the evolution of density parameters in IGG with $n = m = 0$. The values of α are chosen large enough to show the effect of the G_3 term in this scenario, which causes a different evolution of $\tilde{\Omega}_r$ and $\tilde{\Omega}_\sigma$ in the early Universe with respect to IG and Λ CDM.

The middle panel of Fig. 2.12 presents the evolution of the parameter of state of dark energy $w_{\text{DE}} \equiv p_{\text{DE}}/\rho_{\text{DE}}$, it tracks the IG behavior at late times but departs from it at $z \geq 10^3$, in correspondence to the analogous uptick in the evolution of $\tilde{\Omega}_\sigma$. In fact, w_{DE} follows the dominant component: deep in the radiation epoch it has a value close to $1/3$, then in the matter era it decreases towards zero; finally, at present epoch, it becomes negative, $w_{\text{DE}} \simeq -1$, mimicking a cosmological constant. The bump, occurring approximately during the radiation era, corresponds to the time in which the energy density of the field grows and becomes of the same order of that of radiation.

The growth of Ω_σ so early in time is due to inefficient *cosmological analogue of the Vainshtein screening* in this model for the range of parameters considered. In fact, the so-called cosmological analogue of the Vainshtein screening (hereafter cosmological Vainshtein screening), first discussed in Ref. [183], freezes the field to its initial value and after certain timescale the field is released and it starts to evolve. In particular, in a configuration where a single component other than the scalar dominates the energy content of the Universe, the density parameter of the scalar field is approximately

$$\Omega_\sigma \simeq \frac{1}{H} \sqrt{\frac{\xi}{\alpha \sigma^{m+1}}}, \quad (2.53)$$

2.6. Cosmological constraints

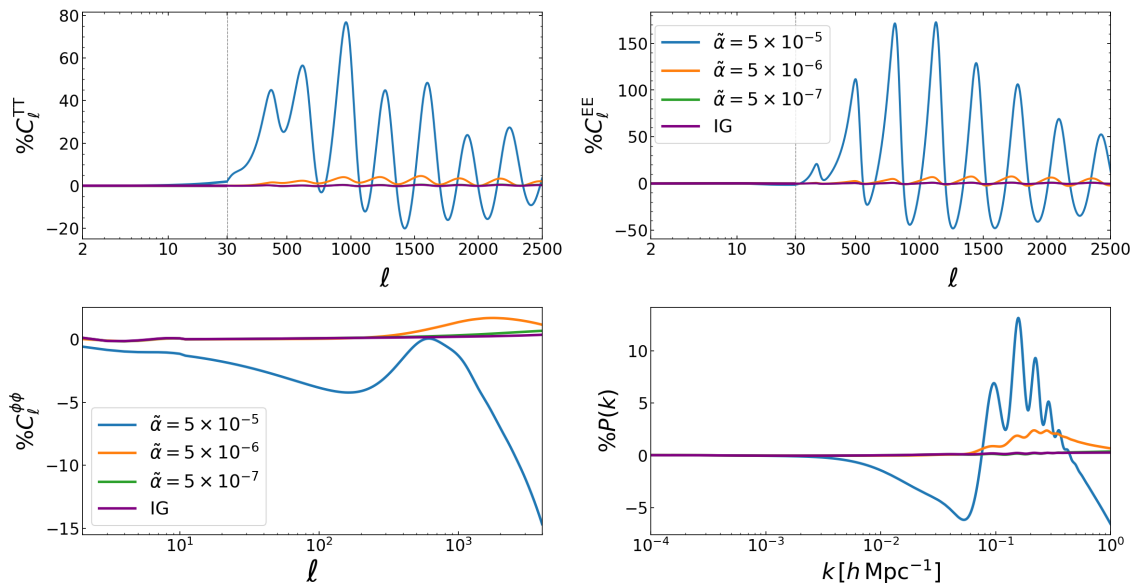


Figure 2.13: Relative differences with respect to Λ CDM for IGG standard with $\xi = 5 \times 10^{-5}$, $V(\sigma) = \Lambda$, $g(\sigma) = \alpha$. CMB TT (top left), EE (top right), lensing potential (bottom left) and linear matter power spectra (bottom right).

and it stays suppressed compared to radiation or matter as long as $H\sqrt{\alpha\sigma^{m+1}}/\sqrt{\xi} \gg 1$, for which we have cosmological Vainshtein screening. After a time $t \sim \sqrt{\alpha\sigma^{m+1}}/\sqrt{\xi}$ the approximation of a single component Universe breaks down as the density parameter of the scalar field begins to grow. Therefore, for smaller values of α we expect the scalar field to start evolving earlier in time. This is confirmed by the peculiar dynamics at early times we highlighted in Fig. 2.12: the values of α are too small to guarantee that the field stays frozen until late-times, and while for larger values of α we have the largest differences with respect to IG, it can be clearly seen from the left and central panels of Fig. 2.12 that the scalar field starts moving earlier for smaller α , reaching the IG line even before matter-radiation equality for $\tilde{\alpha} = 5 \times 10^{-7}$.

In Fig. 2.13 we show the deviations in the temperature and E-mode polarization CMB angular power spectra in the IGGst model with respect to Λ CDM, together with the CMB lensing potential angular power spectrum and the total linear matter power spectrum at $z = 0$.

In the standard branch there are small effects in the temperature power spectrum at at low multipoles, resulting in an ISW effect extremely similar to the one observed in Λ CDM. This behavior is common to all the spectra in IGGst at low multipoles, for which the differences with respect to GR are small. The departure from Λ CDM is more evident on the scales of the acoustic peaks in TT and on smaller scales, where, due to the modification of gravity around the time of recombination, the contribution of the scalar field shifts and enhances the peaks of the power spectrum.

We now turn on the discussion of the results of our data analysis where in addition to the six standard parameters we sample on $\tilde{\alpha}$ at fixed $\xi = 5 \times 10^{-5}$. We present the case $n = m = 0$, as all the findings are stable with respect to changes in the exponents. In Fig. 2.14 and Table 2.5 we show the result for the analysis with *Planck* CMB data

2. Current and novel constraints on modified gravity

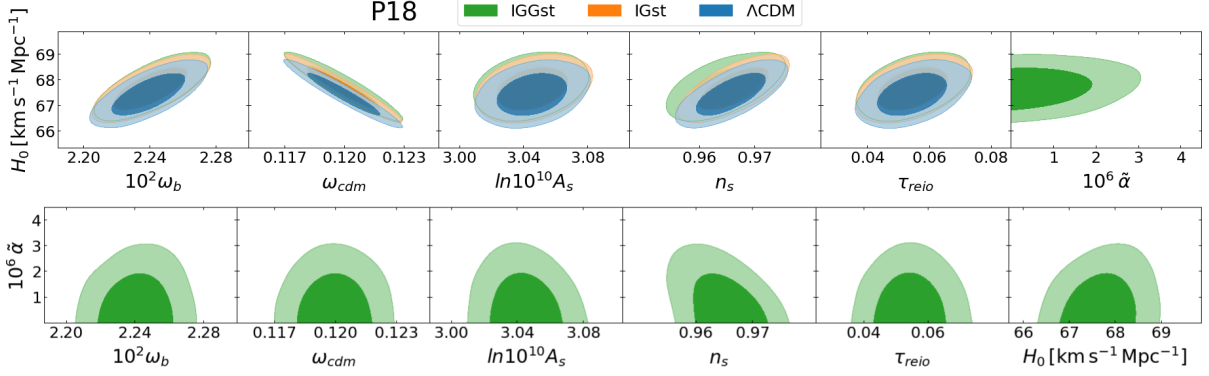


Figure 2.14: Marginalized 68% and 95% CL 2D regions using CMB data alone (P18). IGG standard ($Z = 1$) with $\xi = 5 \times 10^{-5}$, $V(\sigma) = \Lambda$, $g(\sigma) = \alpha$ in green; IG standard with $\xi = 5 \times 10^{-5}$, $V(\sigma) = \Lambda$, in orange and Λ CDM.

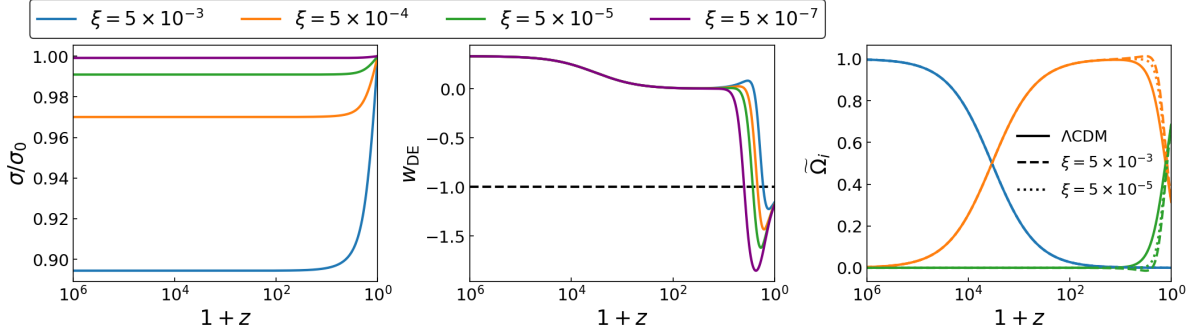


Figure 2.15: Time evolution of the scalar field (left panel), the equation of state parameter for dark energy (middle panel) and the density parameters (right panel) in BDG phantom ($Z = -1$) with no potential and $g(\sigma) = \alpha\sigma^{-1}$, for different values of ξ .

only, with a comparison to Λ CDM, and IG with $\xi = 5 \times 10^{-5}$. We obtain a tight constrain on the Galileon term for P18: i.e. $\tilde{\alpha} < 2.5 \times 10^{-6}$ at 95% CL, showing how CMB data are sufficient to strongly constrain IGG around IG. The contours for all the other parameters overlap with the IG ones. The marginalized mean and uncertainty for the Hubble constant H_0 [$\text{km s}^{-1} \text{Mpc}^{-1}$] at 68% CL corresponds to 67.72 ± 0.54 without any hint at a possible reduction of the Hubble tension, as there is no significant increase either in the mean or in the uncertainty with respect to the Λ CDM value of 67.36 ± 0.54 [1], or the IGst result 67.64 ± 0.54 (when $\xi = 5 \times 10^{-5}$ is fixed in the MCMC). Combining BAO with P18 we obtain tighter constraints but the same qualitative behavior (Tables 2.5 and 2.6): the marginalized upper bound at 95% CL on the amplitude of the Galileon parameter corresponds to $\tilde{\alpha} < 2.2 \times 10^{-6}$, while, the marginalized mean and uncertainty on the Hubble constant is $H_0 = 67.97 \pm 0.44 \text{ km s}^{-1} \text{Mpc}^{-1}$. The cosmological constraints from P18 and P18+BAO on $\tilde{\alpha}$ allow a Vainshtein mechanism to occur only at subparsec scale for an object of a solar mass.

2.6. Cosmological constraints

BDG in the phantom branch ($Z = -1$) with $V = 0$

In the phantom branch we first consider the basic case of BDG without potential and with $g(\sigma) = \alpha\sigma^{-1}$ and $\zeta = \sigma^{-1}g(\sigma)$. This model has no Λ CDM limit and the late time acceleration of the Universe arises from completely dynamical mechanisms thanks to the behaviour of the scalar field [178].

It was shown in Ref. [178] that, in absence of matter and radiation, $\rho = p = 0$, there is a self-accelerating late-time solution with $\dot{H} = \dot{Q} = 0$, with $Q = \dot{\sigma}/\sigma$, satisfying

$$y \equiv \frac{Q}{H} = \xi \frac{-4 \pm \sqrt{-32 - 6Z/\xi}}{Z + 8\xi}. \quad (2.54)$$

The solution is real for $Z = -1$ and $\xi < 3/16$ (equivalent to $\omega_{\text{BD}} < -4/3$), for which the Friedmann and scalar field equations (2.11) and (2.15) give

$$H^2 = \frac{\xi}{\alpha} \frac{3 + 6y + y^2/(2\xi)}{2y^3(3 + 2y)}. \quad (2.55)$$

Thus, without the potential, the Galileon term provides cosmic acceleration, but in order to do so the parameter α should be fine-tuned. This is done by solving Eq. (2.55) for α and using it as an initial guess for a shooting algorithm that fixes the value of α in order to produce the desired $\Omega_{\text{DE}} = 1 - \Omega_{\text{m}} - \Omega_{\text{r}}$ at present time, given the density parameters of matter and radiation as inputs. Since α is fixed by the requirement of cosmic acceleration, the only free parameter of the theory is ξ ; resulting in a theory that can provide late-time cosmic acceleration without a cosmological constant, with as many free parameters as the IG.

The values of α necessary to provide late-time cosmic acceleration of the Universe always guarantee effective Vainshtein screening, for this reason we do not set σ_0 following Eq. (2.16), as the gravitational constant on small scales is $G_{\text{N}} = G_{\text{cosm}}$. Therefore, the present value of the scalar field is fixed such that the Planck mass is $M_{\text{Pl}}^2(z=0) \equiv \xi\sigma_0^2 = 1$.

Departures from Λ CDM are evident already at the background level, especially in the matter era and in the late-time Universe where the field dominates the energy content. During matter domination, before the equality with DE, we observe, from the right panel of Fig. 2.15, that $\tilde{\Omega}_\sigma$ becomes negative and the effect is more prominent for larger values of ξ . When $\tilde{\Omega}_\sigma$ is decreasing and becoming negative, the corresponding Ω_{DE} in the Λ CDM model is growing already: a steeper growth of energy-density parameter of the scalar field is needed in order to reach the Λ CDM value today and for matter-dark energy equality to happen around the same redshift. We want to emphasize that $\tilde{\Omega}_\sigma < 0$ is not a problem from the physical point of view: this parameter just describes the contribution of the scalar field to the total expansion rate when the Friedmann equations are recast in a form resembling Einstein gravity [101, 130].

The evolution of the DE parameter of state, w_{DE} , in the central panel of Fig. 2.15 shows a phantom behavior $w_{\text{DE}} < -1$ in correspondence to $\tilde{\Omega}_\sigma$ becoming negative and growing back to dominate the energy content of the Universe. This behavior is more prominent for a smaller value of ξ , for which the dip tends to be deeper. Today, $w_{\text{DE}} < -1$ and it eventually reaches -1 in the future [178].

2. Current and novel constraints on modified gravity

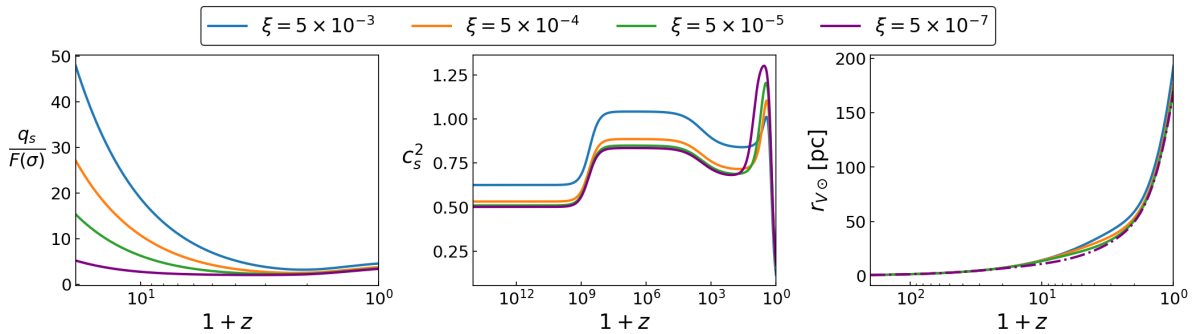


Figure 2.16: Stability conditions: ghost instability (left panel), Laplacian instability (middle panel). Vainshtein radius for a solar mass spherical object (right panel). BDG in the phantom branch ($Z = -1$), without potential, $g(\sigma) = \alpha/\sigma$, for different values of ξ .

In contrast to the standard branch where the scalar field started to evolve in the radiation-dominated epoch, here σ is frozen until late times, and it grows to reach today's value ($\xi\sigma_0^2 = 1$) only at small redshifts. This is the effect of the cosmological Vainshtein screening discussed in section 2.6.3: in the phantom branch α needs to be larger than in the standard case in order for the Galileon term to accelerate the expansion of the Universe, and since the time after which the scalar field is released is $t \sim \sqrt{\alpha/\xi}$, the growth the scalar field energy density is delayed with respect to the standard branch, for which α is constrained to be small.

As we've seen in section 2.3, a STT can be stable thanks to the addition of the G_3 term in the Lagrangian even with a non canonical sign for the kinetic term, it is therefore necessary to check for the stability conditions of the theory given by the Eqs. (2.21) and (2.22). The evolution with redshift of these conditions is presented in the left and central panel of Fig. 2.16: the requirements are satisfied for all the values of ξ considered thanks to the Galileon term. This term is also responsible for effective screening on small scales through the Vainshtein screening mechanism, allowing the theory to reduce to GR within the Vainshtein radius, given by Eq. (2.25). Today, the Vainshtein radius of an object of a solar mass is $r_{V\odot} \sim 100$ pc for all the values of ξ we considered, and its time evolution is shown in the right panel of Fig. 2.16.

In Fig. 2.17 we present the relative differences in the temperature and E-mode polarization CMB angular power spectra with respect to Λ CDM, together with the CMB lensing potential angular power spectrum and the total linear matter power spectrum at $z = 0$. Contrary to the standard branch, we observe very large departures from Λ CDM at large scales in all power spectra, especially in TT, due to the enhanced ISW effect. We point out that since the model has no Λ CDM limit the curves do not flatten out on zero for smaller ξ . Thus, while this model provides late-time cosmic acceleration without a cosmological constant, it presents large differences with respect to Λ CDM for CMB and matter power spectra; this is a disadvantage for differences $> 30\%$ when comparing the predictions against the data, since Λ CDM fits *Planck* data quite well.

We present in Fig. 2.18 and Table 2.5 the results of our P18 analysis where, in addition to the standard cosmological and nuisance parameters we sample on the nonminimal coupling ξ . This is the most radical among the models we studied as it cannot repro-

2.6. Cosmological constraints

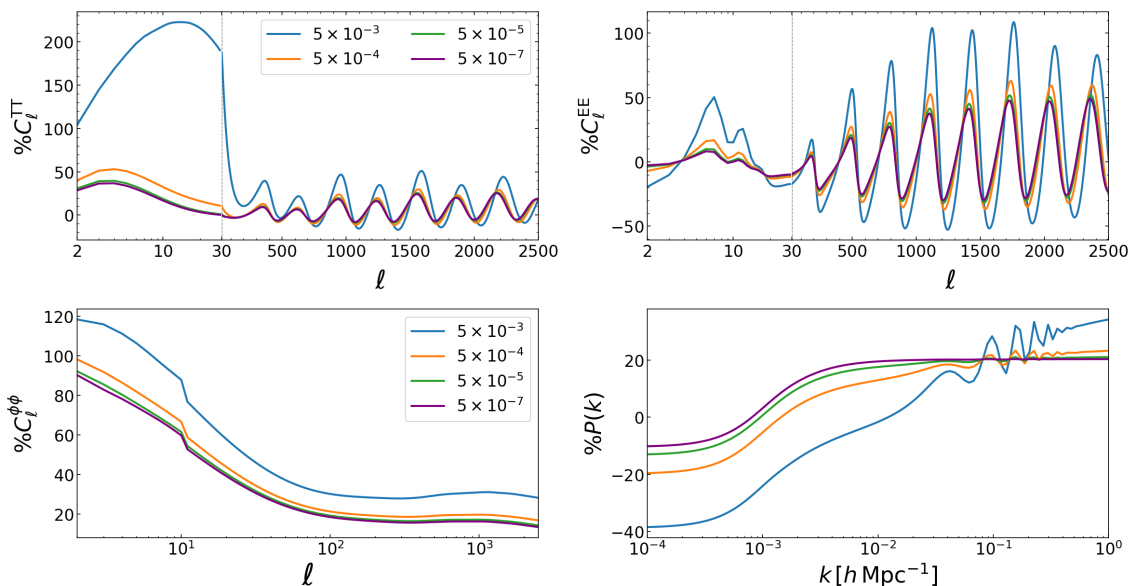


Figure 2.17: Relative differences with respect to Λ CDM for BDG phantom ($Z = -1$) without potential and $g(\sigma) = \alpha\sigma^{-1}$, for different values of ξ . CMB TT (top left), EE (top right), lensing potential (bottom left) and linear matter power spectra (bottom right).

duce the CMB and LSS theoretical prediction of Λ CDM, putting it at a disadvantage when tested against *Planck* data, and a $\Delta\chi^2 = 30.6$ confirms it. CMB alone is therefore sufficient to rule out this model, which has attracted a lot of attention in the scientific community as an alternative to Λ CDM. However, we would like to highlight the following: in addition to the appealing feature of providing cosmic acceleration without a cosmological constant, the marginalized mean and uncertainty on Hubble constant is raised to $H_0 = 79.57 \pm 0.67 \text{ km s}^{-1} \text{ Mpc}^{-1}$. While this result is still far from alleviating the Hubble tension, the ability to produce a Hubble constant larger than the SH0ES value [38] is interesting and could fuel the search for similar models that, while retaining this feature, might provide a better fit to the data.

We conclude this section by stressing the importance our original results in ruling out a compelling theoretical alternative to Λ in explaining the recent acceleration of the Universe. Our results share similarities with analogous previous studies ruling out large classes of $f(R)$ theories [184] as an explanation of the late-time acceleration. $f(R)$ models have been rescued by extending the functional form $f(R)$ [185], and are still considered viable theories, targeted by upcoming observational campaigns such as *Euclid* [186]. For this reasons, it would interesting to see if our results are completely general for any functional form the G_3 , or if the model can be rescued by a modification of the Galileon term.

Whereas this model is ruled out by *Planck* data, in the next section we reinsert the cosmological constant in G_2 to provide a better fit to the data and maintaining, at the same time, the nice properties of the model: stability and efficient screening.

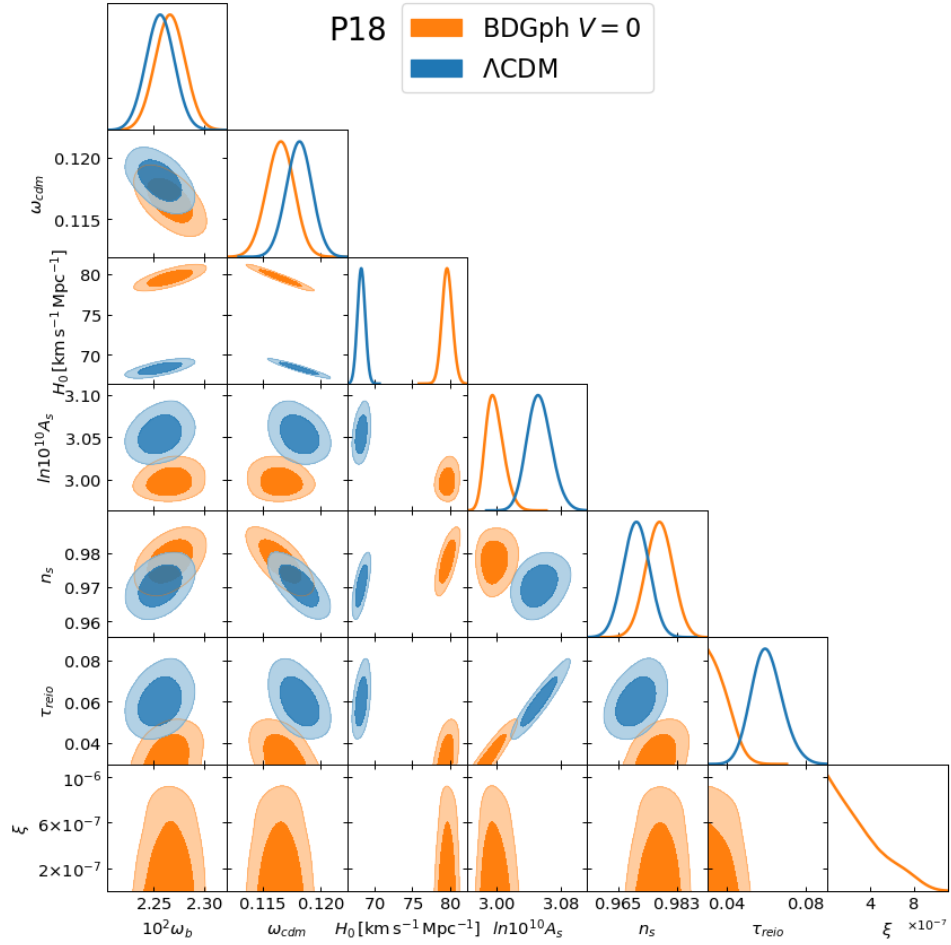


Figure 2.18: Marginalized joint 68% and 95% CL regions 2D parameter space using P18 data alone. In orange BDG phantom ($Z = -1$) without potential, $g(\sigma) = \alpha\sigma^{-1}$ and Λ CDM in blue.

2.6. Cosmological constraints

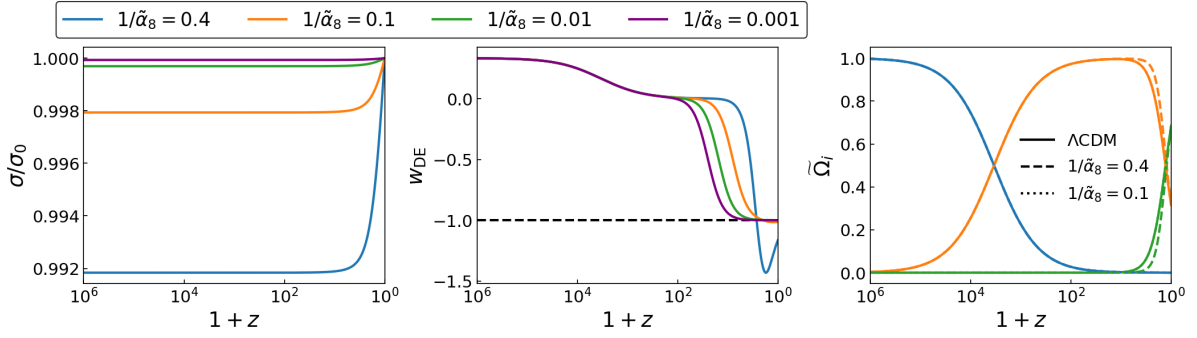


Figure 2.19: Time evolution of the scalar field (left panel), the equation of state parameter for dark energy (middle panel) and the density parameters (right panel) in BDG phantom ($Z = -1$) with $\xi = 5 \times 10^{-5}$, constant $V(\sigma) = \Lambda$ and $g(\sigma) = \alpha\sigma^{-1}$, for different values of $1/\tilde{\alpha}_8$.

BDG in the phantom branch ($Z = -1$) with $V = \Lambda$

We now turn our attention to the study of BDGph with a cosmological constant: $G_2 = ZX - \Lambda + 4\zeta(\sigma)X^2$, always with $g(\sigma) = \alpha\sigma^{-1}$ and $\zeta = \sigma^{-1}g(\sigma)$; in this way we obtain a theory with a Λ CDM limit.

In order to have the late-time cosmic acceleration, the parameters α and Λ need to be fine-tuned: we select a value for α and use a shooting algorithm on the cosmological constant to obtain $\Omega_{0,\text{DE}}(\Lambda, \alpha) = 1 - \Omega_{0,\text{m}} - \Omega_{0,\text{r}}$. In this way the late-time acceleration of the Universe is driven by an interplay between the potential and the Galileon term. This is in contrast to the previous section where there is no potential, but also differing with respect to the standard branch where the Galileon term is too small to significantly contribute to the late-time dynamics.

Analogously to the previous section, we fix the present value of the scalar field in such a way that the gravitational constant on small scales coincides with the cosmological one $G_{\text{N}} = G_{\text{cosm}}$ ($\xi\sigma_0^2 = 1$).

In what follows, we consider $\tilde{\alpha}$ rescaled by a factor 10^8 : $\tilde{\alpha}_8 \equiv 10^{-8}\tilde{\alpha}$. All the plots and the MCMC constraints will be expressed as a function of $1/\tilde{\alpha}_8$. The reason for using the inverse of $\tilde{\alpha}$ is that the Λ CDM limit is obtained when $\tilde{\alpha} \rightarrow \infty$ ($1/\tilde{\alpha} \rightarrow 0$); this is a manifestation of the cosmological Vainshtein screening mechanism. Indeed, as discussed in section section 2.6.3, the energy-density parameter of the Galileon field, during either matter or radiation domination goes as $\Omega_\sigma \simeq H^{-1}(\alpha/\xi)^{-1/2}$, and it stays suppressed compared to the dominant component as long as $H\sqrt{\alpha/\xi} \gg 1$, meaning that for $\alpha \rightarrow \infty$ the energy density of the Galileon is always suppressed, or, in other words, the scalar field is always frozen. In this model, in addition to the Galileon terms contributing to the budget of the Universe we also have a cosmological constant, and therefore, in the limit of large α the theory with a frozen scalar field plus a cosmological constant is indistinguishable from Λ CDM. We wish to emphasize that the correct Λ CDM limit is obtained only if the boundary condition for the scalar field is fixed to the correct value, $\xi\sigma_0^2 = 1$, otherwise, the resulting limit is a Λ CDM with a different gravitational constant. This highlights once more the necessity to be consistent with the measured value of the gravitational constant today here on earth.

2. Current and novel constraints on modified gravity

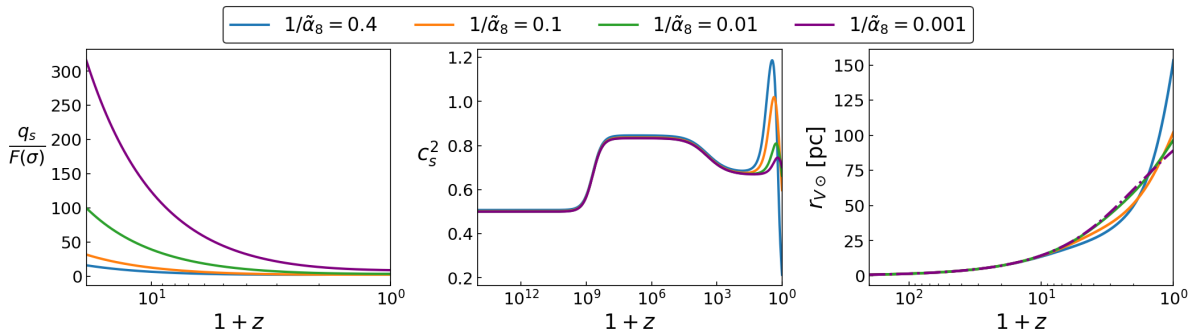


Figure 2.20: Stability conditions: ghost instability (left panel), Laplacian instability (middle panel) and Vainshtein radius for a solar mass spherical object (right panel) in BDG in the phantom branch ($Z = -1$) with $\xi = 5 \times 10^{-5}$, constant $V(\sigma) = \Lambda$ and $g(\sigma) = \alpha\sigma^{-1}$, for different values of $1/\tilde{\alpha}_8$.

In the left panel of Fig. 2.19 we show the time evolution of the scalar field as a function of $1/\tilde{\alpha}_8$: for larger values of this parameter the field starts at a lower initial value and it grows more steeply in the late Universe to reach the required value $\xi\sigma_0^2 = 1$ at $z = 0$. Contrary to the standard branch, where the field starts to evolve deep in the radiation era, here, due to the cosmological Vainshtein screening, the field is frozen until late-times when Ω_σ starts to grow. The field being frozen means that for a large portion of the history of the Universe the gravitational constant is really constant but different from the value measured on Earth today. This gives to the model the characteristic of both an early and late model as gravity is different in the early Universe and the dynamics of the field is relevant at low redshifts, when it is released from the cosmological screening.

In the right panel of Fig. 2.19 the evolution of the density parameters is shown: already for $1/\tilde{\alpha}_8 = 0.1$ the background expansion is indistinguishable from Λ CDM. Only for more extreme values we see appreciable departures from the standard model as the growth of the dark energy density parameter is delayed and steeper for $1/\tilde{\alpha}_8 = 0.4$. The time evolution of the DE parameter of state also confirms this behaviour: it approaches and reaches the value -1 earlier for smaller values of $1/\tilde{\alpha}_8$; while for the larger values we observe a phantom behavior with $w_{\text{DE}} < -1$ and $w_{\text{DE}} \neq -1$ today, reaching -1 in the future.

Analogously to the previous case ($V = 0$) in the phantom branch we check for the stability conditions of the theory: they are satisfied also in this scenario due to the presence of the Galileon term, as it can be seen in Fig. 2.20, where we show the time evolution of Eqs. (2.21) and (2.22).

As it was first observed in Ref. [178] for the case $V = 0$, we note from the figure that the speed of sound of scalar perturbations can become temporarily superluminal close to the transition to dark energy domination for large values of $1/\tilde{\alpha}_8$. The viability of a theory with temporarily superluminal propagation of scalar perturbations is a debated issue: some authors claim it is not problematic [187, 188], whereas others argue the opposite [189–191]. Thus, while in principle the requirement $c_s^2 \leq 1$ can potentially constrain the value of $1/\tilde{\alpha}_8$, we conservatively do not impose any theoretical prior $c_s^2 \leq 1$ in our MCMC analysis. As pointed out in section 2.3 the stability conditions in the tensor sector are

2.6. Cosmological constraints

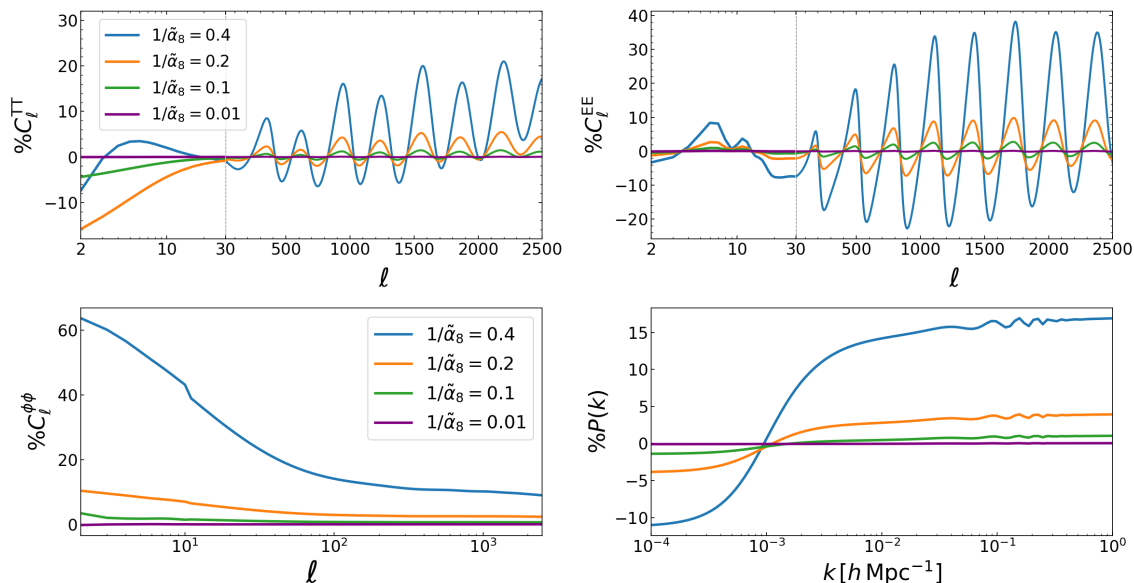


Figure 2.21: Relative differences with respect to Λ CDM for BDG phantom ($Z = -1$) with $\xi = 5 \times 10^{-5}$, constant $V(\sigma) = \Lambda$ and $g(\sigma) = \alpha\sigma^{-1}$, for different values of $1/\tilde{\alpha}_8$. CMB TT (top left), EE (top right), lensing potential (bottom left) and linear matter power spectra (bottom right).

automatically satisfied by the choice of our Lagrangian and parameters.

Moreover, in the right panel Fig. 2.20 we show the cosmological evolution of the Vainshtein radius for an object of mass, confirming that screening is effective and the Vainshtein radius begins to grow for $z \lesssim 10$, reaching $r_{V\odot} \gtrsim 90$ pc today, successfully recovering GR in the Solar System.

Fig. 2.21 shows the relative differences in the temperature and E-mode polarization CMB angular power spectra with respect to Λ CDM, together with the CMB lensing potential angular power spectrum and the total linear matter power spectrum at redshift $z = 0$. We observe large departures from Λ CDM at low multipoles in TT, due to the interplay of G_3 and the ISW effect [192, 193]. While we see differences on all scales in all power spectra of Fig. 2.21, we recover the predictions of the Λ CDM model as $1/\tilde{\alpha}_8$ gets smaller, thanks to the presence of the cosmological constant. Therefore, there is room to provide a good fit to the data even with $1/\tilde{\alpha}_8 \neq 0$ but small. The differences in the matter power spectrum with respect to the standard model, presented in the bottom right panel of Fig. 2.21, are interesting targets for upcoming large scale structure data such as DESI³, Euclid⁴, or Vera Rubin observatory⁵, which will significantly tighten constraints on these models.

We now turn to the results of our analysis with publicly available cosmological datasets, in addition to the standard cosmological and nuisance parameters we sample on $1/\tilde{\alpha}_8$ in order to have the Λ CDM limit at zero and not at infinity, as we would if we had sampled

³<https://www.desi.lbl.gov>

⁴https://www.esa.int/Science_Exploration/Space_Science/Euclid

⁵<https://www.vro.org/>, <https://www.lsst.org/>

2. Current and novel constraints on modified gravity

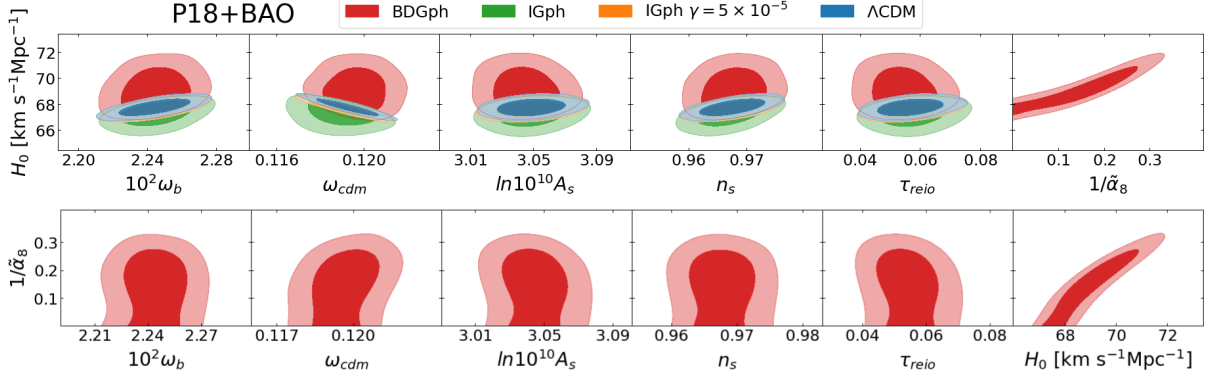


Figure 2.22: Marginalized 68% and 95% CL 2D regions, using the combination P18 + BAO. BDG phantom ($Z = -1$) with $\xi = 5 \times 10^{-5}$, $g(\sigma) = \alpha\sigma^{-1}$ in red, IGph and IGph with fixed $\xi = 5 \times 10^{-5}$ respectively in green and orange; in all cases $V(\sigma) = \Lambda$. Λ CDM in blue.

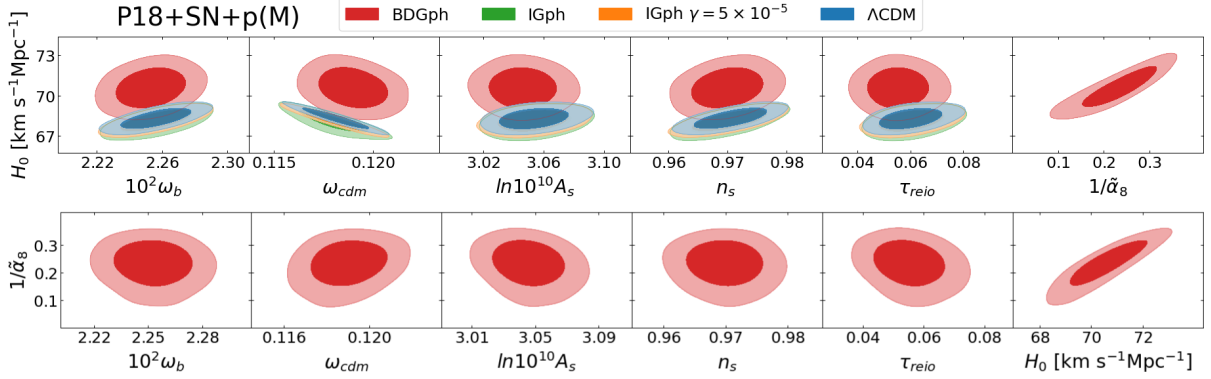


Figure 2.23: Marginalized 68% and 95% CL 2D regions, using the combination P18 + SN + p(M). BDG phantom ($Z = -1$) with $\xi = 5 \times 10^{-5}$, $g(\sigma) = \alpha\sigma^{-1}$ in red, IGph and IGph with fixed $\xi = 5 \times 10^{-5}$ respectively in green and orange; in all cases $V(\sigma) = \Lambda$. Λ CDM in blue.

on α . In this analysis the nonminimal coupling parameter is fixed: $\xi = 5 \times 10^5$ and we add BAO to P18 data in order to constrain the parameter $1/\tilde{\alpha}_8$ within our prior range, $1/\tilde{\alpha}_8 = 10^8/\tilde{\alpha} \in [0, 0.4]$. Indeed, current CMB data are indeed not enough to constrain this seven parameter model with ξ fixed.

The results for the P18+BAO analysis are presented in Fig. 2.22 and Table 2.7; the presence of the cosmological constant helps in providing posterior distributions closer to Λ CDM and the marginalized means and uncertainties for most of the cosmological parameters are similar. The Hubble constant is an exception: due to the shape of the posterior in the plane $1/\tilde{\alpha}_8$ - H_0 (see Fig. 2.22), higher values of H_0 compared to Λ CDM ones are allowed. Indeed, using the combination P18+BAO (Table 2.7) the marginalized mean and uncertainty for H_0 [$\text{km s}^{-1} \text{Mpc}^{-1}$] at 68% CL correspond to $69.1_{-1.3}^{+0.9}$. For the same dataset, IG phantom with the nonminimal coupling constant fixed at the same value considered here for BDGph, $\xi = 5 \times 10^{-5}$, gives 67.62 ± 0.42 , while it gives $67.20_{-0.55}^{+0.68}$ when ξ is a free parameter. Thus, BDGph raises the inferred value of the Hubble constant relatively to IGph and it reduces the Hubble tension to a significance of 2.5σ .

These results motivate our subsequent analysis using the Pantheon catalog with the addition of a prior on the peak absolute magnitude of SN Ia. We present the out-

2.6. Cosmological constraints

comes of this analysis in Fig. 2.23 and Table 2.8. When considering this combination of datasets (P18+SN+p(M)), the Hubble tension is alleviated: it has a significance of only 1.7σ in BDGph, since the marginalized mean and uncertainty at 68% CL are $H_0 = 70.58 \pm 0.97 \text{ km s}^{-1} \text{ Mpc}^{-1}$. The corresponding values in IGph, with $\xi = 5 \times 10^{-5}$ and ξ free to vary in the MCMC are, respectively, 68.15 ± 0.52 and 68.07 ± 0.56 . *This means that the Galileon term is not only necessary to avoid instabilities present in IGph (see section 2.6.2) but it also plays an important role in alleviating the Hubble tension.* Moreover, we obtain $\Delta\chi^2 = -8.5$ and $\Delta\text{AIC} = -6.5$, showing a weak preference for the model with respect to ΛCDM , whereas in all other cases there is no significant improvement, if any, with respect to the standard cosmological model.

We also wish to emphasize another aspect of our findings in terms of the Vainshtein radius. For P18 + SN + p(M) the mean and uncertainty on the Galileon coupling constant correspond to $1/\tilde{\alpha}_8 = 0.23^{+0.06}_{-0.05}$ at 68% CL; in other words, we see high statistical significance for $1/\tilde{\alpha}_8 \neq 0$, and consequently a Vainshtein radius of $\mathcal{O}(100)$ pc for a solar mass. This is in contrast with the analysis done using P18+BAO where $1/\tilde{\alpha}_8$ is consistent with zero at 1σ and we only obtain an upper limit, $1/\tilde{\alpha}_8 < 0.28$ at 95% CL, perfectly consistent with the ΛCDM limit of the theory.

Summary of the results

We have studied the cosmological dynamics and inferred the cosmological constraints for MG models with a nonminimally coupled scalar field and a cubic Galileon term. Since the extensions of IG and BD with a Galileon term are not equivalent theories, we have studied the two models separately: IGG and BDG; these models are equipped with the Vaishtein screening mechanism, potentially reconciling the theory with GR inside the so-called Vainshtein radius. Moreover, the presence of the Galileon term is also necessary to ensure that the theory is free of ghost and Laplacian instabilities even for a noncanonical sign of the kinetic term, $Z = -1$. We have therefore considered the Lagrangian (2.7) in the standard ($Z = 1$) and phantom ($Z = -1$) branch, comparing the theoretical predictions of the models with observations.

For a standard kinetic term, the scalar field starts evolving during the radiation dominated era due to the absence of cosmological Vainshtein screening. This behavior is then dissipated in the matter dominated era, in which the Galileon term is subleading. We find that the CMB anisotropy pattern is sensitive to these effects and constrains the Galileon term to be small close to the CMB last scattering surface. For BDG in the standard branch the results are identical to the ones of IGG, we have therefore reported them only once for IGG with $\xi = 5 \times 10^{-5}$ and $n = m = 0$. *Planck* 2018 and BAO data tightly constrain the amplitude of the Galileon parameter as $\tilde{\alpha} < 2.2 \times 10^{-6}$ at 95 % CL (Table 2.6), and the resulting posterior probabilities for cosmological parameters are very similar to those of IG. The cosmological constraint on $\tilde{\alpha}$ are such that the Vainshtein mechanism can occur only at subparsec scale for an object of a solar mass.

In the phantom branch we have considered only BDG. The presence of a Galileon term leads to a healthy theory for all the values of ξ , i.e. for any negative value of ω_{BD} , therefore rescuing the range $\omega_{\text{BD}} < -3/2$ which would contain a ghost in the BD/IG. The phenomenology in the phantom branch is quite different with respect to the $Z = +1$

2. Current and novel constraints on modified gravity

case, in fact, the Galileon field is frozen for most of the matter dominated era and it is released only at lower redshift.

BDGph with $m = -1$, $V = \Lambda$ and fixed $\xi = 5 \times 10^{-5}$, leads to a value of H_0 larger than in Λ CDM with a screening of ~ 100 pc for a solar mass, as desired. Indeed, our results using *Planck* 2018 joint with BAO data are $H_0 = 69.1^{+0.9}_{-1.3} \text{ km s}^{-1} \text{ Mpc}^{-1}$ at 68% CL, and $\tilde{\alpha}^{-1} < 0.28 \times 10^{-8}$ at 95% CL (Table 2.7 and Fig. 2.22).

By adding the *Pantheon* dataset with a prior on the supernovae peak absolute magnitude, we get $H_0 = 70.58 \pm 0.97 \text{ km s}^{-1} \text{ Mpc}^{-1}$ and $\tilde{\alpha}^{-1} = 0.23^{+0.06}_{-0.05} \times 10^{-8}$ at 68% CL, always for $\xi = 5 \times 10^{-5}$ and $m = -1$ (Table 2.8 and Fig. 2.23). In addition, the value and the posterior of S_8 are unchanged with respect to Λ CDM, not aggravating the σ_8 tension [71].

We have also analyzed the theoretical predictions of BDGph with no potential and the late-time acceleration driven exclusively by the Galileon term. The model is physically viable and provides screening on Solar System scales, but it leads to CMB predictions which are at odds with the *Planck* data, with a $\Delta\chi^2 = 30.6$ with respect to Λ CDM. Therefore, although theoretically interesting because the acceleration is not driven by an effective cosmological constant, the model with no potential is ruled out by observations. It would be interesting to see if these conclusions hold for any functional form of the G_3 .

In conclusion, we have demonstrated how rather nontrivial cosmological effects arise in the presence of a Galileon term, as it can lead simultaneously to a value of H_0 larger than in Λ CDM and to effective screening for a large volume of parameter space.

2.6. Cosmological constraints

Tables

We collect in this section the tables for IGGst and BDGph.

	IGGst	IGst	BDGph $V = 0$	Λ CDM
$10^2\omega_b$	2.242 ± 0.014	2.240 ± 0.014	2.266 ± 0.015	2.237 ± 0.015
ω_{cdm}	0.1200 ± 0.0012	0.1200 ± 0.0012	0.1165 ± 0.0012	0.1200 ± 0.0012
H_0 [km s ⁻¹ Mpc ⁻¹]	67.72 ± 0.54	67.64 ± 0.54	79.57 ± 0.67	67.36 ± 0.54
$\ln(10^{10}A_s)$	3.044 ± 0.014	3.046 ± 0.014	$2.9979^{+0.0093}_{-0.013}$	3.044 ± 0.014
n_s	0.9647 ± 0.0044	0.9662 ± 0.0041	0.9776 ± 0.0041	0.9649 ± 0.0042
τ_{reio}	0.0545 ± 0.0073	0.0546 ± 0.0075	< 0.0475 (95% CL)	0.0544 ± 0.0073
$10^6\tilde{\alpha}$	< 2.5 (95% CL)	—	—	—
ξ	5×10^{-5}	5×10^{-5}	$< 7.70 \cdot 10^{-7}$ (95% CL)	—
$\Delta\chi^2$ (ΔAIC)	0.2 (2.2)	0.2 (0.2)	30.6 (32.6)	—

Table 2.5: Constraints on the main parameters (at 68% CL unless otherwise stated) considering **P18** for **IGG standard** ($Z = 1$ and $g(\sigma) = \alpha$), **IG standard**, both with $\xi = 5 \times 10^{-5}$, $V(\sigma) = \Lambda$, **BDG phantom** ($Z = -1$) with $V(\sigma) = 0$ and $g(\sigma) = \alpha\sigma^{-1}$ and Λ CDM.

	IGGst	IGst $\xi = 5 \times 10^{-5}$	Λ CDM
$10^2\omega_b$	2.245 ± 0.014	2.244 ± 0.013	2.244 ± 0.013
ω_{cdm}	0.11940 ± 0.00096	0.11937 ± 0.00093	0.11925 ± 0.00094
H_0 [km s ⁻¹ Mpc ⁻¹]	67.97 ± 0.44	67.91 ± 0.42	67.75 ± 0.43
$\ln(10^{10}A_s)$	3.047 ± 0.014	3.048 ± 0.014	3.049 ± 0.014
n_s	0.9662 ± 0.0041	0.9676 ± 0.0036	0.9675 ± 0.0037
τ_{reio}	0.0562 ± 0.0073	0.0563 ± 0.0071	0.0568 ± 0.0072
$10^6\tilde{\alpha}$	< 2.2 (95% CL)	—	—
ξ	5×10^{-5}	5×10^{-5}	—
$\Delta\chi^2$ (ΔAIC)	-0.1 (1.9)	-0.1 (-0.1)	—

Table 2.6: Constraints on the main parameters (at 68% CL unless otherwise stated) considering the combination **P18+BAO** for **IGG standard** ($Z = 1$) with $g(\sigma) = \alpha$, **IG standard** with $\xi = 5 \times 10^{-5}$ fixed and Λ CDM. In all cases $V(\sigma) = \Lambda$.

	BDGph	IGph $\xi = 5 \times 10^{-5}$	IGph
$10^2 \omega_b$	2.244 ± 0.014	2.245 ± 0.013	2.245 ± 0.014
ω_{cdm}	0.11966 ± 0.00097	0.11910 ± 0.00093	0.11884 ± 0.00099
H_0 [km s $^{-1}$ Mpc $^{-1}$]	$69.1_{-1.3}^{+0.9}$	67.62 ± 0.42	$67.20_{-0.55}^{+0.68}$
$\ln(10^{10} A_s)$	3.045 ± 0.014	$3.048_{-0.015}^{+0.014}$	3.048 ± 0.015
n_s	0.9678 ± 0.0038	0.9675 ± 0.0037	0.9671 ± 0.0038
τ_{reio}	0.0543 ± 0.0073	$0.0568_{-0.0077}^{+0.0068}$	0.0575 ± 0.0075
$1/\tilde{\alpha}_8$	< 0.28 (95% CL)	—	—
ξ	5×10^{-5}	5×10^{-5}	< 0.00047 (95% CL)
$\Delta\chi^2$	-1.1	0.2	0
ΔAIC	0.9	0.2	2

Table 2.7: Constraints on the main parameters (at 68% CL unless otherwise stated) considering the combination **P18+BAO** for **BDG phantom** ($Z = -1$) with $g(\sigma) = \alpha\sigma^{-1}$, **IG phantom** with $\xi = 5 \times 10^{-5}$ fixed and **IG phantom** with ξ free to vary. In all cases unless otherwise specified $\xi = 5 \times 10^{-5}$ and $V(\sigma) = \Lambda$.

	BDGph	IGph $\xi = 5 \times 10^{-5}$	IGph	ΛCDM
$10^2 \omega_b$	2.253 ± 0.014	2.256 ± 0.014	2.257 ± 0.014	2.256 ± 0.014
ω_{cdm}	0.1190 ± 0.0012	0.1180 ± 0.0011	0.1180 ± 0.0011	0.1181 ± 0.0011
H_0 [km s $^{-1}$ Mpc $^{-1}$]	70.58 ± 0.97	68.15 ± 0.52	68.07 ± 0.56	68.31 ± 0.50
$\ln(10^{10} A_s)$	3.046 ± 0.015	3.053 ± 0.015	3.054 ± 0.015	$3.054_{-0.016}^{+0.014}$
n_s	0.9699 ± 0.0040	0.9703 ± 0.0041	0.9702 ± 0.0041	0.9705 ± 0.0040
τ_{reio}	0.0555 ± 0.0077	$0.0602_{-0.0085}^{+0.0076}$	0.0608 ± 0.0079	$0.0602_{-0.0083}^{+0.0072}$
$1/\tilde{\alpha}_8$	$0.23_{-0.05}^{+0.06}$	—	—	—
ξ	5×10^{-5}	5×10^{-5}	< 0.00022 (95% CL)	—
$\Delta\chi^2$	-8.5	1.1	0	—
ΔAIC	-6.5	1.1	2	—

Table 2.8: Constraints on the main parameters (at 68% CL unless otherwise stated) considering the combination **P18+SN+p(M)** for **IG phantom** ($Z = -1$) with $\xi = 5 \times 10^{-5}$ fixed and free to vary, **BDG phantom** with $\xi = 5 \times 10^{-5}$, $g(\sigma) = \alpha\sigma^{-1}$ and ΛCDM . In all cases $V(\sigma) = \Lambda$.

Chapter 3

Euclid and cross-correlation of its probes with CMB

Euclid is a medium class space mission of the European Space Agency (ESA), selected in 2011 and launched into orbit around the Sun-Earth Lagrangian point L2 on July 1st 2023. The primary objectives of the mission are to better characterize dark matter, dark energy and the accelerated expansion of the Universe, test gravity on cosmological scales and study the role of neutrinos in the growth of structure. In order to reach these goals, *Euclid* will combine complementary probes: weak lensing and galaxy clustering through BAO and RSD (see section 1.7.3). The WL is sensitive to all nonrelativistic matter but this probe depends on a combination of angular distances (sensitive to the expansion rate) and the mass density contrast (sensitive to the growth rate of structures); on the other hand, BAO probe the expansion of the Universe and RSD are sensitive to the growth rate of structure. Thus, the combination of all these probes will allow *Euclid* to strongly constrain the dark sector of the Universe.

3.1 The *Euclid* mission

The nominal mission will last six years, during which the so-called *wide survey* will be performed: *Euclid* will measure the redshifts and shapes of galaxies on a patch of the sky of about $15\,000\text{ deg}^2$, up to redshift $z \simeq 2.5$, covering in this way the late-time cosmic acceleration period. During the wide survey *Euclid* will observe objects with a minimum magnitude of 26.2 (visible) and 24.5 (near infrared) [194] by scanning the sky and observing about 15 deg^2 per day ($\sim 400\text{ deg}^2$ per month), and every 6 months it will be pointed to the opposite direction to survey the other hemisphere. In this way, *Euclid* will measure the images and photometric redshifts of 1.5 billion galaxies, and the spectroscopic redshifts of 35 million galaxies over a wide field of view. The mission will benefit from collaborations with ground-based surveys for a better estimate of photometric redshifts.

While the wide survey constitutes the core of the mission, another survey, observing objects 2 magnitudes fainter than the wide survey, will be carried out by repeatedly scanning the same areas of the sky at regular intervals during the mission. This survey is comprised of the three *Euclid deep fields*, covering a total of 50 deg^2 , observing high-redshift galaxies, quasars, and active galactic nuclei. The deep fields have the capabilities of discovering $\mathcal{O}(10^5)$ galaxies at $z > 6$ [195] and are therefore relevant for studying the formation and evolution of galaxies. Moreover, they are required to calibrate the wide survey data and assess the redshift purity and completeness of the spectroscopic wide survey. The regions of the sky covered by the wide and deep fields are shown in Fig. 3.1.

Even if *Euclid* is primarily a cosmological mission, it will bring major advances in nearly all areas of astronomy, from the study of nearby solar system objects to extrasolar

3. Euclid and cross-correlation of its probes with CMB

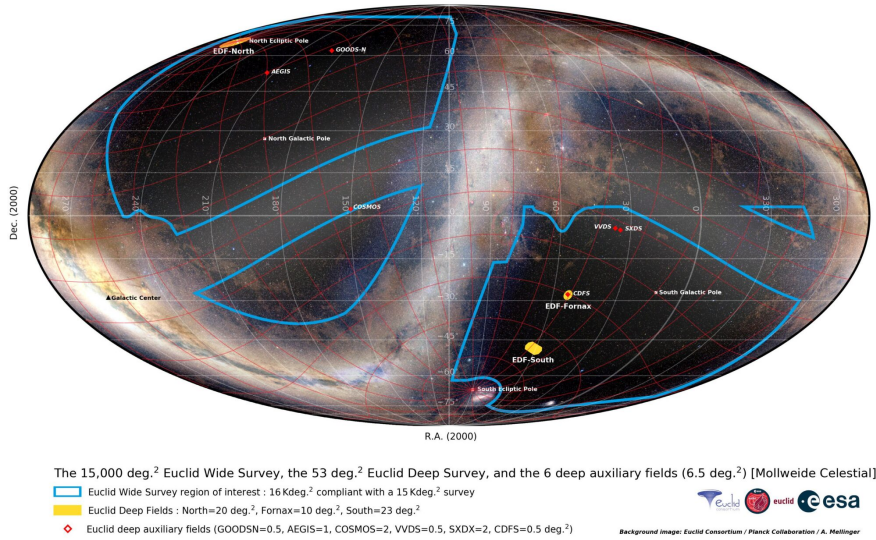


Figure 3.1: Regions of the sky covered by the *Euclid* mission in the equatorial coordinate system in Mollweide projection. The wide survey area is highlighted in blue and the deep survey in yellow. The region where the Milky-way is present and the ecliptic plane are avoided during the mission. Figure taken from the [EC website](#).

planets and star formation as well as galaxies at all epochs of the Universe. For example, the mission is expected to characterise at least 100 000 solar system bodies, to find extrasolar planets thanks to the microlensing effect, to discover thousands of supernovae up to $z = 2$, and to increase the observed number of strong gravitational lenses (galaxy scale) by a factor of 10.

For the specifications of the satellite and the instruments summarized in the following sections we refer to the [ESA](#)¹ and [Euclid consortium \(EC\)](#)² website.

3.1.1 The satellite

The *Euclid* spacecraft, shown in Fig. 3.2, consists of two modules: the service module (SVM) designed and built by Thales Alenia Space, and the payload module (PLM) responsibility of Airbus (Defence and Space). The SVM hosts the sunshield and the spacecraft subsystems for payload operations, including telemetry, power, thermal control, and attitude and orbit control (AOCS) systems. The sunshield protects the PLM from sun radiation and holds up the photovoltaic panels that supply electrical power to the spacecraft.

The PLM consists of the telescope, the PLM thermal control system, the Fine Guidance Sensor (FGS), the VIS and NISP instruments (delivered by the EC), which are described in the next section, and the detectors (delivered by ESA). VIS stands for VISible instrument and NISP for Near Infrared Spectrometer and Photometer.

The telescope is a 3-mirror Korsch cold telescope with a field of view of $1.25 \times$

¹https://www.esa.int/Science_Exploration/Space_Science/Euclid

²<https://www.euclid-ec.org/>

3.1. The Euclid mission



Figure 3.2: Pictures of the *Euclid* spacecraft at Thales Alenia Space in Cannes. Both images taken from the [ESA website](#).

0.727 deg^2 . The mirrors and the structures are made in Silicon Carbide; the primary mirror (M1), with a diameter of 1.2 m is kept at temperature below 130 K with thermal stability lower than 50 mK. The secondary mirror (M2) with a diameter of 0.35 m has a 3-degrees of freedom mechanism for adjusting tilt and focus to meet all requirements on image quality for weak lensing science and to allow the correction of possible alignment errors after the launch. The telescope utilizes a dichroic filter in the exit pupil to simultaneously guide light to both instruments: the reflected light is directed to VIS, while the transmitted light to NISP, as illustrated in the right panel of Fig. 3.3. This configuration enables both instruments to cover the same field-of-view and take advantage of comparable exposure times.

3.1.2 The instruments: VIS and NISP

The *Euclid* satellite hosts two instruments: the VISible instrument (VIS) and the Near Infrared Spectrometer and Photometer (NISP).

The VIS instrument provides high-quality images for weak lensing, with high resolution in order to measure the shape of the observed galaxies. It is composed of a mosaic of 36 charge coupled devices (CCDs), each of which contains 4096×4132 12-micron pixels, this constitutes the so called focal plane array (FPA) towards which the light is directed. The instrument is equipped with a single very broad band filter covering the wavelength range from 530 to 920 nm, with an effective angular resolution of about 0.18 arcsec. The field of view of VIS is very large: it can image 0.57 deg^2 of the sky at a time, equivalent to the area of 2.5 full moons as seen from Earth. Other components of the VIS instrument are a shutter unit which screens the FPA from light during the read-out of the detectors, a calibration unit which sends light at different wavelengths to the FPA and it's used for flat-field calibration. A more detailed overview of the various VIS subsystems is shown in Fig. 3.4. A single VIS observation has an exposure time of about 565 s after which the data are digitalised and compressed; the same observation on the same field of view

3. Euclid and cross-correlation of its probes with CMB

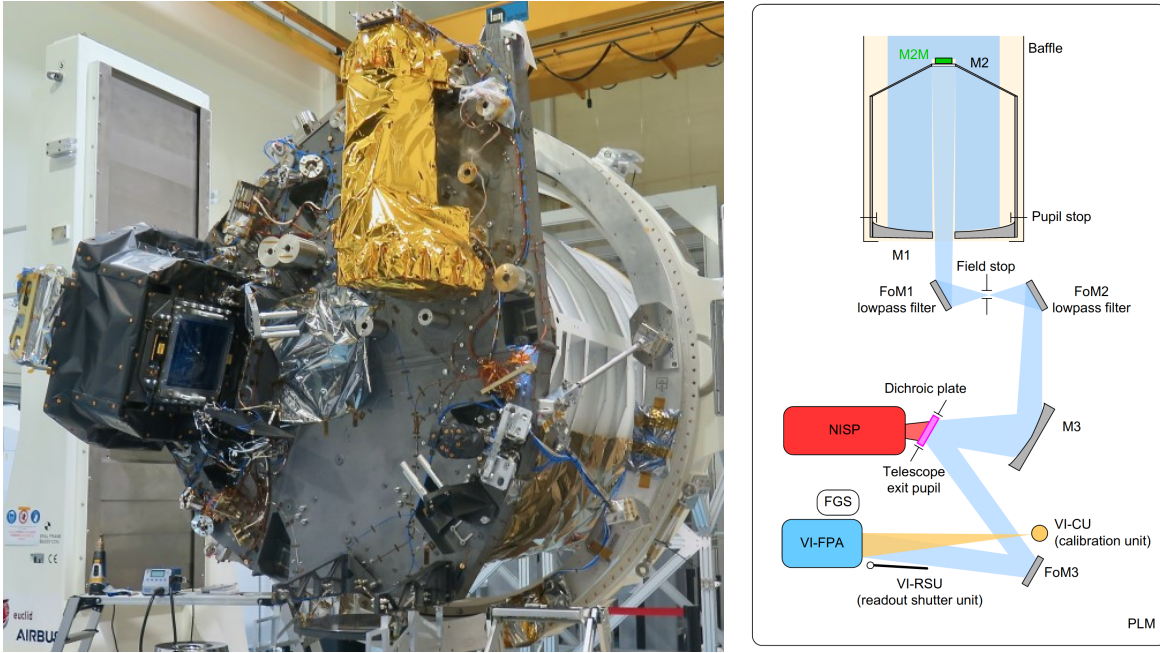


Figure 3.3: **Left:** *Euclid*'s PLM, which consists of a silicon baseplate supporting the telescope and two instruments. The VIS on the left while The NISP is towards the top. The telescope's primary and secondary mirrors are hidden from view and are underneath the baseplate in this orientation. Image taken from [ESA website](#). **Right:** Overview of the PLM sub-systems and optical design. Figure taken from the [EC website](#).

is then repeated three more times with displacements between the various observations in order to cover the gaps in the detector array.

One of the earliest images of VIS taken during the commissioning phase in July 2023 is shown in Fig. 3.5.

The NISP instrument is composed by a slitless spectrograph (NISP-S) and a photometer (NISP-P) with 3 broad band filters. The instrument measures near-infrared light (900-2000 nm) using a grid of 16 detectors, each containing 2040×2040 18-micron pixels with a field of view of 0.53 deg^2 shared with VIS. This is the largest field of view for an infrared instrument flown in space. Before reaching the detector, the incoming light is sent through either a photometry filter or a spectrometry grating prism (grism). In fact, in front of the detector there are two wheels which allow to switch from photometric to spectroscopic mode and vice versa. A schematic view of the NISP is presented in Fig. 3.6. The filters wheel contains the band pass filters in the Y, J and H bands for the photometric channel; these bands correspond, respectively, to $[950 - 1212]$ nm, $[1168 - 1567]$ nm and $[1521 - 2021]$ nm [196]. The other wheel contains four low resolution near-infrared grisms: one "blue" grism (926-1366 nm) and three "red" grisms with same wavelength range (1206-1892 nm) but with a different orientation. The reason for this is that the spectra of observed galaxies are diffracted directly on the detector and the resulting image is composed by all spectra of the galaxies in the field of view, which may overlap (see Fig. 3.7). Imaging the same field of view with different grism orientations allows to decontaminate each slitless spectrum and ensure the correct extraction

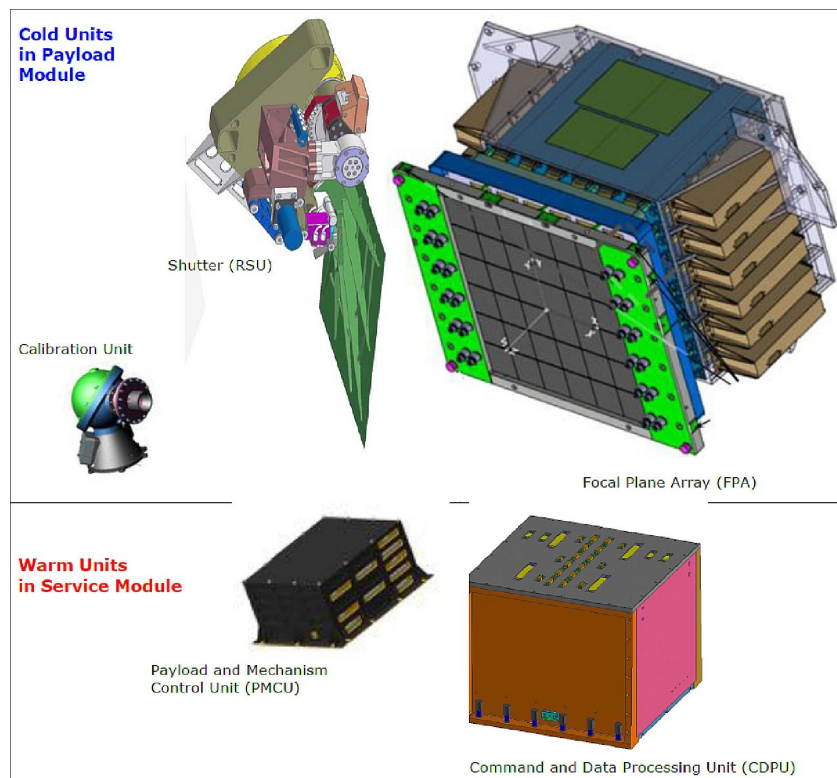


Figure 3.4: Overview of all the units composing the VIS instrument. The shutter, the calibration unit and the focal plane array are positioned in the cold PLM environment to reduce the thermal noise, while the payload and mechanism control unit and the command and data processing units reside in the SVM. Image credit: *Euclid* Consortium.

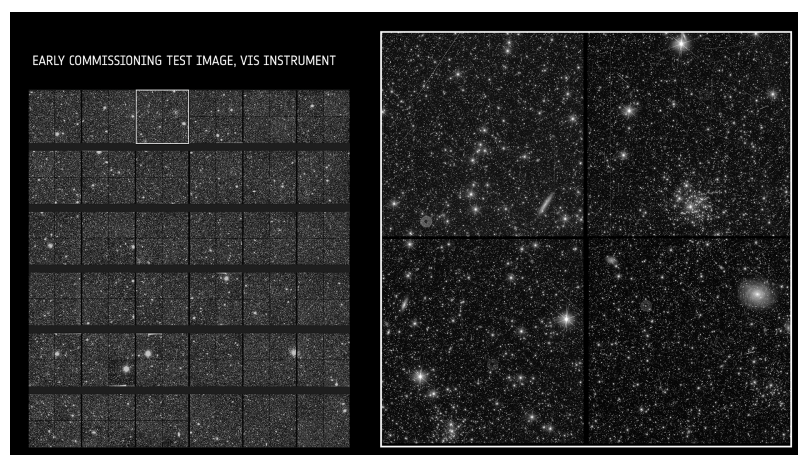


Figure 3.5: Early commissioning test image from the VIS. Image taken from the [ESA website](#).

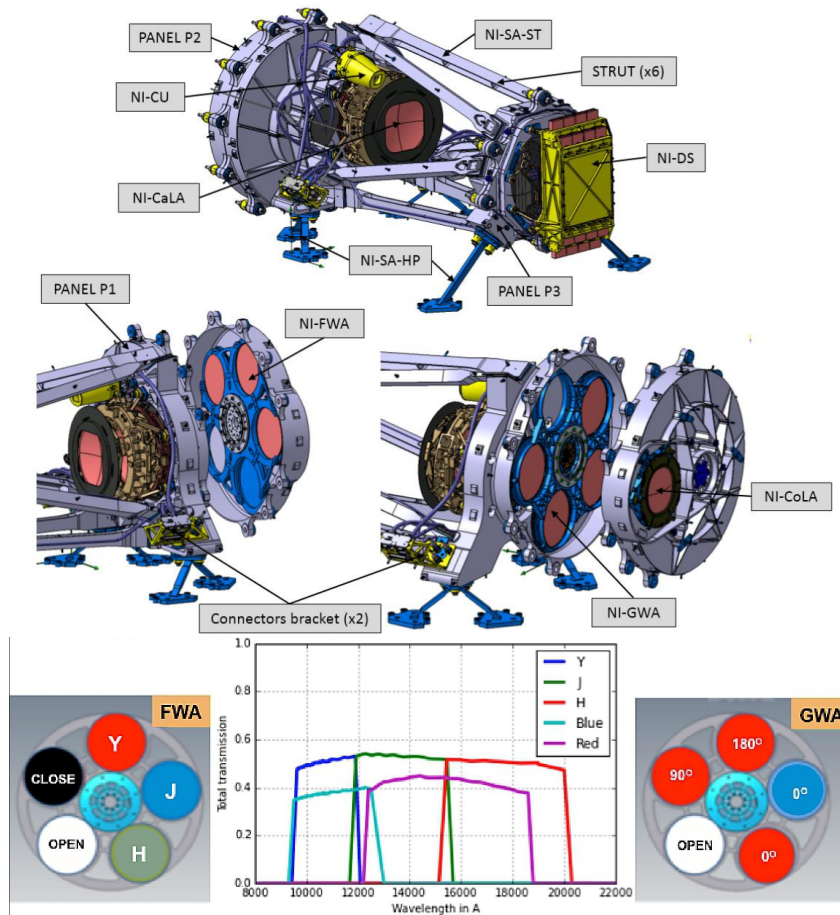


Figure 3.6: Overview of the subsystems comprising the NISP instrument (the warm electronic subsystem is not shown on this figure). The top panel shows the elements of the NISP optomechanical assembly and detector assembly: NISP calibration unit (NI-CU), NISP camera lens assembly (NI-CaLA), NISP structure assembly (NI-SA-ST and NI-SA-HP), NISP corrector lens assembly (NI-CoLA) and the NISP detector system (NI-DS). The NI-FWA is the NISP filter wheel assembly and NI-GWA is the grism wheel assembly. The bottom panel shows the filter positions (left), grism positions (right) and the transmission curves of the photometric filters and the grisms.

3.1. The Euclid mission

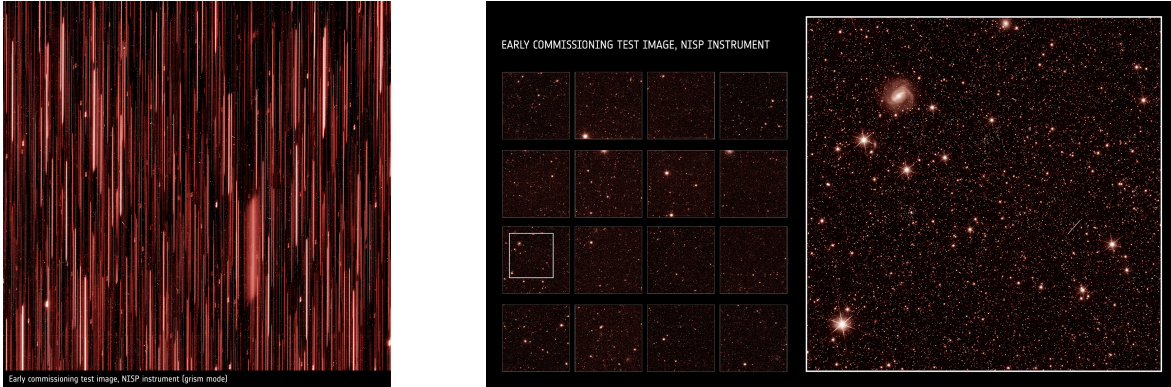


Figure 3.7: Early commissioning test images by the NISP in spectroscopic mode (left) and photometric mode (right). Both images taken from the [ESA website](#).

of the spectra of galaxies. The uncertainty on the spectroscopic redshift measurements is expected to be $\sigma_z = 0.001(1+z)$. One of the earliest images of NISP taken during the commissioning phase in July 2023 is shown in Fig. 3.7.

The spectroscopic survey will target the $H\alpha$ emission line of galaxies, corresponding to the electron transition from $n = 3$ to $n = 2$ in the hydrogen atom, which emits a photon at 656.3 nm in the rest frame of the emitter. This line is commonly emitted by ionized hydrogen atoms recombining with free electrons, thus we typically observe it in environments rich of ionized hydrogen such as star forming galaxies where the young stars ionize the hydrogen in the interstellar medium.

The two instruments work in conjunction: in addition to the low resolution-spectra of millions of galaxies, the NISP will provide near infrared photometry for all the galaxies observed by the VIS, allowing, in combination with data from ground based surveys in other bands, to determine the photometric redshift of the VIS galaxies. The estimated precision of the photometric redshifts is $\sigma_z = 0.05(1+z)$. These redshifts are obtained by fitting spectral energy distribution (SED) templates on the fluxes of the four bands of the survey. In this procedure there is however a risk of “catastrophic” redshift estimation when the fit is wrong. In Ref. [197] this outlier fraction was estimated to be around 10%.

3.1.3 The Science Ground Segment

As previously discussed, *Euclid* photometric observations are carried out in three infrared bands (Y, J and H) and one visible band. The observations in the remaining visible bands (g, r, i, z), needed for the estimation of photometric redshifts, will be provided by several ground-based surveys³. Thus, in addition to the large data volume provided by *Euclid* this poses the challenge to process, analyze and mix heterogeneous data coming from space and ground-based surveys which differ in depth and resolution.

This task is performed by the so-called Science Ground Segment (SGS) of *Euclid*, which is composed of the ESA Science Operations Centre (SOC) and the *Euclid* Consortium

³Pan-STARRS (<https://outerspace.stsci.edu/display/PANSTARRS/>), DES (<https://www.darkenergysurvey.org/>), Vera Rubin Observatory (<https://rubinobservatory.org/>), CFIS (<https://www.cfht.hawaii.edu/Science/CFIS/>), KIDS (<https://kids.strw.leidenuniv.nl/>).

3. *Euclid* and cross-correlation of its probes with CMB

Science Ground Segment (EC SGS). The SOC is responsible for the survey planning, managing the downlinked data and providing the EC with the data necessary to perform further processing of the science data.

The EC SGS will perform the scientific processing of the data, down to the production of the scientific results. The processing activity will occur in the Science Data Centers (SDCs). Two SDCs are dedicated to monitor instrument performance, while other SDCs will be providing external data sets obtained from ground based surveys to complement the *Euclid* data.

Moreover, the SGS will be responsible for the archive and the production of the official *Euclid* data releases.

3.1.4 The *Euclid* Consortium

Selected by ESA in 2012, the *Euclid* Consortium is the official scientific consortium entrusted with the tasks of managing the instruments, producing and leading the scientific exploitation of the data in the proprietary period. In collaboration with ESA, the EC has planned, constructed, and will be overseeing the operation of the *Euclid* mission. For this reason the consortium includes researchers in many fields of physics and astronomy, along with engineers, technicians, management and administrative staff, for a total of ~ 2500 people and 17 countries involved (Austria, Belgium, Denmark, Finland, France, Germany, Italy, the Netherlands, Norway, Portugal, Romania, Spain, Switzerland and United Kingdom, Canada, USA and Japan).

Going into further detail, the EC is in charge of delineating the scientific goals, the mission concept, specifying the science requirements and the survey. The EC also successfully designed, built, tested, integrated, and delivered the VIS and NISP instruments to ESA.

An important part of the EC is the EC SGS which bears the responsibility for the design, development tests, integration and operation of the data processing tools, pipelines and SDCs. It is composed of several Organizational Units (OUs), each dedicated to a distinct task, such as providing the photometric redshifts, or measurements of the spectral features.

The EC SGS together with the EC Science Working Groups (SWG) manages the production and delivery of *Euclid* data releases, and their scientific exploitation. The SWGs are divided into three categories: the cosmology SWGs (like weak lensing, galaxy clustering, CMB cross-correlation or theory), the legacy SWGs (like planets, or the Milky Way), and the cosmological simulations SWG.

The EC is led by the *Euclid* Consortium Lead (ECL) and a *Euclid* Consortium Board (ECB), they are also the primary contact points between the EC members and ESA.

3.2 *Euclid* main probes

By *Euclid* primary probes we mean weak lensing and galaxy clustering. *Euclid* will measure shapes, photometric/spectroscopic redshifts and angular positions of galaxies on the sky and in order to analyze these data we need to relate them to quantities that

3.2. Euclid main probes

can be reliably computed in a given theory: power spectra⁴.

Both photometric and spectroscopic galaxy populations will be divided into redshift bins allowing to perform a tomographic analysis and increase the signal-to-noise ratio (SNR), as this tomographic approach is necessary in order to achieve high-precision dark energy measurements [198–200]. The error in the measured redshifts of a galaxy thus becomes an important factor in the binning procedure, for this reason spectroscopic galaxies can be divided into thin bins while photometric bins are usually wider. The binning is commonly done in such a way to either have the same number of galaxies in each bin (equipopulated bins) or equispaced bin edges (equidistant bins).

We discuss in this section how to model these two main *Euclid* observables.

3.2.1 *Euclid* spectroscopic galaxy clustering

Euclid will reconstruct the 3D galaxy field in the redshift range (0.9, 1.8) by performing slitless spectroscopy of $H\alpha$ emitting galaxies with an accuracy on measured redshifts of $\sigma_z = 0.001(1+z)$. The main observable is therefore the power spectrum of these galaxies $P_{\text{gg}}^{\text{spectro}}(\mathbf{k}, z)$, which is given, in first approximation and in the linear regime, by Eq. (1.92). In practice, several other effects need to be taken into account. Redshift uncertainties modify the power spectrum in the following way:

$$P_{\text{zerr}}^{\text{spectro}}(k, \mu_k, z) = P^{\text{spectro}}(k, \mu_k, z)F_z(k, \mu_k, z), \quad (3.1)$$

where $F_z(k, \mu_k, z) = \exp(-k^2 \mu_k^2 \sigma_r(z))$ accounts for the smearing of the galaxy density field along the line of sight caused by possible redshift errors. This error is given by $\sigma_r(z) = c \sigma_z / H(z)$.

Moreover, to measure the galaxy power spectrum, the observed redshifts have to be transformed into distances, in order to do so it is necessary to assume a fiducial cosmological model; in this sense the true underlying power spectrum is not directly observable. The difference between the true cosmology and the assumed model leads to a rescaling of the wavevector components parallel and perpendicular to the line of sight k_{\perp} and k_{\parallel} :

$$k_{\parallel} = \frac{k_{\perp}^{\text{fid}}}{q_{\perp}}, \quad q_{\perp}(z) = \frac{D_A(z)}{D_A^{\text{fid}}(z)}; \quad k_{\parallel} = \frac{k_{\parallel}^{\text{fid}}}{q_{\parallel}}, \quad q_{\parallel}(z) = \frac{H^{\text{fid}}(z)}{H(z)}. \quad (3.2)$$

This rescaling can be used to relate the reference k^{fid} and μ_k^{fid} to the true k and μ_k

$$k(k^{\text{fid}}, \mu_k^{\text{fid}}, z) = \frac{k^{\text{fid}}}{q_{\perp}} \left[1 + (\mu_k^{\text{fid}})^2 \left(\frac{q_{\perp}^2}{q_{\parallel}^2} - 1 \right) \right]^{1/2}, \quad (3.3)$$

$$\mu_k(\mu_k^{\text{fid}}, z) = \mu_k^{\text{fid}} \frac{q_{\perp}}{q_{\parallel}} \left[1 + (\mu_k^{\text{fid}})^2 \left(\frac{q_{\perp}^2}{q_{\parallel}^2} - 1 \right) \right]^{1/2}. \quad (3.4)$$

⁴The analysis can be also carried out in configuration space rather than harmonic space. Configuration space is more directly related to the measurements but the theoretical predictions are more straightforward in the harmonic space. All codes compute quantities in the harmonic space to eventually project them in the configuration one, thus we will restrict to power spectra.

3. Euclid and cross-correlation of its probes with CMB

Additionally, deviations from the fiducial cosmology rescale the power spectrum by a factor $(q_{\perp}^2 q_{\parallel})^{-1}$.

Combining all these effects, the observed linear matter power spectrum of the spectroscopic galaxies of *Euclid* can be written as

$$P_{\text{obs}}^{\text{spectro}}(k^{\text{fid}}, \mu_k^{\text{fid}}, z) = \frac{1}{q_{\perp}^2 q_{\parallel}} [b^{\text{spectro}}(z) + f(z)\mu_k^2]^2 P_{\delta\delta}(k, z) F_z(k, \mu_k, z), \quad (3.5)$$

where all $k = k(k^{\text{fid}}, \mu_k^{\text{fid}}, z)$ and $\mu_k = \mu_k(\mu_k^{\text{fid}}, z)$ and we have specified $b^{\text{spectro}}(z)$ for the spectroscopic galaxies since this bias is different from the one of the photometric survey. This is due to the fact that the samples are selected following different criteria and consist of galaxies with different properties. We will not specify $b^{\text{photo}}(z)$ for the photometric sample in the following, but simply use $b(z)$.

The expression given in Eq. (3.5) can be further refined to include an offset between the true density of clustering objects and the measured one, the density of random outliers (non-clustering objects), and the effects of nonlinear galaxy clustering, but it goes beyond the scope of this thesis.

3.2.2 *Euclid* photometric probes

In photometric galaxy surveys the resolution of the redshift measurements is not enough to study directly the 3D matter power spectrum, it is then common to consider the projection of this 3D distribution on the 2D celestial sphere, linking the matter power spectrum to angular power spectra. Studying the projection of the density and shear fields on the sky also allows to account more easily for their cross-correlation and perform the so-called 3×2 pt analysis which considers three combinations of the two point correlation functions of galaxy lensing WL, and galaxy positions GCp: $\langle \text{WL WL} \rangle$, $\langle \text{GCp GCp} \rangle$, $\langle \text{WL GCp} \rangle$. Working with angular power spectra it is also more straightforward to cross-correlate *Euclid* probes with CMB fields.

The projected angular power spectrum between two fields X and Y, in the i -th and j -th redshift bin, is in general given by

$$C_{\ell}^{\text{X}_i \text{Y}_j} = \frac{2}{\pi} \int_0^{\infty} dk k^2 P_{\mathcal{R}}(k) \int_0^{\infty} dz_1 \mathcal{W}^{\text{X}_i}(k, z_1) j_{\ell}(k\chi(z_1)) \int_0^{\infty} dz_2 \mathcal{W}^{\text{Y}_j}(k, z_2) j_{\ell}(k\chi(z_2)), \quad (3.6)$$

where, the letters X and Y can stand either for WL, photometric galaxy clustering (GCp), and j_{ℓ} are the spherical Bessel functions of order ℓ . $\mathcal{W}(k, z)$ are so-called kernel functions of the observables, they relate the underlying power spectrum to the observables and characterize the time evolution of a perturbation of the cosmological quantity sourcing the considered observable, for example the matter density field for the GCp.

For cosmic shear the kernel function is

$$\mathcal{W}_i^{\gamma}(k, z) = \frac{3\Omega_{\text{m}0}H_0^2}{2} \frac{(1+z)\chi(z)}{H(z)} \delta(k, z) \int_z^{z_{\text{max}}} d\tilde{z} n(\tilde{z}) \left[1 - \frac{\chi(z)}{\chi(\tilde{z})} \right] \quad (3.7)$$

with z_{max} the maximum redshift of the source redshift distribution $n_i(z)$, which represents the normalized observed number density of galaxies in the i -th redshift bin.

3.2. Euclid main probes

The kernel for GCp is

$$\mathcal{W}_i^{\text{GCp}}(k, z) = n_i(z)b(z)\delta(k, z) \quad (3.8)$$

where, the galaxy bias $b(z)$ is assumed to be scale-independent.

In general, these kernel functions do not have a closed-form expression and require the use of Boltzmann codes to be computed; moreover, integrating the Bessel functions renders Eq. (3.6) computationally expensive. It is possible to simplify Eq. (3.6) and the integral over the Bessel functions by using the Limber approximation [201–203], valid on small angular scales:

$$\int dk k^2 f(k) j_\ell(k\chi_1) j_\ell(k\chi_2) \rightarrow \frac{\pi}{2} \frac{1}{\chi_1^2} f(k_\ell) \delta_{\text{Dirac}}(\chi_1 - \chi_2), \quad (3.9)$$

with $k_\ell = (\ell + 1/2)/\chi(z)$; in the Limber approximation and with the change of variables $d\chi = dz/H(z)$, Eq. (3.6) becomes, as a function of the matter power spectrum $P_{\delta\delta}$

$$C_\ell^{X_i Y_j} = \int \frac{dz}{H(z)\chi^2(z)} W^{X_i}(z) W^{Y_j}(z) P_{\delta\delta}(k_\ell, z). \quad (3.10)$$

The kernels $W(z)$ appearing in this simplified formula different from the ones in Eq. (3.6) and depend only on redshift. For WL the kernel includes contributions from both the cosmic shear signal (γ) and the intrinsic alignment (IA) systematic, it is given by

$$W^{\text{WL}_i}(z) = W^{\gamma_i}(z) - \frac{\mathcal{P}_{\text{IA}}\Omega_{\text{m}0}}{D(z)} W^{\text{IA}_i}(z). \quad (3.11)$$

The IA is due to tidal processes during the formation and evolution of galaxies which induce a preferred orientation in the shapes of galaxies. This intrinsic correlation of the orientation of galaxies is a contaminant of the shear power spectrum, and must be properly taken into account in a WL survey. In particular the modelling of the function \mathcal{P}_{IA} is described in Ref. [197] and it introduces three nuisance parameters named \mathcal{A}_{IA} , η_{IA} and β_{IA} , which are, respectively, the amplitude, the redshift dependence and the dependence on the galaxy luminosity of the IA. The kernels for shear and IA are

$$\begin{aligned} W^{\gamma_i}(z) &= \frac{3}{2} H_0^2 \Omega_{\text{m}0} (1+z) \chi(z) \int_z^{z_{\text{max}}} d\tilde{z} n_i(\tilde{z}) \left[1 - \frac{\chi(z)}{\chi(\tilde{z})} \right], \\ W^{\text{IA}_i}(z) &= n_i(z) H(z). \end{aligned} \quad (3.12)$$

In these expressions, $D(z)$ is the linear growth factor introduced in section 1.7.3.

The kernel for GCp is

$$W^{\text{GCp}_i} = b(z)n_i(z)H(z). \quad (3.13)$$

In principle, the redshift distributions $n_i(z)$ entering Eqs. (3.11) and (3.13) can be different depending on the probe. In Ref. [197, 204], the same $n_i(z)$ was assumed both for WL and GCp, given by the photometric convolution of the true galaxy distribution $n(z)$ with the photometric redshift error, which is characterised by the probability $p_{\text{ph}}(z_p|z)$ of a galaxy at redshift z to be measured via photometry at redshift z_p

$$n_i(z) = \frac{\int_{z_i^-}^{z_i^+} dz_p n(z) p_{\text{ph}}(z_p|z)}{\int_{z_{\text{min}}}^{z_{\text{max}}} dz \int_{z_i^-}^{z_i^+} dz_p n(z) p_{\text{ph}}(z_p|z)}, \quad (3.14)$$

3. Euclid and cross-correlation of its probes with CMB

where $z_i^- = z_i$ and $z_i^+ = z_{i+1}$ are the edges of the i th redshift bin. The underlying true distribution $n(z)$ appearing in this expression is chosen to be in agreement with the *Euclid* Red Book [205, 206]:

$$n(z) \propto \left(\frac{z}{z_0}\right)^2 \exp\left[-\left(\frac{z}{z_0}\right)^{3/2}\right], \quad (3.15)$$

where $z_0 = z_m/\sqrt{2}$, with $z_m = 0.9$ being the median redshift and the surface density of galaxies is taken to be $\bar{n}_g = 30 \text{ arcmin}^{-2}$. With this choice, the baseline in Ref. [197] was 10 equi-populated bins, with bin edges given by

$$z_i = \{0.0010, 0.42, 0.56, 0.68, 0.79, 0.90, 1.02, 1.15, 1.32, 1.58, 2.50\}. \quad (3.16)$$

We note that the minimum redshift considered in Ref. [197] is an optimistic value of 0.001, which is lower than in Ref. [205], where a minimum of 0.2 was used as a conservative limit to avoid potential catastrophic redshift outliers.

The probability distribution function $p_{\text{ph}}(z_p|z)$, describing the probability that a galaxy with redshift z has a measured redshift z_p , is parameterized in the following way

$$p_{\text{ph}}(z_p|z) = \frac{1 - f_{\text{out}}}{\sqrt{2\pi}\sigma_b(1+z)} \exp\left\{-\frac{1}{2}\left[\frac{z - c_b z_p - z_b}{\sigma_b(1+z)}\right]^2\right\} + \frac{f_{\text{out}}}{\sqrt{2\pi}\sigma_o(1+z)} \exp\left\{-\frac{1}{2}\left[\frac{z - c_o z_p - z_o}{\sigma_o(1+z)}\right]^2\right\} \quad (3.17)$$

where, for a fraction $(1 - f_{\text{out}})$ of sources with reasonably well measured redshifts, σ_b is the photometric redshift error distribution, while z_b and c_b are an additive and a multiplicative bias. The terms σ_o , z_o and c_o are the corresponding quantities for catastrophic outliers. The fraction of catastrophic outliers is represented by the parameter f_{out} . The choice for these parameters is summarized in Table 3.1, and the redshift distributions $n_i(z)$ computed with these values for 3, 5 and 10 equi-populated bins are shown in Fig. 3.8; they have been obtained using using the publicly available code `euclid_windows`⁵.

c_b	z_b	σ_b	c_o	z_o	σ_o	f_{out}
1.0	0.0	0.05	1.0	0.1	0.05	0.1

Table 3.1: Parameters adopted to describe the photometric redshift distribution of sources of Eq. (3.17).

We emphasize that while these specifications can still be considered a good approximation of *Euclid* capabilities, they have been surpassed in recent years by the use of redshift distributions extracted from simulations, such as the Flagship 1 [207] and now the Flagship 2 mock galaxy catalogues, which are the largest simulated galaxy catalogues

⁵https://github.com/paganol/euclid_windows

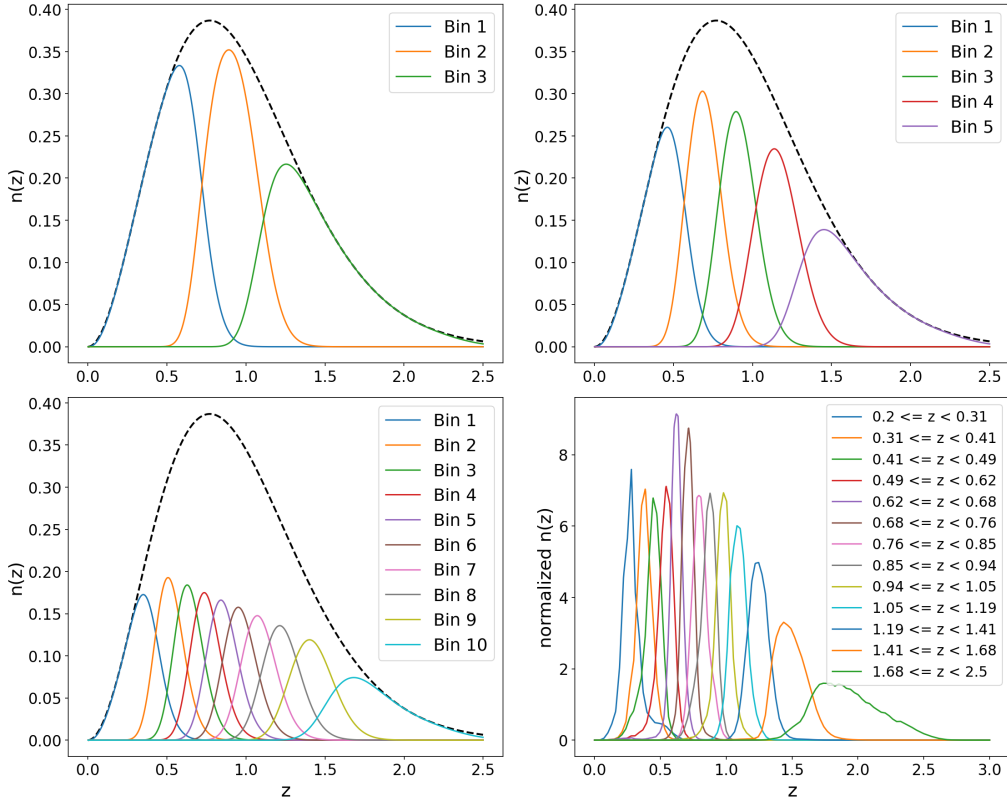


Figure 3.8: Redshift distributions (unnormalized) for 3 (upper left), 5 (upper right) and 10 (bottom left) equi-populated bins obtained from `euclid_windows` using Eq. (3.14). In the bottom right panel we show the redshift distributions extracted from the Flagship 2 simulation. The difference in the y-axis scale is due to the fact that the Flagship 2 n_i 's are already normalized.

ever produced. Products extracted from the Flagship 2 simulation, including the galaxy distribution and the galaxy bias, are EC internal material at the moment, and have not yet been published, but are used within the EC as the baseline for upcoming papers. In the bottom right panel of Fig. 3.8 we show the 13 equipopulated redshift bins, spanning the redshift range $0.2 < z < 2.5$, extracted from the Flagship 2 simulation. The total number density of galaxies in this scenario is $n_g = 24.3$ galaxies/arcmin².

In chapter 5, in addition we will also use this Flagship 2 galaxy distribution to characterize *Euclid* specifications.

3.2.3 Combination of spectroscopic and photometric probes

One of the strengths of *Euclid* is the ability to analyze the same galaxy field with photometric and spectroscopic probes and make the best use of their complementary nature. Indeed, combining photometry and spectroscopy allows to break degeneracies on cosmological and nuisance parameters, tightening therefore the final constraints. To exemplify this, we present in Fig. 3.9 the forecasts from Ref. [197] on a w_0w_a CDM model, obtained by considering spectroscopic galaxy clustering (GCs) alone, WL alone, WL+GCp, and WL+ GCp + XC + GCs, where XC means the cross-correlation between the photometric probes GCp and WL. The GCs is added independently to the other probes. The combination of GCs and WL is extremely powerful as it breaks degeneracies among cosmological parameters, indeed the purple (GCs) and the blue (WL) contours are orthogonal or close to orthogonal for several 2D parameter spaces, especially the planes with h, Ω_b, σ_8 and n_s . This highlights the fact that to reach the expected levels of accuracy in the estimates of parameters it's important to rely on the complementarity of the various probes and not just on the individual constraining power.

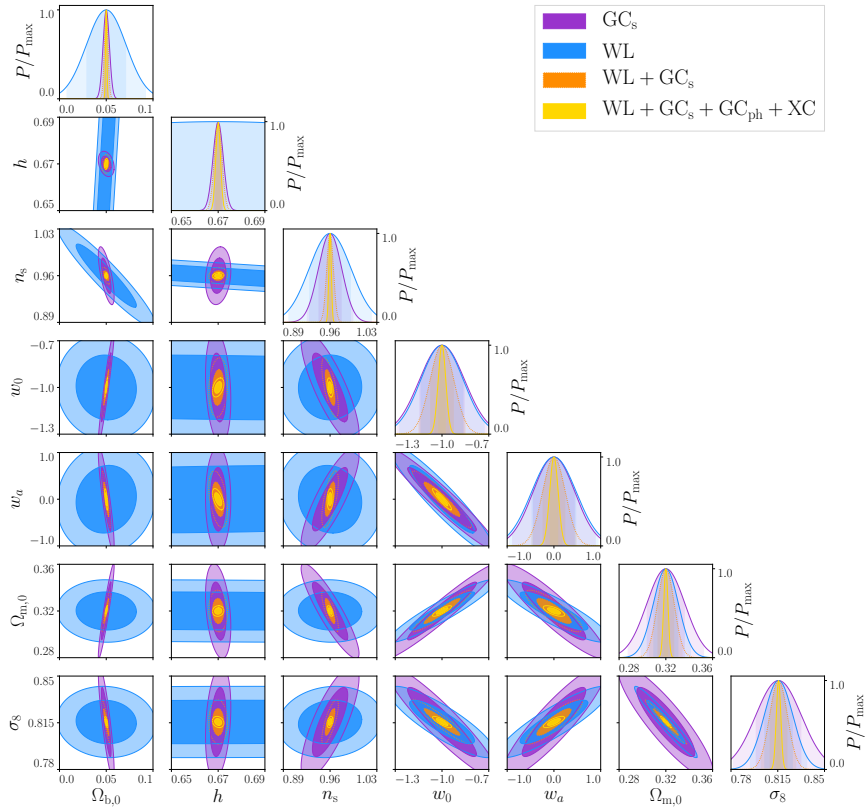


Figure 3.9: Fisher-matrix-marginalised contours for the Euclid space mission for a w_0w_a flat cosmology, for GCs (purple), WL (blue), their combination (orange), and with the addition of GCph and its cross-correlation with WL (yellow). Figure from Ref. [197].

3.3 CMB cross-correlation

The relevance of CMB and LSS probes combination has been widely demonstrated (see e.g. Refs. [208, 209]) as it reduces the significance of systematic effects, breaks degeneracies between cosmological parameters, and is crucial for discovering inconsistencies between the different datasets.

A more recent example from Ref. [1] is illustrated in Fig. 3.10, which shows that combining BAO with CMB allows to break the degeneracy between Ω_m and Ω_k , indicating that the observable Universe is flat to a very good approximation. In the right panel, the same combination of datasets with the addition of SNe in one case, and galaxy weak lensing in the other, highlights the importance of probe combination for tightening constraints on the dark energy parameters w_0 - w_a . In Ref. [1], however, these observables are assumed to be uncorrelated. This assumption is valid in their analysis since the CMB probes the early Universe, while the BAO measurements at a low redshift $z < 1$, and SN are local probes uncorrelated with the others.

Nonetheless, the matter density field traced by the galaxies is correlated with the CMB observables, since the overdensities observed in the CMB are the seeds for the subsequent structures and galaxies formation. Moreover, the CMB photons interact with the LSS which generate the secondary CMB anisotropies described in section 1.7.1. For this reason, in current and upcoming surveys, due to their deepness in redshift and extension on the sky it is not valid to assume CMB and galaxy surveys as independent, in particular when the footprints of the CMB experiments and the surveys overlap, as it happens for *Euclid* and *Planck*, or for DES and the South Pole Telescope⁶ (SPT). Without this assumption, the modelling of the covariances between different probes is necessary in order to perform a joint analysis.

A joint analysis between two completely different datasets is much more difficult than cross-correlating probes coming from the same observational campaign. However, it has been shown to be a very promising path already in Refs. [210–213] where it was demonstrated that a combined analysis of CMB lensing and galaxy probes for next generation surveys will be useful in breaking degeneracies between the amplitude of the matter power spectrum, the galaxy bias and the WL calibration bias. Breaking these degeneracies with systematic parameters can greatly improve the constraints on cosmological parameters.

Nowadays, joint analysis are planned early on in the development stage of observational campaigns. For example, DES and SPT have been designed to maximize the overlap between the galaxy and the CMB observations. Indeed, they have carried out a joint analysis by cross-correlating the galaxy weak lensing, the galaxy clustering and the CMB lensing field from SPT and *Planck* [214–216]. This type of studies are called 6×2 pt analysis because they consider six combinations of the two point correlation functions of CMB lensing ϕ , galaxy lensing WL, and galaxy positions GCp: $\langle\phi\phi\rangle$, $\langle\text{WL WL}\rangle$, $\langle\text{GCp GCp}\rangle$, $\langle\phi\text{WL}\rangle$, $\langle\phi\text{GCp}\rangle$, $\langle\text{WL GCp}\rangle$. This combination of probes, beside improving the cosmological constraints in Ref. [214–216], was crucial in checking for inconsistencies between the datasets and was a powerful consistency test for the results of each

⁶<https://pole.uchicago.edu/public/Home.html>

3.3. CMB cross-correlation

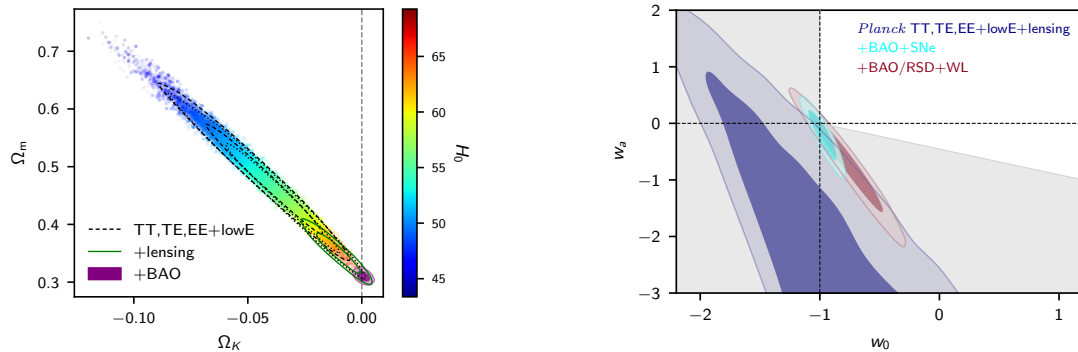


Figure 3.10: Figures from Ref. [1] showing the degeneracy between Ω_k and Ω_m (left), and between w_0 and w_a (right) from different datasets: CMB constraints from *Planck* to which external datasets such as BAO, SNe, WL are added.

experiment, including comparisons with results derived from cross-correlations only, and comparisons designed to test the robustness of the galaxy lensing and clustering measurements from DES.

In addition to the cross-correlation with CMB lensing it is also possible to cross-correlate galaxy observables with the CMB temperature and polarization fields. Indeed, on large scales ($\ell < 30$) the cross-correlation of CMB temperature with galaxy clustering will be dominated by the late ISW effect. Even if this signal has a very low SNR, it is expected to be sensitive to DE and modified gravity models. An example of sensitivity of CMB-LSS cross-correlation to DE parameters is illustrated in Fig. 3.11, taken from Ref. [217]. The figure shows the forecasted constraints on the dark energy equation of state parameters using only cross-correlation probes, on the left for a *Euclid*-like photometric survey combined with *Planck*, and on the right for the combination of future CMB experiments: LiteBIRD⁷ + Stage-4 (S4)⁸[218] with the first phase of SKAO (SKA1)⁹.

Within the EC, the data analysis and the exploitation of the cross-correlation between *Euclid* and CMB anisotropies are carried out in the *CMB cross-correlation science working group* (CMBX-SWG) which is responsible for the development and validation of the end-to-end pipeline to measure the cross-correlation between CMB lensing and galaxy probes, together with the LISW signal by cross-correlating CMB temperature and *Euclid* GCp data. The pipeline goes from the numerical simulations to build the covariances and from the estimators of the cross-correlation power spectrum from maps, to the full analysis to constrain a given model with the likelihood module which takes the estimated power spectra and covariances as inputs. Additional activities within the group also include cross-correlation with cosmic voids, and cross-correlation of *Euclid* probes with the Sunyaev–Zeldovich effect and the cosmic infrared background (CIB).

The first output of the group is a paper forecasting the relevance of CMB cross-correlation for *Euclid* in Λ CDM and its minimal extensions, and we are currently working

⁷<https://www.isas.jaxa.jp/en/missions/spacecraft/future/litebird.html>

⁸<https://cmb-s4.org/>

⁹<https://www.skao.int/en/science-users/118/ska-telescope-specifications>

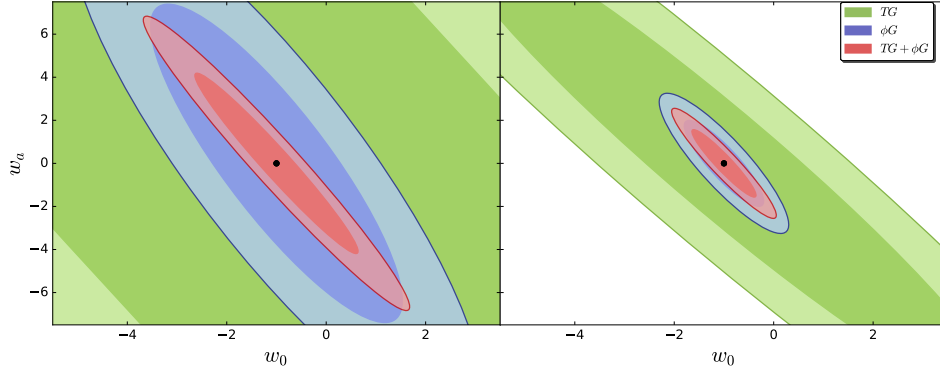


Figure 3.11: Marginalized 68% and 95% 2D confidence regions for the constraints from TG , ϕG and the combination of both for the $w_0 w_a$ CDM model. The left panel corresponds to $Planck \otimes Euclid$ -ph-like and the right panel to LiteBIRD+S4 \otimes SKA1. The green contours correspond to the temperature-galaxy cross-correlation constraints (TG) the blue contours to the lensing-galaxy cross-correlation (ϕG) and the red contours to the sum of both ($TG + \phi G$). Figure from Ref. [217].

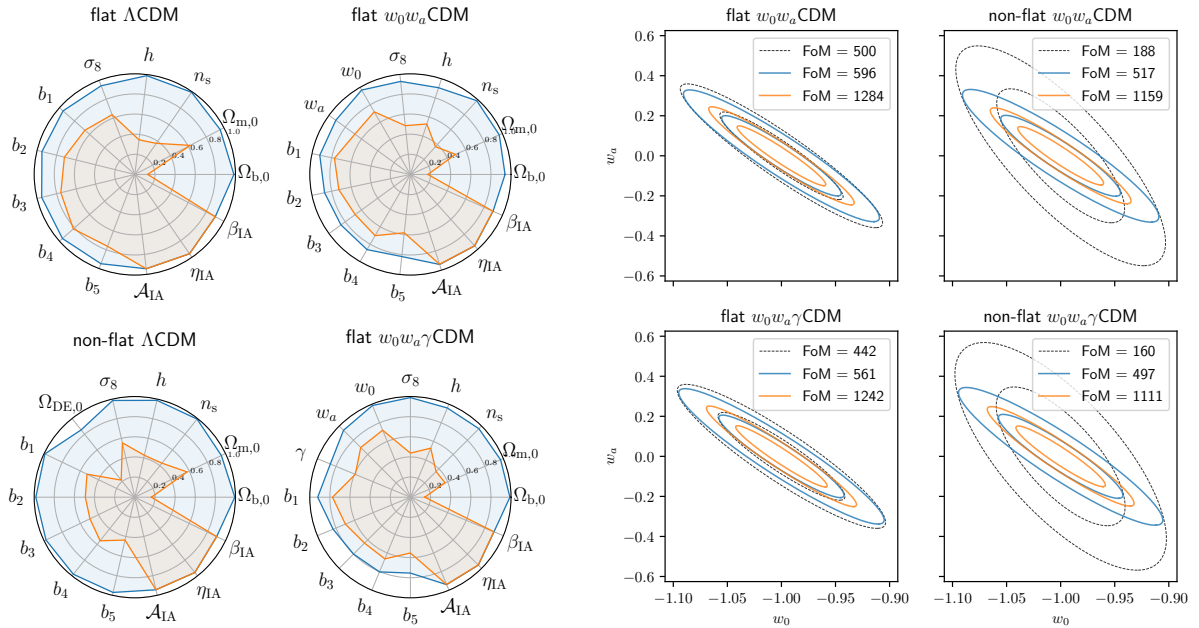


Figure 3.12: Left: ratio of predicted 1σ uncertainties showing tightened constraints after adding CMB lensing (blue) or all CMB probes (orange) when compared to the Euclid-only constraints (black outer rim), assuming a pessimistic Euclid scenario and SO-like CMB data, for four cosmological models: flat Λ CDM, flat $w_0 w_a$ CDM, non-flat Λ CDM, and flat $w_0 w_a \gamma$ CDM. **Right:** marginalized 2D distributions for the w_0 - w_a for four cosmological model: flat (nonflat) $w_0 w_a$ CDM and flat (nonflat) $w_0 w_a \gamma$ CDM. Figures from [204].

3.3. CMB cross-correlation

on extending these forecasts with more updated specifications to modified gravity models, primordial non Gaussianity and neutrino masses; this will be the topic of chapter 5. Some of the main results of the first forecast paper [204] are presented in Fig. 3.12 where we show the improvements of the expected 1σ uncertainties when combining CMB probes (CMB lensing alone or all the probes) to the *Euclid* photometric survey, in four different cosmological models. The figure also shows the 2D marginalized distributions for w_0 - w_a and the relative improvements in the figure of merit (FoM) due to the inclusion of CMB probes. The FoM quantifies how well constrained two parameters are, as it is related to the area of the ellipsis representing the 2D posterior distribution of the two parameters: large (small) FoM means small (large) area and therefore small (large) errors.

In the following we focus on the cross-correlation between CMB and *Euclid* photometric probes since cross-correlation with GCs is also possible but has a lower signal-to-noise.

3.3.1 Cross-correlation with the late-ISW effect

The LISW effect described in section 1.7.1 is hard to detect directly in the CMB temperature power spectrum because of its low SNR due cosmic variance at large scales. The most direct way to detect it, is to cross-correlate the large-angle CMB anisotropies with large-scale structure at low redshifts, such as angular galaxy correlations [18], or the lensing of the CMB itself. Indeed, the ISW effect is due to time varying gravitational potentials along the line of sight, which affect the temperature fluctuation as

$$\theta_{\text{ISW}}(\hat{\mathbf{n}}) = - \int_0^{\chi_*} d\chi e^{-\tau_{\text{reio}}} \frac{d}{d\chi} (\phi_N + \psi_N), \quad (3.18)$$

where ϕ_N and ψ_N are the gravitational potential in the Newtonian gauge (1.37), and χ_* is the comoving distance to the last scattering surface. These potentials are generated by the matter distribution of the Universe, we therefore expect some correlation between the distribution of matter and the ISW pattern imprinted in the CMB temperature angular anisotropies. The evolution of the gravitational potential is suppressed in a matter-dominated universe and the ISW effect cannot occur until the late stage of accelerated expansion when DE dominates the energy budget of the Universe, causing the decaying of the potentials. Matter-DE equality happens approximately at $z \simeq 0.3$, meaning that the CMB temperature anisotropies due to the LISW were created at $z < 0.3$, when the Hubble scale is comparable to its current value. This implies that the scales are affected are generally large scales $\ell < 100$. From this basic picture, we expect the ISW effect to be sensitive to DE in whatever forms one chooses to parameterize it, be it a cosmological constant, a fluid with time varying equation of state or, for example, the potential of a scalar field. This is confirmed by Fig. 3.13 where we show the dependence of the cross-correlation power spectrum between the temperature field and the density field as a function of the cosmological constant density parameter Ω_Λ on the left, and of the w_0 parameter of state of DE on the right. Most of the power is at $\ell < 100$, with peaks at about $10 < \ell < 50$, depending on the DE parameters.

The power spectrum is obtained from Eq. (3.6) with the galaxy clustering kernel \mathcal{W}^{GCpi}

3. Euclid and cross-correlation of its probes with CMB

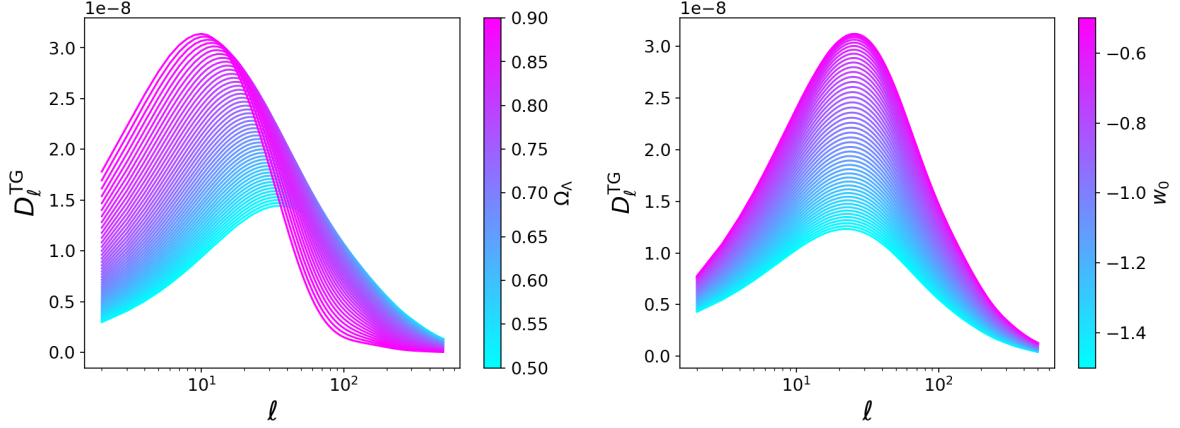


Figure 3.13: Dependence of the TG power spectrum on dark energy, parameterized as the cosmological constant density parameter Ω_Λ on the left and the equation of state parameter w_0 on the right. The y-axis is $D_\ell = C_\ell \times \ell(\ell + 1)/(2\pi)$.

given in Eq. (3.8) and the ISW kernel

$$\mathcal{W}^{\text{ISW}}(k, z) = -e^{-\tau_{\text{reio}}} \frac{d}{dz} (\phi_N + \psi_N), \quad (3.19)$$

Assuming no anisotropic stress in Eq. (1.52) and a scale independent growth factor for the density contrast it is possible to write the kernel in the following form

$$\mathcal{W}^{\text{ISW}}(k, z) = \frac{3\Omega_{\text{m}0}H_0^2}{k^2} \frac{d}{dz} \left(\frac{D(z)}{a(z)} \right) \frac{\delta(k, z)}{D(z)}. \quad (3.20)$$

Instead, for the simplified expression (3.10) in the Limber approximation, the ISW kernel is

$$W^{\text{ISW}}(z) = \frac{3\Omega_{\text{m}0}H_0^2}{k_\ell^2} \frac{d}{dz} \left(\frac{D(z)}{a(z)} \right) \frac{H(z)}{D(z)}, \quad (3.21)$$

and, consequently, the angular power spectrum of the cross-correlation between the galaxy field in the i -th redshift bin and CMB temperature can be written as

$$C_\ell^{TG_i} = \frac{3\Omega_{\text{m}0}H_0^2}{(\ell + 1/2)^2} \int dz H(z) \frac{d}{dz} \left(\frac{D(z)}{a(z)} \right) b(z) n_i(z) D(z) P_{\delta\delta}(k_\ell, z = 0). \quad (3.22)$$

The plots in Fig. 3.13 have been obtained considering the unbinned galaxy distribution (3.15).

Detections of the ISW effect by cross correlating the CMB with LSS tracers have not been conclusive yet; for example, the *Planck* 2015 results [219] show a detection with a significance of 2.9σ by cross-correlating temperature and polarization with galaxies from SDSS, radio sources from the NVSS catalogue¹⁰, and the infrared WISE¹¹ surveys. The significance is improved when combined the primary CMB with CMB lensing (3.2σ),

¹⁰<https://www.cv.nrao.edu/nvss/>

¹¹<https://www.jpl.nasa.gov/missions/wide-field-infrared-survey-explorer-wise>

3.3. CMB cross-correlation

and the joint cross-correlation of the CMB with all the tracers yields a detection at 4σ . Note that a 4σ detection has been obtained also recently [220] considering only the cross correlation of temperature with CMB lensing, by making use of the latest PR4 *Planck* data maps and lensing reconstruction [221].

One of the goal of the CMBX-SWG is the detection of the ISW effect by cross-correlating the CMB temperature field from the *Planck* mission with *Euclid* photometric galaxies, for this reason, many efforts within the group are devoted to building a likelihood to capture the signal. At present, the likelihood module for the ISW cross-correlation developed does not rely on an Einstein-Boltzmann code to compute the theoretical power spectra but it computes them internally in the Limber approximation using Eq. (3.22). I have been involved in the development and validation of this likelihood in the `MontePython`¹² [162, 163] framework, this module was mostly used to perform the validation of the expression used to compute theoretical power spectra and the parameter constraints obtained using it. The validation of the implementation was crucial as it is the basis for what the group implemented in the official likelihood package of *Euclid*: CLOE (Cosmology Likelihood for Observables in *Euclid*).

The ISW-galaxy cross-correlation is also often included in the forecasts presented in chapter 5 but computed with the more general Eq. (3.6) with kernels (3.8) and (3.19).

3.3.2 CMB lensing and its cross-correlation

Since CMB lensing is a probe of the late-time matter distribution of the Universe, we are interested both in the auto-power spectrum and the cross correlations with *Euclid* primary probes.

We discussed the basics of weak lensing section 1.7.3 in the context of galaxies and the distortion of their shapes due to intervening matter along the line of sight. The CMB acts as a source extended over the entire sky at a given comoving distance χ_* and its photons are deflected by the large scale structure of the Universe, causing a remapping of the CMB fluctuations given by

$$X^{\text{len}}(\hat{\mathbf{n}}) = X^{\text{unl}}(\hat{\mathbf{n}} + \boldsymbol{\alpha}(\hat{\mathbf{n}})), \quad (3.23)$$

where $X \in \{T, Q \pm iU\}$ are the fields describing CMB temperature and polarization. The angle $\boldsymbol{\alpha} = \nabla\phi(\hat{\mathbf{n}})$ is a field of deflection vectors, and ϕ is the lensing potential

$$\phi(\hat{\mathbf{n}}) = -2 \int_0^{\chi_*} d\chi \frac{f_K(\chi_* - \chi)}{f_K(\chi_*)f_K(\chi)} \Psi(\chi\hat{\mathbf{n}}; \tau_0 - \chi). \quad (3.24)$$

Here, Ψ is the Weyl potential. Expanding the lensing potential into spherical harmonics $\phi_{\ell m}$, its angular power spectrum $\langle \phi_{\ell m} \phi_{\ell' m'}^* \rangle = \delta_{\ell m} \delta_{\ell' m'} C_\ell^{\phi\phi}$ can be written as [5]

$$C_\ell^{\phi\phi} = \frac{8}{\pi} \int dk k^2 \int_0^{\chi_*} d\chi_1 \int_0^{\chi_*} d\chi_2 P_\Psi(k; \tau_0 - \chi_1, \tau_0 - \chi_2) \times j_\ell(k\chi_1) j_\ell(k\chi_2) \frac{f_K(\chi_* - \chi_1)}{f_K(\chi_*)f_K(\chi_1)} \frac{f_K(\chi_* - \chi_2)}{f_K(\chi_*)f_K(\chi_2)}, \quad (3.25)$$

¹²https://github.com/brinckmann/montepython_public

3. Euclid and cross-correlation of its probes with CMB

where P_Ψ is the Weyl potential power spectrum. For a flat universe $f_K(\chi) = \chi$, and for simplicity we shall assume flatness from now on.

It is also common to consider the lensing convergence, which is the Laplacian of the lensing potential $\kappa = -\frac{1}{2}\nabla^2\phi$, its multipole coefficients and power spectrum are related to the ones of the lensing potential by [222]

$$\kappa_{\ell m} = \frac{\ell(\ell+1)}{2}\phi_{\ell m}; \quad C_\ell^{\kappa\kappa} = \frac{\ell^2(\ell+1)^2}{4}C_\ell^{\phi\phi}. \quad (3.26)$$

In our likelihood, the observable is the convergence power spectrum $C_\ell^{\kappa\kappa}$, which can also be written in the general form Eq. (3.6) with the kernel given by

$$\mathcal{W}^\kappa(k, z) = -2\frac{\Psi(k, z)}{H(z)}\frac{\chi_* - \chi(z)}{\chi_*\chi(z)}, \quad (3.27)$$

or, in the Limber approximation Eq. (3.10) with

$$W^\kappa(z) = \frac{3\Omega_{m0}H_0^2}{2}(1+z)\chi(z)\left[1 - \frac{\chi(z)}{\chi_*}\right]. \quad (3.28)$$

The CMB lensing kernel is similar to the WL one, the key difference is that for the CMB the source is at a known redshift while for WL we need to integrate on the redshift distribution of source galaxies.

With these kernels it is possible to compute the CMB lensing auto-power spectrum and its cross-correlation with WL or GCp.

Phenomenologically, gravitational lensing imprints distinctive statistical signatures onto the observed CMB fluctuations such as generating statistical anisotropies (non diagonal correlations in the CMB fields), new non-Gaussian signals and B-mode polarization. It also smooths the observed power spectra. These effects allow us to reconstruct the lensing potential (and therefore the large scale structure of the Universe) from the observed lensed CMB.

We show in Fig. 3.14 the smoothing effect of lensing on the CMB temperature power spectrum, and the CMB lensing power spectrum reconstructed by the *Planck* collaboration [32], which claimed a 40σ detection of the lensing signal. The figure also contains the measurements by the ACTPol [223], SPTpol [224], and SPT-SZ [225] collaboration. More recent measurement of CMB lensing come from the use of the latest PR4 *Planck* data maps and lensing reconstruction [221], and from ACT DR6 [226].

I have been involved in the development and validation of the CMB lensing likelihood as well, especially in the implementation of the theoretical predictions in the likelihood module joint with the production of mock data vectors, using quadratic estimators (QE), to validate the end-to-end pipeline. As we've seen in section 3.3, since the CMB lensing is a probe of the matter distribution of the Universe, it is common to employ it in a combined analysis with galaxy clustering and weak lensing in a 6×2 pt analysis; for this reason, in chapter 5 we will put some emphasis on the 6×2 pt forecasts.

In the following chapters, I will discuss my contributions to the CMBX-SWG and also present some of the results that are allowed to be published by the rules of the EC. In

3.3. CMB cross-correlation

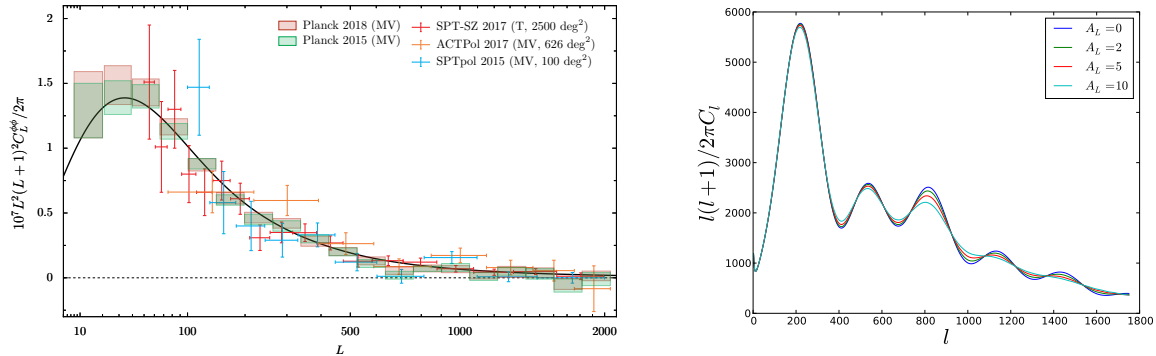


Figure 3.14: Left: CMB lensing potential power spectrum reconstructed by the *Planck* collaboration, showing also the measurements by the ACTPol [223], SPTpol [224], and SPT-SZ [225] collaboration. Figure from Ref. [32]. **Right:** The impact on the lensed CMB temperature power spectrum of varying the lensing amplitude parameter A_L ($C_L^{\phi\phi} \rightarrow A_L C_L^{\phi\phi}$) for $A_L = [0, 2, 5, 10]$. Figure from Ref. [227].

chapter 4 we use Eq. (3.10) with appropriate kernels to discuss the implementation and validation of those formulas in the likelihood code for the cross-correlation T-GCp and for the CMB lensing auto power spectrum; instead, for the forecasts in chapter 5 we compute the observables employing Eq. (3.6).

3.3.3 Signal-to-noise for CMB-cross correlations

In this section we calculate the signal-to-noise ratio (SNR) of the cross-correlation of the CMB temperature with photometric galaxy clustering galaxy for the detection of the ISW effect. We also consider the SNR for the cross-correlations between CMB lensing with photometric galaxy clustering and galaxy weak lensing. The SNR are calculated for different combinations of a *Euclid*-like photometric survey with different CMB experiments. For the the cross-correlation between temperature and the galaxy field we consider only *Planck* as it as has mapped the CMB temperature anisotropies at the largest scales ($\ell = 2$), and those are sensitive to the T-GCp cross-correlation. For CMB lensing, we consider the cross-correlations with GCp and WL, between *Euclid* and three CMB experiments: *Planck*, Simons Observatory (SO)¹³[228] and S4.

The SNR of the tomographic cross-correlation between a CMB field and galaxy probes (GC or WL) is given by [229]

$$\left(\frac{S}{N}\right)^2 = \sum_{i,j} \sum_{\ell_{\min}}^{\ell_{\max}} (2\ell + 1) f_{\text{sky}}^{XY} C_{\ell}^{XY_i} [\text{Cov}_{\ell}^{-1}]_{ij} C_{\ell}^{XY_j}, \quad (3.29)$$

where the i, j indices stand for the redshift bins, $X \in \{T, \kappa\}$, $Y \in \{\text{GCp}, \text{WL}\}$, and f_{sky}^{XY} is the fraction of the sky that is jointly mapped by the two surveys: $f_{\text{sky}}^{XY} = 0.36$ for all the surveys considered in this section. The covariance matrix Cov_{ℓ} is defined as

$$[\text{Cov}_{\ell}]_{ij} = \overline{C}_{\ell}^{Y_i Y_j} \overline{C}_{\ell}^{XX} + C_{\ell}^{XY_i} C_{\ell}^{XY_j}, \quad (3.30)$$

¹³<https://simonsobservatory.org/>

3. Euclid and cross-correlation of its probes with CMB

where

$$\overline{C}_\ell^{Y_i Y_j} = C_\ell^{Y_i Y_j} + N_\ell^{Y_i Y_j}; \quad \overline{C}_\ell^{XX} = C_\ell^{XX} + N_\ell^{XX}. \quad (3.31)$$

The shot-noise terms for the *Euclid* auto-spectra are

$$N_\ell^{Y_i Y_j} = \delta_{ij} \frac{\sigma^2}{\bar{n}_i}, \quad (3.32)$$

where $\sigma = \sigma_\epsilon$ when $Y = \text{WL}$ is the total intrinsic ellipticity dispersion, and we have $\sigma = 1$ when $Y = \text{GCp}$, and 0 otherwise. We use $\sigma_\epsilon = 0.30$ as in Refs. [197, 204]. The term \bar{n}_i in the equation above is the galaxy surface density per redshift bin expressed in inverse steradians, in our case it is simply given by the total surface density of galaxies $\bar{n}_g = 30 \text{ arcmin}^{-2}$ divided by the number of bins considered, because we are working with equi-populated bins. All the cross-spectra are assumed to have zero noise, and for CMB temperature we adopt isotropic noise deconvolved with the instrument beam

$$N_\ell^{\text{TT}} = (\Delta T)^2 b_\ell^{-2}, \quad b_\ell = \exp\left(-\frac{1}{2}\ell(\ell+1)\frac{\theta_{\text{FWHM}}^2}{8 \ln 2}\right), \quad (3.33)$$

where θ_{FWHM} is the full-width-half-maximum of the beam given in radians, and ΔT is the detector noise levels, expressed in $\mu\text{K arcmin}$. For *Planck* we adopt $\theta_{\text{FWHM}} = 7 \text{ arcmin}$ and $\Delta T = 33 \mu\text{K arcmin}$ as in Ref. [204]¹⁴.

Regarding the CMB lensing noise we use of latest PR4 *Planck* data maps and lensing reconstruction [221] with associated noise; while for SO and S4 we employ the reconstructed minimum-variance estimator for $N_\ell^{\kappa\kappa}$ [230] of Ref. [204], which corresponds to the so-called N0 bias. In section 4.2.2 we will provide more details on the CMB lensing reconstruction and associated noises.

Concerning the multipole range in the sum in Eq. (3.29), we consider the *Euclid* observables starting from $\ell = 10$, therefore $\ell_{\text{min}} = 10$ as that is the largest minimum multipole for the combinations of probes studied in this section ($T\text{-GCp}$, $\kappa\text{-GCp}$, and $\kappa\text{-WL}$). For $T\text{-GCp}$ we cut the sum at $\ell_{\text{max}} = 500$ since most of the signal is at low ℓ 's. For $\kappa\text{-GCp}$ and $\kappa\text{-WL}$ we have $\ell_{\text{max}} = 400$ for *Planck* because that is the maximum multipole considered in the *Planck* CMB lensing analysis; whereas, for SO and S4, that will measure CMB lensing up to $\ell = 3000$, we set $\ell_{\text{max}}(\kappa\text{-GCp}) = \ell_{\text{max}}(\text{GCp}) = 750$ and $\ell_{\text{max}}(\kappa\text{-WL}) = \ell_{\text{max}}(\text{WL}) = 1500$. These multipole ranges for the *Euclid* observables corresponds to the pessimistic cuts of Ref. [197].

We compute the observables in a fiducial ΛCDM model using the redshift distributions described in section 3.2.2 and given by Eqs. (3.14), (3.15) and (3.17), with the photometric nuisance parameters fixed at the valued provided in Table 3.1.

In Fig. 3.15, the cumulative SNR for $T\text{-GCp}$ is shown as a function of ℓ_{max} for one, three and ten redshift bins, highlighting how multipoles $\ell \lesssim 100$ do not add information in the for the ISW signal. The figure shows the relevance of tomography for a probe with such a low SNR, indeed between the non-tomographic case and the 10 bins scenario there is an improvement of 27%, and we also see a 14% improvement going from three

¹⁴Note that in Ref. [204] there is a typo as the quoted value is $\Delta T = 23 \mu\text{K arcmin}$ instead of 33.

3.3. CMB cross-correlation

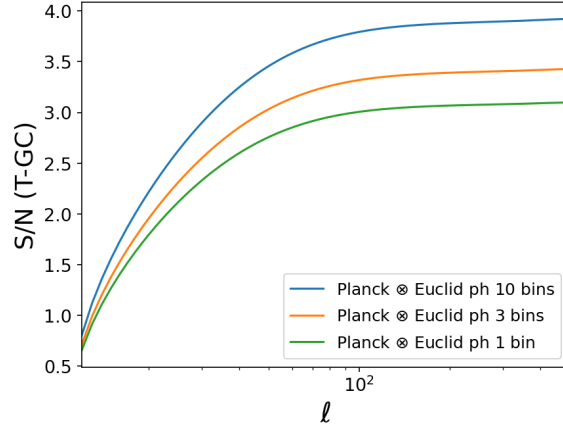


Figure 3.15: T-GCp cumulative signal-to-noise as function of ℓ_{\max} for a *Planck*-like CMB experiment combined with *Euclid* with one, three and ten redshift bins.

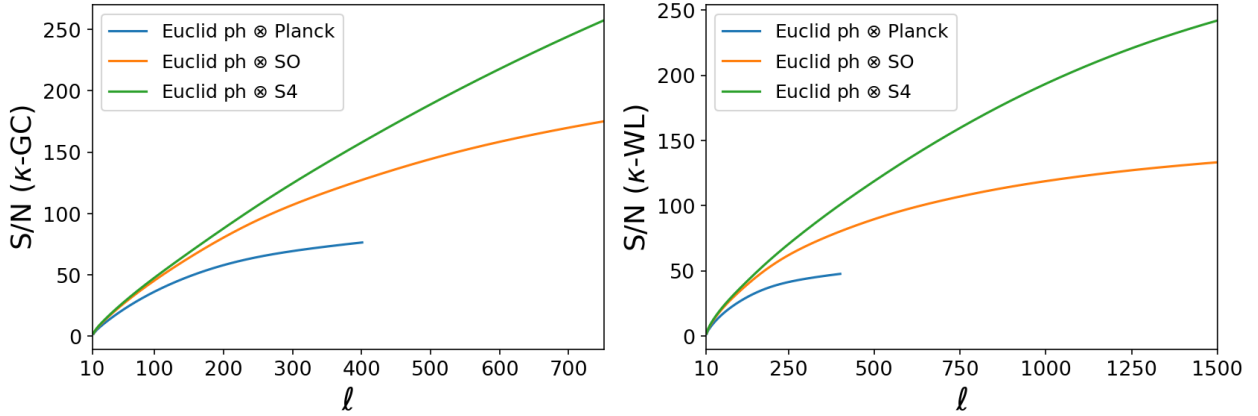


Figure 3.16: κ -GCp and κ -WL cumulative signal-to-noise as functions of ℓ_{\max} for the combination of a *Euclid*-like photometric survey (10 bins) with *Planck*, SO and S4.

to ten bins. We therefore expect to reach a $\sim 4\sigma$ detection of the ISW using the cross-correlation between *Euclid* photometric galaxies and *Planck* CMB temperature maps, for 10 bins. The exact values of the SNR are reported in Table 3.2.

In the case of κ -GCp, there is a larger margin of improvement expected with respect to the current $\sim 20\sigma$ detection obtained by *Planck* and NVSS [231]. Indeed, we obtain a SNR of 76 when cross-correlating *Planck* with *Euclid* and we get a larger SNR for the combinations of the other CMB experiments with *Euclid*. We show the cumulative SNR for κ -Gcp (left panel) and κ -WL (right panel) in Fig. 3.16 for the combination of a *Euclid*-like photometric survey with *Planck*, SO and S4.

For these observables the CMB lensing noise is dominant for *Planck*, whereas it decreases significantly for SO and S4, this is due to their ability to map the small scales in CMB temperature and polarization, which will allow a much less noisier reconstruction of CMB lensing. As a consequence, the SNR for κ -GCp and κ -WL can go up to a factor of 3 for SO, and 5 for S4, with respect to *Planck*, when considering the cross-correlation observables. The exact values of the SNR for these probes are reported in Table 3.3.

	1 bin	3 bins	10 bins
<i>Euclid</i> ph-like \otimes <i>Planck</i> -like	3.1	3.4	3.9

Table 3.2: T-GCp signal-to-noise for a *Planck*-like CMB experiment combined with *Euclid* with one, three and ten redshift bins

	κ -GCp	κ -WL
<i>Euclid</i> ph-like \otimes <i>Planck</i> -like	76	48
<i>Euclid</i> ph-like \otimes SO-like	175	133
<i>Euclid</i> ph-like \otimes S4-like	257	242

Table 3.3: κ -GCp and κ -WL signal-to-noise for the combination of a *Euclid*-like photometric survey (10 bins) with *Planck*, SO and S4.

Chapter 4

Euclid-CMB cross-correlation likelihood

One of the main activities of the CMBX-SWG is the development of the likelihood involving the CMB-cross correlation observables described in section 3.3 (for the basics of Bayesian statistical analysis, likelihood and MCMC we refer to appendix A). Concerning the development and testing of the likelihood, the group works independently from the so-called Inter Science Taskforce: Likelihood (IST:L), which develops the official *Euclid* likelihood package CLOE, but the final products are implemented in the CLOE fork of the CMBX-SWG, and they will be merged with the official likelihood code. This means that when CLOE is released it will be shipped with the inclusion of the CMBX probes and the possibility to carry out the analysis with or without them. For this reason, our independent likelihoods have been developed taking into account that the primary goal of this activity is the integration of our pipeline into CLOE, and we have pursued maximal consistency with the official *Euclid* likelihood from the inception. For example, the theoretical predictions for the various observables presented in section 3.2 are computed within the likelihood module, and we have followed the same philosophy, thoroughly testing and validating the theoretical predictions for the cross-correlation spectra computed within our likelihood, before implementing them in the CMBX-SWG fork of CLOE. Beside the implementation of the theoretical predictions, we have also provided a covariance matrix that includes the CMBX observables as well as the *Euclid* photometric probes; we call this covariance a $7 \times 2\text{pt}$ covariance since in addition to the $6 \times 2\text{pt}$ it also incorporates the T-GCp cross correlation.

The likelihood under consideration is a Gaussian function for all the photometric and CMBX probes:

$$-2 \ln \mathcal{L}(\mathbf{D}|\boldsymbol{\theta}) = (\mathbf{D} - \mathbf{T}(\boldsymbol{\theta}))^t \text{Cov}^{-1} (\mathbf{D} - \mathbf{T}(\boldsymbol{\theta})), \quad (4.1)$$

where \mathbf{D} is the data vector, while \mathbf{T} represents the vector of theoretical prediction which depend on the cosmological parameters $\boldsymbol{\theta}$. The covariance matrix has an analytical form as in [204]:

$$\text{Cov} \left[C_\ell^{XY}, C_{\ell'}^{X'Y'} \right] = \frac{\delta_{\ell\ell'}^{\text{K}}}{(2\ell + 1)f_{\text{sky}}} \left\{ \left[C_\ell^{XX'} + N_\ell^{XX'} \right] \left[C_{\ell'}^{YY'} + N_{\ell'}^{YY'} \right] + \left[C_\ell^{XY'} + N_\ell^{XY'} \right] \left[C_{\ell'}^{YX'} + N_{\ell'}^{YX'} \right] \right\}, \quad (4.2)$$

where f_{sky} is the fraction of the sky that is jointly mapped by the different probes, for *Euclid* at the end of the survey $f_{\text{sky}} \simeq 0.36$. The term δ^{K} is the Kronecker delta (no correlations between different multipoles), and the indices X, Y, X' and Y' refer to the considered observables: T, E, κ , WL $_i$ or GCp $_i$. The shot-noise terms for the *Euclid* auto-spectra are given by Eq. (3.32), which we report here

$$N_\ell^{XY} = \frac{\sigma^2}{\bar{n}_i}, \quad (4.3)$$

where $\sigma = \sigma_\epsilon$ when $X = Y = \text{WL}_i$ is the total intrinsic ellipticity dispersion, and we have $\sigma = 1$ when $X = Y = \text{GCp}_i$, and 0 otherwise. The term \bar{n}_i in the equation above is the galaxy surface density per redshift bin expressed in inverse steradians. All the cross-spectra are assumed to have zero noise, and the noise for the CMB observables are described in sections 4.1 and 4.2.

In this chapter, we focus on the tests of the Gaussian likelihood for the isolated cases of the T-GCp and CMB lensing, with particular emphasis on the validation of theoretical predictions and the approximations used in their computations.

The group has carried out the development of both the ISW and CMB lensing likelihood modules, therefore, I will first discuss my contribution to the ISW-likelihood validation in the `MontePython`¹ [162, 163] framework and then my activities regarding the CMB lensing likelihood, with consequent implementation into `CLOE`. These activities span from tests on the accuracy of the theoretical predictions to the productions of mock-data vectors, with the goal of building a more realistic pipeline able to take into account, at the likelihood level, peculiar effects related to the CMB lensing reconstruction from CMB maps.

4.1 Validation of the ISW-galaxy cross-correlation likelihood

The observable to detect the ISW effect is the angular power spectrum of the cross correlation between the CMB temperature and the galaxy field, discussed in section 3.3.1. At present, the likelihood module for the ISW cross-correlation developed within the CMBX-SWG does not rely on an Einstein-Boltzmann code to compute the theoretical power spectra but it computes them internally in the Limber approximation using Eq. (3.22). In obtaining that formula for the cross-spectrum, in addition to the Limber approximation, we have assumed the absence of anisotropic stresses and a scale independent growth of matter perturbations $\delta(\mathbf{k}, z) = D(z)\delta(\mathbf{k}, \tilde{z})$. Using Eq. (3.22) allows us to be completely consistent with the development of the main *Euclid* likelihood package for the primary probes and implement this additional probe consistently within `CLOE`. Moreover, the use of these approximations significantly reduces the computation time of the likelihood, which is crucial to perform a MCMC. Nonetheless, using an approximate expression might introduce unwanted effects in the estimate of parameters, biasing the results. I discuss in this section some validations I performed regarding the computation of the theoretical prediction within our likelihood implementation in `MontePython`. Since the information contained in the TG² cross-correlation is not enough to constrain all the cosmological parameters, in addition to the TG likelihood we also consider the simplified *Planck* Blue book [232] likelihood. This likelihood will provide most of the constraining power but it is insensitive to certain parameters, for example the galaxy bias, which can only be constrained by the TG probe in this setting.

¹https://github.com/brinckmann/montepython_public

²We use TG to lighten the notation when referring to the cross-correlation between temperature and photometric galaxy clustering T-GCp.

4.1.1 Likelihood and specifications

To perform the validation of the theoretical prediction for the TG power spectrum, we first need to specify the various ingredients that enter the *Euclid* and CMB-cross observables described in sections 3.2 and 3.3, such as the galaxy distributions n_i and the galaxy bias. The latter is modeled as $b(z) = b_g \sqrt{1+z}$, where the parameter b_g is a free nuisance parameter to be varied. We evaluate the bias at the mean redshift of each bin $b(z_i) = b_g \sqrt{1+z_i}$ and consider it constant in each bin; the fiducial value is $b_g = 1$. Since this parameter is redshift independent, it comes out of the integral in Eq. (3.22) and, if there is no additional information from galaxy clustering to constrain it independently, it can play the role of an amplitude for the C_ℓ^{TG} power spectrum. In this section we consider information coming from galaxy clustering only in the covariance matrix, therefore, constraints on b_g can be interpreted as constraints on the amplitude of the ISW effect.

We use the redshift distributions described in section 3.2.2 and given by Eqs. (3.14), (3.15) and (3.17) with the photometric nuisance parameters fixed at the values provided in Table 3.1, for 3 and 10 equi-populated redshift bins whose edges are given by

$$z_i = \{0.0010, 0.71, 1.102.50\}, \quad (4.4)$$

$$z_i = \{0.0010, 0.42, 0.56, 0.68, 0.79, 0.90, 1.02, 1.15, 1.32, 1.58, 2.50\}. \quad (4.5)$$

In this section we consider the Gaussian likelihood Eq. (4.25) for the TG power spectrum:

$$-2 \ln \mathcal{L}(C_\ell^{\text{TG}_i}) = \sum_{ij} \sum_{\ell} \left(\hat{C}_\ell^{\text{TG}_i} - C_\ell^{\text{TG}_i} \right) [\text{Cov}^{-1}]_{ij,\ell\ell}^{\text{fid}} \left(\hat{C}_\ell^{\text{TG}_j} - C_\ell^{\text{TG}_j} \right), \quad (4.6)$$

with covariance matrix defined as

$$[\text{Cov}_{TG_i, TG_j}]_{\ell\ell'} = \frac{\delta_{\ell\ell'}}{(2\ell+1) f_{\text{sky}}} \left[\left(C_\ell^{\text{TG}_i} C_{\ell'}^{\text{TG}_j} \right) + \left(C_\ell^{\text{TT}} + N_\ell^{\text{TT}} \right) \left(C_{\ell'}^{\text{G}_i \text{G}_j} + N_{\ell'}^{\text{G}_i \text{G}_j} \right) \right], \quad (4.7)$$

where f_{sky} is the *effective* fraction of the sky that is jointly mapped by the different probes, for which we consider $f_{\text{sky}} = 0.36$, and we have assumed the cross-spectra to have zero noise. N_ℓ^{TT} is the noise in the CMB temperature power spectrum, given by Eq. (3.33) (isotropic noise deconvolved with the instrument beam). For the simplified *Planck* Blue book [232] likelihood we employ in the remaining of the section, we consider only one frequency channel with $\theta_{\text{FWHM}} = 7.1$ arcmin and $\Delta T = 42.6 \mu\text{K arcmin}$. The term $N_\ell^{\text{G}_i \text{G}_j}$ represents the shot-noise of the galaxy density contrast given by Eq. (4.3) where \bar{n}_i is simply the total surface density of galaxies $\bar{n}_g = 30 \text{ arcmin}^{-2}$ divided by the number of bins considered, because we are working with equi-populated bins.

4.1.2 Validation of the theoretical prediction

We first quantify how much the approximation (3.22) changes the power spectrum compared to exact computation (3.6) with the kernel (3.19), by comparing the power

4. Euclid-CMB cross-correlation likelihood

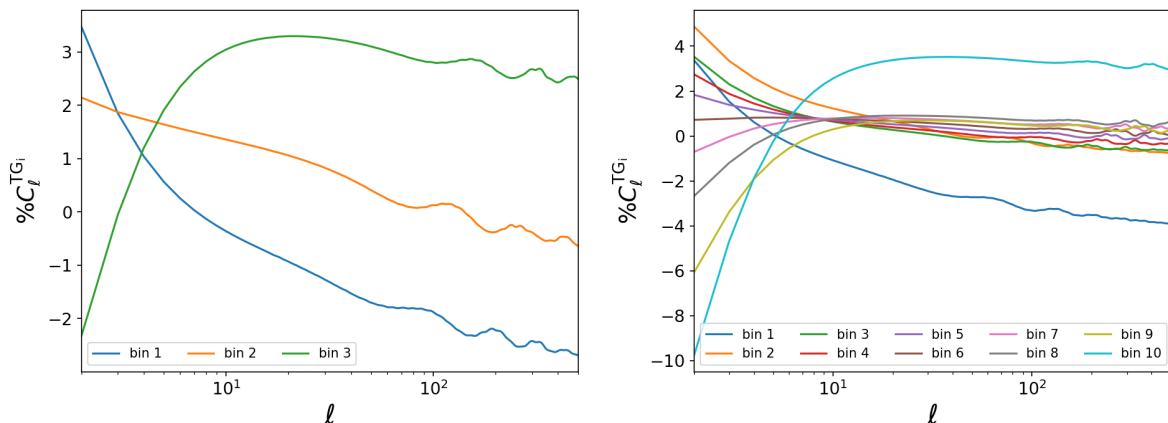


Figure 4.1: Percentage difference between the Temperature-Galaxy power spectra computed within our likelihood module and with CLASS, for 3 redshift bins on the left and 10 on the right

spectrum computed within our likelihood module with that produced by the Einstein-Boltzmann code CLASS³ [20, 26] where the integral (3.6) is computed without any assumptions, such as the separability of wavenumber and redshift in the growth of matter perturbations. We also check the precision settings of CLASS to ensure that the difference between the power spectra is not due to an inaccurate computation, and set the precision parameters such that the Limber approximation is not adopted at any scale. Fig. 4.1 shows the percentage difference in the power spectra, for 3 bins on the left panel and 10 bins on the right panel. These differences are never larger than 4% in the 3 bins case and always within 10% for the 10 bins, where, as expected, we observe the highest differences on large scales. There is a tendency that Fig. 4.1 highlights: for the broadest bins in redshift, the relative differences at small and large scales are comparable. This holds true for the first and the tenth bin in the right panel and for all 3 bins in left panel, which are the more extended bins in z (see Eqs. (3.16) and (4.4) and Fig. 3.8).

We now wish to disentangle the Limber approximation from the other assumption that lead from Eqs. (3.6) and (3.19) to Eq. (3.22), we do this by adopting the exact formula and applying only the Limber approximation at different multipoles, without assuming linear growth of matter perturbation or complete absence of anisotropic stresses. Therefore, we derive fiducial power spectra using CLASS without the Limber approximation at all multipoles and then compute the χ^2 between this fiducial and the power spectra obtained using the Limber approximation only after a certain multipole, called ℓ_{switch} , as

$$\Delta\chi^2 = \sum_{ij} \sum_{\ell} \left[C_{\ell \text{NoLimber}}^{\text{TG}_i} - C_{\ell}^{\text{TG}_i}(\ell_{\text{switch}}) \right] [\text{Cov}^{-1}]_{ij,\ell\ell}^{\text{fid}} \left[C_{\ell \text{NoLimber}}^{\text{TG}_j} - C_{\ell}^{\text{TG}_j}(\ell_{\text{switch}}) \right], \quad (4.8)$$

where the covariance matrix is computed using the fiducial power spectra $C_{\ell \text{NoLimber}}^{\text{TG}_i}$. The result is shown, for 3 and 10 redshift bins, in the left panel of Fig. 4.2, as a function of ℓ_{switch} , meaning that on the extreme left the Limber approximation is used for all multipoles while on the right it is not used at any scale. The difference in χ^2 is negligible for the 3 bins case even when the power spectra use the Limber approximation at all

³https://lesgourg.github.io/class_public/class.html

4.1. Validation of the ISW-galaxy cross-correlation likelihood

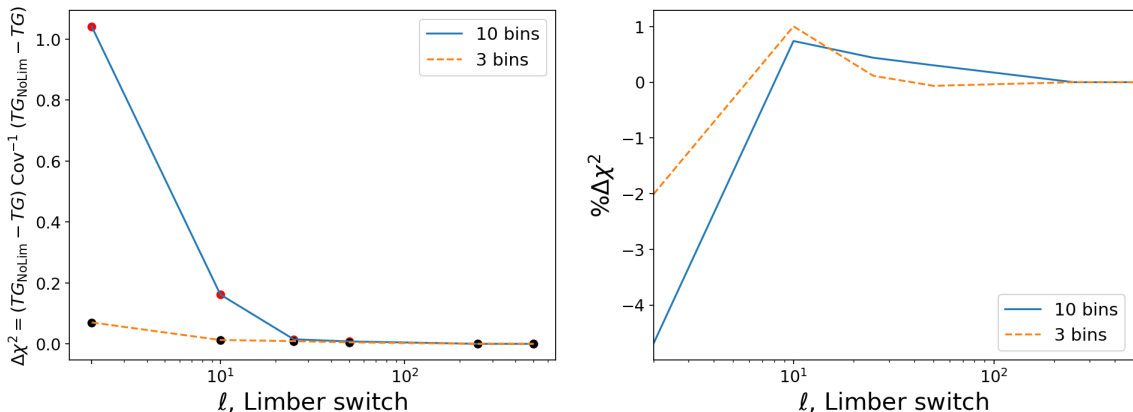


Figure 4.2: Left: χ^2 computed using Eq. (4.8) between the power spectra without the Limber as fiducial, and the power spectra with the Limber approximation employed after a certain multipole ℓ_{switch} . **Right:** percentage difference in the χ^2 computed using Eqs. (4.9) to (4.11).

scales, while for 10 bins, we obtain $\chi^2 \simeq 1$ for $\ell_{\text{switch}} = 2$. This should not produce any bias in parameter estimations, as we will discuss shortly. Increasing the multipole at which we apply the Limber approximation, the χ^2 tends to zero, as expected.

The right plot of Fig. 4.2 shows the percentage difference

$$\% \Delta\chi^2 = 100 [\chi_{\text{noLimber}}^2 - \chi_{\text{Limber}}^2(\ell_{\text{switch}})] / \chi_{\text{noLimber}}^2, \quad (4.9)$$

between the χ^2 computed without the Limber approximation and with the Limber approximation starting from a given multipole ℓ_{switch} :

$$\chi_{\text{noLimber}}^2 = C_{\text{noLimber}}^{\text{TG}} [\text{Cov}^{-1}]^{\text{fid}} C_{\text{noLimber}}^{\text{TG}}, \quad (4.10)$$

$$\chi_{\text{Limber}}^2(\ell_{\text{switch}}) = C_{\text{Limber}}^{\text{TG}}(\ell_{\text{switch}}) [\text{Cov}^{-1}]^{\text{fid}} C_{\text{Limber}}^{\text{TG}}(\ell_{\text{switch}}), \quad (4.11)$$

where we have omitted the indices ij and ℓ to lighten the notation. This difference is at most of 4% for 10 bins when using the Limber approximation from $\ell_{\text{switch}} = 2$, but it is already consistent with zero from $\ell_{\text{switch}} = 10$.

Before adopting Eq. (3.22) as our theoretical prediction in the likelihood module, we also performed the following test: take the power spectra from CLASS as fiducial data, and perform an MCMC analysis computing the theoretical predictions in the various points of parameter space with our approximated formula, and check if this results in any bias in the estimation of cosmological parameters. We also perform an analogous MCMC analysis where the role of both the fiducial data and the theoretical prediction are computed using the approximated power spectrum, and compare the two results. The latter case will recover the fiducial cosmology because the mock data and the theoretical prediction are computed in the same way; this is our benchmark, and we compare it to the run performed using the exact spectra as data. If the two analysis agree we can conclude that our approximation did not induce any biases in the parameter estimation.

As anticipated, since the information contained in the cross correlation between the late ISW effect and galaxies is not enough to constrain all the cosmological parameters, in addition to the TG likelihood we also consider the simplified *Planck* Blue book [232]

4. Euclid-CMB cross-correlation likelihood

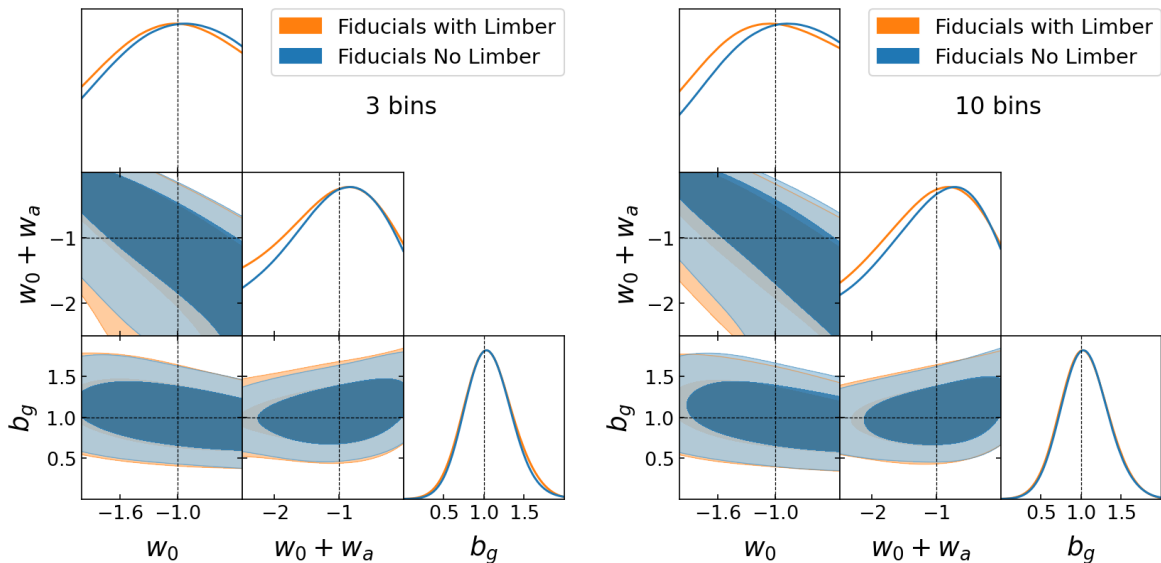


Figure 4.3: Marginalized joint 68% and 95% CL regions 2D parameter space on the DE parameters w_0 , w_0+w_a and the bias b_g , for a combination of the Planck Bluebook likelihood and our `Montepython` likelihood for the cross correlation between CMB temperature and galaxies.

likelihood which will provide most of the constraining power on the cosmological parameters. The free bias parameter, however, can only be constrained by cross-correlation observable in this setting, and we are therefore interested to see if the estimates in the two analysis are consistent with each other and with the fiducial value $b_g = 1$.

Since the LISW is sensitive to the DE parameters we consider for this analysis a w_0w_a CDM model (1.97) where the fiducial values are $w_0 = -1$ and $w_a = 0$, and we sample on w_0 and on the sum of the two w_0+w_a , and the other cosmological parameters.

The results are summarized in Table 4.1 and Fig. 4.3 where we show that there is negligible bias in the estimation of the parameter b_g . In particular, both for 3 and 10 bins the recovered value is consistent with the fiducial $b_g = 1$. Furthermore, the case with mock data from `CLASS` and the one with mock data computed with the approximated formula, provide similar best-fit and 1σ error, showing that the use of the approximated expression does not degrade the constraints. Indeed, as it can be seen from Fig. 4.3 the posteriors are consistent in the two cases. The near overlap between the posteriors further verifies that our approximated modelling of the cross-correlation power spectra introduces negligible bias, and it validates the approximations we introduced.

	3 bins		10 bins	
	fid. Limber	fid. No Limber	fid. Limber	fid. No Limber
Bias in unit of σ (wrt $b_g = 1$)	0.20	0.21	0.14	0.17
1σ	0.30	0.28	0.29	0.29

Table 4.1: Bias in the estimation of the bias parameter b_g in units of the 1σ error, consistent among all the cases.

4.2 CMB lensing mock pipeline

Even if CMB lensing is inferred from the CMB, it is a probe of the late-time matter distribution of the Universe, and it can be connected directly to the matter power spectrum today. For this reason, in addition to the cross-correlation between CMB lensing and *Euclid* probes, we also implemented the CMB lensing auto power spectrum in the likelihood framework of *Euclid*. In this way, we can infer it consistently with all the other Euclid probes.

In this section I discuss my implementation of the CMB lensing theoretical prediction in CLOE and, in section 4.2.2, a CMB lensing quadratic estimator (QE) reconstruction I carried out. The name QE comes from the fact that in order to estimate the lensing potential, a quadratic combination of the CMB fields T, E, B, is used [233]. The reason to reconstruct the power spectrum is to produce a mock-data vector to test the likelihood, and the debiasing of some terms associated with the QE that have to be implemented in the likelihood itself as corrections to the theoretical predictions.

We use capital indices L, M for the CMB lensing power spectrum and multipole coefficients, distinguishing them from ℓ, m of the primary CMB.

4.2.1 CMB lensing in CLOE

The main reason to implement the CMB lensing in the likelihood without relying on the computation from an Einstein-Boltzmann code, is to compute the angular power spectrum using directly the low redshift matter power spectrum provided by the nonlinear module of CLOE, which will allow complete consistency with the computation of *Euclid* primary probes. The main challenge of such implementation is that to reliably compute the CMB lensing power spectrum one needs to integrate Eq. (3.25) up until the last scattering surface, while the maximum redshift for CLOE is $z_{\max} = 4$. Using CLOE with $z_{\max} \simeq 1100$ is unfeasible as it dramatically slows down the code, rendering impossible sampling in parameter space. To overcome this problem we split the integral for the CMB lensing convergence in a low ($z < 4$) and high redshift ($4 < z < z_*$) contribution, as

$$C_L^{\kappa\kappa} = L^2(L+1)^2 \int_{\chi(z=4)}^{\chi_*} d\chi \left(\frac{\chi_* - \chi}{\chi^2 \chi_*} \right)^2 P_\Psi(k_\ell, \tau_0 - \chi) + \int_{z=0}^{z=4} \frac{dz}{H(z)\chi^2(z)} W^\kappa(z)^2 P_{\delta\delta}(k_\ell, z) \quad (4.12)$$

with W^κ given in Eq. (3.28). The high redshift integral is computed independently of other CLOE routines and to obtain it we only need the comoving distance to the last-scattering surface and the Weyl power spectrum up to z_* . Since this task is carried out independently from the rest of the code and it is not a bottleneck in execution time, including or not the CMB lensing in the likelihood results in a minimal slow down of the code, about 3%.

Before implementing Eq. (4.12) in the CLOE fork of the CMBX-SWG, we thoroughly tested and validated the accuracy of the computation against the Einstein-Boltzmann

4.2. CMB lensing mock pipeline

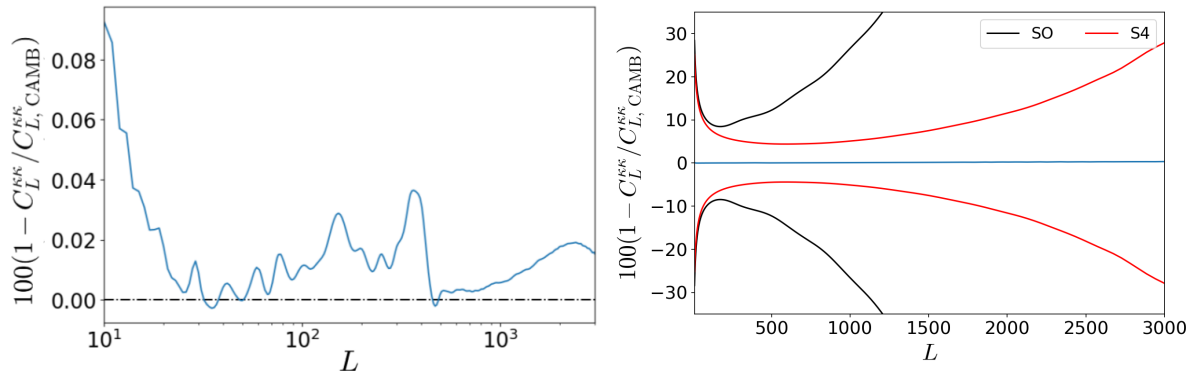


Figure 4.4: **Left:** Percentage difference between the CMB lensing power spectrum computed with Eq. (4.12) and CAMB. **Right:** Same as in the left plot but with the addition of the expected noises in the cmb lensing measurements for SO (black) and S4 (red).

code CAMB⁴ [27]. A comparison between our computation with Eq. (4.12) and CAMB is shown in Fig. 4.4, for multipoles $L \in [10, 3000]$. We can see from the left panel that the agreement between the two codes is extremely good: the largest percentage difference, which occurs at $L = 10$, is less than 0.1%. For comparison, in the right panel of the figure we also add the expected noises in the CMB lensing measurements for the upcoming Simons Observatory (SO)⁵ and the future CMB S4 experiment. The difference with respect to CAMB is completely negligible when compared to the noise, therefore, our computation of the theoretical prediction is validated.

At the moment, the expression in Eq. (4.12) is what is implemented in the CMBX-SWG fork of CLOE and it is currently in the process of review and evaluation for merging our modification into the main CLOE repository.

As we will see in the next sections, due to some subtleties in the QE reconstruction of the lensing potential, the formula we validated needs to be modified in order to be compared with real data, and to sample the parameter space without introducing unwanted biases related to the reconstruction. The next two sections highlight this procedure which is currently under development and testing, with the goal of providing a working pipeline on mock data before the first *Euclid* data release expected in 2025.

4.2.2 Quadratic estimators of the CMB Lensing power spectrum

This section offers an outline of quadratic estimator techniques necessary for this work, it draws heavily from [234], where the CMB lensing reconstruction procedure is discussed in a more detailed way, and effects beyond the scope of thesis are included.

Lensing potential estimator

Considering the CMB multipole coefficients defined in section 1.7.1 $X_{\ell m}, Z_{\ell m} \in \{T_{\ell m}, E_{\ell m}, B_{\ell m}\}$ and ensemble averaging over a fixed realization of the CMB lensing potential, the CMB

⁴<https://camb.info/>

⁵<https://simonsobservatory.org/>

4. Euclid-CMB cross-correlation likelihood

covariance matrix acquires off-diagonal elements given by

$$\langle X_{\ell_1 m_1} Z_{\ell_2 m_2} \rangle = \sum_{LM} (-1)^M \begin{pmatrix} \ell_1 & \ell_2 & L \\ m_1 & m_2 & -M \end{pmatrix} \mathcal{W}_{\ell_1 \ell_2 L}^{XZ} \phi_{LM}, \quad (4.13)$$

where the bracketed term is a Wigner-3j symbol. The terms \mathcal{W}^{XZ} are the covariance response functions, they are linear in the (lensed) CMB power spectra and their explicit expressions can be found in [230].

These off-diagonal terms can be used to estimate the lensing potential, in fact a quadratic estimator of the lensing potential is defined as a function of pairs of inverse-variance-filtered sky maps $\bar{X}_{\ell m}, \bar{Z}_{\ell m} \in \{\bar{T}_{\ell m}, \bar{E}_{\ell m}, \bar{B}_{\ell m}\}$ as

$$\bar{x}_{LM}[\bar{X}, \bar{Z}] = \frac{(-1)^M}{2} \sum_{\ell_1 m_1, \ell_2 m_2} \begin{pmatrix} \ell_1 & \ell_2 & L \\ m_1 & m_2 & -M \end{pmatrix} W_{\ell_1 \ell_2 L}^x \bar{X}_{\ell_1 m_1} \bar{Z}_{\ell_2 m_2}, \quad (4.14)$$

where $W_{\ell_1 \ell_2 L}^x$ is a set of weight functions characteristic of the estimator x , and the inverse-variance filtered maps are

$$\bar{X}_{\ell m} = \frac{X_{\ell m}}{C_{\ell}^{XX} + N_{\ell}^{XX}} = F_{\ell}^X X_{\ell m} \quad (4.15)$$

with N_{ℓ}^{TT} the noise spectrum of the map. Filtering the maps downweights noise-dominated modes. For optimal lensing estimators the weight functions coincide with the covariance response function of Eq. (4.13). For example, for the temperature-only optimal estimator $W^{TT} = \mathcal{W}^{TT}|_{\text{fid}}$, where the ‘‘fid’’ subscript indicates that the lensing weight function is evaluated for the fiducial cosmological model chosen for the lensing reconstruction. In general, there are eight possible lensing estimators based on the possible combinations of T , E , and B , provided that one neglects the lensing of any primordial B -mode signal. This number reduces to 5 possible estimators (TT, TE, TB, EE, EB) as there is no distinction between TE and ET , and the BB estimator has no linear response to lensing in the absence of primordial B -modes [32].

The response of a quadratic estimator to the covariance (4.13) is

$$\langle \bar{x}_{LM} \rangle = \mathcal{R}_L^{x\phi} \phi_{LM}, \quad (4.16)$$

where

$$\mathcal{R}_L^{x\phi} = \frac{1}{2(2L+1)} \sum_{\ell_1 \ell_2} W_{\ell_1 \ell_2 L}^x \mathcal{W}_{\ell_1 \ell_2 L}^{XZ} F_{\ell_1}^X F_{\ell_2}^Z. \quad (4.17)$$

To calculate the estimator response we use a fiducial Λ CDM cosmology with given values of the parameters, meaning that the response depends on the fiducial. For this reason, when sampling in parameter space during an MCMC, the normalization has to be recomputed using the CMB power spectra at the particular point in parameter space.

We note that the quadratic estimators (4.14) takes contribution also from effects different from lensing, such as the masking of the maps or the inhomogeneity of the instrumental noise. These effects, in fact, introduce correlations between different scales and

4.2. CMB lensing mock pipeline

can mimic lensing; thus, they have to be removed from the lensing potential estimate. It is possible to do so by performing several reconstructions over many simulations that include these effects and then averaging, obtaining the so-called mean field \bar{x}_{LM}^{MF} which is subtracted to the estimator (4.14). Since the lensing reconstruction we discuss in section 4.2.3 is performed on full sky CMB maps we created using `healpy`⁶, we can ignore the mean field in what follows, and our estimate of the lensing potential is therefore

$$\hat{\phi}_{LM}^x = \frac{\bar{x}_{LM}}{\mathcal{R}_L^{x\phi}}. \quad (4.18)$$

The so-called minimum variance (MV) estimator is obtained by combining the individual estimators as

$$\hat{\phi}_{LM}^{MV} = \frac{\sum_x \hat{\phi}_{LM}^x \mathcal{R}_L^{x\phi}}{\sum_x \mathcal{R}_L^{x\phi}}, \quad (4.19)$$

with the sum taken over the eight possible lensing estimators (TT , EE , TE , TB , EB , ET , BT , and BE).

Power spectrum estimator

The CMB lensing power spectrum $C_L^{\phi\phi}$ enters the connected 4-point function of the CMB fields as [235]

$$\begin{aligned} \langle X_{\ell_1 m_1} Z_{\ell_2 m_2} C_{\ell_3 m_4} D_{\ell_4 m_4} \rangle_c &= \sum_{LM} \begin{pmatrix} \ell_1 & \ell_2 & L \\ m_1 & m_2 & M \end{pmatrix} \begin{pmatrix} \ell_3 & \ell_4 & L \\ m_3 & m_4 & -M \end{pmatrix} \\ &\quad \times (-1)^M C_L^{\phi\phi} \mathcal{W}_{\ell_1 \ell_2 L}^{XZ} \mathcal{W}_{\ell_3 \ell_4 L}^{CD} + 2 \text{ perms.} \end{aligned} \quad (4.20)$$

Since the response functions \mathcal{W} enter the above equation, it is possible to estimate the CMB lensing power spectrum $C_L^{\phi\phi}$ from the quadratic estimators of the lensing potential:

$$C_{L,xy}^{\hat{\phi}\hat{\phi}}[\bar{X}, \bar{Z}, \bar{C}, \bar{D}] \equiv \frac{f_{sky}^{-1}}{2L+1} \sum_M \hat{\phi}_{LM}^x[\bar{X}, \bar{Z}] \hat{\phi}_{LM}^{y*}[\bar{C}, \bar{D}], \quad (4.21)$$

where f_{sky} is the unmasked sky fraction. We note that the power spectrum comes from the combination of four CMB fields since each quadratic estimator of the lensing potential contains a combination of two CMB fields. Starting from Eq. (4.21) it is possible to write an estimate of the lensing potential power spectrum based on the estimators x and y as

$$\hat{C}_{L,xy}^{\phi\phi} = C_{L,xy}^{\hat{\phi}\hat{\phi}} - \Delta C_{L,xy}^{\hat{\phi}\hat{\phi}} \Big|_{N_0} - \Delta C_{L,xy}^{\hat{\phi}\hat{\phi}} \Big|_{N_1}, \quad (4.22)$$

where we have omitted two correction terms related to the mean field and point sources contribution to the CMB lensing power spectrum.

There are two correction terms in Eq. (4.22). The $\Delta C_{L,xy}^{\hat{\phi}\hat{\phi}} \Big|_{N_0}$ term is the disconnected contribution to the 4-point function, which would be non-zero even in the absence of

⁶<https://github.com/healpy/healpy>

4. Euclid-CMB cross-correlation likelihood

lensing, it is commonly called N0 bias. It is possible to estimate the N0 bias with a procedure called *realization dependent debiaser*, which allows to make the lensing power spectrum estimate robust to possible mismatches between the assumed fiducial cosmology and noise level used for the reconstruction, and the real ones [236]. It consists of replacing some of the data fields with those from two sets of independent simulations (labelled MC1 and MC2), and then average over realizations as

$$\begin{aligned} \Delta C_{L,xy}^{\hat{\phi}\hat{\phi}} \Big|_{\text{N0}} = & \left\langle -C_{L,xy}^{\hat{\phi}\hat{\phi}}[\bar{X}_{\text{MC1}}, \bar{Z}_{\text{MC2}}, \bar{C}_{\text{MC2}}, \bar{D}_{\text{MC1}}] + C_{L,xy}^{\hat{\phi}\hat{\phi}}[\bar{X}_{\text{MC1}}, \bar{Z}, \bar{C}_{\text{MC1}}, \bar{D}] \right. \\ & + C_{L,xy}^{\hat{\phi}\hat{\phi}}[\bar{X}_{\text{MC1}}, \bar{Z}, \bar{C}, \bar{D}_{\text{MC1}}] + C_{L,xy}^{\hat{\phi}\hat{\phi}}[\bar{X}, \bar{Z}_{\text{MC1}}, \bar{C}_{\text{MC1}}, \bar{D}] \\ & \left. + C_{L,xy}^{\hat{\phi}\hat{\phi}}[\bar{X}, \bar{Z}_{\text{MC1}}, \bar{C}, \bar{D}_{\text{MC1}}] - C_{L,xy}^{\hat{\phi}\hat{\phi}}[\bar{X}_{\text{MC1}}, \bar{Z}_{\text{MC2}}, \bar{C}_{\text{MC1}}, \bar{D}_{\text{MC2}}] \right\rangle_{\text{MC1, MC2}}. \quad (4.23) \end{aligned}$$

This estimate of the N0 is stable if the simulations have a covariance differing from reality up to linear order [236]. Thus, even if we didn't choose the correct cosmology as the fiducial for the lensing reconstruction, the realization-dependent procedure can correct the mismatch and accurately estimate the N0 bias.

The so-called N1 bias, $\Delta C_L^{\hat{\phi}\hat{\phi}} \Big|_{\text{N1}}$, represents the non-Gaussian secondary contractions (the other permutations in Eq. (4.20)) due to lensing [237]. In the flat-sky approximation in 2D Fourier space it is given by

$$\begin{aligned} \Delta C_{L,xy}^{\hat{\phi}\hat{\phi}} \Big|_{\text{N1}} = & \frac{1}{\mathcal{R}_L^{x\phi} \mathcal{R}_L^{y\phi}} \int \frac{d^2 \vec{\ell}_1}{(2\pi)^2} \int \frac{d^2 \vec{\ell}'_1}{(2\pi)^2} \left[C_{|\vec{\ell}_1 - \vec{\ell}'_1|}^{\phi\phi} \mathcal{W}^{XC}(-\vec{\ell}_1, \vec{\ell}'_1) \mathcal{W}^{ZD}(-\vec{\ell}_2, \vec{\ell}_2) \right. \\ & \left. + C_{|\vec{\ell}_1 - \vec{\ell}_2|}^{\phi\phi} \mathcal{W}^{XD}(-\vec{\ell}_1, \vec{\ell}_2) \mathcal{W}^{ZC}(-\vec{\ell}_2, \vec{\ell}_1) \right] F_{|\vec{\ell}_1|}^X F_{|\vec{\ell}_2|}^Z F_{|\vec{\ell}'_1|}^C F_{|\vec{\ell}_2|}^D W^x(\vec{\ell}_1, \vec{\ell}_2) W^y(\vec{\ell}'_1, \vec{\ell}_2), \quad (4.24) \end{aligned}$$

where $\vec{\ell}_1 + \vec{\ell}_2 = \vec{\ell}'_1 + \vec{\ell}_2 = \vec{L}$ and the flat-sky lensing weight functions can be found in [233]. This correction, unlike the realization dependent **N0** (RD**N0**) depends on the assumed fiducial cosmology and needs to be corrected when sampling the likelihood in parameter space.

4.2.3 Mock CMB lensing data vector and likelihood corrections

In this section we provide the details of an idealized CMB lensing reconstruction with the goal of producing a mock data vector for testing and validating purposes of the lensing likelihood. This reconstruction is in fact realistic enough to capture some effects that need to be taken into account at the likelihood level when comparing theoretical predictions against reconstructed CMB lensing power spectra. In particular, the expression given in Eq. (4.12) has to be modified as a consequence of the quadratic estimator of CMB lensing that will be used as data. Therefore, after discussing the lensing reconstruction we provide more details on the lensing likelihood and how to take this into account.

Starting from a fiducial Λ CDM cosmology, we compute the CMB power spectra $C_\ell|_{\text{fid}}$, from them we create CMB maps using `healpy`, we then lens the maps with the fiducial

4.2. CMB lensing mock pipeline

lensing potential employing `lenspyx`⁷. At this stage we are able to reconstruct the CMB lensing potential using the procedure described in the previous section with the `plancklens`⁸ code, which allows to estimate the CMB lensing potential starting from lensed maps (be them real or simulated), the noise of the observation and a set of primary CMB C_ℓ 's assumed as fiducials for the reconstruction. We use the noise models provided by the SO collaboration [228]⁹, since this will be the main CMB lensing dataset that will be used for the final 6×2 pt analysis of the *Euclid* mission. We consider a sky fraction $f_{\text{sky}} = 1$ in order to avoid having to deal with mean field subtraction and numerous simulations, since the goal is not a realistic reconstruction in itself, but rather the implementation in the likelihood of the debiasing terms, for which we need pre-computed inputs coming from the QE. Note that, to create and lens the CMB maps we use a set of fiducials $C_\ell|_{\text{fid}}$, but for the lensing reconstruction we assume a different set $C_\ell = 0.9C_\ell|_{\text{fid}}$, biasing therefore our assumed cosmology, like it would happen in a real reconstruction in which one doesn't know a priori what are the true underlying C_ℓ 's, but still needs to assume a set of fiducials in order to perform the reconstruction. As we said in the previous section, the mismatch is not a problem if one uses the realization dependent N0 to debias the QE of the lensing potential, as this procedure is insensitive to the assumed cosmology. This is confirmed by the results of the reconstruction presented in Fig. 4.5, where we show on the left panel the fiducial CMB lensing power spectrum we used to lens the maps in black, the reconstructed minimum variance estimator of the power spectrum in blue, and in red the sum of the fiducial with the N0, N1 terms: $C_L^{\phi\phi}|_{\text{fid}} + \Delta C_{L, \text{MV}}^{\hat{\phi}\hat{\phi}}|_{\text{N0}} + \Delta C_{L, \text{MV}}^{\hat{\phi}\hat{\phi}}|_{\text{N1}}$.

We can see that the latter agrees with the QE quite well, we have therefore reconstructed the CMB lensing power spectrum with the expected accuracy. We quantify the agreement by plotting the residual bias in the estimation of the $C_L^{\phi\phi}$ on the right panel of Fig. 4.5, compared with the expected error in the measurement of the CMB lensing assuming a Gaussian covariance with N0 noise. Our estimator is consistent with this 1σ Gaussian error.

At this point, we have a mock-data vector for the CMB lensing power spectrum, given by Eq. (4.22), similar to what we expect to estimate from the CMB maps of SO. However, in the quadratic estimator procedures we have encountered terms that depend on the assumed fiducial cosmology, such as the N1 bias term or the normalization of the power spectrum given by the response from Eq. (4.17). Unlike the N0 bias, to debias the estimator from these terms, they are computed in the fiducial cosmology and they are therefore reliable only in one point in parameter space. When sampling the likelihood, in principle we have to recompute these terms for each point of parameter space.

We provide more detail of our lensing likelihood here and how we take care of these terms. The likelihood for the convergence power spectrum is a Gaussian likelihood

$$-2 \log \mathcal{L}_\kappa = (\hat{C}_L^{\kappa\kappa} - C_L^{\kappa\kappa, \text{th}}) [\text{Cov}^{-1}] (\hat{C}_L^{\kappa\kappa} - C_L^{\kappa\kappa, \text{th}}). \quad (4.25)$$

The dependence on cosmological parameters enters in Eq. (4.25) through the theory

⁷<https://github.com/carronj/lenspyx>

⁸<https://github.com/carronj/plancklens>

⁹https://github.com/simonsobs/so_noise_models

4. Euclid-CMB cross-correlation likelihood

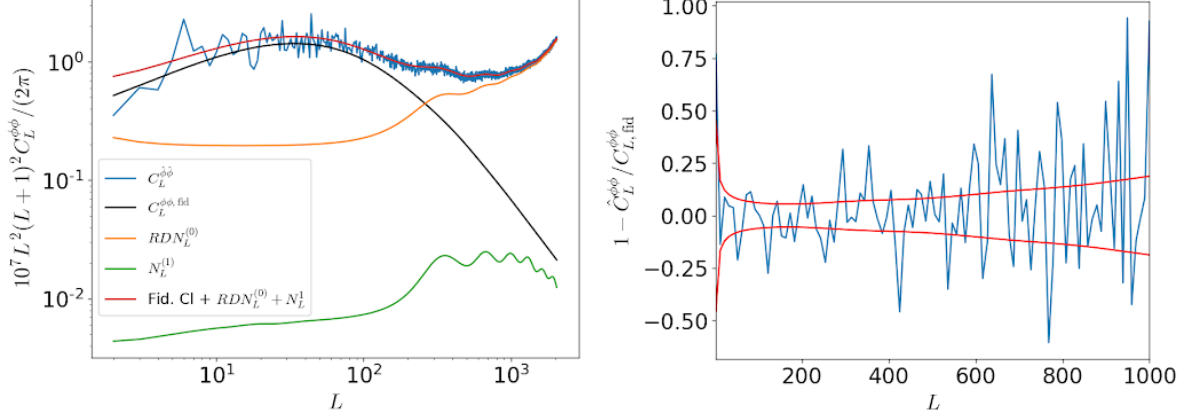


Figure 4.5: Left: results of our CMB lensing reconstruction, the blue line is the reconstructed power spectrum, which correctly fits the sum of the fiducial power spectrum (black) with the N0 (orange) and N1 (green) bias, shown in red. **Right:** Residual bias in the estimation of the power spectrum compared with the expected error in the measurement of the CMB lensing, assuming a Gaussian covariance with N0 noise.

spectrum at each point in parameter space, $C_L^{\kappa\kappa, \text{th}}$. In first approximation and without any corrections it is given by the expression (4.12) we validated in section 4.2.1. Thus, the likelihood depends on the cosmological parameters θ in the following ways:

- directly, through the theory spectrum $C_L^{\kappa\kappa} |_{\theta}$;
- indirectly (but linearly) on $C_L^{\kappa\kappa} |_{\theta}$, via the theory-dependence of N1 (Eq. 4.24);
- indirectly, and non-linearly, on the CMB power spectra C_ℓ^{TT} , C_ℓ^{TE} , and C_ℓ^{EE} through the estimator normalization and N1 (from the theory-dependent covariance response \mathcal{W} of Eq. 4.13).

So, for a given set of cosmological parameters θ , the theory power spectrum that we should calculate is given by

$$C_L^{\kappa\kappa, \text{th}} = \frac{(\mathcal{R}_L^{x\kappa} \mathcal{R}_L^{y\kappa}) |_{\theta}}{(\mathcal{R}_L^{x\kappa} \mathcal{R}_L^{y\kappa}) |_{\text{fid}}} C_L^{\kappa\kappa} |_{\theta} - \Delta C_{L,xy}^{\kappa\kappa} |_{\text{N1, fid}} + \Delta C_{L,xy}^{\kappa\kappa} |_{\text{N1, } \theta}. \quad (4.26)$$

Computing the above equation for each sampled point in parameter space would render an MCMC unfeasible due to the large computation time. Therefore, we choose apply an approximation for small deviations from the fiducial model, following Ref. [32, 234]. Expanding the CMB power spectrum dependence to linear order around the fiducial model one gets [234]

$$C_L^{\kappa\kappa, \text{th}} \approx C_L^{\kappa\kappa} |_{\theta} + \frac{d \ln(\mathcal{R}_L^{x\kappa} \mathcal{R}_L^{y\kappa})}{dC_{\ell'}^j} \left(C_{\ell'}^j |_{\theta} - C_{\ell'}^j |_{\text{fid}} \right) C_L^{\kappa\kappa} |_{\text{fid}} + M_{LL',xy}^{(1)\kappa} (C_{L'}^{\kappa\kappa} |_{\theta} - C_{L'}^{\kappa\kappa} |_{\text{fid}}) + \frac{d \Delta C_{L,xy}^{\kappa\kappa} |_{\text{N1}}}{dC_{\ell'}^j} \left(C_{\ell'}^j |_{\theta} - C_{\ell'}^j |_{\text{fid}} \right), \quad (4.27)$$

where j sums over the primary CMB power spectra. The matrix $M_{LL'}^{(1)\kappa}$ captures the linear dependence of N1 on the lensing potential for fixed CMB power spectra, while

4.3. Discussion and future perspectives

the other matrices give the dependence of the response and of the $N1$ on the primary CMB power spectra. These matrices, which are the computationally expensive part, are pre-computed for the fiducial model.

At present, the term involving the response of the quadratic estimator \mathcal{R} has been implemented in the likelihood and is under testing. We plan, in the near future, to pre-compute the matrices $M_{LL'}^{(1)\kappa}$ and $\frac{d\Delta C_{L,xy}^{\kappa\kappa}}{dC_{\ell'}^j}|_{N1}$ and implement the remaining terms, in order to have a likelihood ready to be used with a realistic data vector and deliver a working pipeline including CMB lensing for the first *Euclid* data release.

Additionally, the group in charge of simulations in the CMBX-SWG will provide numerical covariances and power spectra estimated from simulations, containing correlations between the CMB lensing field and the galaxy fields (GCp and WL). At that stage we will be able to completely test the likelihood with these more realistic products and assess the readiness for the upcoming analysis with real data.

In this context, it is important to point out that the non-Gaussian distribution of the density field creates a bias in the lensing reconstruction called $N_{3/2}$. This bias can be quite small for a CMB lensing only analysis, and in fact we have ignored it so far, but it could be necessary to take it into account for the cross-correlation with galaxy clustering and galaxy weak lensing [238]. We therefore plan to estimate how relevant such a term can be for a 6×2 pt analysis and eventually include it in our pipeline.

4.3 Discussion and future perspectives

We have presented in this chapter the validation of our CMB cross-correlation likelihood. In particular, we discussed the validation of the theoretical predictions for the cross-correlation between the the CMB temperature field and galaxy number counts, and for CMB lensing. Concerning the ISW effect we shown that the approximation introduced in the computation do not cause any significant bias in the analysis, while for CMB lensing, beside validating our code against **CAMB**, we have performed a quadratic estimator reconstruction with the goal of pre-computing the necessary quantities for the debiasing of the power spectrum in the likelihood. At the moment, we have implemented the correction for the normalization of the power spectrum, while the correction for the $N1$ bias is ongoing. On this note, current and future activities on the likelihood module are

- the inclusion of masks and their effects on covariances;
- test of the end-to-end pipeline with power spectra estimated from simulation;
- assessment of the relevance and eventual implementation of the $N_{3/2}$ bias for the cross-correlation between CMB lensing and galaxy probes.

We are therefore confident to complete the end-to-end pipeline and likelihood module to analyze the upcoming data of the first *Euclid* data release in 2025.

Chapter 5

Euclid-CMB cross-correlation forecasts in extended models

The first paper of the CMBX-SWG [204] forecasts the relevance of the combination and cross-correlation with CMB for *Euclid* in Λ CDM and its minimal extensions, we presented some of the results in section 3.3. One of the messages of this work concerns the increased impact of the cross correlation in models with more parameters than Λ CDM, as it was also shown in [217]. For this reason the group is currently working on extending the forecasts to modified gravity models, neutrino masses and primordial non Gaussianity, also with more updated and realistic specifications.

In this chapter we discuss some of the preliminary results assessing the constraining power of CMB cross-correlations in the simplest scalar-tensor theories of gravity, with the addition of the sum of the neutrino masses as a free parameter. We first emphasize the role of CMB lensing in complementing the photometric galaxy clustering and galaxy weak lensing of the *Euclid* survey, highlighting in this way the information that can be obtained through LSS probes alone, without considering the CMB primaries; and then discuss a full CMB-*Euclid* joint analysis which will provide the most constraining results.

Since this work follows on the efforts of the CMBX-SWG group in Ref. [204], we use the same methodology and Fisher code developed for those forecasts: SFX_CLASS [204]. In order to produce the results presented in this chapter, I have extended this code and integrated it with the dedicated Einstein-Boltzmann code for scalar-tensor theories CLASSig [98], that we use to compute the observables.

Some of the results contained in this chapter will be published in a key project paper of the CMBX-SWG.

5.1 Fisher forecast formalism

We use the Fisher matrix formalism [239] to forecast uncertainties of cosmological parameters when combining *Euclid* with several CMB experiments. In the Fisher formalism, the likelihood \mathcal{L} is assumed to be a multivariate Gaussian and the Fisher matrix \mathcal{F} is defined as:

$$\mathcal{F}_{\alpha\beta} = \left\langle \frac{\partial^2 \mathcal{L}}{\partial \theta_\alpha \partial \theta_\beta} \right\rangle = \frac{1}{2} \text{Tr} \left[\frac{\partial \mathcal{C}}{\partial \theta_\alpha} \mathcal{C}^{-1} \frac{\partial \mathcal{C}}{\partial \theta_\beta} \mathcal{C}^{-1} \right], \quad (5.1)$$

where the average is over observational data, \mathcal{C} is the theoretical covariance matrix and $\theta_\alpha, \theta_\beta$ are the cosmological parameters. By taking into account that the number of modes

5. Euclid-CMB cross-correlation forecasts in extended models

is $(2\ell + 1)f_{\text{sky}}/2$, Eq. (5.1) becomes

$$\mathcal{F}_{\alpha\beta} = \sum_{\ell_{\min}}^{\ell_{\max}} \sum_{abcd} \frac{2\ell + 1}{2} f_{\text{sky}}^{abcd} \frac{\partial C_{\ell}^{ab}}{\partial \theta_{\alpha}} (\mathcal{C}^{-1})^{bc} \frac{\partial C_{\ell}^{cd}}{\partial \theta_{\beta}} (\mathcal{C}^{-1})^{da}, \quad (5.2)$$

where $abcd \in \{T, E, \kappa, G_1, \dots, G_N, \text{WL}_1, \dots, \text{WL}_N\}$, and $f_{\text{sky}}^{abcd} \equiv \sqrt{f_{\text{sky}}^{ab} f_{\text{sky}}^{cd}}$ is the effective sky fraction for each pair of probes. The theoretical covariance matrix \mathcal{C} is defined as

$$\mathcal{C} = \begin{bmatrix} \bar{C}_{\ell}^{TT} & C_{\ell}^{TE} & C_{\ell}^{T\kappa} & C_{\ell}^{TG_1} & \dots & C_{\ell}^{TG_N} & C_{\ell}^{T\text{WL}_1} & \dots & C_{\ell}^{T\text{WL}_N} \\ C_{\ell}^{TE} & \bar{C}_{\ell}^{EE} & C_{\ell}^{E\kappa} & C_{\ell}^{EG_1} & \dots & C_{\ell}^{EG_N} & C_{\ell}^{E\text{WL}_1} & \dots & C_{\ell}^{E\text{WL}_N} \\ C_{\ell}^{T\kappa} & C_{\ell}^{E\kappa} & \bar{C}_{\ell}^{\kappa\kappa} & C_{\ell}^{\kappa G_1} & \dots & C_{\ell}^{\kappa G_N} & C_{\ell}^{\kappa \text{WL}_1} & \dots & C_{\ell}^{\kappa \text{WL}_N} \\ C_{\ell}^{TG_1} & C_{\ell}^{EG_1} & C_{\ell}^{\kappa G_1} & \bar{C}_{\ell}^{G_1 G_1} & \dots & C_{\ell}^{G_1 G_N} & C_{\ell}^{G_1 \text{WL}_1} & \dots & C_{\ell}^{G_1 \text{WL}_N} \\ \vdots & \vdots & \vdots & \vdots & \ddots & \vdots & \vdots & \ddots & \vdots \\ C_{\ell}^{TG_N} & C_{\ell}^{EG_N} & C_{\ell}^{\kappa G_N} & C_{\ell}^{G_1 G_N} & \dots & \bar{C}_{\ell}^{G_N G_N} & C_{\ell}^{G_N \text{WL}_1} & \dots & C_{\ell}^{G_N \text{WL}_N} \\ C_{\ell}^{T\text{WL}_1} & C_{\ell}^{E\text{WL}_1} & C_{\ell}^{\kappa \text{WL}_1} & C_{\ell}^{G_1 \text{WL}_1} & \dots & C_{\ell}^{G_N \text{WL}_1} & \bar{C}_{\ell}^{\text{WL}_1 \text{WL}_1} & \dots & C_{\ell}^{\text{WL}_1 \text{WL}_N} \\ \vdots & \vdots & \vdots & \vdots & \ddots & \vdots & \vdots & \ddots & \vdots \\ C_{\ell}^{T\text{WL}_N} & C_{\ell}^{E\text{WL}_N} & C_{\ell}^{\kappa \text{WL}_N} & C_{\ell}^{G_1 \text{WL}_N} & \dots & C_{\ell}^{G_N \text{WL}_N} & C_{\ell}^{\text{WL}_1 \text{WL}_N} & \dots & \bar{C}_{\ell}^{\text{WL}_N \text{WL}_N} \end{bmatrix}. \quad (5.3)$$

The expected minimum uncertainties on the cosmological parameters are given by the diagonal of the inverse of the Fisher matrix as

$$\sigma_{\alpha} \geq \sqrt{(\mathcal{F}^{-1})_{\alpha\alpha}}. \quad (5.4)$$

where we have marginalized on all the remaining parameters.

The so-called figure of merit (FoM) quantifies the capability of constraining two parameters (α, β) , it is given by [240]

$$\text{FoM}_{\alpha,\beta} = \frac{1}{\sqrt{\det(\mathcal{F}_{\alpha,\beta}^{-1})}}, \quad (5.5)$$

where $\mathcal{F}_{\alpha,\beta}^{-1}$ is the 2x2 covariance matrix of the two parameters, hence we have marginalized on all but two parameters by selecting the rows and columns of the two parameters of interest in the covariance matrix. In general, it is possible to define the FoM for N parameters [172, 241]:

$$\text{FoM}_{\alpha_i} = \left[\frac{1}{\det(\mathcal{F}_{\alpha_i}^{-1})} \right]^{1/N}, \quad (5.6)$$

where $\mathcal{F}_{\alpha_i}^{-1}$ is the $N \times N$ covariance corresponding to the considered parameters. We use the latter to quantify the reduction in parameter space volume, both for cosmological and nuisance parameters, obtained by combining CMB observables with *Euclid* galaxy probes.

5.2 Specifications for *Euclid* and CMB experiments

5.2.1 *Euclid*

For the Euclid-like photometric survey (hereafter *Euclid*-ph-like or more simply Eph) we use several different specifications in order to assess the relevance of the tomography and of the shot-noise in our forecasts. We consider the redshift distributions described in section 3.2.2 and given by Eqs. (3.14), (3.15) and (3.17) with the photometric nuisance parameters fixed at the values provided in Table 3.1, for 5 and 10 equi-populated redshift bins whose edges are given by

$$z_i = \{0.0010, 0.56, 0.79, 1.02, 1.32, 2.50\}, \quad (5.7)$$

$$z_i = \{0.0010, 0.42, 0.56, 0.68, 0.79, 0.90, 1.02, 1.15, 1.32, 1.58, 2.50\}. \quad (5.8)$$

We refer to these specifications as IST:F-like. Note that the 5 bins case is different from the one studied in Ref. [197]. In this scenario, the shot-noise is given by Eq. (3.32) with $\bar{n}_g = 30$ galaxies/arcmin², but for the 10 bins case we additionally study the effect of doubling the shot-noise, which corresponds to $\bar{n}_g = 15$ galaxies/arcmin². In the IST:F-like specifications we adopt a constant galaxy bias in a given redshift bin, with fiducial values $b_i = \sqrt{1 + z_i}$, where z_i is the central redshift of the i th bin. The resulting bias parameters b_i are part of the Fisher analysis, where they are considered as nuisance parameters.

In addition to the IST:F-like specifications, we also consider the numerical redshift distributions shown in the bottom right panel of Fig. 3.8, extracted from the Flagship 2 mock galaxy catalogue. It comprises 13 equi-populated redshift bins with the following bin edges

$$z_i = \{0.2, 0.31, 0.41, 0.49, 0.62, 0.68, 0.76, 0.85, 0.94, 1.05, 1.19, 1.41, 1.68, 2.5\}, \quad (5.9)$$

and total surface density of galaxies $\bar{n}_g = 24.3$ galaxies/arcmin². In this scenario the galaxy bias is measured in each redshift bin from the simulation and fitted with the following polynomial

$$b(z) = b_0 + b_1 z + b_2 z^2 + b_3 z^3, \quad (5.10)$$

where the coefficients are $b_0 = 0.83$, $b_1 = 1.19$, $b_2 = -0.93$, $b_3 = 0.42$; these are the fiducial values we consider for these parameters. The galaxy bias as a function of z in the different cases is shown in Fig. 5.1.

In addition to the galaxy biases, we have three more nuisance parameters describing the intrinsic alignment, introduced in section 3.2.2: \mathcal{A}_{IA} , η_{IA} and β_{IA} , which are, respectively, the amplitude, the redshift dependence and the dependence on the galaxy luminosity of the IA.

The observables considered are photometric galaxy clustering, weak lensing and their cross-correlation, as described in section 3.2.2, in the following baseline multipole ranges: $10 < \ell_{\text{GC}} < 750$, $10 < \ell_{\text{WL}} < 1500$, which corresponds to the so-called pessimistic scenario of Ref. [197]. The multipoles for all the cross-correlations start at the minimum

5. Euclid-CMB cross-correlation forecasts in extended models

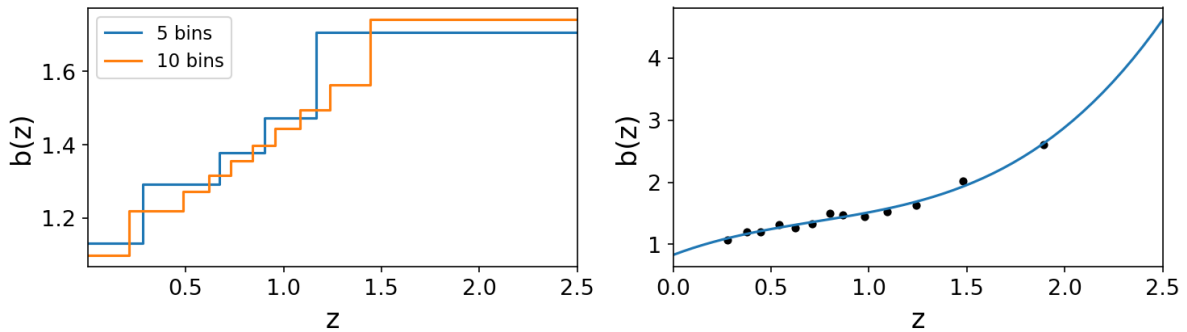


Figure 5.1: Galaxy bias adopted for the different binning schemes: stepwise for 5 and 10 bins for the IST:F-like specifications in the left panel, polynomial fit (blue) for the galaxy bias measured from Flagship 2 (black dots) in the right panel.

common multipole between the two probes considered ($\ell_{\text{GC}}^{\text{min}} = \ell_{\text{WL}}^{\text{min}} = 10$), as in Ref. [197], where the most conservative ranges were used.

In all the cases discussed above, we adopt the sky fraction for the full survey, corresponding to an area of $14\,700 \text{ deg}^2$ ($f_{\text{sky}} \simeq 0.36$).

5.2.2 CMB surveys

For CMB experiments, we consider Planck-like synthetic data reproducing the *Planck* 2018 results for the Λ CDM model [1], the ground-based future experiments Simons Observatory and CMB Stage-4.

We consider the power spectra C_ℓ^{TT} , C_ℓ^{EE} , C_ℓ^{TE} as signal for temperature, polarization and temperature-polarization cross-correlation, respectively. We adopt isotropic noise deconvolved with the instrument beam as given in Eq. (3.33) and generalized here for polarization as well

$$N_\ell^{\text{XX}} = (\Delta X)^2 b_\ell^{-2}, \quad b_\ell = \exp\left(-\frac{1}{2}\ell(\ell+1)\frac{\theta_{\text{FWHM}}^2}{8 \ln 2}\right), \quad (5.11)$$

where $X = T, E$ and all the quantities entering the above equation have been described in section 3.3.3. We neglect the noise for the cross-correlation between CMB signals.

For CMB lensing, starting from the noise in temperature and polarization for SO and S4, we employ the reconstructed minimum-variance estimator for $N_\ell^{\kappa\kappa}$ [230] of Ref. [204], which corresponds to the N0 bias. For the *Planck* mission, we use instead the latest PR4 data maps and lensing reconstruction [221] with associated noise. In Fig. 5.2 we show the CMB lensing power spectrum with the associated noises just described, we also present in the other panels the TT and EE power spectrum and related noises for the different experiments.

Planck

The entire data processing pipelines, including foreground contamination, systematics and other uncertainties cannot be represented in our Fisher formalism. Therefore, to

5.2. Specifications for Euclid and CMB experiments

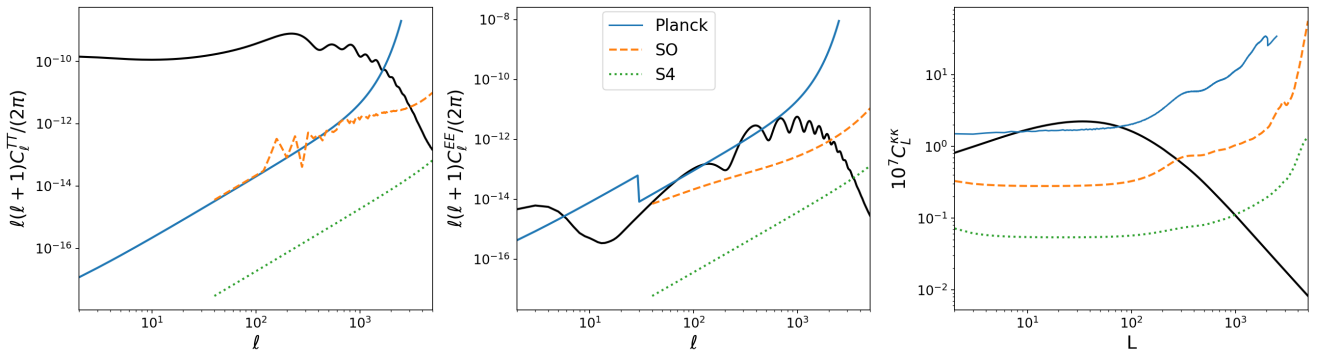


Figure 5.2: Noise power spectra used to reproduce the CMB experiments considered: *Planck* (blue), SO (dashed orange) and CMB-S4 (dotted green). Left, middle and right panels corresponds to temperature, polarization and CMB lensing.

reproduce a realistic *Planck*-like experiment, we choose our specifications as in Ref. [204, 217] to match the *Planck* 2018 results for the Λ CDM model with the Fisher formalism. We use only the 143 GHz channel of the HFI instrument [242] with $\Delta T = 33 \mu\text{K}^2 \text{ arcmin}^2$, $\Delta E = 70.2 \mu\text{K}^2 \text{ arcmin}^2$ and $\theta_{\text{FWHM}} = 7$, and as in Ref. [217] we inflate the noise in polarization by a factor of eight for $\ell < 30$. This is visible in the blue line in the central panel of Fig. 5.2. Moreover, we consider a sky fraction $f_{\text{sky}} = 0.7$ and a maximum multipole $\ell_{\text{max}} = 1500$ for TT, TE, EE, while for CMB lensing we adopt the conservative range $8 < L < 400$.

Simons Observatory

The Simons Observatory is a set of ground-based telescopes located in the Chilean Andes, which will begin observations in the early 2024. The initial configuration of SO will have three small-aperture 0.5-m telescopes (SATs) and one large-aperture 6-m telescope (LAT). The detector count, both on SATs and LAT, will double in 2028. It will cover a fraction of the sky of about $f_{\text{sky}} = 0.4$ over the frequency range from 27 to 280 GHz, with beam FWHM between 0.9 and 7.4 arcmin over six frequency bands in the range from 27 through 280 GHz. Over the six bands, the temperature sensitivity are expected to be from 71 to 54 $\mu\text{K arcmin}$, with the goal of reaching a factor of $\sqrt{2}$ better [228]. For the noise in temperature and polarization we use the publicly available noise curves provided by the SO collaboration in [228]¹.

We consider the multipole range $40 \leq \ell \leq 3000$ for TT and TE, $40 \leq \ell \leq 5000$ for EE, and $2 \leq \ell \leq 3000$ for $\kappa\kappa$ and $T\kappa$. In order to retain the information at the largest scales add the *Planck*-like specifications as described above for $2 \leq \ell \leq 39$ with $f_{\text{sky}} = 0.7$ in temperature and polarization. We note that even though the SO sky fraction is only 40%, it is possible to measure CMB lensing at low multipoles due to the lensing reconstruction from high-order T and E correlations on small angles, to which all scales of the lensing signal contribute and can thus be inferred.

¹github.com/simonsobs/so_noise_models.

CMB stage 4

CMB stage-4 refers to the next generation ground-based CMB experiment with telescopes in Antarctica and Atacama, it will follow the SO and it is scheduled to take data from 2027. Similarly to SO it will cover 40% of the sky, and for the noise we use $\Delta T = 1 \mu\text{K arcmin}$, $\Delta E = \sqrt{2} \mu\text{K arcmin}$ and $\theta_{\text{FWHM}} = 1 \mu\text{K arcmin}$. For the minimum multipole in temperature and polarization we consider $\ell_{\text{min}} = 40$, and as previously discussed for SO we add the large scale information from *Planck*. CMB-S4 is expected to collect data up to $\ell_{\text{max}} = 3000$ in temperature and $\ell_{\text{max}} = 5000$ in polarization, these are the values we use. The lensing power spectrum will be reconstructed from $2 \leq \ell \leq 3000$, and its noise curve is taken as the so-called *N0* bias, from [204] where it was computed using the `quicklens`² code.

5.3 Models

Here we discuss the models and the fiducials we consider for our Fisher analysis. Since [204] studied the ΛCDM and its minimal extensions (w_0w_a and curvature), we wish to go beyond that, incorporating in our forecasts some of the modified gravity models presented in chapter 2 and assessing the constraining power of the joint analysis of *Euclid* and CMB experiments on these extensions of GR. Furthermore, we also consider the sum of neutrino masses m_ν as an additional parameter.

We select two of the simplest STTs: Induced Gravity (see Eq. (2.4)) and Non Minimal Coupling (see Eq. (2.5)). IG has one extra parameter, ξ , with respect to ΛCDM , which modulates the coupling between the scalar field and the Ricci constant in the Lagrangian. For the potential in IG we consider here a cosmological constant $V(\sigma) = \Lambda$. For NMC we employ its flavour with the additional parameter Δ , which allows for an imbalance between the effective gravitational constant G_{eff} between two test masses, and Newton's constant G_{N} : $G_{\text{eff}}(z=0) = G_{\text{N}}(1 + \Delta)^2$, while $N_{\text{Pl}} = M_{\text{Pl}}$ is kept fixed. In this model we have therefore two extra parameters with respect to ΛCDM : ξ and Δ , and we take as fiducials for $\xi = 10^{-3}$ and $\Delta = -0.01$ (since ξ is positive this model is what was called NMC+ in chapter 2). For NMC+ we consider the massless theory $V(\sigma) \propto F^2(\sigma)$. Both models are studied with a canonical sign of the kinetic term.

Concerning the other cosmological parameters, our primary density parameters are Ω_{m} and Ω_{b} , therefore, when varying the neutrino mass, we shift the value of Ω_{cdm} by the corresponding amount in order to keep Ω_{m} fixed to its fiducial value. The fiducial values of the cosmological parameters considered in the analysis are summarized in Table 5.1. Note that we have a different value for σ_8 in the two models, this is because we choose to use the same amplitude of the primordial power spectrum $A_{\text{s}} = 2.13 \times 10^{-9}$ for both models, and consequently the derived value of σ_8 differs.

²<https://github.com/dhanson/quicklens>

5.4. Results

$\Omega_{b,0}$	$\Omega_{m,0}$	h	n_s	σ_8	τ	$m_\nu[\text{eV}]$	ξ	Δ
0.05	0.32	0.67	0.96	0.819 (NMC)	0.058	0.06	10^{-3} (NMC)	-0.01
				0.816 (IG)			10^{-5} (IG)	

Table 5.1: Fiducial values of the cosmological parameters considered.

5.4 Results

In this section we present the forecasted constraints on cosmological parameters from the combination of the *Euclid*-like photometric survey and the CMB experiments described in section 5.2 on the IG and NMC+ models. In order to quantify the relevance of including the CMB cross-correlation, we compare the forecasted uncertainties obtained using *Euclid* alone to those obtained by combining *Euclid* with CMB probes.

Recently, a $6 \times 2\text{pt}$ analysis was carried out with real data by the DES collaboration with CMB lensing from *Planck* and SPT [214–216], showing that in addition to the improvement in constraining power, this cross-correlation analysis was crucial in checking for inconsistencies between the datasets and was a powerful consistency test for the results of each experiment. Therefore, we first put some emphasis on the impact of $6 \times 2\text{pt}$ analysis when varying the specifications of *Euclid*, and at the end of the section we discuss the combination of all the CMB probes with *Euclid* in order to forecast the maximum constraining power.

5.4.1 Baseline results with IST:F-like specifications

Our baseline for IST:F-like specifications is described in section 5.2.1, it corresponds to 10 equipopulated redshift bins with a total galaxy number density $n_g = 30$ galaxies/arcmin² and one galaxy bias nuisance parameter for each bin. The results for these specifications combined with the CMB lensing of the experiments discussed in section 5.2.2 are shown in Fig. 5.3 and Table 5.2. The figure highlights the gradual improvement due to the $6 \times 2\text{pt}$ analysis with respect to *Euclid*-ph alone when considering more powerful CMB surveys, going from *Planck*-like to SO and S4. The table presents the ratio of marginalised 1σ uncertainties over their corresponding fiducial values of the cosmological parameters for the *Euclid* $3 \times 2\text{pt}$ analysis. The subsequent rows show the improvement on these errors with the inclusion of CMB lensing, quantified by the ratio $\sigma_{3 \times 2} / \sigma_{6 \times 2}$, with larger values meaning larger improvements (smaller error bars for the $6 \times 2\text{pt}$). The combination with *Planck* improves the constraints on the modified gravity parameters by ξ and Δ by 10%, for a total improvement in the FoM (5.6) of the cosmological (nuisance) parameters of 5% (4%). Larger improvements on these parameters are expected for combinations with future surveys, with a 20% increase in precision for the joint analysis with SO and 50%-60% with S4. In general, the improvements are maximum for the parameters characterizing the extended model. For S4, also the predictions on the sum of neutrino masses and σ_8 are improved by a factor 1.4 and 1.6, respectively, showing that the cross-correlation can help constraining fluctuations amplitudes. The percentage improvement

5. Euclid-CMB cross-correlation forecasts in extended models

in the total FoM for the cosmological parameters is of 14% (35%) for SO (S4). Because *Euclid* observables alone and their combination with CMB lensing cannot constrain the optical depth at reionization τ_{reio} , this parameter is absent from those tables and plots.

These are our baseline results with *Euclid* IST:F-like specifications, in the next sections we assess the impact of changing some of them separately, namely the number of bins and the shot-noise.

		$\Omega_{\text{m},0}$	$\Omega_{\text{b},0}$	h	n_{s}	σ_8	$m_{\nu}[\text{eV}]$	ξ	Δ
<i>Euclid</i> -ph	$\sigma_{3 \times 2}/\theta$	0.0070	0.069	0.12	0.045	0.051	2.6	100	11
Eph \otimes <i>Planck</i>	$\sigma_{3 \times 2}/\sigma_{6 \times 2}$	1.0	1.0	1.0	1.0	1.1	1.0	1.1	1.1
Eph \otimes SO	$\sigma_{3 \times 2}/\sigma_{6 \times 2}$	1.1	1.0	1.1	1.1	1.2	1.1	1.2	1.2
Eph \otimes S4	$\sigma_{3 \times 2}/\sigma_{6 \times 2}$	1.2	1.1	1.4	1.2	1.6	1.4	1.5	1.6

	Eph \otimes <i>Planck</i>	Eph \otimes SO	Eph \otimes S4
%FoM(cosmo)	5	14	35
%FoM(nuisance)	4	10	19

Table 5.2: First row: ratio of marginalised 1σ uncertainties over their corresponding fiducial values in NMC+ for ***Euclid*-ph (IST:F-like with 10 redshift bins)**. Other rows show the ratio of the 1σ forecasted errors between the 3×2 pt and 6×2 pt. Also quoted the percentage improvement in the FoM (5.6) of the cosmological and nuisance parameters.

5.4.2 Impact of number bins

In this section we consider a *Euclid*-like photometric survey with a reduced number of bins, going from the 10 of our baseline to 5, but keeping the galaxy surface density the same as the baseline ($\bar{n}_g = 30$ galaxies/arcmin²) in order to isolate the impact of tomography on *Euclid* and on the cross-correlation. Reducing the number of bins slightly worsens the constraints for *Euclid*-alone, rendering probe combination more relevant and the 6×2 pt more stringent with respect to the 3×2 pt. The parameters more affected by the smaller number of bins are Ω_{b} and h , as the constraining power of *Euclid*-alone in this settings is reduced by 36 and 32% for them. As a consequence, the CMB lensing has a larger impact than it had in the baseline scenario, indeed, in that case the *Planck* CMB lensing did not play a significant role in reducing the error on the measured value of the Hubble constant, while here it provides an improvement of 10%. The predicted constraints on h are improved with respect to the 3×2 pt by a factor 1.1, 1.2 and 1.6 respectively, when combining Euclid with *Planck*, SO, and S4 (see Table 5.3). As in the previous case, the parameters most affected by the cross-correlation with CMB lensing are the modified gravity parameters ξ and Δ , followed by σ_8 and m_{ν} . For this reason we show graphically the impact of the joint analysis in Fig. 5.4 as a rectangle plot in the plane Δ - θ_i where θ_i are cosmological and nuisance parameters. The figure highlights the fact

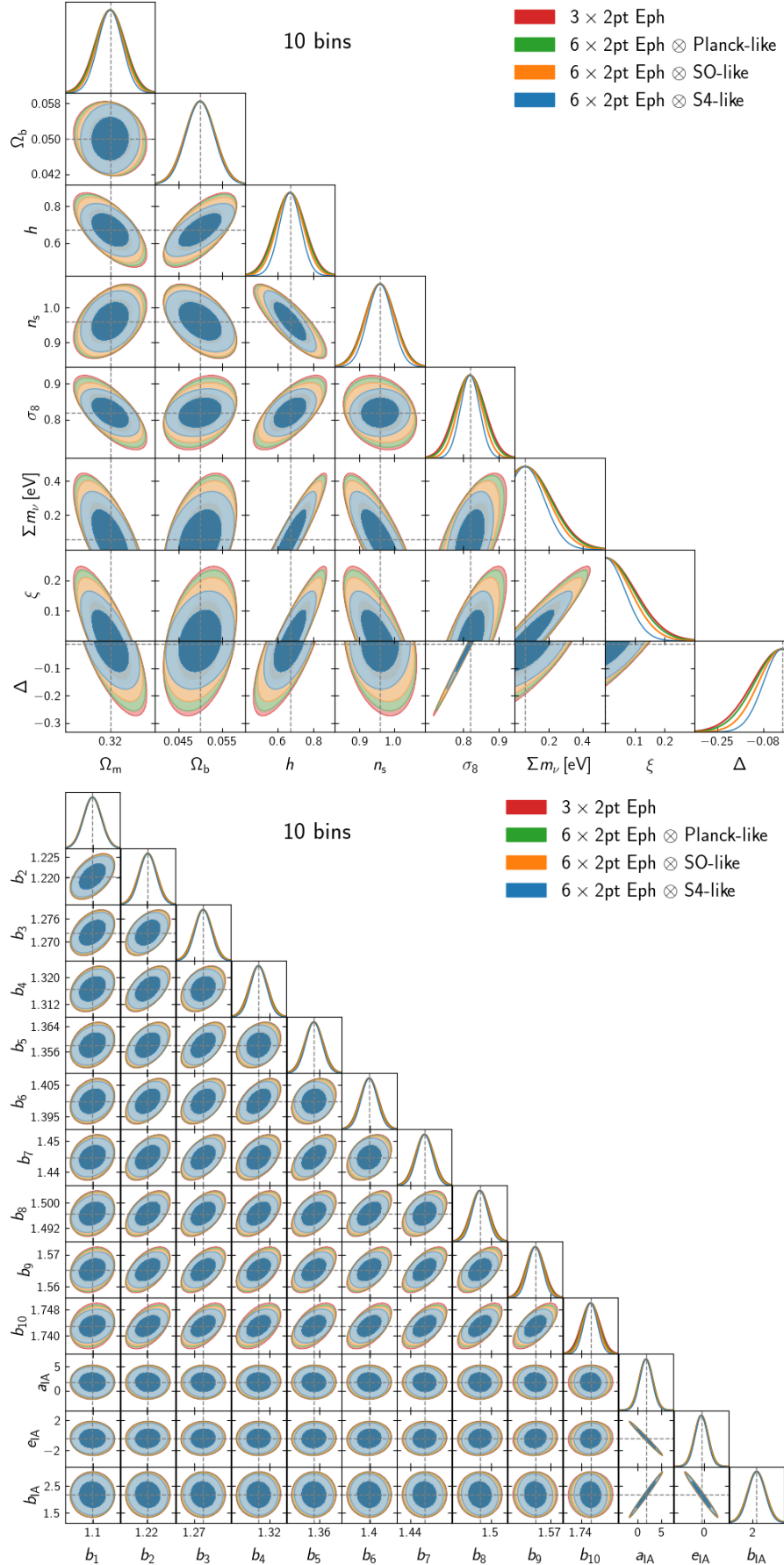


Figure 5.3: Marginalized 68% and 95% 2D confidence regions for the joint constraints on the cosmological (top) and nuisance (bottom) parameters in **NMC+** for a **Euclid-ph-like** survey (**IST:F-like with 10 bins**) (red), combined with the CMB lensing from **Planck** (green), **SO** (orange), **S4** (blue).

5. Euclid-CMB cross-correlation forecasts in extended models

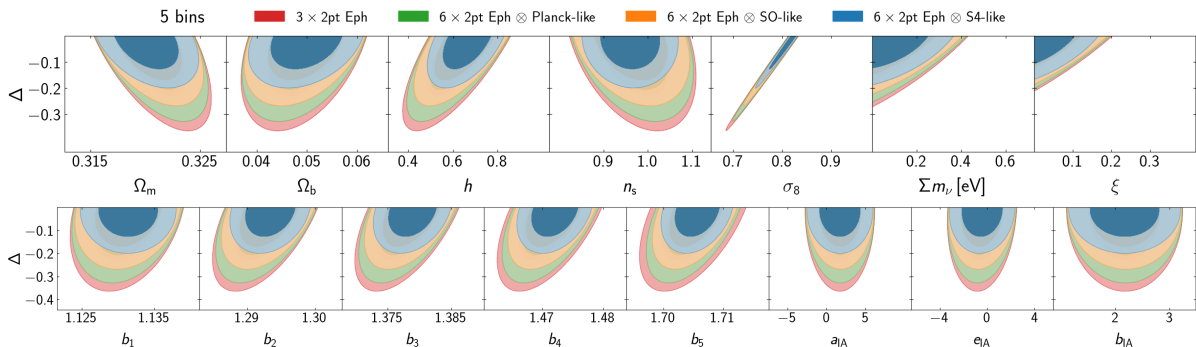


Figure 5.4: Marginalized 68% and 95% 2D confidence regions for the joint constraints on the cosmological and nuisance parameters in the plane with the NMC+ parameter Δ , for a ***Euclid-ph-like* survey (IST:F-like with 5 bins)** (red) combined with the CMB lensing from **Planck** (green), **SO** (orange), **S4** (blue).

that the $6 \times 2\text{pt}$ also improves the constraints on the galaxy biases and IA parameters, in this case through the increased precision on the error on Δ . The reduction of parameter space volume for the cosmological parameters that we quantify with the FoM (5.6), is more prominent in this scenario, going from the 5% of the baseline case to 7% for the combination with *Planck* CMB lensing. For the upcoming SO we obtain a percentage improvement of 20% and 52% for S4.

		$\Omega_{m,0}$	$\Omega_{b,0}$	h	n_s	σ_8	$m_\nu[\text{eV}]$	ξ	Δ
<i>Euclid-ph</i>	$\sigma_{3 \times 2} / \theta$	0.0077	0.11	0.18	0.063	0.067	3.7	140	14
Eph \otimes <i>Planck</i>	$\sigma_{3 \times 2} / \sigma_{6 \times 2}$	1.1	1.0	1.1	1.0	1.1	1.1	1.1	1.1
Eph \otimes SO	$\sigma_{3 \times 2} / \sigma_{6 \times 2}$	1.1	1.0	1.2	1.1	1.4	1.2	1.3	1.4
Eph \otimes S4	$\sigma_{3 \times 2} / \sigma_{6 \times 2}$	1.2	1.1	1.6	1.4	1.8	1.6	1.8	1.9

	Eph \otimes <i>Planck</i>	Eph \otimes SO	Eph \otimes S4
%FoM(cosmo)	7	20	52
%FoM(nuisance)	10	20	39

Table 5.3: First row: ratio of marginalised 1σ uncertainties over their corresponding fiducial values in NMC+ for ***Euclid-ph* (IST:F-like with 5 redshift bins)**. Other rows show the ratio of the 1σ forecasted errors between the $3 \times 2\text{pt}$ and $6 \times 2\text{pt}$. Also quoted the percentage improvement in the FoM (5.6) of the cosmological and nuisance parameters.

5.4.3 Impact of shot-noise

In this section we consider a *Euclid*-like photometric survey with IST:F-like specifications, using 10 redshift bins but doubling the shot-noise, which corresponds to take the

5.4. Results

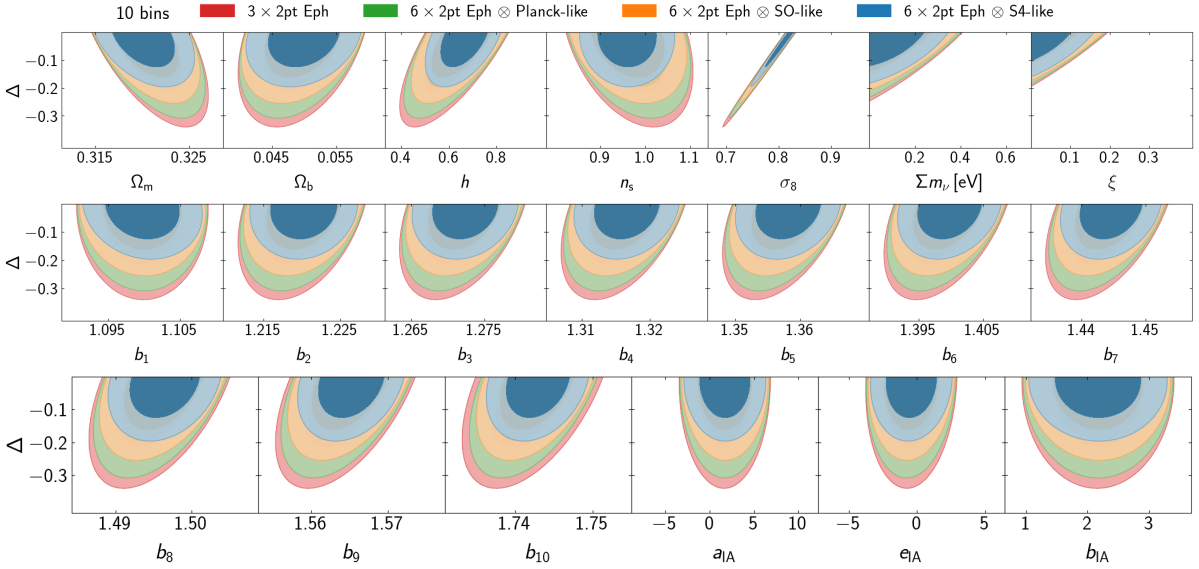


Figure 5.5: Marginalized 68% and 95% 2D confidence regions for the joint constraints on the cosmological and nuisance parameters in the plane with the NMC+ parameter Δ , for a *Euclid*-ph-like survey (IST:F-like with 10 bins and doubled shot-noise wrt baseline) (red) combined with the CMB lensing from *Planck* (green), SO (orange), S4 (blue)

surface galaxy density as $\bar{n}_g = 15$ galaxies/arcmin², isolating therefore the impact of the shot-noise on our analysis.

On the cosmological parameters, the effect of doubling the shot-noise is similar to halving the number of bins, as it can be seen by comparing the first row of Table 5.4 with Table 5.3. The only exception is Ω_b , as the constraining power of the 3×2 pt analysis dropped by 36% with respect to baseline in the 5 bins scenario, while in this case we see a reduction of only 18%. The fact that our results are similar to the previous section, where the survey was considered with 5 bins, shows the importance of tomography: it is possible to have comparable or better constraints even with twice the shot-noise by increasing the number of bins. However, we see a non negligible impact of the combination with *Planck* CMB lensing, especially on the modified gravity parameters, as it can be seen also from Fig. 5.5, where we present the 2D confidence regions for the cosmological and nuisance parameters in the plane with Δ . As before, we can almost double the constraining power on ξ and Δ for the combination with S4, while for SO we get, respectively, a factor of 1.3, and 1.4 improvement on these parameters. Also the constraints on the sum of neutrino masses and σ_8 are tighter when CMB lensing is included in the analysis. These results are summarized by the percentage improvement on the FoM of the cosmological and nuisance parameters in Table 5.4, with an increase of %FoM(cosmo) of 6%, 17% and 46% when combining *Euclid*-ph probes with CMB lensing in a 6×2 pt analysis with *Planck*, SO and S4.

5. Euclid-CMB cross-correlation forecasts in extended models

		$\Omega_{m,0}$	$\Omega_{b,0}$	h	n_s	σ_8	$m_\nu[\text{eV}]$	ξ	Δ
<i>Euclid</i> -ph	$\sigma_{3\times 2}/\theta$	0.0089	0.085	0.17	0.062	0.063	3.6	140	13
Eph \otimes <i>Planck</i>	$\sigma_{3\times 2}/\sigma_{6\times 2}$	1.1	1.0	1.1	1.0	1.1	1.1	1.1	1.1
Eph \otimes SO	$\sigma_{3\times 2}/\sigma_{6\times 2}$	1.1	1.0	1.2	1.1	1.3	1.2	1.3	1.3
Eph \otimes S4	$\sigma_{3\times 2}/\sigma_{6\times 2}$	1.3	1.1	1.6	1.4	1.7	1.6	1.8	1.8

	Eph \otimes <i>Planck</i>	Eph \otimes SO	Eph \otimes S4
%FoM(cosmo)	6	17	46
%FoM(nuisance)	5	12	22

Table 5.4: First row: ratio of marginalised 1σ uncertainties over their corresponding fiducial values in NMC+ for *Euclid*-ph (IST:F-like with 10 redshift bins but double shot-noise wrt baseline). Other rows show the ratio of the 1σ forecasted errors between the 3×2 pt and 6×2 pt. Also quoted the percentage improvement in the FoM (5.6) of the cosmological and nuisance parameters.

5.4.4 Baseline results with Flagship 2 specifications

In this section we turn our attention to the combination of *Euclid* with CMB experiments by considering the Flagship 2 specifications for *Euclid* described in section 5.2.1. In this scenario the galaxy bias is parameterized by the polynomial function (5.10), reducing therefore the numbers of nuisance bias parameters to four. The shot-noise is also increased with respect to the IST:F-like baseline, because the surface density of galaxy measured from the Flagship 2 mock catalogue is $\bar{n}_g = 24.3$ galaxies/arcmin². This is compensated by the larger number of redshift bins: 13.

Fig. 5.6 shows in red the 2D confidence regions for the cosmological parameters in the 3×2 pt analysis with these settings. On the left panel the results are for the IG model, while on the right for NMC+. The other colors show the gradual improvement with respect to *Euclid*-alone from the combination with CMB lensing. The improvement is larger for NMC+ with respect to IG, highlighting the fact that the cross-correlation is more relevant for models with a larger number of parameters. Indeed, in IG, the inclusion of *Planck* lensing is marginal with respect to *Euclid* alone, while more advanced future surveys that will better characterize CMB lensing are still able to contribute to the constraints on cosmological parameters, especially on Ω_m , σ_8 , and m_ν . In IG, the percentage improvement on the FoM for the cosmological parameter is 6% for SO and 20% for S4.

For NMC+ the results are qualitatively similar to the baseline with IST:F-like specifications, with the parameter Δ being the most sensitive to the cross-correlations: already in the 6×2 pt with *Planck* we see an improvement by a factor 1.1 in the precision of the forecasted 1σ error. While we gain constraining power by using the future CMB surveys, this gain is not as dramatic as it was in the IST:F-like case. Indeed, the forecasted 1σ

5.4. Results

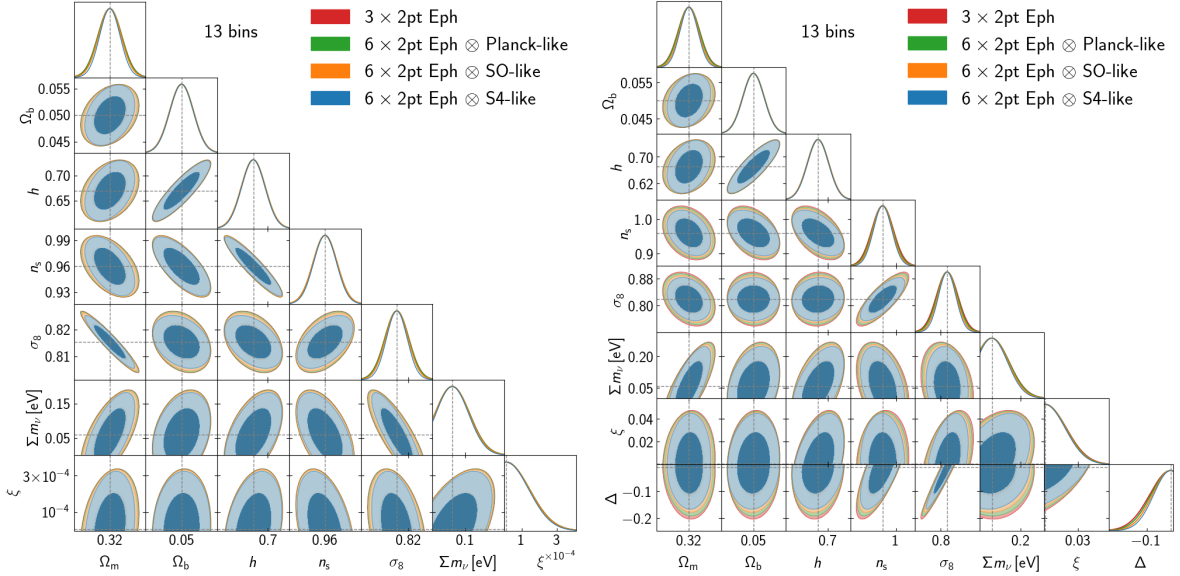


Figure 5.6: Marginalized 68% and 95% 2D confidence regions for the joint constraints on the cosmological parameters in **IG** (left) and **NMC+** (right) for a *Euclid*-ph-like survey (**13 bins from Flagship 2**) (red), combined with the CMB lensing from **Planck** (green), **SO** (orange), **S4** (blue).

error on Δ improves only by 20% when combining *Euclid* with S4 CMB lensing. As a consequence, the percentage increase in the FoM of the cosmological parameters is driven by a slight improvement on all the parameters, rather than being mostly due to the more accurate measurement of ξ and Δ . This is the most pessimistic scenario we analyzed for the $6 \times 2\text{pt}$ and even in this case the contribution given by the cross-correlation with CMB lensing is non-negligible in both models considered, especially in NMC where the FoM of cosmological parameters increases by 12% (26%) when combining *Euclid*-ph with SO.

We expect the $6 \times 2\text{pt}$ analysis to be even more relevant we will introduce in our pipeline additional and more realistic features characterizing the *Euclid* photometric survey. One of these is the inclusion of the shear multiplicative bias, which can be calibrated by the inclusion of CMB lensing in the analysis [213, 218], leading to a better understanding of the *Euclid* systematics and better constraints on cosmological parameters.

		$\Omega_{m,0}$	$\Omega_{b,0}$	h	n_s	σ_8	$m_\nu[\text{eV}]$	ξ
<i>Euclid-ph</i>	$\sigma_{3 \times 2} / \theta$	0.0091	0.047	0.037	0.015	0.0058	0.89	13
Eph \otimes <i>Planck</i>	$\sigma_{3 \times 2} / \sigma_{6 \times 2}$	1.0	1.0	1.0	1.0	1.0	1.0	1.0
Eph \otimes SO (+ <i>Planck</i> low- ℓ)	$\sigma_{3 \times 2} / \sigma_{6 \times 2}$	1.1	1.0	1.0	1.0	1.1	1.0	1.0
Eph \otimes S4 (+ <i>Planck</i> low- ℓ)	$\sigma_{3 \times 2} / \sigma_{6 \times 2}$	1.2	1.0	1.0	1.0	1.2	1.1	1.0

	Eph \otimes <i>Planck</i>	Eph \otimes SO (+ <i>Planck</i> low- ℓ)	Eph \otimes S4 (+ <i>Planck</i> low- ℓ)
%FoM(cosmo)	1	6	20
%FoM(nuisance)	1	5	13

Table 5.5: First row: ratio of marginalised 1σ uncertainties over their corresponding fiducial values in **IG** for *Euclid-ph* (**Flagship 2 with 13 bins**). Other rows show the ratio of the 1σ forecasted errors between the 3×2 pt and 6×2 pt. Also quoted the percentage improvement in the FoM (5.6) of the cosmological and nuisance parameters.

		$\Omega_{m,0}$	$\Omega_{b,0}$	h	n_s	σ_8	$m_\nu[\text{eV}]$	ξ	Δ
<i>Euclid-ph</i>	$\sigma_{3 \times 2} / \theta$	0.014	0.061	0.050	0.033	0.040	1.4	19	7.9
Eph \otimes <i>Planck</i>	$\sigma_{3 \times 2} / \sigma_{6 \times 2}$	1.0	1.0	1.0	1.0	1.1	1.0	1.0	1.1
Eph \otimes SO (+ <i>Planck</i> low- ℓ)	$\sigma_{3 \times 2} / \sigma_{6 \times 2}$	1.1	1.0	1.0	1.1	1.1	1.1	1.0	1.1
Eph \otimes S4 (+ <i>Planck</i> low- ℓ)	$\sigma_{3 \times 2} / \sigma_{6 \times 2}$	1.2	1.0	1.0	1.2	1.2	1.1	1.1	1.2

	Eph \otimes <i>Planck</i>	Eph \otimes SO (+ <i>Planck</i> low- ℓ)	Eph \otimes S4 (+ <i>Planck</i> low- ℓ)
%FoM(cosmo)	4	12	26
%FoM(nuisance)	2	8	13

Table 5.6: First row: ratio of marginalised 1σ uncertainties over their corresponding fiducial values in **NMC+** for *Euclid-ph* (**Flagship 2 with 13 bins**). Other rows show the ratio of the 1σ forecasted errors between the 3×2 pt and 6×2 pt. Also quoted the percentage improvement in the FoM (5.6) of the cosmological and nuisance parameters.

5.4.5 Full CMB-*Euclid* joint analysis

So far we have presented the combination of the CMB lensing with the galaxy number counts and weak lensing of galaxies from the *Euclid* photometric survey. Here, we turn our attention to forecasts for the combination of all the CMB probes (temperature, polarization and lensing) and their cross-correlations with the *Euclid* photometric probes. We do this by using the latest *Euclid* specifications extracted from the Flagship 2 mock galaxy catalogue and described in section 5.2.1. In this analysis, the future CMB surveys are complemented by the information coming from *Planck* at $\ell < 40$ in temperature and polarization, so when we refer to SO and S4 it is implicit that they are combined with *Planck*'s large scales. The joint analysis with all CMB probes, beside highlighting the role of CMB primary anisotropies in breaking degeneracies, can provide an idea of what we can expect for constraints on modified gravity models from the full combination of CMB, galaxy and weak lensing surveys in the next decade.

Figs. 5.7 and 5.8 for *Planck*, and Figs. 5.9 and 5.10 for SO, show the 2D confidence regions for the cosmological parameters in IG and NMC+, for CMB probes, *Euclid*-ph and their combination. We want to stress the complementarity between CMB and LSS that the figure depicts: most of the contours are orthogonal to each other, allowing to completely break degeneracies between parameters. This is due to the very different regimes under which each observable probes the Universe: early times and large scales for the CMB, late times and smaller scales for *Euclid*. Exploiting this complementarity will allow a determination of the cosmological parameters with unprecedented precision, for example, the forecasted 95% CL constraint on the determination of ξ in IG is $\xi < 2.2 \times 10^{-4}$ when combining *Planck* with *Euclid*-ph. This is a factor of 2.5 better than the present constraint discussed in section 2.6, which can only be improved if one also considers the *Euclid* spectroscopic survey. For the combination with SO (S4) we forecast $\xi < 1.8 \times 10^{-4}$ ($\xi < 1.6 \times 10^{-4}$) at 95% CL, far better than has ever been obtained with cosmological datasets.

All the other cosmological parameters are affected by the joint analysis as it can be seen from Tables 5.7 and 5.8 both for IG and NMC. The relative error in the parameters in the 3×2 pt analysis is already quoted in Tables 5.5 and 5.6, therefore we have omitted it in the tables of this section.

The Hubble constant, the baryon density and the tilt of the power spectrum n_s are the parameters that benefit the most by the inclusion of all CMB probes. These are all parameters to which the primary CMB is very sensitive and the largest improvements are expected, especially on Ω_b , because the galaxy survey probes are sensitive to the total matter (dark matter and baryons) and not specifically to baryons.

Since the determination of the sum of neutrino masses from cosmological datasets alone is model dependent and it can be far less stringent in extended models [1], we also point out that in IG the absolute 1σ error on the determination of the sum of neutrino masses for the combination of *Euclid*-ph with CMB-S4, is $\sigma(m_\nu) = 27$ m eV, allowing a 95% CL detection of the neutrino mass in this extended model. This constraint could be significantly improved by adding the spectroscopic information contained in *Euclid* data.

In the NMC+ model, we have noticeable improvement with respect to the 3×2 pt

5. Euclid-CMB cross-correlation forecasts in extended models

		$\Omega_{m,0}$	$\Omega_{b,0}$	h	n_s	σ_8	τ_{reio}	$m_\nu[\text{eV}]$	ξ
Eph \otimes <i>Planck</i>	$R(\theta)$	1.2	6.6	10.8	6.3	1.3	1.4	1.6	1.2
Eph \otimes SO (+ <i>Planck</i> low- ℓ)	$R(\theta)$	1.3	8.0	11.7	7.5	1.4	1.4	1.8	1.4
Eph \otimes S4 (+ <i>Planck</i> low- ℓ)	$R(\theta)$	1.8	10.5	15.2	8.6	2.0	1.4	2.0	1.7

Table 5.7: IG model: ratio of marginalised 1σ uncertainties for the parameter θ , $R(\theta) = \sigma_{3 \times 2\text{pt}}(\theta)/\sigma_{\text{joint}}(\theta)$, where σ_{joint} is the expected error of the combination of **Euclid-ph (Flagship 2 with 13 bins)** with the given CMB experiment. For the optical depth at reionization τ_{reio} we quote the improvement obtained after combining *Euclid* with CMB data alone: $R(\tau_{\text{reio}}) = \sigma_{\text{CMB}}/\sigma_{\text{joint}}$.

		$\Omega_{m,0}$	$\Omega_{b,0}$	h	n_s	σ_8	τ_{reio}	$m_\nu[\text{eV}]$	ξ	Δ
Eph \otimes <i>Planck</i>	$R(\theta)$	1.3	5.6	7.7	9.4	2.9	1.2	1.7	1.4	3.6
Eph \otimes SO (+ <i>Planck</i> low- ℓ)	$R(\theta)$	1.5	7.9	11.2	10.8	4.1	1.3	2.1	2.8	5.4
Eph \otimes S4 (+ <i>Planck</i> low- ℓ)	$R(\theta)$	2.4	11.7	16.9	12.7	5.7	1.2	2.5	3.8	7.2

Table 5.8: NMC+ model: ratio of marginalised 1σ uncertainties for the parameter θ , $R(\theta) = \sigma_{3 \times 2\text{pt}}(\theta)/\sigma_{\text{joint}}(\theta)$, where σ_{joint} is the expected error of the combination of **Euclid-ph (Flagship 2 with 13 bins)** with the given CMB experiment. For the optical depth at reionization τ_{reio} we quote the improvement obtained after combining *Euclid* with CMB data alone: $R(\tau_{\text{reio}}) = \sigma_{\text{CMB}}/\sigma_{\text{joint}}$.

in all cosmological parameters, similarly to the IG case, but also on ξ and Δ , with the results summarized in Table 5.8.

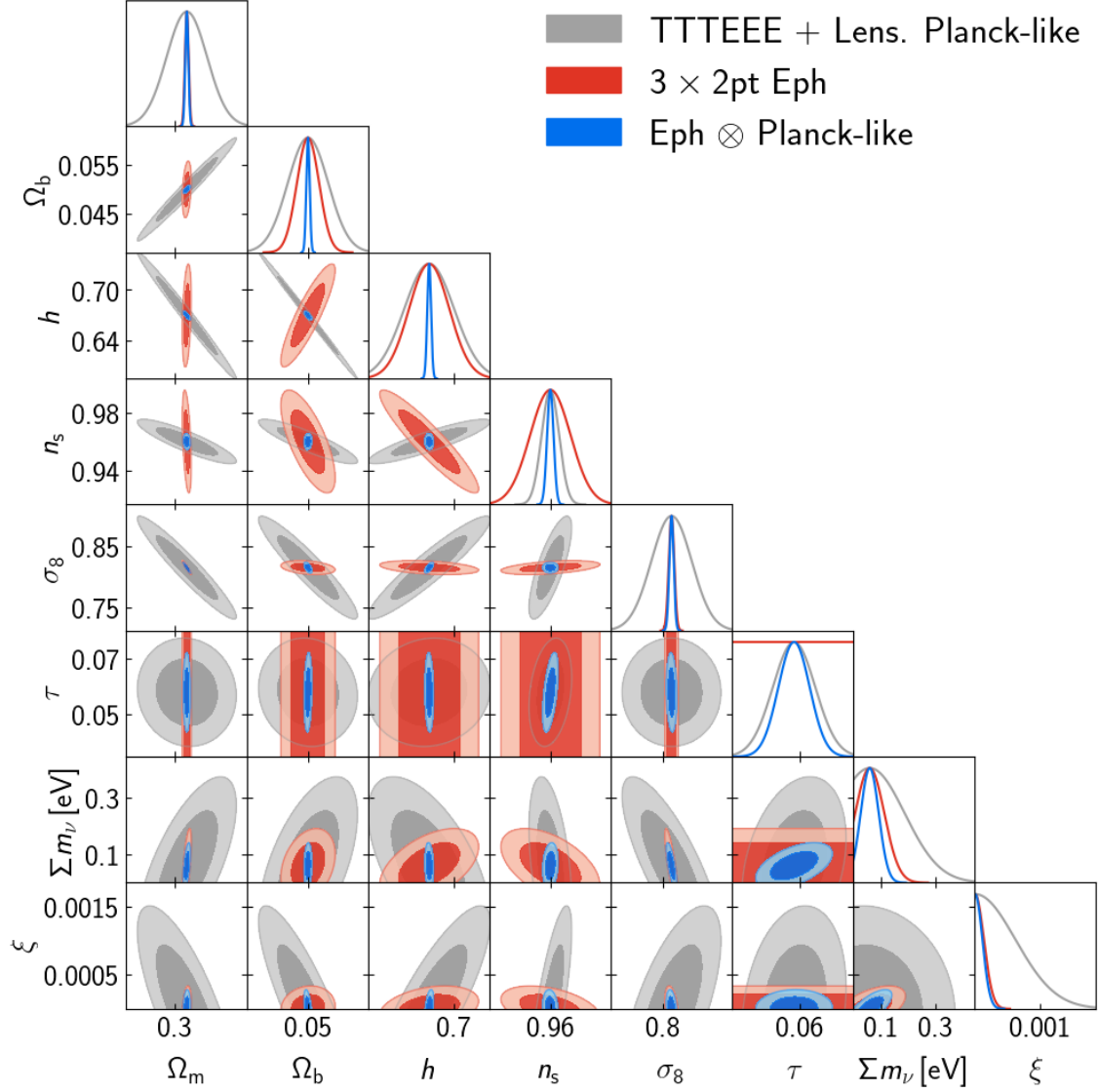


Figure 5.7: Marginalized 68% and 95% 2D confidence regions for the joint constraints on the cosmological parameters in **IG** for a *Euclid-ph-like* survey (13 bins from **Flagship 2**) (red), **Planck-like** (grey), and combination of the two (blue).

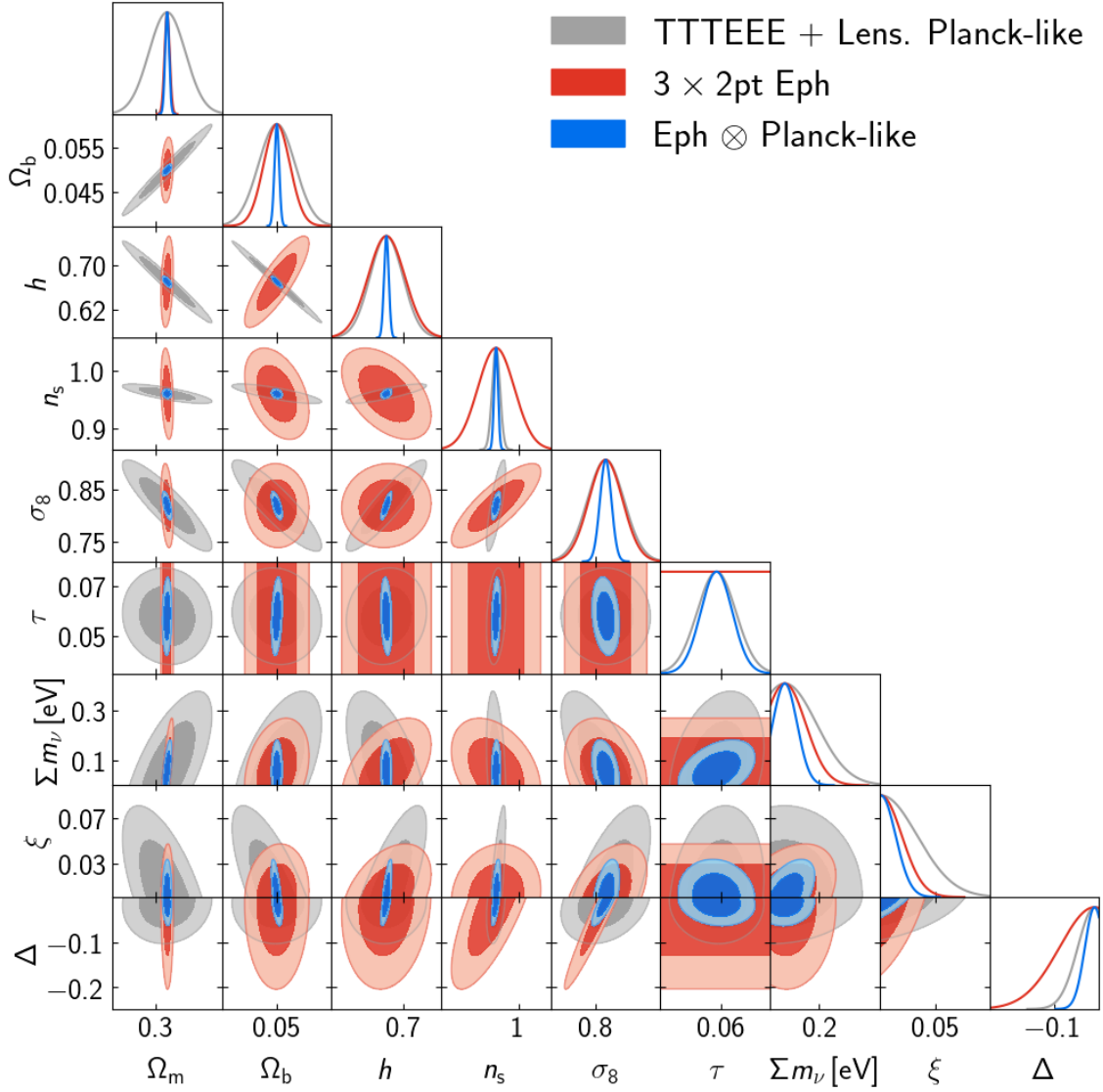


Figure 5.8: Marginalized 68% and 95% 2D confidence regions for the joint constraints on the cosmological parameters in **NMC+** for a *Euclid-ph-like* survey (13 bins from **Flagship 2**) (red), **Planck-like** (grey), and combination of the two (blue).

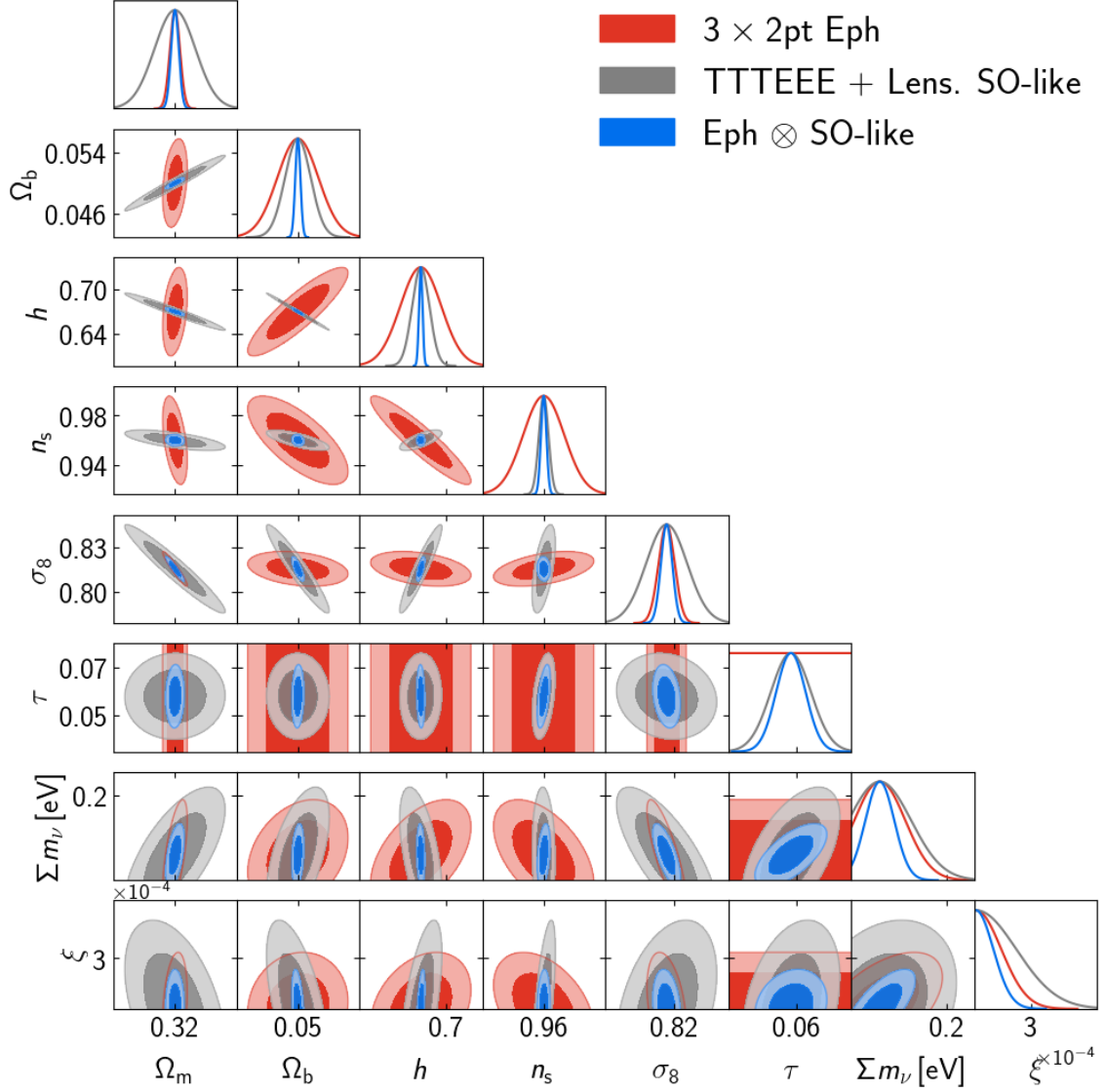


Figure 5.9: Marginalized 68% and 95% 2D confidence regions for the joint constraints on the cosmological parameters in **IG** for a *Euclid*-ph-like survey (13 bins from **Flagship 2**) (red), **SO**-like (grey), and combination of the two (blue).

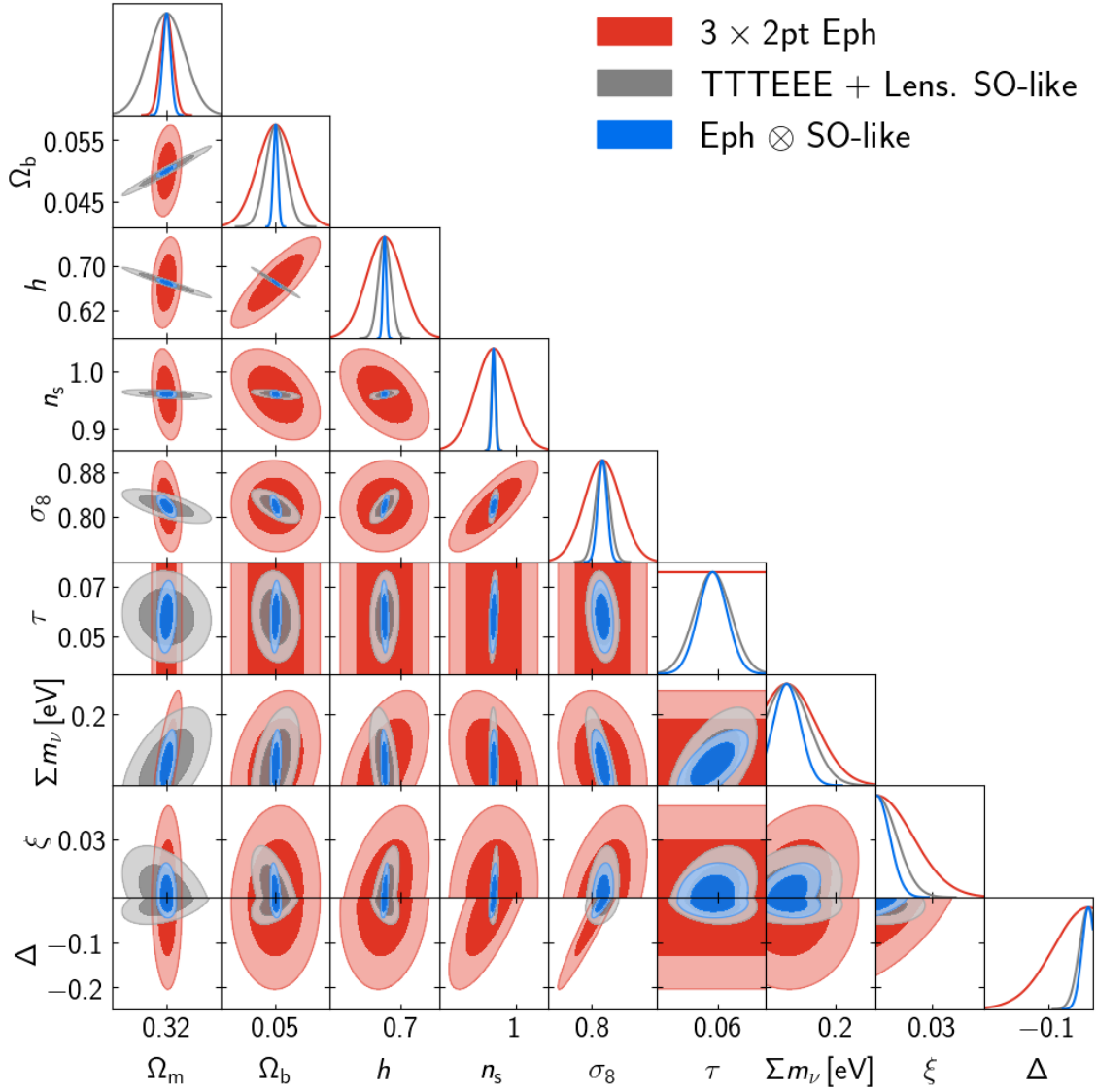


Figure 5.10: Marginalized 68% and 95% 2D confidence regions for the joint constraints on the cosmological parameters in NMC+ for a *Euclid-ph-like* survey (13 bins from Flagship 2) (red), SO-like (grey), and combination of the two (blue).

5.5 Discussion and future directions

We have presented in this chapter a forecast analysis in two modified gravity models (IG and NMC+) for the *Euclid* photometric survey and its combination with several CMB experiments, focusing first on the combination with CMB lensing in the 6×2 pt analysis and discussing at the end the impact of a full joint analysis with all the CMB probes. We have considered different specifications for *Euclid*: an IST:F-like baseline setting that we have then modified to assess the effect of tomography and shot-noise; and a more updated characterization of the survey coming from the Flagship 2 simulation.

On this note, striving to better parameterize the *Euclid* survey, at the moment we are including more realistic effects in our pipeline, which we list below.

- Inclusion of the shear multiplicative bias, which can be calibrated by the inclusion of CMB lensing in the analysis [213, 218], leading to a better understanding of the *Euclid* systematics and better constraints on cosmological parameters.
- The inclusion of relativistic corrections for the number counts and consequent marginalization on magnification bias, which has been shown to be sensitive to the cross-correlation in [217].
- Redshift dependent multipole cuts in order to employ different ℓ ranges in different bins.
- Inclusion of super sample covariance (SSC) which can degrade the constraining power of *Euclid* [243], especially in extended models, rendering the CMB cross-correlation a precious ally to recover some of this constraining power, since the CMB is less affected by this SSC effect.
- Usage of different redshift distributions for the different probes, especially in light of the early *Euclid* data releases where the binning for photometric galaxy clustering could be considered up to redshift smaller than the redshift of the full survey $z < 2.5$.

Improvements on the CMB side include the addition of LiteBIRD³ [244, 245] to complement the small scales of CMB-S4, given the similar timelines of the two experiments.

These refinements are a work-in-progress and once finished they will set the baseline specification for the upcoming article on the forecasts in extended models of the CMBX-SWG.

³<https://www.isas.jaxa.jp/en/missions/spacecraft/future/litebird.html>

Conclusions

The next decade holds great promise for precision cosmology. Accurate maps of CMB anisotropies, as generated by experiments such as *Planck*, have provided crucial insights into the early Universe and have placed constraints on the Λ CDM model. Future CMB experiments are poised to build upon these findings and improve these measurements. Moreover, several galaxy surveys will map the 3D distribution of matter with diverse methodologies and providing a complementary probe of the Universe at low redshift, constraining in this way dark matter and late-time effects such as dark energy, but also improving our knowledge of the theory of gravity at cosmological scales.

The joint analysis of both type of datasets, accounting also for the cross-correlations between CMB and LSS, will allow to constrain extensions of the Λ CDM model. The upcoming data will therefore weigh in the open questions of cosmology such as the Hubble tension and the nature of dark energy and dark matter, and it is imperative to test generalizations of the standard model with all the available data and their combination, to assess whether or not new physics is required.

In this thesis we have discussed the preparation for this endeavor in the context of the ESA *Euclid* mission and the *Euclid* Consortium of which I am a member. In particular, we have detailed the status and the validation of the CMB cross-correlation likelihood for the detection of the ISW effect through the correlation between the CMB temperature field and the galaxy density field, and for the addition of CMB lensing and its cross-correlation with *Euclid* main probes in a joint likelihood. The goal of this activities is to build the final steps of an end-to-end pipeline that is being developed in the CMBX-SWG within the *Euclid* consortium. The group is indeed developing numerical simulations to build covariances, employing estimators techniques to extract the cross-correlation power spectra from maps, and investigating the impact of the cross-correlation on the *Euclid* survey. All these ingredients will have their final application in the likelihood module that we are developing in order to perform a *Euclid*-CMB joint analysis. The main results presented in this thesis in the context of the CMBX likelihood are listed below.

- Validation of the theoretical approximations used to compute the cross-correlation between the CMB temperature field and galaxy number counts, necessary to detect the ISW effect in the cross-correlation data. The main assumptions in the computation of the theoretical power spectra are the Limber approximation and the scale independence of the growth of matter perturbations. These validations have been carried out on several levels: by comparing the power spectra in our approximated implementation with the exact spectra obtained from the Einstein-Boltzmann code CLASS, by computing the difference in χ^2 values with and without any approximations, and by performing an MCMC analysis where the role of the data is played by the power spectra computed without approximations. We have repeated this analysis considering the *Euclid* survey with 3 and 10 redshift bins and we have obtained positive results in all cases, demonstrating that the percentage differences in the power spectra and in the χ^2 are small enough to not induce any bias in the estimate of cosmological parameters in the dynamical dark energy models, which are one of the main targets of *Euclid*.
- Validation of the theoretical computation for CMB lensing and its implementation

Conclusions

in the official likelihood package of *Euclid*: CLOE. While CMB lensing is observed from the CMB, it is a probe of the late-time distribution of matter. We have therefore included CMB lensing in the likelihood to compute it consistently with all the other LSS probes. The main challenge was to reliably compute the power spectrum without slowing down the code and we have achieved this result. Additionally, we have implemented in the likelihood some necessary terms that take into account biases in the estimated power spectrum of the CMB lensing, due to peculiarities of the lensing reconstruction from CMB temperature and polarization. In order to include these terms, we need some pre-computed matrices coming from the lensing reconstruction. Therefore we have performed a CMB lensing reconstruction with noise levels from the Simons Observatory to obtain these matrices and successfully implemented the correction for the normalization of the power spectrum in the likelihood. The computation of the matrices to correct for the so-called $N1$ bias are ongoing.

Once the likelihood is finalized, and we discuss at the end of this section some steps taken towards this direction, we will be able to ingest *Euclid* data and their cross correlations with CMB fields, and test, firstly the Λ CDM model and then its extensions such as dynamical dark energy models, modified gravity theories and neutrino masses.

In this thesis we have provided some context for the study of a subset of these extended models: scalar-tensor theories (STTs) of gravity, discussing the current constraints and producing novel cosmological constraints with publicly available datasets.

In particular, we have studied the cosmological dynamics of the simplest STTs such as induced gravity (IG), non minimal coupling models (NMC) and early modified gravity (EMG), with non standard sign of the kinetic term, dubbed phantom branch. We have assessed the effect of the sign of the kinetic term on cosmological observables and obtained the marginalized constraints for different combination of cosmological datasets by allowing the coupling to the Ricci scalar (and the amplitude of the potential in EMG) to vary together with the rest of the cosmological and nuisance parameters an MCMC analysis:

- The analysis in IG and NMC showed that the modified evolution of the scalar field in the phantom branch, connected to a different time evolution of the effective gravitational constant, inverts the degeneracy between these parameters and the coupling ones. For this reason, we obtain a lower values for σ_8 and H_0 compared to the standard branch.
- In the phantom version of EMG we showed that while the evolution of the scalar field is very similar to the standard case, different signatures appear on the cosmological observables. We have further constrained the parameters of this model with a combination of cosmological datasets showing a statistical preference with respect to Λ CDM.

Furthermore, we have analyzed the cosmological dynamics and inferred the cosmological constraints for the extension of the simplest nonminimally coupled STTs with a cubic Galileon term, which ensures the stability of the theory in the phantom branch and provides the Vainshtein screening mechanism, potentially reconciling the theory with GR inside the so-called Vainshtein radius. We have shown the peculiar dynamics both

in the standard and phantom branch, comparing the theoretical predictions of the models with observations, obtaining the following results:

- For a standard kinetic term, we find that the CMB anisotropy pattern constrains the Galileon term to be small close to the CMB last scattering surface, resulting in a Vainshtein mechanism that can occur only at subparsec scale for an object of a solar mass.
- In the phantom branch, we have shown that the presence of a Galileon term leads to a healthy theory for all the values of the coupling constant ξ , rescuing the range which would contain a ghost in the IG theory. We have highlighted the different phenomenology with respect to the standard branch and constrained the theory with different datasets. We considered one case where the potential is given by a cosmological constant and another case where there is no potential and the late-time acceleration is driven exclusively by the Galileon term. This latter model is physically viable and provides screening on Solar System scales, but it leads to CMB predictions which are at odds with the *Planck* data, with a $\Delta\chi^2 = 30.6$ with respect to Λ CDM, we have therefore ruled out the model by making use of CMB data.

The results of the data analysis for the case with a cosmological constant, show instead a reduction in the significance of the Hubble tension at 2.5σ with CMB + BAO and 1.7σ when including Supernovae with a prior on their absolute magnitude. With this latter dataset, we see high statistical significance for the Galileon parameter $1/\tilde{\alpha}_8 \neq 0$, and consequently a Vainshtein radius of $\mathcal{O}(100)$ pc for a solar mass.

With the goal of assessing the relevance of CMB cross-correlation with *Euclid* in extended models we have forecasted what we can expect from the combination and cross-correlation of CMB observables with *Euclid* photometric survey, by considering all the cross-correlations between fields in the harmonic space. Most of the forecasts focused on the so called 6×2 pt analysis which considers six combinations of the two point correlation functions of CMB lensing, galaxy weak lensing, and galaxy positions. This type of analysis shows the maximal constraining power that can be obtained by LSS probes alone, without considering the CMB temperature and polarization, which are dominated by the physics at last scattering. We discussed the relevance of the 6×2 pt analysis in several different settings and specification for *Euclid*, assessing the impact of reducing the number of bins and increasing shot-noise separately. We have found that the 6×2 pt analysis always provides important additional information and helps increasing the constraining power of both the cosmological and nuisance parameters, especially the parameters of the extended models. By reducing the number of bins and increasing the shot-noise we have highlighted even more this combination with CMB lensing.

We have also studied and compared the 6×2 pt analysis against the 3×2 pt analysis with updated specifications for the *Euclid*-photometric survey, extracted from the Flagship 2 mock galaxy catalogue. With these *Euclid* specifications, the combination with the CMB lensing from *Planck* does not add much constraining power and it is necessary to cross-correlate the survey with future CMB experiments, such as SO and S4, to see some improvement in the cosmological constraints.

Conclusions

However, we have demonstrated that when considering the entirety of CMB probes, the combination with *Planck* allows to break degeneracies on almost all the cosmological parameters, highlighting the strong complementarity of these two types of observations: early-times and large scales for the CMB and late-times and small scales for *Euclid*. The maximal constraining power is obtained by adding the large scale information of *Planck* in temperature and polarization to the future CMB experiments SO and S4, and then performing a joint analysis with the *Euclid* photometric probes. This full combination allows to constrain the parameters of the extended models with precision never reached by any cosmological dataset. For example, we have shown that the combination of the *Euclid* photometric survey with S4 will provide a 95% CL detection of the neutrino mass, without even considering the precious spectroscopic information contained in *Euclid* data. In the context of modified gravity, we have forecasted that already the combination of *Planck* with *Euclid* will allow to noticeably improve the present cosmological constraint on the simplest STTs.

Concerning future prospects, the work carried out in this thesis can be extended in several directions:

- **Modified gravity:** we plan to extend the works performed in this thesis by extending the parameter space in our MCMC analysis and to study variations of the models discussed here, with different functional forms for the Horndeski functions.
- **Likelihood:** current work on the likelihood is focused on including more realistic effects, such as the use of the mask for *Euclid* and the CMB surveys, and their effect on the covariance. We will also test the likelihood with power spectra estimated from simulations, both for CMB lensing, the CMB temperature field and their cross-correlations with galaxy probes.
- **Forecasts:** ongoing activities are devoted to the inclusion in the pipeline of additional nuisance parameters, such as the shear multiplicative bias, to better characterize the *Euclid* photometric survey, together with the addition of the super sample covariance in the forecasts.

These steps are planned for the near future, in order to be able to properly analyze the first *Euclid* data in one year time.

Appendix A

Statistical methods for data analysis in Cosmology

Most of the data analysis in cosmology and in this thesis employs Bayesian statistics and MCMC (Markov chain Monte Carlo) methods. Therefore, in this appendix we review some of the fundamental concepts of Bayesian statistics, and MCMC algorithms with particular emphasis on parameter inference and model comparison.

In a Bayesian framework the parameters of interest have probability distributions, and the central pillar Bayesian statistical analyses is Bayes' theorem:

$$P(\boldsymbol{\theta}|\mathbf{d}, \mathcal{M}) = \frac{\mathcal{L}(\mathbf{d}|\boldsymbol{\theta}, \mathcal{M})\pi(\boldsymbol{\theta}|\mathcal{M})}{P(\mathbf{d}|\mathcal{M})}. \quad (\text{A.1})$$

$P(\boldsymbol{\theta}|\mathbf{d}, \mathcal{M})$ is the *posterior* probability for the parameters $\boldsymbol{\theta}$ of the model \mathcal{M} , given the data \mathbf{d} ; finding this probability distribution function (pdf) is the goal of Bayesian inference. The *likelihood* function \mathcal{L} is a measure of the chance that we would have obtained the observed data \mathbf{d} , given a model \mathcal{M} with parameter values $\boldsymbol{\theta}$; it is often written simply as a function of the parameters $\mathcal{L}(\boldsymbol{\theta})$. The *prior* π is the probability distribution of the parameters $\boldsymbol{\theta}$, obtained from all external information available before performing the experiment. This prior information might come from theoretical constraint, as well as from the results of previous experiments. Finally, the evidence $P(\mathbf{d}|\mathcal{M})$ is the probability of the data and is given by $P(\mathbf{d}|\mathcal{M}) = \int d\boldsymbol{\theta} \mathcal{L}(\mathbf{d}|\boldsymbol{\theta}, \mathcal{M})\pi(\boldsymbol{\theta}|\mathcal{M})$; for this reason, it is also called the *marginal likelihood*. Since it does not depend on $\boldsymbol{\theta}$, the evidence is not relevant for parameter estimation, but it plays an important model comparison.

A.1 Parameter inference

The parameters $\boldsymbol{\theta}$ can be divided in a set of interesting quantities $\boldsymbol{\varphi}$ and a set of uninteresting ones $\boldsymbol{\psi}$. The latter might correspond to nuisance parameters related to uncertainties in the measuring process or unconstrained physical properties, or simply to all the parameters except one or two we wish to constrain simultaneously. It is possible to obtain the pdf of the parameters of interest by integrating over all the nuisance parameters:

$$P(\boldsymbol{\varphi}|\mathbf{d}, \mathcal{M}) \propto \int d\boldsymbol{\psi} \mathcal{L}(\boldsymbol{\varphi}, \boldsymbol{\theta}) \pi(\boldsymbol{\varphi}, \boldsymbol{\theta}|\mathcal{M}). \quad (\text{A.2})$$

This procedure is called *marginalization* and in many cases it is not possible to do it analytically. Moreover, the likelihood is often assumed to be Gaussian in the observables, this means that it is non-Gaussian for the cosmological parameters, and computing analytically the integrals to find the expectation values and other quantities of interests could be unfeasible.

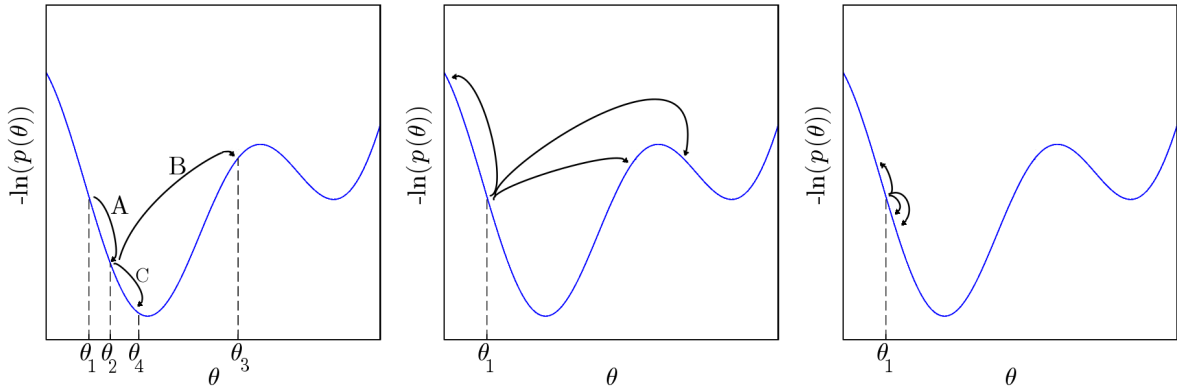


Figure A.1: **Left:** example of a chain constructed by the Metropolis-Hastings algorithm: starts at θ_1 , θ_2 is proposed and accepted (step A), θ_3 is proposed and refused (step B), θ_4 is proposed and accepted (step C). The resulting chain is $\{\theta_1, \theta_2, \theta_2, \theta_4, \dots\}$. **Central:** example with a too large jump size, it causes most proposals to be rejected. **Right:** example with a too small jump size and inefficient sampling of parameter space. Figure taken from Ref. [247].

It is therefore necessary to infer the posterior distributions of the parameters numerically, by sampling the likelihood over a wide range of parameter values. If mapping the likelihood in a one-dimensional parameter space requires n evaluations, then for a p -dimensional parameter space we would need n^p evaluations. For cosmological parameter estimation the typical number of parameters is of order ten to one hundred, rendering a brute force approach impossible; we therefore need different techniques to evaluate the likelihood in the entire parameter space. Markov chains Monte Carlo (MCMC) are the most widespread techniques to numerically sample the posterior, the main reason for this popularity is that the number of evaluations necessary to obtain a good estimate of the distribution and related quantities of interests scales linearly with the number of parameters [246]. In this procedure it is possible to generate a set of points in parameter space whose distribution function is the same as the distribution we wish to study, called target distribution (usually the likelihood or the posterior). The ‘‘Monte Carlo’’ part of the name comes from the fact that the points are drawn randomly, while the ‘‘Markov’’ part signifies that the chain is a Markov process, meaning that the next point of the chain depends only on the present one and not on the sequence of previous ones. An important property of a Markov chain is that it converges to a stationary state where successive elements of the chain are samples from the target distribution. We can therefore estimate quantities of interest directly from it.

There are several sampling algorithms to perform an MCMC, the Metropolis-Hastings [248, 249] algorithm is one of the most popular and it is the one used in this work. It can be outlined as follows:

- (i) Randomly select a point in parameter space as starting point.
- (ii) Select a second point θ' by drawing it from a distribution $q(\theta'|\theta)$ centered on θ . This distribution is called proposal distribution and it is usually a multivariate Gaussian.
- (iii) Compute the ratio of the likelihood of the two samples, the point θ' is then accepted

A.1. Parameter inference

with probability

$$P_{\text{acc}} = \min \left\{ 1, \frac{\mathcal{L}(\boldsymbol{\theta}')q(\boldsymbol{\theta}'|\boldsymbol{\theta})}{\mathcal{L}(\boldsymbol{\theta})q(\boldsymbol{\theta}|\boldsymbol{\theta}')} \right\}. \quad (\text{A.3})$$

If $\boldsymbol{\theta}'$ is accepted it becomes a new state of the chain. Otherwise, we reject it and the chain stays at $\boldsymbol{\theta}$. The cycle is then repeated from step (ii).

An illustration of the MH algorithm is shown in Fig. A.1. In practice, in order to explore the target distribution as fast as possible, a series of refinements are applied to the proposal distribution $q(\boldsymbol{\theta}'|\boldsymbol{\theta})$. If the proposal is too small, in the sense that the typical jump in parameter space is small, then the sampling is inefficient and it will take very long before the posterior distribution is explored, as almost all the points are accepted. On the other hand if the proposal distribution is too large, then the majority of proposed points will be in regions of low probability, far from the peak, and will be rejected. One possibility to solve these issues is to run exploratory chains to get an idea of the size of the target distribution by computing the covariance matrix from the samples and then using it as the covariance of the Gaussian proposal for new chains. Another possibility is to update the covariance matrix on the fly during the chain, in both cases the points computed using a proposal distribution different from the final one have to be discarded and cannot be part of the final analysis.

Since the starting point of a chain is chosen randomly, the subsequent points will be outside the stationary region and the chain is not sampling the target distribution until after a while, when it reaches higher probability regions. It is therefore common to also discard a certain percentage (usually $\sim 30\%$) of the beginning of the chain, called *burn-in*. Doing so, any dependence on the starting point is removed.

Finally, when performing an MCMC analysis it is necessary to ensure that the chains are stationary and have converged to the target distribution. The usual diagnostic for this purpose is the so-called Gelman-Rubin convergence criterion [164]. This test consists of comparing the variance within individual chains to the variance between chains. Their ratio, R , should be close to unity when the chains have converged. In Cosmology, the convergence criterion is usually $R - 1 < 0.01$.

A limitation of the Gelman-Rubin criterion is that it might misdiagnose convergence if R happens to be very close to unity by chance. A list of some of the most popular convergence diagnostics for MCMC can be found in Ref. [250].

Once the posterior distribution is sampled, it is possible to estimate any integrals of any function of the parameters (such as the expected value or the variance) simply as

$$\langle f(\boldsymbol{\theta}) \rangle \simeq \frac{1}{N} \sum_{i=1}^N f(\boldsymbol{\theta}_i), \quad (\text{A.4})$$

where i labels the points of the chain.

Also, marginalization becomes trivial: it is sufficient to build an histogram counting the number of samples in each bin of some subset of parameters, ignoring the values of the parameters we wish to marginalize over.

A.1.1 Credible intervals

In addition to estimates obtained with Eq. (A.4), one needs credible regions in parameter space that express the degree of uncertainty in the inference. A closed but not necessarily connected hypersurface ∂A_γ , called a $100\gamma\%$ credible region, can be constructed such that the hypervolume A_γ contains a fraction γ of the total posterior volume

$$\int_{A_\gamma} d\boldsymbol{\theta} P(\boldsymbol{\theta}|\mathbf{d}, \mathcal{M}) = \gamma \quad (\text{A.5})$$

This definition is not unique, the two most popular choices in the 1D case are

- equal-tailed intervals (ETI), where equal fractions of the posterior volume lie in the two tails of the distribution, meaning that being below the interval is as likely as being above it, with probability $(1 - \gamma)/2$;
- highest density intervals (HDI), within them the posterior at any point is larger than at any point outside. These intervals have equal posterior density at the upper and lower endpoint, and the areas of the two tails are not necessarily equal.

In chapter 2 we quote HDI intervals when referring to parameter constraints in all cases except when only an upper or lower limit on a parameter can be found. In this latter case we quote one-tailed intervals where the fraction $(1 - \gamma)$ of the posterior volume lies in one of the tails.

A.2 Model comparison

The reason to analyze a dataset is to find the best model describing the Universe. Thus, we are interested in knowing whether a model \mathcal{M}_1 is statistically preferred over another model \mathcal{M}_2 . The performance of a model given the data is quantified by $P(\mathcal{M}|\mathbf{d})$, which is called *posterior odd* and it is proportional to the product of the prior probability for the model itself, $P(\mathcal{M})$, and of the Bayesian evidence $P(\mathbf{d}|\mathcal{M})$ encountered in Eq. (A.1). To compare two models we then compute the ratio of their posterior odds [251]

$$O_{12} \equiv \frac{P(\mathcal{M}_1|\mathbf{d})}{P(\mathcal{M}_2|\mathbf{d})} = \frac{P(\mathbf{d}|\mathcal{M}_1)P(\mathcal{M}_1)}{P(\mathbf{d}|\mathcal{M}_2)P(\mathcal{M}_2)} \equiv B_{12} \frac{P(\mathcal{M}_1)}{P(\mathcal{M}_2)} \quad (\text{A.6})$$

where, in the first equality we applied Bayes theorem to $P(\mathcal{M}|\mathbf{d})$, and $P(\mathcal{M})$ is the prior probability for the model itself. The term B_{12} is called *Bayes factor* and it corresponds to the ratio of the evidences. It is common to choose non-committal priors on the models, i.e., $P(\mathcal{M}_1) = P(\mathcal{M}_2)$, in this case the ratio of the posterior odds is the Bayes factor, $O_{12} = B_{12}$. A value of B_{12} greater (smaller) than one means that the data favor model \mathcal{M}_1 (\mathcal{M}_2). The Bayes factor is the ratio of the evidences and the evidence is the integral of the likelihood times the prior, this highlights the relevance of the prior choice $\pi(\boldsymbol{\theta}, \mathcal{M})$ in Eq. (A.1). In fact there could be parameters which are exclusive of one model, or another parameter which has a wider range in a particular model; all this is encapsulated in the prior which in turn affects the evidence, favouring one model over another one. Thus, the Bayes factor is radically different from the ratio of the likelihoods: a more

A.2. Model comparison

complicated model will always provide higher or equal likelihood values whereas the evidence will favor a simpler model if the fit is nearly as good, through the smaller prior volume.

Obtaining $P(\mathcal{M}|\mathbf{d})$ can be unfeasible due to the large number of samples required to carry out the integration. For this reason, the so-called information criteria are defined as alternatives to the Bayes factor. These criteria are based on the likelihood but also penalize a model depending on the number of parameters, to take into account the fact that a model with more parameters leads to higher likelihood values. One of the most popular information criterion, also employed in chapter 2, is the Akaike information criterion (AIC) [169], defined as

$$AIC = -2 \ln \mathcal{L} + 2p, \tag{A.7}$$

where p is the number of parameters, and the quantity $-2 \ln \mathcal{L}$ is often denoted with the symbol χ^2 . Among all the models considered in order to fit the data, the model with lower AIC is the preferred one. The AIC, however, can only quantify the quality of a model relative to other models and it doesn't quantify how good a given model fits the data. Another limitation of the AIC is that it penalizes extra parameters regardless of whether they are constrained by the data or not [252].

Appendix B

Linearly perturbed equations in scalar-tensor theories

B.1 Einstein equations

Using the same formalism developed in the section 1.6 we present here in the synchronous gauge the linearly perturbed Einstein and scalar field equations for the modified gravity theory given by Eqs. (2.6) and (2.7). The perturbed Einstein equations are

$$k^2\eta - \frac{1}{2}\mathcal{H}h' = -\frac{a^2}{2}(\delta\tilde{\rho} + \delta\tilde{\rho}^{(G)}), \quad (\text{B.1})$$

$$k^2\eta' = \frac{a^2}{2}\left[(\tilde{\rho} + \tilde{P})\tilde{\theta} + (\tilde{\rho}^{(G)} + \tilde{P}^{(G)})\tilde{\theta}^{(G)}\right], \quad (\text{B.2})$$

$$h'' + 2\mathcal{H}h' - 2k^2\eta = -3a^2(\delta\tilde{P} + \delta\tilde{P}^{(G)}), \quad (\text{B.3})$$

$$h'' + 6\eta'' + 2\mathcal{H}(h' + 6\eta') - 2k^2\eta = -3a^2(\tilde{\rho} + \tilde{P})\tilde{\Theta}, \quad (\text{B.4})$$

where a tilde denotes the effective perturbations defined below.

In Eqs. (B.1) to (B.4) we distinguished explicitly between the quantities coming from IG and the ones arising from the Galileon term to make as manifest as possible the reduction of IGG and BDG to the IG equations of [79, 253] when $g(\sigma) = \zeta(\sigma) = 0$.

The coefficients appearing in the perturbed Einstein equations are

$$\begin{aligned} \delta\tilde{\rho} \equiv & -\frac{2}{a^2}\left\{\frac{F_{,\sigma}}{2F}\delta\sigma\left[a^2\rho_{\text{M}} + \frac{Z\sigma'^2}{2} + a^2\left(\frac{V}{F} - \frac{V_{,\sigma}}{F_{,\sigma}}\right) + 3\mathcal{H}\sigma'\left(\frac{F_{,\sigma\sigma}}{F_{,\sigma}} - \frac{F_{,\sigma}}{F}\right) + k^2\right]\right. \\ & \left. + \frac{\delta\sigma'}{2F}(3\mathcal{H}F_{,\sigma} - Z\sigma')\right\} + \frac{\delta\rho_{\text{M}}}{F} - \frac{h'\sigma'F_{,\sigma}}{2a^2F}, \end{aligned} \quad (\text{B.5})$$

$$\begin{aligned} \delta\tilde{\rho}^{(G)} \equiv & -\frac{2\sigma'^2}{a^4F}\left\{\delta\sigma\left[3\mathcal{H}\sigma'\left(\frac{gF_{,\sigma}}{F} - g_{,\sigma}\right) + \frac{\sigma'^2}{2}\left(g_{,\sigma,\sigma} - \frac{g_{,\sigma}F_{,\sigma}}{F}\right) - k^2g\right.\right. \\ & \left. + \frac{3\sigma'^2}{2}\left(\frac{\zeta F_{,\sigma}}{F} - \zeta_{,\sigma}\right)\right] + \delta\sigma'\left(\sigma'(2g_{,\sigma} - 6\zeta) - 9\mathcal{H}g\right) - \frac{1}{2}h'\sigma'g\right\}, \end{aligned} \quad (\text{B.6})$$

$$(\tilde{\rho} + \tilde{P})\tilde{\theta} \equiv \frac{(\rho_{\text{M}} + P_{\text{M}})}{F}\theta_{\text{M}} + \frac{k^2}{a^2F}\left\{\delta\sigma\left[\sigma'(Z + F_{,\sigma\sigma}) - \mathcal{H}F_{,\sigma}\right] + \delta\sigma'F_{,\sigma}\right\}, \quad (\text{B.7})$$

$$(\tilde{\rho}^{(G)} + \tilde{P}^{(G)})\tilde{\theta}^{(G)} \equiv \frac{2k^2\sigma'^2}{a^4F}\left[\delta\sigma(3\mathcal{H}g - g_{,\sigma}\sigma' + 2\zeta\sigma') - \delta\sigma'g\right], \quad (\text{B.8})$$

B. Linearly perturbed equations in scalar-tensor theories

$$\delta\tilde{P} \equiv \frac{\delta P_M}{F} + \frac{F_{,\sigma}}{a^2 F} \left\{ \delta\sigma'' + \frac{h'\sigma'}{3} + \delta\sigma' \left[\frac{\sigma'}{F_{,\sigma}} (Z + 2F_{,\sigma\sigma}) + \mathcal{H} \right] - \delta\sigma \left[\frac{a^2 P_M}{F} - \frac{2k^2}{3} \right. \right. \\ \left. \left. + a^2 \left(\frac{V_{,\sigma}}{F_{,\sigma}} - \frac{V}{F} \right) + \frac{\sigma'^2}{F} \left(\frac{Z}{2} + F_{,\sigma\sigma} \right) + (\sigma'' + \mathcal{H}\sigma') \left(\frac{F_{,\sigma}}{F} - \frac{F_{,\sigma\sigma}}{F_{,\sigma}} \right) \right] \right\}, \quad (\text{B.9})$$

$$\delta\tilde{P}^{(G)} \equiv \frac{\sigma'^2}{a^4 F} \left\{ \delta\sigma \left[2 \left(g \frac{F_{,\sigma}}{F} - g_{,\sigma} \right) (\sigma'' - \mathcal{H}\sigma') + \sigma'^2 \left(\frac{F_{,\sigma}}{F} (g_{,\sigma} - \zeta) - g_{,\sigma,\sigma} + \zeta_{,\sigma} \right) \right] \right. \\ \left. - \delta\sigma' \left(4g \frac{\sigma''}{\sigma'} + 4\sigma' (g_{,\sigma} - \zeta) - 6\mathcal{H}g \right) - 2g\delta\sigma'' \right\}, \quad (\text{B.10})$$

$$(\tilde{\rho} + \tilde{P})\tilde{\Theta} \equiv \frac{(\rho_M + P_M)\Theta}{F} + \frac{2}{3a^2} \frac{F_{,\sigma}}{F} \left[k^2 \delta\sigma + \frac{(h' + 6\eta')\sigma'}{2} \right]. \quad (\text{B.11})$$

B.2 Scalar field equation

The equation for the evolution of the scalar field fluctuation in Fourier space is

$$\delta\sigma'' = \delta\tilde{\mathcal{G}} \left\{ Z + \frac{3F_{,\sigma}^2}{2F} + \frac{2\sigma'}{a^2} \left[g \left(6\mathcal{H} - \frac{3F_{,\sigma}\sigma'}{2F} \right) + \sigma'(6\zeta - 2g_{,\sigma}) \right] \right\}^{-1}, \quad (\text{B.12})$$

where the explicit expression for $\delta\tilde{\mathcal{G}}$ is given below:

$$\begin{aligned} \delta\tilde{\mathcal{G}} \equiv & \frac{a^2 F_{,\sigma}}{2F} (\delta\rho_{\text{M}} - 3\delta P_{\text{M}}) - \frac{h'}{2a^2} \left[\frac{a^2\sigma'}{2F} (2ZF + 3F_{,\sigma}^2) + 2g\sigma' \left(3\mathcal{H}\sigma' - \frac{\sigma'^2}{\sigma} + 2\sigma'' \right) + 4\zeta\sigma'^3 \right] \\ & - \frac{h''g\sigma'^2}{a^2} + \frac{\delta\sigma}{a^2} \left\{ a^4 \left[\frac{3P_{\text{M}} - \rho_{\text{M}}}{2F} \left(\frac{F_{,\sigma}^2}{F} - F_{,\sigma\sigma} \right) + \frac{2V}{F} \left(F_{,\sigma\sigma} - \frac{F_{,\sigma}^2}{F} \right) + \frac{2V_{,\sigma}F_{,\sigma}}{F} - V_{,\sigma\sigma} \right] \right. \\ & + a^2 \left[\frac{Z\sigma'^2}{2F} \left(\frac{F_{,\sigma}^2}{F} - F_{,\sigma\sigma} \right) + \frac{3\mathcal{H}\sigma'F_{,\sigma}}{F} \left(\frac{F_{,\sigma}^2}{F} - 2F_{,\sigma\sigma} \right) + \frac{3F_{,\sigma}\sigma''}{F} \left(\frac{F_{,\sigma}^2}{2F} - F_{,\sigma\sigma} \right) \right. \\ & + \left. \frac{3\sigma'^2}{2F} \left(\frac{F_{,\sigma}^2 F_{,\sigma\sigma}}{F} - F_{,\sigma}F_{,\sigma\sigma\sigma} - F_{,\sigma\sigma}^2 \right) - k^2 \left(Z + \frac{3F_{,\sigma}^2}{2F} \right) \right] \\ & + g \left[k^2 \left(\frac{\sigma'^2 F_{,\sigma}}{F} - 4(\mathcal{H}\sigma' - \sigma'') \right) + \frac{3\sigma'^2\sigma''}{F} \left(F_{,\sigma\sigma} - \frac{F_{,\sigma}^2}{F} \right) \right] - 4k^2\zeta\sigma'^2 \\ & + g_{,\sigma}\sigma' \left[\frac{\sigma'^3}{F} \left(F_{,\sigma\sigma} - \frac{F_{,\sigma}^2}{F} \right) + 3\sigma'' \left(\frac{F_{,\sigma}\sigma'}{F} - 4\mathcal{H} \right) - 6\mathcal{H}\sigma' \right] \\ & + \sigma'^2 \left[g_{,\sigma\sigma} \left(\frac{\sigma'^2 F_{,\sigma}}{F} + 4(\sigma'' - \mathcal{H}\sigma') \right) - 12\zeta_{,\sigma}\sigma'' \right] + \sigma'^4 (g_{,\sigma\sigma\sigma} - 3\zeta_{,\sigma\sigma}) \left. \right\} \\ & + \frac{\delta\sigma'}{a^2} \left\{ a^2 \left[-2Z \left(\mathcal{H} + \frac{\sigma'F_{,\sigma}}{2F} \right) - 3\frac{F_{,\sigma}}{F} (\mathcal{H}F_{,\sigma} + \sigma'F_{,\sigma\sigma}) \right] + 6g \left[\sigma'' \left(\frac{\sigma'F_{,\sigma}}{F} - 2\mathcal{H} \right) - 2\mathcal{H}'\sigma' \right] \right. \\ & \left. - 24\zeta\sigma'\sigma'' + 4g_{,\sigma}\sigma' \left(2\sigma'' + \frac{\sigma'^2 F_{,\sigma}^2}{F} - 3\mathcal{H}\sigma' \right) + 4\sigma'^3 (g_{,\sigma\sigma} - 3\zeta_{,\sigma}) \right\}. \quad (\text{B.13}) \end{aligned}$$

Bibliography

Bibliography

- [1] N. Aghanim et al. “Planck 2018 results. VI. Cosmological parameters”. In: *Astron. Astrophys.* 641 (2020). [Erratum: *Astron. Astrophys.* 652, C4 (2021)], A6. DOI: [10.1051/0004-6361/201833910](https://doi.org/10.1051/0004-6361/201833910). arXiv: [1807.06209](https://arxiv.org/abs/1807.06209) [[astro-ph.CO](#)].
- [2] J. G. de Swart, G. Bertone, and J. van Dongen. “How dark matter came to matter”. In: *Nature Astronomy* 1, 0059 (Mar. 2017), p. 0059. DOI: [10.1038/s41550-017-0059](https://doi.org/10.1038/s41550-017-0059). arXiv: [1703.00013](https://arxiv.org/abs/1703.00013) [[astro-ph.CO](#)].
- [3] N. Afshordi. “Integrated Sachs-Wolfe effect in cross - correlation: The Observer’s manual”. In: *Phys. Rev. D* 70 (2004), p. 083536. DOI: [10.1103/PhysRevD.70.083536](https://doi.org/10.1103/PhysRevD.70.083536). arXiv: [astro-ph/0401166](https://arxiv.org/abs/astro-ph/0401166).
- [4] S. Ho et al. “Correlation of CMB with large-scale structure: I. ISW Tomography and Cosmological Implications”. In: *Phys. Rev. D* 78 (2008), p. 043519. DOI: [10.1103/PhysRevD.78.043519](https://doi.org/10.1103/PhysRevD.78.043519). arXiv: [0801.0642](https://arxiv.org/abs/0801.0642) [[astro-ph](#)].
- [5] A. Lewis and A. Challinor. “Weak gravitational lensing of the CMB”. In: *Phys. Rept.* 429 (2006), pp. 1–65. DOI: [10.1016/j.physrep.2006.03.002](https://doi.org/10.1016/j.physrep.2006.03.002). arXiv: [astro-ph/0601594](https://arxiv.org/abs/astro-ph/0601594).
- [6] A. Einstein. “The Foundation of the General Theory of Relativity”. In: *Annalen Phys.* 49.7 (1916). [*Annalen Phys.*354,no.7,769(1916)], pp. 769–822. DOI: [10.1002/andp.200590044](https://doi.org/10.1002/andp.200590044), [10.1002/andp.19163540702](https://doi.org/10.1002/andp.19163540702).
- [7] C. M. Will. “The Confrontation between General Relativity and Experiment”. In: *Living Reviews in Relativity* 17.1 (June 2014). ISSN: 1433-8351. DOI: [10.12942/lrr-2014-4](https://doi.org/10.12942/lrr-2014-4). URL: <http://dx.doi.org/10.12942/lrr-2014-4>.
- [8] S. M. Carroll. *Spacetime and Geometry: An Introduction to General Relativity*. Cambridge University Press, 2019. DOI: [10.1017/9781108770385](https://doi.org/10.1017/9781108770385).
- [9] S. Weinberg. *Cosmology*. Cosmology. OUP Oxford, 2008. ISBN: 9780191523601. URL: <https://books.google.it/books?id=nqQZdg020fsC>.
- [10] E. Hubble. “A relation between distance and radial velocity among extra-galactic nebulae”. In: *Proceedings of the National Academy of Sciences* 15.3 (1929), pp. 168–173. ISSN: 0027-8424. DOI: [10.1073/pnas.15.3.168](https://doi.org/10.1073/pnas.15.3.168). eprint: <https://www.pnas.org/content/15/3/168.full.pdf>. URL: <https://www.pnas.org/content/15/3/168>.
- [11] S. Weinberg. “The Cosmological Constant Problem”. In: *Rev. Mod. Phys.* 61 (1989). Ed. by J.-P. Hsu and D. Fine, pp. 1–23. DOI: [10.1103/RevModPhys.61.1](https://doi.org/10.1103/RevModPhys.61.1).
- [12] Planck Collaboration et al. “Planck 2018 results. I. Overview and the cosmological legacy of Planck”. In: *arXiv e-prints*, arXiv:1807.06205 (July 2018), arXiv:1807.06205. arXiv: [1807.06205](https://arxiv.org/abs/1807.06205) [[astro-ph.CO](#)].
- [13] R. H. Dicke et al. “Cosmic Black-Body Radiation”. In: *Astrophys. J.* 142 (1965), pp. 414–419. DOI: [10.1086/148306](https://doi.org/10.1086/148306).
- [14] A. M. Boesgaard and G. Steigman. “Big Bang Nucleosynthesis: Theories and Observations”. In: *Ann. Rev. Astron. Astrophys.* 23 (1985), pp. 319–378. DOI: [10.1146/annurev.aa.23.090185.001535](https://doi.org/10.1146/annurev.aa.23.090185.001535).
- [15] C.-P. Ma and E. Bertschinger. “Cosmological Perturbation Theory in the Synchronous and Conformal Newtonian Gauges”. In: *ApJ* 455 (Dec. 1995), p. 7. DOI: [10.1086/176550](https://doi.org/10.1086/176550). arXiv: [astro-ph/9506072](https://arxiv.org/abs/astro-ph/9506072) [[astro-ph](#)].

Bibliography

- [16] J. Lesgourgues. “Cosmological Perturbations”. In: *Theoretical Advanced Study Institute in Elementary Particle Physics: Searching for New Physics at Small and Large Scales*. 2013, pp. 29–97. DOI: [10.1142/9789814525220_0002](https://doi.org/10.1142/9789814525220_0002). arXiv: [1302.4640](https://arxiv.org/abs/1302.4640) [[astro-ph.CO](#)].
- [17] D. Baumann. *Cosmology*. 2012. URL: http://physics.bu.edu/~schmaltz/PY555/baumann_notes.pdf.
- [18] S. Dodelson and F. Schmidt. *Modern Cosmology*. 2020. DOI: [10.1016/C2017-0-01943-2](https://doi.org/10.1016/C2017-0-01943-2).
- [19] J. M. Bardeen. “Gauge-invariant cosmological perturbations”. In: *Phys. Rev. D* 22.8 (Oct. 1980), pp. 1882–1905. DOI: [10.1103/PhysRevD.22.1882](https://doi.org/10.1103/PhysRevD.22.1882).
- [20] D. Blas, J. Lesgourgues, and T. Tram. “The Cosmic Linear Anisotropy Solving System (CLASS) II: Approximation schemes”. In: *JCAP* 07 (2011), p. 034. DOI: [10.1088/1475-7516/2011/07/034](https://doi.org/10.1088/1475-7516/2011/07/034). arXiv: [1104.2933](https://arxiv.org/abs/1104.2933) [[astro-ph.CO](#)].
- [21] W. Hu and M. J. White. “A CMB polarization primer”. In: *New Astron.* 2 (1997), p. 323. DOI: [10.1016/S1384-1076\(97\)00022-5](https://doi.org/10.1016/S1384-1076(97)00022-5). arXiv: [astro-ph/9706147](https://arxiv.org/abs/astro-ph/9706147).
- [22] M. Bucher, K. Moodley, and N. Turok. “General primordial cosmic perturbation”. In: *Phys. Rev. D* 62.8, 083508 (Oct. 2000), p. 083508. DOI: [10.1103/PhysRevD.62.083508](https://doi.org/10.1103/PhysRevD.62.083508). arXiv: [astro-ph/9904231](https://arxiv.org/abs/astro-ph/9904231) [[astro-ph](#)].
- [23] A. R. Liddle and D. H. Lyth. *Cosmological Inflation and Large-Scale Structure*. Cambridge University Press, 2000. DOI: [10.1017/CB09781139175180](https://doi.org/10.1017/CB09781139175180).
- [24] Planck Collaboration et al. “Planck 2018 results. X. Constraints on inflation”. In: *arXiv e-prints*, arXiv:1807.06211 (July 2018), arXiv:1807.06211. arXiv: [1807.06211](https://arxiv.org/abs/1807.06211) [[astro-ph.CO](#)].
- [25] H. Kurki-Suonio. *Cosmological Perturbation Theory, part 1*. Lecture notes for a course on cosmological perturbation theory given at the University of Helsinki. 2015.
- [26] J. Lesgourgues. “The Cosmic Linear Anisotropy Solving System (CLASS) I: Overview”. In: *arXiv e-prints*, arXiv:1104.2932 (Apr. 2011), arXiv:1104.2932. arXiv: [1104.2932](https://arxiv.org/abs/1104.2932) [[astro-ph.IM](#)].
- [27] A. Lewis, A. Challinor, and A. Lasenby. “Efficient computation of CMB anisotropies in closed FRW models”. In: *ApJ* 538 (2000), pp. 473–476. DOI: [10.1086/309179](https://doi.org/10.1086/309179). arXiv: [astro-ph/9911177](https://arxiv.org/abs/astro-ph/9911177) [[astro-ph](#)].
- [28] D. J. Fixsen. “The Temperature of the Cosmic Microwave Background”. In: *ApJ* 707.2 (Dec. 2009), pp. 916–920. DOI: [10.1088/0004-637X/707/2/916](https://doi.org/10.1088/0004-637X/707/2/916). arXiv: [0911.1955](https://arxiv.org/abs/0911.1955) [[astro-ph.CO](#)].
- [29] R. K. Sachs and A. M. Wolfe. “Perturbations of a Cosmological Model and Angular Variations of the Microwave Background”. In: *ApJ* 147 (Jan. 1967), p. 73. DOI: [10.1086/148982](https://doi.org/10.1086/148982).
- [30] A. Challinor and H. Peiris. “Lecture notes on the physics of cosmic microwave background anisotropies”. In: *Cosmology and Gravitation: XIII Brazilian School on Cosmology and Gravitation (XIII BSCG)*. Ed. by M. Novello and S. Perez. Vol. 1132. American Institute of Physics Conference Series. May 2009, pp. 86–140. DOI: [10.1063/1.3151849](https://doi.org/10.1063/1.3151849). arXiv: [0903.5158](https://arxiv.org/abs/0903.5158) [[astro-ph.CO](#)].

Bibliography

- [31] N. Aghanim et al. “Planck 2018 results. V. CMB power spectra and likelihoods”. In: *Astron. Astrophys.* 641 (2020), A5. DOI: [10.1051/0004-6361/201936386](https://doi.org/10.1051/0004-6361/201936386). arXiv: [1907.12875](https://arxiv.org/abs/1907.12875) [[astro-ph.CO](#)].
- [32] N. Aghanim et al. “Planck 2018 results. VIII. Gravitational lensing”. In: *Astron. Astrophys.* 641 (2020), A8. DOI: [10.1051/0004-6361/201833886](https://doi.org/10.1051/0004-6361/201833886). arXiv: [1807.06210](https://arxiv.org/abs/1807.06210) [[astro-ph.CO](#)].
- [33] S. Chandrasekhar and E. A. Milne. “The Highly Collapsed Configurations of a Stellar Mass”. In: *Monthly Notices of the Royal Astronomical Society* 91.5 (Mar. 1931), pp. 456–466. ISSN: 0035-8711. DOI: [10.1093/mnras/91.5.456](https://doi.org/10.1093/mnras/91.5.456). eprint: <https://academic.oup.com/mnras/article-pdf/91/5/456/3079698/mnras91-0456.pdf>. URL: <https://doi.org/10.1093/mnras/91.5.456>.
- [34] A. Goobar and B. Leibundgut. “Supernova Cosmology: Legacy and Future”. In: *Annual Review of Nuclear and Particle Science* 61.1 (Nov. 2011), pp. 251–279. DOI: [10.1146/annurev-nucl-102010-130434](https://doi.org/10.1146/annurev-nucl-102010-130434). arXiv: [1102.1431](https://arxiv.org/abs/1102.1431) [[astro-ph.CO](#)].
- [35] P. Schneider. *Extragalactic Astronomy and Cosmology*. Berlin, Heidelberg: Springer Berlin Heidelberg, 2006. ISBN: 978-3-540-33174-2. DOI: [10.1007/978-3-540-33175-9](https://doi.org/10.1007/978-3-540-33175-9). URL: <http://dx.doi.org/10.1007/978-3-540-33175-9>.
- [36] A. G. Riess et al. “Observational evidence from supernovae for an accelerating universe and a cosmological constant”. In: *Astron. J.* 116 (1998), pp. 1009–1038. DOI: [10.1086/300499](https://doi.org/10.1086/300499). arXiv: [astro-ph/9805201](https://arxiv.org/abs/astro-ph/9805201).
- [37] S. Perlmutter et al. “Measurements of Ω and Λ from 42 high redshift supernovae”. In: *Astrophys. J.* 517 (1999), pp. 565–586. DOI: [10.1086/307221](https://doi.org/10.1086/307221). arXiv: [astro-ph/9812133](https://arxiv.org/abs/astro-ph/9812133).
- [38] A. G. Riess et al. “A Comprehensive Measurement of the Local Value of the Hubble Constant with 1 km s⁻¹ Mpc⁻¹ Uncertainty from the Hubble Space Telescope and the SH0ES Team”. In: *Astrophys. J. Lett.* 934.1 (2022), p. L7. DOI: [10.3847/2041-8213/ac5c5b](https://doi.org/10.3847/2041-8213/ac5c5b). arXiv: [2112.04510](https://arxiv.org/abs/2112.04510) [[astro-ph.CO](#)].
- [39] D. M. Scolnic et al. “The Complete Light-curve Sample of Spectroscopically Confirmed SNe Ia from Pan-STARRS1 and Cosmological Constraints from the Combined Pantheon Sample”. In: *Astrophys. J.* 859.2 (2018), p. 101. DOI: [10.3847/1538-4357/aab9bb](https://doi.org/10.3847/1538-4357/aab9bb). arXiv: [1710.00845](https://arxiv.org/abs/1710.00845) [[astro-ph.CO](#)].
- [40] D. Camarena and V. Marra. “On the use of the local prior on the absolute magnitude of Type Ia supernovae in cosmological inference”. In: *Mon. Not. Roy. Astron. Soc.* 504 (2021), pp. 5164–5171. DOI: [10.1093/mnras/stab1200](https://doi.org/10.1093/mnras/stab1200). arXiv: [2101.08641](https://arxiv.org/abs/2101.08641) [[astro-ph.CO](#)].
- [41] R. E. Smith et al. “Stable clustering, the halo model and nonlinear cosmological power spectra”. In: *Mon. Not. Roy. Astron. Soc.* 341 (2003), p. 1311. DOI: [10.1046/j.1365-8711.2003.06503.x](https://doi.org/10.1046/j.1365-8711.2003.06503.x). arXiv: [astro-ph/0207664](https://arxiv.org/abs/astro-ph/0207664).
- [42] S. Bird, M. Viel, and M. G. Haehnelt. “Massive Neutrinos and the Non-linear Matter Power Spectrum”. In: *Mon. Not. Roy. Astron. Soc.* 420 (2012), pp. 2551–2561. DOI: [10.1111/j.1365-2966.2011.20222.x](https://doi.org/10.1111/j.1365-2966.2011.20222.x). arXiv: [1109.4416](https://arxiv.org/abs/1109.4416) [[astro-ph.CO](#)].
- [43] R. Takahashi et al. “Revising the Halofit Model for the Nonlinear Matter Power Spectrum”. In: *Astrophys. J.* 761 (2012), p. 152. DOI: [10.1088/0004-637X/761/2/152](https://doi.org/10.1088/0004-637X/761/2/152). arXiv: [1208.2701](https://arxiv.org/abs/1208.2701) [[astro-ph.CO](#)].

Bibliography

- [44] A. Mead et al. “Accurate halo-model matter power spectra with dark energy, massive neutrinos and modified gravitational forces”. In: *Mon. Not. Roy. Astron. Soc.* 459.2 (2016), pp. 1468–1488. DOI: [10.1093/mnras/stw681](https://doi.org/10.1093/mnras/stw681). arXiv: [1602.02154](https://arxiv.org/abs/1602.02154) [[astro-ph.CO](#)].
- [45] A. Mead et al. “HMcode-2020: Improved modelling of non-linear cosmological power spectra with baryonic feedback”. In: (Sept. 2020). DOI: [10.1093/mnras/stab082](https://doi.org/10.1093/mnras/stab082). arXiv: [2009.01858](https://arxiv.org/abs/2009.01858) [[astro-ph.CO](#)].
- [46] N. Kaiser. “Clustering in real space and in redshift space”. In: *MNRAS* 227 (July 1987), pp. 1–21. DOI: [10.1093/mnras/227.1.1](https://doi.org/10.1093/mnras/227.1.1).
- [47] J. Tonry and M. Davis. “A survey of galaxy redshifts. I. Data reduction techniques.” In: *AJ* 84 (Oct. 1979), pp. 1511–1525. DOI: [10.1086/112569](https://doi.org/10.1086/112569).
- [48] S. Alam et al. “Completed SDSS-IV extended Baryon Oscillation Spectroscopic Survey: Cosmological implications from two decades of spectroscopic surveys at the Apache Point Observatory”. In: *Phys. Rev. D* 103.8 (2021), p. 083533. DOI: [10.1103/PhysRevD.103.083533](https://doi.org/10.1103/PhysRevD.103.083533). arXiv: [2007.08991](https://arxiv.org/abs/2007.08991) [[astro-ph.CO](#)].
- [49] I. Sevilla-Noarbe et al. “Dark Energy Survey Year 3 Results: Photometric Data Set for Cosmology”. In: *Astrophys. J. Suppl.* 254.2 (2021), p. 24. DOI: [10.3847/1538-4365/abeb66](https://doi.org/10.3847/1538-4365/abeb66). arXiv: [2011.03407](https://arxiv.org/abs/2011.03407) [[astro-ph.CO](#)].
- [50] T. M. C. Abbott et al. “Dark Energy Survey Year 3 results: Cosmological constraints from galaxy clustering and weak lensing”. In: *Phys. Rev. D* 105.2 (2022), p. 023520. DOI: [10.1103/PhysRevD.105.023520](https://doi.org/10.1103/PhysRevD.105.023520). arXiv: [2105.13549](https://arxiv.org/abs/2105.13549) [[astro-ph.CO](#)].
- [51] D. J. Eisenstein et al. “Detection of the Baryon Acoustic Peak in the Large-Scale Correlation Function of SDSS Luminous Red Galaxies”. In: *Astrophys. J.* 633 (2005), pp. 560–574. DOI: [10.1086/466512](https://doi.org/10.1086/466512). arXiv: [astro-ph/0501171](https://arxiv.org/abs/astro-ph/0501171).
- [52] S. Alam et al. “The clustering of galaxies in the completed SDSS-III Baryon Oscillation Spectroscopic Survey: cosmological analysis of the DR12 galaxy sample”. In: *Mon. Not. Roy. Astron. Soc.* 470.3 (2017), pp. 2617–2652. DOI: [10.1093/mnras/stx721](https://doi.org/10.1093/mnras/stx721). arXiv: [1607.03155](https://arxiv.org/abs/1607.03155) [[astro-ph.CO](#)].
- [53] P. Zarrouk et al. “The clustering of the SDSS-IV extended Baryon Oscillation Spectroscopic Survey DR14 quasar sample: measurement of the growth rate of structure from the anisotropic correlation function between redshift 0.8 and 2.2”. In: *Mon. Not. Roy. Astron. Soc.* 477.2 (2018), pp. 1639–1663. DOI: [10.1093/mnras/sty506](https://doi.org/10.1093/mnras/sty506). arXiv: [1801.03062](https://arxiv.org/abs/1801.03062) [[astro-ph.CO](#)].
- [54] V. de Sainte Agathe et al. “Baryon acoustic oscillations at $z = 2.34$ from the correlations of Ly α absorption in eBOSS DR14”. In: *Astron. Astrophys.* 629 (2019), A85. DOI: [10.1051/0004-6361/201935638](https://doi.org/10.1051/0004-6361/201935638). arXiv: [1904.03400](https://arxiv.org/abs/1904.03400) [[astro-ph.CO](#)].
- [55] M. Blomqvist et al. “Baryon acoustic oscillations from the cross-correlation of Ly α absorption and quasars in eBOSS DR14”. In: *Astron. Astrophys.* 629 (2019), A86. DOI: [10.1051/0004-6361/201935641](https://doi.org/10.1051/0004-6361/201935641). arXiv: [1904.03430](https://arxiv.org/abs/1904.03430) [[astro-ph.CO](#)].
- [56] A. G. Riess et al. “Large Magellanic Cloud Cepheid Standards Provide a 1% Foundation for the Determination of the Hubble Constant and Stronger Evidence for Physics beyond Λ CDM”. In: *Astrophys. J.* 876.1 (2019), p. 85. DOI: [10.3847/1538-4357/ab1422](https://doi.org/10.3847/1538-4357/ab1422). arXiv: [1903.07603](https://arxiv.org/abs/1903.07603) [[astro-ph.CO](#)].

Bibliography

- [57] M. Colless et al. “The 2dF Galaxy Redshift Survey: Spectra and redshifts”. In: *Mon. Not. Roy. Astron. Soc.* 328 (2001), p. 1039. DOI: [10.1046/j.1365-8711.2001.04902.x](https://doi.org/10.1046/j.1365-8711.2001.04902.x). arXiv: [astro-ph/0106498](https://arxiv.org/abs/astro-ph/0106498).
- [58] F. Beutler et al. “The 6dF Galaxy Survey: baryon acoustic oscillations and the local Hubble constant”. In: *MNRAS* 416.4 (Oct. 2011), pp. 3017–3032. DOI: [10.1111/j.1365-2966.2011.19250.x](https://doi.org/10.1111/j.1365-2966.2011.19250.x). arXiv: [1106.3366](https://arxiv.org/abs/1106.3366) [[astro-ph.CO](https://arxiv.org/abs/1106.3366)].
- [59] A. J. Ross et al. “The clustering of the SDSS DR7 main Galaxy sample – I. A 4 per cent distance measure at $z = 0.15$ ”. In: *Mon. Not. Roy. Astron. Soc.* 449.1 (2015), pp. 835–847. DOI: [10.1093/mnras/stv154](https://doi.org/10.1093/mnras/stv154). arXiv: [1409.3242](https://arxiv.org/abs/1409.3242) [[astro-ph.CO](https://arxiv.org/abs/1409.3242)].
- [60] A. Cuceu et al. “Baryon Acoustic Oscillations and the Hubble Constant: Past, Present and Future”. In: *JCAP* 10 (2019), p. 044. DOI: [10.1088/1475-7516/2019/10/044](https://doi.org/10.1088/1475-7516/2019/10/044). arXiv: [1906.11628](https://arxiv.org/abs/1906.11628) [[astro-ph.CO](https://arxiv.org/abs/1906.11628)].
- [61] H. Gil-Marín et al. “The clustering of galaxies in the SDSS-III Baryon Oscillation Spectroscopic Survey: RSD measurement from the LOS-dependent power spectrum of DR12 BOSS galaxies”. In: *Mon. Not. Roy. Astron. Soc.* 460.4 (2016), pp. 4188–4209. DOI: [10.1093/mnras/stw1096](https://doi.org/10.1093/mnras/stw1096). arXiv: [1509.06386](https://arxiv.org/abs/1509.06386) [[astro-ph.CO](https://arxiv.org/abs/1509.06386)].
- [62] G. D’Amico, L. Senatore, and P. Zhang. “Limits on w CDM from the EFTofLSS with the PyBird code”. In: *JCAP* 01 (2021), p. 006. DOI: [10.1088/1475-7516/2021/01/006](https://doi.org/10.1088/1475-7516/2021/01/006). arXiv: [2003.07956](https://arxiv.org/abs/2003.07956) [[astro-ph.CO](https://arxiv.org/abs/2003.07956)].
- [63] N. Kaiser. “Weak lensing and cosmology”. In: *Astrophys. J.* 498 (1998), p. 26. DOI: [10.1086/305515](https://doi.org/10.1086/305515). arXiv: [astro-ph/9610120](https://arxiv.org/abs/astro-ph/9610120).
- [64] D. J. Bacon, A. R. Refregier, and R. S. Ellis. “Detection of weak gravitational lensing by large-scale structure”. In: *Mon. Not. Roy. Astron. Soc.* 318 (2000), p. 625. DOI: [10.1046/j.1365-8711.2000.03851.x](https://doi.org/10.1046/j.1365-8711.2000.03851.x). arXiv: [astro-ph/0003008](https://arxiv.org/abs/astro-ph/0003008).
- [65] L. van Waerbeke et al. “Detection of correlated galaxy ellipticities on CFHT data: First evidence for gravitational lensing by large scale structures”. In: *Astron. Astrophys.* 358 (2000), pp. 30–44. arXiv: [astro-ph/0002500](https://arxiv.org/abs/astro-ph/0002500).
- [66] D. M. Wittman et al. “Detection of weak gravitational lensing distortions of distant galaxies by cosmic dark matter at large scales”. In: *Nature* 405 (2000), pp. 143–149. DOI: [10.1038/35012001](https://doi.org/10.1038/35012001). arXiv: [astro-ph/0003014](https://arxiv.org/abs/astro-ph/0003014).
- [67] M. Chevallier and D. Polarski. “Accelerating universes with scaling dark matter”. In: *Int. J. Mod. Phys. D* 10 (2001), pp. 213–224. DOI: [10.1142/S0218271801000822](https://doi.org/10.1142/S0218271801000822). arXiv: [gr-qc/0009008](https://arxiv.org/abs/gr-qc/0009008).
- [68] E. V. Linder. “Exploring the expansion history of the universe”. In: *Phys. Rev. Lett.* 90 (2003), p. 091301. DOI: [10.1103/PhysRevLett.90.091301](https://doi.org/10.1103/PhysRevLett.90.091301). arXiv: [astro-ph/0208512](https://arxiv.org/abs/astro-ph/0208512).
- [69] E. Di Valentino et al. “Snowmass2021 - Letter of interest cosmology intertwined II: The hubble constant tension”. In: *Astropart. Phys.* 131 (2021), p. 102605. DOI: [10.1016/j.astropartphys.2021.102605](https://doi.org/10.1016/j.astropartphys.2021.102605). arXiv: [2008.11284](https://arxiv.org/abs/2008.11284) [[astro-ph.CO](https://arxiv.org/abs/2008.11284)].
- [70] L. Perivolaropoulos and F. Skara. “Challenges for Λ CDM: An update”. In: *New Astron. Rev.* 95 (2022), p. 101659. DOI: [10.1016/j.newar.2022.101659](https://doi.org/10.1016/j.newar.2022.101659). arXiv: [2105.05208](https://arxiv.org/abs/2105.05208) [[astro-ph.CO](https://arxiv.org/abs/2105.05208)].

Bibliography

- [71] E. Di Valentino et al. “Cosmology intertwined III: $f\sigma_8$ and S_8 ”. In: *Astropart. Phys.* 131 (2021), p. 102604. DOI: [10.1016/j.astropartphys.2021.102604](https://doi.org/10.1016/j.astropartphys.2021.102604). arXiv: [2008.11285](https://arxiv.org/abs/2008.11285) [astro-ph.CO].
- [72] K. Koyama. “Cosmological Tests of Modified Gravity”. In: *Rept. Prog. Phys.* 79.4 (2016), p. 046902. DOI: [10.1088/0034-4885/79/4/046902](https://doi.org/10.1088/0034-4885/79/4/046902). arXiv: [1504.04623](https://arxiv.org/abs/1504.04623) [astro-ph.CO].
- [73] P. Jordan. *Schwerkraft und Weltall: Grundlagen der theoretischen Kosmologie*. Die Wissenschaft. F. Vieweg, 1955. URL: <https://books.google.it/books?id=snJTcgAACAAJ>.
- [74] C. Brans and R. H. Dicke. “Mach’s Principle and a Relativistic Theory of Gravitation”. In: *Phys. Rev.* 124 (3 Nov. 1961), pp. 925–935. DOI: [10.1103/PhysRev.124.925](https://doi.org/10.1103/PhysRev.124.925). URL: <https://link.aps.org/doi/10.1103/PhysRev.124.925>.
- [75] P. A. M. Dirac. “A New Basis for Cosmology”. In: *Proceedings of the Royal Society of London Series A* 165.921 (Apr. 1938), pp. 199–208. DOI: [10.1098/rspa.1938.0053](https://doi.org/10.1098/rspa.1938.0053).
- [76] Y. Fujii and K. Maeda. *The scalar-tensor theory of gravitation*. Cambridge Monographs on Mathematical Physics. Cambridge University Press, 2007. ISBN: 9780521037525, 9780521811590, 9780511029882. DOI: [10.1017/CB09780511535093](https://doi.org/10.1017/CB09780511535093). URL: <http://www.cambridge.org/uk/catalogue/catalogue.asp?isbn=0521811597>.
- [77] G. W. Horndeski. “Second-order scalar-tensor field equations in a four-dimensional space”. In: *Int. J. Theor. Phys.* 10 (1974), pp. 363–384. DOI: [10.1007/BF01807638](https://doi.org/10.1007/BF01807638).
- [78] A. G. Ferrari. “Cosmological effects of the Galileon term in scalar-tensor theories”. PhD thesis. URL: <http://amslaurea.unibo.it/20760/>.
- [79] M. Ballardini, A. G. Ferrari, and F. Finelli. “Phantom scalar-tensor models and cosmological tensions”. In: *JCAP* 04 (2023), p. 029. DOI: [10.1088/1475-7516/2023/04/029](https://doi.org/10.1088/1475-7516/2023/04/029). arXiv: [2302.05291](https://arxiv.org/abs/2302.05291) [astro-ph.CO].
- [80] A. G. Ferrari et al. “Cosmological effects of the Galileon term in scalar-tensor theories”. In: *Phys. Rev. D* 108.6 (2023), p. 063520. DOI: [10.1103/PhysRevD.108.063520](https://doi.org/10.1103/PhysRevD.108.063520). arXiv: [2307.02987](https://arxiv.org/abs/2307.02987) [astro-ph.CO].
- [81] R. P. Woodard. “Ostrogradsky’s theorem on Hamiltonian instability”. In: *Scholarpedia* 10.8 (2015), p. 32243. DOI: [10.4249/scholarpedia.32243](https://doi.org/10.4249/scholarpedia.32243). arXiv: [1506.02210](https://arxiv.org/abs/1506.02210) [hep-th].
- [82] C. Deffayet, G. Esposito-Farese, and A. Vikman. “Covariant Galileon”. In: *Phys. Rev. D* 79 (2009), p. 084003. DOI: [10.1103/PhysRevD.79.084003](https://doi.org/10.1103/PhysRevD.79.084003). arXiv: [0901.1314](https://arxiv.org/abs/0901.1314) [hep-th].
- [83] C. Deffayet et al. “From k-essence to generalised Galileons”. In: *Phys. Rev. D* 84 (2011), p. 064039. DOI: [10.1103/PhysRevD.84.064039](https://doi.org/10.1103/PhysRevD.84.064039). arXiv: [1103.3260](https://arxiv.org/abs/1103.3260) [hep-th].
- [84] A. Nicolis, R. Rattazzi, and E. Trincherini. “The Galileon as a local modification of gravity”. In: *Phys. Rev. D* 79 (2009), p. 064036. DOI: [10.1103/PhysRevD.79.064036](https://doi.org/10.1103/PhysRevD.79.064036). arXiv: [0811.2197](https://arxiv.org/abs/0811.2197) [hep-th].
- [85] T. Kobayashi, M. Yamaguchi, and J. Yokoyama. “Generalized G-inflation: Inflation with the most general second-order field equations”. In: *Prog. Theor.*

Bibliography

- Phys.* 126 (2011), pp. 511–529. DOI: [10.1143/PTP.126.511](https://doi.org/10.1143/PTP.126.511). arXiv: [1105.5723](https://arxiv.org/abs/1105.5723) [[hep-th](#)].
- [86] C. Armendáriz-Picón, T. Damour, and V. Mukhanov. “k-Inflation”. In: *Physics Letters B* 458.2-3 (July 1999), 209–218. ISSN: 0370-2693. DOI: [10.1016/S0370-2693\(99\)00603-6](https://doi.org/10.1016/S0370-2693(99)00603-6). URL: [http://dx.doi.org/10.1016/S0370-2693\(99\)00603-6](http://dx.doi.org/10.1016/S0370-2693(99)00603-6).
- [87] T. Chiba, T. Okabe, and M. Yamaguchi. “Kinetically driven quintessence”. In: *Physical Review D* 62.2 (June 2000). ISSN: 1089-4918. DOI: [10.1103/PhysRevD.62.023511](https://doi.org/10.1103/PhysRevD.62.023511). URL: <http://dx.doi.org/10.1103/PhysRevD.62.023511>.
- [88] C. Armendariz-Picon, V. Mukhanov, and P. J. Steinhardt. “Dynamical Solution to the Problem of a Small Cosmological Constant and Late-Time Cosmic Acceleration”. In: *Phys. Rev. Lett.* 85.21 (Nov. 2000), pp. 4438–4441. DOI: [10.1103/PhysRevLett.85.4438](https://doi.org/10.1103/PhysRevLett.85.4438). arXiv: [astro-ph/0004134](https://arxiv.org/abs/astro-ph/0004134) [[astro-ph](#)].
- [89] C. Armendariz-Picon, V. Mukhanov, and P. J. Steinhardt. “Essentials of k-essence”. In: *Phys. Rev. D* 63.10, 103510 (May 2001), p. 103510. DOI: [10.1103/PhysRevD.63.103510](https://doi.org/10.1103/PhysRevD.63.103510). arXiv: [astro-ph/0006373](https://arxiv.org/abs/astro-ph/0006373) [[astro-ph](#)].
- [90] P. J. E. Peebles and B. Ratra. “Cosmology with a Time-Variable Cosmological “Constant””. In: *ApJ* 325 (Feb. 1988), p. L17. DOI: [10.1086/185100](https://doi.org/10.1086/185100).
- [91] P. J. Peebles and B. Ratra. “The cosmological constant and dark energy”. In: *Reviews of Modern Physics* 75.2 (Apr. 2003), pp. 559–606. DOI: [10.1103/RevModPhys.75.559](https://doi.org/10.1103/RevModPhys.75.559). arXiv: [astro-ph/0207347](https://arxiv.org/abs/astro-ph/0207347) [[astro-ph](#)].
- [92] B. Bertotti, L. Iess, and P. Tortora. “A test of general relativity using radio links with the Cassini spacecraft”. In: *Nature* 425.6956 (Sept. 2003), pp. 374–376. DOI: [10.1038/nature01997](https://doi.org/10.1038/nature01997).
- [93] A. D. Sakharov. “Vacuum quantum fluctuations in curved space and the theory of gravitation”. In: *Sov. Phys. Dokl.* 12 (1968). [Dokl. Akad. Nauk Ser. Fiz.177,70(1967); *Sov. Phys. Usp.*34,no.5,394(1991); *Gen. Rel. Grav.*32,365(2000); *Usp. Fiz. Nauk*161,no.5,64(1991),51(1967)], pp. 1040–1041.
- [94] A. Zee. “Broken-Symmetric Theory of Gravity”. In: *Phys. Rev. Lett.* 42 (7 Feb. 1979), pp. 417–421. DOI: [10.1103/PhysRevLett.42.417](https://doi.org/10.1103/PhysRevLett.42.417). URL: <https://link.aps.org/doi/10.1103/PhysRevLett.42.417>.
- [95] S. L. Adler. “Einstein gravity as a symmetry-breaking effect in quantum field theory”. In: *Rev. Mod. Phys.* 54 (3 July 1982), pp. 729–766. DOI: [10.1103/RevModPhys.54.729](https://doi.org/10.1103/RevModPhys.54.729). URL: <https://link.aps.org/doi/10.1103/RevModPhys.54.729>.
- [96] F. Finelli, A. Tronconi, and G. Venturi. “Dark Energy, Induced Gravity and Broken Scale Invariance”. In: *Phys. Lett. B* 659 (2008), pp. 466–470. DOI: [10.1016/j.physletb.2007.11.053](https://doi.org/10.1016/j.physletb.2007.11.053). arXiv: [0710.2741](https://arxiv.org/abs/0710.2741) [[astro-ph](#)].
- [97] A. Cerioni et al. “Inflation and reheating in induced gravity”. In: *Physics Letters B* 681.5 (Nov. 2009), pp. 383–386. DOI: [10.1016/j.physletb.2009.10.066](https://doi.org/10.1016/j.physletb.2009.10.066). arXiv: [0906.1902](https://arxiv.org/abs/0906.1902) [[astro-ph.CO](#)].
- [98] C. Umiltà et al. “CMB and BAO constraints for an induced gravity dark energy model with a quartic potential”. In: *JCAP* 08 (2015), p. 017. DOI: [10.1088/1475-7516/2015/08/017](https://doi.org/10.1088/1475-7516/2015/08/017). arXiv: [1507.00718](https://arxiv.org/abs/1507.00718) [[astro-ph.CO](#)].

Bibliography

- [99] M. Ballardini et al. “Cosmological constraints on induced gravity dark energy models”. In: *Journal of Cosmology and Astroparticle Physics* 2016.5, 067 (May 2016), p. 067. DOI: [10.1088/1475-7516/2016/05/067](https://doi.org/10.1088/1475-7516/2016/05/067). arXiv: [1601.03387](https://arxiv.org/abs/1601.03387) [[astro-ph.CO](#)].
- [100] D. Paoletti et al. “Isocurvature fluctuations in the effective Newton’s constant”. In: *Physics of the Dark Universe* 25, 100307 (Sept. 2019), p. 100307. DOI: [10.1016/j.dark.2019.100307](https://doi.org/10.1016/j.dark.2019.100307). arXiv: [1809.03201](https://arxiv.org/abs/1809.03201) [[astro-ph.CO](#)].
- [101] R. Gannouji et al. “Scalar-Tensor Models of Normal and Phantom Dark Energy”. In: *JCAP* 09 (2006), p. 016. DOI: [10.1088/1475-7516/2006/09/016](https://doi.org/10.1088/1475-7516/2006/09/016). arXiv: [astro-ph/0606287](https://arxiv.org/abs/astro-ph/0606287).
- [102] M. Gasperini and G. Veneziano. “Pre-big-bang in string cosmology”. In: *Astroparticle Physics* 1.3 (July 1993), pp. 317–339. DOI: [10.1016/0927-6505\(93\)90017-8](https://doi.org/10.1016/0927-6505(93)90017-8). arXiv: [hep-th/9211021](https://arxiv.org/abs/hep-th/9211021) [[hep-th](#)].
- [103] T. Damour and K. Nordtvedt. “Tensor - scalar cosmological models and their relaxation toward general relativity”. In: *Phys. Rev. D* 48 (1993), pp. 3436–3450. DOI: [10.1103/PhysRevD.48.3436](https://doi.org/10.1103/PhysRevD.48.3436).
- [104] T. Damour and A. M. Polyakov. “The string dilation and a least coupling principle”. In: *Nuclear Physics B* 423.2-3 (July 1994), pp. 532–558. DOI: [10.1016/0550-3213\(94\)90143-0](https://doi.org/10.1016/0550-3213(94)90143-0). arXiv: [hep-th/9401069](https://arxiv.org/abs/hep-th/9401069) [[hep-th](#)].
- [105] L. Amendola. “Scaling solutions in general nonminimal coupling theories”. In: *Phys. Rev. D* 60.4, 043501 (Aug. 1999), p. 043501. DOI: [10.1103/PhysRevD.60.043501](https://doi.org/10.1103/PhysRevD.60.043501). arXiv: [astro-ph/9904120](https://arxiv.org/abs/astro-ph/9904120) [[astro-ph](#)].
- [106] T. Chiba. “Quintessence, the gravitational constant, and gravity”. In: *Phys. Rev. D* 60.8, 083508 (Oct. 1999), p. 083508. DOI: [10.1103/PhysRevD.60.083508](https://doi.org/10.1103/PhysRevD.60.083508). arXiv: [gr-qc/9903094](https://arxiv.org/abs/gr-qc/9903094) [[gr-qc](#)].
- [107] F. Perrotta, C. Baccigalupi, and S. Matarrese. “Extended quintessence”. In: *Phys. Rev. D* 61.2, 023507 (Jan. 2000), p. 023507. DOI: [10.1103/PhysRevD.61.023507](https://doi.org/10.1103/PhysRevD.61.023507). arXiv: [astro-ph/9906066](https://arxiv.org/abs/astro-ph/9906066) [[astro-ph](#)].
- [108] B. Boisseau et al. “Reconstruction of a scalar tensor theory of gravity in an accelerating universe”. In: *Phys. Rev. Lett.* 85 (2000), p. 2236. DOI: [10.1103/PhysRevLett.85.2236](https://doi.org/10.1103/PhysRevLett.85.2236). arXiv: [gr-qc/0001066](https://arxiv.org/abs/gr-qc/0001066).
- [109] M. Rossi et al. “Cosmological constraints on post-Newtonian parameters in effectively massless scalar-tensor theories of gravity”. In: *Phys. Rev. D* 100.10 (2019), p. 103524. DOI: [10.1103/PhysRevD.100.103524](https://doi.org/10.1103/PhysRevD.100.103524). arXiv: [1906.10218](https://arxiv.org/abs/1906.10218) [[astro-ph.CO](#)].
- [110] M. Ballardini et al. “Scalar-tensor theories of gravity, neutrino physics, and the H_0 tension”. In: *arXiv e-prints*, arXiv:2004.14349 (Apr. 2020), arXiv:2004.14349. arXiv: [2004.14349](https://arxiv.org/abs/2004.14349) [[astro-ph.CO](#)].
- [111] M. Ballardini, F. Finelli, and D. Sapone. “Cosmological constraints on the gravitational constant”. In: *JCAP* 06.06 (2022), p. 004. DOI: [10.1088/1475-7516/2022/06/004](https://doi.org/10.1088/1475-7516/2022/06/004). arXiv: [2111.09168](https://arxiv.org/abs/2111.09168) [[astro-ph.CO](#)].
- [112] M. Braglia et al. “Early modified gravity in light of the H_0 tension and LSS data”. In: *Phys. Rev. D* 103.4 (2021), p. 043528. DOI: [10.1103/PhysRevD.103.043528](https://doi.org/10.1103/PhysRevD.103.043528). arXiv: [2011.12934](https://arxiv.org/abs/2011.12934) [[astro-ph.CO](#)].

Bibliography

- [113] R. Kase and S. Tsujikawa. “Dark energy in Horndeski theories after GW170817: A review”. In: *International Journal of Modern Physics D* 28.5, 1942005 (Jan. 2019), p. 1942005. DOI: [10.1142/S0218271819420057](https://doi.org/10.1142/S0218271819420057). arXiv: [1809.08735](https://arxiv.org/abs/1809.08735) [gr-qc].
- [114] C. Deffayet et al. “Imperfect dark energy from kinetic gravity braiding”. In: *Journal of Cosmology and Astroparticle Physics* 2010.10 (Oct. 2010), 026–026. ISSN: 1475-7516. DOI: [10.1088/1475-7516/2010/10/026](https://doi.org/10.1088/1475-7516/2010/10/026). URL: <http://dx.doi.org/10.1088/1475-7516/2010/10/026>.
- [115] O. Pujolàs, I. Sawicki, and A. Vikman. “The imperfect fluid behind kinetic gravity braiding”. In: *Journal of High Energy Physics* 2011.11 (Nov. 2011). ISSN: 1029-8479. DOI: [10.1007/jhep11\(2011\)156](https://doi.org/10.1007/jhep11(2011)156). URL: [http://dx.doi.org/10.1007/JHEP11\(2011\)156](http://dx.doi.org/10.1007/JHEP11(2011)156).
- [116] P. G. Bergmann. “Comments on the scalar-tensor theory”. In: *International Journal of Theoretical Physics* 1.1 (May 1968), pp. 25–36. DOI: [10.1007/BF00668828](https://doi.org/10.1007/BF00668828).
- [117] T. V. Ruzmaïkina and A. A. Ruzmaïkin. “Quadratic Corrections to the Lagrangian Density of the Gravitational Field and the Singularity”. In: *Soviet Journal of Experimental and Theoretical Physics* 30 (Jan. 1969), p. 372.
- [118] A. A. Starobinsky. “A New Type of Isotropic Cosmological Models Without Singularity”. In: *Phys. Lett. B* 91 (1980). Ed. by I. M. Khalatnikov and V. P. Mineev, pp. 99–102. DOI: [10.1016/0370-2693\(80\)90670-X](https://doi.org/10.1016/0370-2693(80)90670-X).
- [119] S. Nojiri, S. D. Odintsov, and M. Sasaki. “Gauss-Bonnet dark energy”. In: *Phys. Rev. D* 71 (2005), p. 123509. DOI: [10.1103/PhysRevD.71.123509](https://doi.org/10.1103/PhysRevD.71.123509). arXiv: [hep-th/0504052](https://arxiv.org/abs/hep-th/0504052).
- [120] T. Koivisto and D. F. Mota. “Gauss-Bonnet Quintessence: Background Evolution, Large Scale Structure and Cosmological Constraints”. In: *Phys. Rev. D* 75 (2007), p. 023518. DOI: [10.1103/PhysRevD.75.023518](https://doi.org/10.1103/PhysRevD.75.023518). arXiv: [hep-th/0609155](https://arxiv.org/abs/hep-th/0609155).
- [121] T. Koivisto and D. F. Mota. “Cosmology and Astrophysical Constraints of Gauss-Bonnet Dark Energy”. In: *Phys. Lett. B* 644 (2007), pp. 104–108. DOI: [10.1016/j.physletb.2006.11.048](https://doi.org/10.1016/j.physletb.2006.11.048). arXiv: [astro-ph/0606078](https://arxiv.org/abs/astro-ph/0606078).
- [122] S. Tsujikawa and M. Sami. “String-inspired cosmology: Late time transition from scaling matter era to dark energy universe caused by a Gauss-Bonnet coupling”. In: *JCAP* 01 (2007), p. 006. DOI: [10.1088/1475-7516/2007/01/006](https://doi.org/10.1088/1475-7516/2007/01/006). arXiv: [hep-th/0608178](https://arxiv.org/abs/hep-th/0608178).
- [123] S. Nojiri and S. D. Odintsov. “Modified Gauss-Bonnet theory as gravitational alternative for dark energy”. In: *Phys. Lett. B* 631 (2005), pp. 1–6. DOI: [10.1016/j.physletb.2005.10.010](https://doi.org/10.1016/j.physletb.2005.10.010). arXiv: [hep-th/0508049](https://arxiv.org/abs/hep-th/0508049).
- [124] A. De Felice and S. Tsujikawa. “Construction of cosmologically viable $f(G)$ dark energy models”. In: *Phys. Lett. B* 675 (2009), pp. 1–8. DOI: [10.1016/j.physletb.2009.03.060](https://doi.org/10.1016/j.physletb.2009.03.060). arXiv: [0810.5712](https://arxiv.org/abs/0810.5712) [hep-th].
- [125] T. Kobayashi. “Horndeski theory and beyond: a review”. In: *Reports on Progress in Physics* 82.8, 086901 (Aug. 2019), p. 086901. DOI: [10.1088/1361-6633/ab2429](https://doi.org/10.1088/1361-6633/ab2429). arXiv: [1901.07183](https://arxiv.org/abs/1901.07183) [gr-qc].
- [126] G. Gubitosi, F. Piazza, and F. Vernizzi. “The Effective Field Theory of Dark Energy”. In: *JCAP* 02 (2013), p. 032. DOI: [10.1088/1475-7516/2013/02/032](https://doi.org/10.1088/1475-7516/2013/02/032). arXiv: [1210.0201](https://arxiv.org/abs/1210.0201) [hep-th].

Bibliography

- [127] J. K. Bloomfield et al. “Dark energy or modified gravity? An effective field theory approach”. In: *JCAP* 08 (2013), p. 010. DOI: [10.1088/1475-7516/2013/08/010](https://doi.org/10.1088/1475-7516/2013/08/010). arXiv: [1211.7054](https://arxiv.org/abs/1211.7054) [[astro-ph.CO](#)].
- [128] M. Hohmann. “Parametrized post-Newtonian limit of Horndeski’s gravity theory”. In: *Phys. Rev. D* 92.6 (2015), p. 064019. DOI: [10.1103/PhysRevD.92.064019](https://doi.org/10.1103/PhysRevD.92.064019). arXiv: [1506.04253](https://arxiv.org/abs/1506.04253) [[gr-qc](#)].
- [129] I. Quiros et al. “An issue with the classification of the scalar–tensor theories of gravity”. In: *Int. J. Mod. Phys. D* 29.07 (2020), p. 2050047. DOI: [10.1142/S0218271820500479](https://doi.org/10.1142/S0218271820500479). arXiv: [1905.08177](https://arxiv.org/abs/1905.08177) [[gr-qc](#)].
- [130] D. F. Torres. “Quintessence, superquintessence and observable quantities in Brans-Dicke and nonminimally coupled theories”. In: *Phys. Rev. D* 66 (2002), p. 043522. DOI: [10.1103/PhysRevD.66.043522](https://doi.org/10.1103/PhysRevD.66.043522). arXiv: [astro-ph/0204504](https://arxiv.org/abs/astro-ph/0204504).
- [131] E. Bellini and I. Sawicki. “Maximal freedom at minimum cost: linear large-scale structure in general modifications of gravity”. In: *JCAP* 07 (2014), p. 050. DOI: [10.1088/1475-7516/2014/07/050](https://doi.org/10.1088/1475-7516/2014/07/050). arXiv: [1404.3713](https://arxiv.org/abs/1404.3713) [[astro-ph.CO](#)].
- [132] A. De Felice and S. Tsujikawa. “Conditions for the cosmological viability of the most general scalar-tensor theories and their applications to extended Galileon dark energy models”. In: *JCAP* 02 (2012), p. 007. DOI: [10.1088/1475-7516/2012/02/007](https://doi.org/10.1088/1475-7516/2012/02/007). arXiv: [1110.3878](https://arxiv.org/abs/1110.3878) [[gr-qc](#)].
- [133] J. Khoury and A. Weltman. “Chameleon Fields: Awaiting Surprises for Tests of Gravity in Space”. In: *Phys. Rev. Lett.* 93.17, 171104 (Oct. 2004), p. 171104. DOI: [10.1103/PhysRevLett.93.171104](https://doi.org/10.1103/PhysRevLett.93.171104). arXiv: [astro-ph/0309300](https://arxiv.org/abs/astro-ph/0309300) [[astro-ph](#)].
- [134] J. Khoury and A. Weltman. “Chameleon cosmology”. In: *Phys. Rev. D* 69.4, 044026 (Feb. 2004), p. 044026. DOI: [10.1103/PhysRevD.69.044026](https://doi.org/10.1103/PhysRevD.69.044026). arXiv: [astro-ph/0309411](https://arxiv.org/abs/astro-ph/0309411) [[astro-ph](#)].
- [135] K. Hinterbichler and J. Khoury. “Screening Long-Range Forces through Local Symmetry Restoration”. In: *Phys. Rev. Lett.* 104.23, 231301 (June 2010), p. 231301. DOI: [10.1103/PhysRevLett.104.231301](https://doi.org/10.1103/PhysRevLett.104.231301). arXiv: [1001.4525](https://arxiv.org/abs/1001.4525) [[hep-th](#)].
- [136] K. Hinterbichler et al. “Symmetron cosmology”. In: *Phys. Rev. D* 84.10, 103521 (Nov. 2011), p. 103521. DOI: [10.1103/PhysRevD.84.103521](https://doi.org/10.1103/PhysRevD.84.103521). arXiv: [1107.2112](https://arxiv.org/abs/1107.2112) [[astro-ph.CO](#)].
- [137] E. Babichev, C. Deffayet, and R. Ziour. “k-MOUFLAGE Gravity”. In: *International Journal of Modern Physics D* 18.14 (Jan. 2009), pp. 2147–2154. DOI: [10.1142/S0218271809016107](https://doi.org/10.1142/S0218271809016107). arXiv: [0905.2943](https://arxiv.org/abs/0905.2943) [[hep-th](#)].
- [138] A. Vainshtein. “To the problem of nonvanishing gravitation mass”. In: *Phys. Lett. B* 39 (1972), pp. 393–394. DOI: [10.1016/0370-2693\(72\)90147-5](https://doi.org/10.1016/0370-2693(72)90147-5).
- [139] R. Kimura, T. Kobayashi, and K. Yamamoto. “Vainshtein screening in a cosmological background in the most general second-order scalar-tensor theory”. In: *Phys. Rev. D* 85 (2012), p. 024023. DOI: [10.1103/PhysRevD.85.024023](https://doi.org/10.1103/PhysRevD.85.024023). arXiv: [1111.6749](https://arxiv.org/abs/1111.6749) [[astro-ph.CO](#)].
- [140] E. Babichev, C. Deffayet, and G. Esposito-Farese. “Constraints on Shift-Symmetric Scalar-Tensor Theories with a Vainshtein Mechanism from Bounds on the Time Variation of G ”. In: *Phys. Rev. Lett.* 107 (2011), p. 251102. DOI: [10.1103/PhysRevLett.107.251102](https://doi.org/10.1103/PhysRevLett.107.251102). arXiv: [1107.1569](https://arxiv.org/abs/1107.1569) [[gr-qc](#)].

Bibliography

- [141] T. Baker, D. Psaltis, and C. Skordis. “Linking Tests of Gravity On All Scales: from the Strong-Field Regime to Cosmology”. In: *Astrophys. J.* 802 (2015), p. 63. DOI: [10.1088/0004-637X/802/1/63](https://doi.org/10.1088/0004-637X/802/1/63). arXiv: [1412.3455](https://arxiv.org/abs/1412.3455) [[astro-ph.CO](#)].
- [142] A. Albrecht et al. “Report of the Dark Energy Task Force”. In: (Sept. 2006). arXiv: [astro-ph/0609591](https://arxiv.org/abs/astro-ph/0609591).
- [143] B. P. Abbott et al. “GW170817: Observation of Gravitational Waves from a Binary Neutron Star Inspiral”. In: *Phys. Rev. Lett.* 119.16 (2017), p. 161101. DOI: [10.1103/PhysRevLett.119.161101](https://doi.org/10.1103/PhysRevLett.119.161101). arXiv: [1710.05832](https://arxiv.org/abs/1710.05832) [[gr-qc](#)].
- [144] B. P. Abbott et al. “Gravitational Waves and Gamma-rays from a Binary Neutron Star Merger: GW170817 and GRB 170817A”. In: *Astrophys. J. Lett.* 848.2 (2017), p. L13. DOI: [10.3847/2041-8213/aa920c](https://doi.org/10.3847/2041-8213/aa920c). arXiv: [1710.05834](https://arxiv.org/abs/1710.05834) [[astro-ph.HE](#)].
- [145] B. P. Abbott et al. “Multi-messenger Observations of a Binary Neutron Star Merger”. In: *Astrophys. J. Lett.* 848.2 (2017), p. L12. DOI: [10.3847/2041-8213/aa91c9](https://doi.org/10.3847/2041-8213/aa91c9). arXiv: [1710.05833](https://arxiv.org/abs/1710.05833) [[astro-ph.HE](#)].
- [146] J. M. Ezquiaga and M. Zumalacárregui. “Dark Energy After GW170817: Dead Ends and the Road Ahead”. In: *Phys. Rev. Lett.* 119.25 (2017), p. 251304. DOI: [10.1103/PhysRevLett.119.251304](https://doi.org/10.1103/PhysRevLett.119.251304). arXiv: [1710.05901](https://arxiv.org/abs/1710.05901) [[astro-ph.CO](#)].
- [147] T. Baker et al. “Strong constraints on cosmological gravity from GW170817 and GRB 170817A”. In: *Phys. Rev. Lett.* 119.25 (2017), p. 251301. DOI: [10.1103/PhysRevLett.119.251301](https://doi.org/10.1103/PhysRevLett.119.251301). arXiv: [1710.06394](https://arxiv.org/abs/1710.06394) [[astro-ph.CO](#)].
- [148] C. de Rham and S. Melville. “Gravitational Rainbows: LIGO and Dark Energy at its Cutoff”. In: *Phys. Rev. Lett.* 121.22 (2018), p. 221101. DOI: [10.1103/PhysRevLett.121.221101](https://doi.org/10.1103/PhysRevLett.121.221101). arXiv: [1806.09417](https://arxiv.org/abs/1806.09417) [[hep-th](#)].
- [149] C. J. Copi, A. N. Davis, and L. M. Krauss. “A New nucleosynthesis constraint on the variation of G”. In: *Phys. Rev. Lett.* 92 (2004), p. 171301. DOI: [10.1103/PhysRevLett.92.171301](https://doi.org/10.1103/PhysRevLett.92.171301). arXiv: [astro-ph/0311334](https://arxiv.org/abs/astro-ph/0311334).
- [150] C. Bambi, M. Giannotti, and F. L. Villante. “The Response of primordial abundances to a general modification of G(N) and/or of the early Universe expansion rate”. In: *Phys. Rev. D* 71 (2005), p. 123524. DOI: [10.1103/PhysRevD.71.123524](https://doi.org/10.1103/PhysRevD.71.123524). arXiv: [astro-ph/0503502](https://arxiv.org/abs/astro-ph/0503502).
- [151] J. Alvey et al. “Improved BBN Constraints on the Variation of the Gravitational Constant”. In: *Eur. Phys. J. C* 80.2 (2020), p. 148. DOI: [10.1140/epjc/s10052-020-7727-y](https://doi.org/10.1140/epjc/s10052-020-7727-y). arXiv: [1910.10730](https://arxiv.org/abs/1910.10730) [[astro-ph.CO](#)].
- [152] I. I. Shapiro. “Fourth Test of General Relativity”. In: *Phys. Rev. Lett.* 13 (1964), pp. 789–791. DOI: [10.1103/PhysRevLett.13.789](https://doi.org/10.1103/PhysRevLett.13.789).
- [153] P. Brax, C. Burrage, and A.-C. Davis. “Laboratory Tests of the Galileon”. In: *JCAP* 09 (2011), p. 020. DOI: [10.1088/1475-7516/2011/09/020](https://doi.org/10.1088/1475-7516/2011/09/020). arXiv: [1106.1573](https://arxiv.org/abs/1106.1573) [[hep-ph](#)].
- [154] C. Xue et al. “Precision measurement of the Newtonian gravitational constant”. In: *National Science Review* 7.12 (July 2020), pp. 1803–1817. ISSN: 2095-5138. DOI: [10.1093/nsr/nwaa165](https://doi.org/10.1093/nsr/nwaa165). eprint: <https://academic.oup.com/nsr/article-pdf/7/12/1803/38880653/nwaa165.pdf>. URL: <https://doi.org/10.1093/nsr/nwaa165>.

Bibliography

- [155] Q. Li et al. “Measurements of the gravitational constant using two independent methods”. In: *Nature* 560.7720 (Aug. 2018), pp. 582–588. ISSN: 1476-4687. DOI: [10.1038/s41586-018-0431-5](https://doi.org/10.1038/s41586-018-0431-5). URL: <https://doi.org/10.1038/s41586-018-0431-5>.
- [156] R. Kimura, T. Kobayashi, and K. Yamamoto. “Observational Constraints on Kinetic Gravity Braiding from the Integrated Sachs-Wolfe Effect”. In: *Phys. Rev. D* 85 (2012), p. 123503. DOI: [10.1103/PhysRevD.85.123503](https://doi.org/10.1103/PhysRevD.85.123503). arXiv: [1110.3598](https://arxiv.org/abs/1110.3598) [[astro-ph.CO](https://arxiv.org/abs/1110.3598)].
- [157] A. Barreira et al. “The observational status of Galileon gravity after Planck”. In: *JCAP* 08 (2014), p. 059. DOI: [10.1088/1475-7516/2014/08/059](https://doi.org/10.1088/1475-7516/2014/08/059). arXiv: [1406.0485](https://arxiv.org/abs/1406.0485) [[astro-ph.CO](https://arxiv.org/abs/1406.0485)].
- [158] E. Bellini et al. “Constraints on deviations from Λ CDM within Horndeski gravity”. In: *JCAP* 02 (2016). [Erratum: *JCAP* 06, E01 (2016)], p. 053. DOI: [10.1088/1475-7516/2016/06/E01](https://doi.org/10.1088/1475-7516/2016/06/E01). arXiv: [1509.07816](https://arxiv.org/abs/1509.07816) [[astro-ph.CO](https://arxiv.org/abs/1509.07816)].
- [159] S. Peirone et al. “Do current cosmological observations rule out all Covariant Galileons?” In: *Phys. Rev. D* 97.6 (2018), p. 063518. DOI: [10.1103/PhysRevD.97.063518](https://doi.org/10.1103/PhysRevD.97.063518). arXiv: [1711.04760](https://arxiv.org/abs/1711.04760) [[astro-ph.CO](https://arxiv.org/abs/1711.04760)].
- [160] S. Peirone et al. “Cosmological data favor Galileon ghost condensate over Λ CDM”. In: *Phys. Rev. D* 100.6 (2019), p. 063540. DOI: [10.1103/PhysRevD.100.063540](https://doi.org/10.1103/PhysRevD.100.063540). arXiv: [1905.05166](https://arxiv.org/abs/1905.05166) [[astro-ph.CO](https://arxiv.org/abs/1905.05166)].
- [161] N. Frusciante et al. “Phenomenology of the generalized cubic covariant Galileon model and cosmological bounds”. In: *Phys. Rev. D* 101.6 (2020), p. 064001. DOI: [10.1103/PhysRevD.101.064001](https://doi.org/10.1103/PhysRevD.101.064001). arXiv: [1912.07586](https://arxiv.org/abs/1912.07586) [[astro-ph.CO](https://arxiv.org/abs/1912.07586)].
- [162] B. Audren et al. “Conservative constraints on early cosmology with MONTE PYTHON”. In: *J. Cosmology Astropart. Phys.* 2013.2, 001 (Feb. 2013), p. 001. DOI: [10.1088/1475-7516/2013/02/001](https://doi.org/10.1088/1475-7516/2013/02/001). arXiv: [1210.7183](https://arxiv.org/abs/1210.7183) [[astro-ph.CO](https://arxiv.org/abs/1210.7183)].
- [163] T. Brinckmann and J. Lesgourgues. “MontePython 3: boosted MCMC sampler and other features”. In: *Phys. Dark Univ.* 24 (2019), p. 100260. DOI: [10.1016/j.dark.2018.100260](https://doi.org/10.1016/j.dark.2018.100260). arXiv: [1804.07261](https://arxiv.org/abs/1804.07261) [[astro-ph.CO](https://arxiv.org/abs/1804.07261)].
- [164] A. Gelman and D. B. Rubin. “Inference from Iterative Simulation Using Multiple Sequences”. In: *Statist. Sci.* 7 (1992), pp. 457–472. DOI: [10.1214/ss/1177011136](https://doi.org/10.1214/ss/1177011136).
- [165] A. Lewis. “GetDist: a Python package for analysing Monte Carlo samples”. In: *arXiv e-prints*, arXiv:1910.13970 (Oct. 2019), arXiv:1910.13970. arXiv: [1910.13970](https://arxiv.org/abs/1910.13970) [[astro-ph.IM](https://arxiv.org/abs/1910.13970)].
- [166] O. Pisanti et al. “PARthENoPE: Public Algorithm Evaluating the Nucleosynthesis of Primordial Elements”. In: *Comput. Phys. Commun.* 178 (2008), pp. 956–971. DOI: [10.1016/j.cpc.2008.02.015](https://doi.org/10.1016/j.cpc.2008.02.015). arXiv: [0705.0290](https://arxiv.org/abs/0705.0290) [[astro-ph](https://arxiv.org/abs/0705.0290)].
- [167] R. Consiglio et al. “PARthENoPE reloaded”. In: *Comput. Phys. Commun.* 233 (2018), pp. 237–242. DOI: [10.1016/j.cpc.2018.06.022](https://doi.org/10.1016/j.cpc.2018.06.022). arXiv: [1712.04378](https://arxiv.org/abs/1712.04378) [[astro-ph.CO](https://arxiv.org/abs/1712.04378)].
- [168] N. Schöneberg et al. “The H0 Olympics: A fair ranking of proposed models”. In: *Phys. Rept.* 984 (2022), pp. 1–55. DOI: [10.1016/j.physrep.2022.07.001](https://doi.org/10.1016/j.physrep.2022.07.001). arXiv: [2107.10291](https://arxiv.org/abs/2107.10291) [[astro-ph.CO](https://arxiv.org/abs/2107.10291)].

Bibliography

- [169] H. Akaike. “A new look at the statistical model identification”. In: *IEEE Transactions on Automatic Control* 19.6 (1974), pp. 716–723. DOI: [10.1109/TAC.1974.1100705](https://doi.org/10.1109/TAC.1974.1100705).
- [170] M. J. Reid, D. W. Pesce, and A. G. Riess. “An Improved Distance to NGC 4258 and its Implications for the Hubble Constant”. In: *Astrophys. J. Lett.* 886.2 (2019), p. L27. DOI: [10.3847/2041-8213/ab552d](https://doi.org/10.3847/2041-8213/ab552d). arXiv: [1908.05625](https://arxiv.org/abs/1908.05625) [[astro-ph.GA](#)].
- [171] M. Braglia et al. “A larger value for H_0 by an evolving gravitational constant”. In: *arXiv e-prints*, arXiv:2004.11161 (Apr. 2020), arXiv:2004.11161. arXiv: [2004.11161](https://arxiv.org/abs/2004.11161) [[astro-ph.CO](#)].
- [172] D. Alonso et al. “Observational future of cosmological scalar-tensor theories”. In: *Phys. Rev. D* 95.6 (2017), p. 063502. DOI: [10.1103/PhysRevD.95.063502](https://doi.org/10.1103/PhysRevD.95.063502). arXiv: [1610.09290](https://arxiv.org/abs/1610.09290) [[astro-ph.CO](#)].
- [173] M. Ballardini et al. “Testing extended Jordan-Brans-Dicke theories with future cosmological observations”. In: *JCAP* 05 (2019), p. 049. DOI: [10.1088/1475-7516/2019/05/049](https://doi.org/10.1088/1475-7516/2019/05/049). arXiv: [1902.01407](https://arxiv.org/abs/1902.01407) [[astro-ph.CO](#)].
- [174] G. Esposito-Farese and D. Polarski. “Scalar tensor gravity in an accelerating universe”. In: *Phys. Rev. D* 63 (2001), p. 063504. DOI: [10.1103/PhysRevD.63.063504](https://doi.org/10.1103/PhysRevD.63.063504). arXiv: [gr-qc/0009034](https://arxiv.org/abs/gr-qc/0009034).
- [175] M. Zumalacarregui. “Gravity in the Era of Equality: Towards solutions to the Hubble problem without fine-tuned initial conditions”. In: *Phys. Rev. D* 102.2 (2020), p. 023523. DOI: [10.1103/PhysRevD.102.023523](https://doi.org/10.1103/PhysRevD.102.023523). arXiv: [2003.06396](https://arxiv.org/abs/2003.06396) [[astro-ph.CO](#)].
- [176] J. Solà Peracaula et al. “Brans–Dicke cosmology with a Λ -term: a possible solution to Λ CDM tensions”. In: *Class. Quant. Grav.* 37.24 (2020), p. 245003. DOI: [10.1088/1361-6382/abbc43](https://doi.org/10.1088/1361-6382/abbc43). arXiv: [2006.04273](https://arxiv.org/abs/2006.04273) [[astro-ph.CO](#)].
- [177] M. Ballardini and F. Finelli. “Type Ia supernovae data with scalar-tensor gravity”. In: *Phys. Rev. D* 106.6 (2022), p. 063531. DOI: [10.1103/PhysRevD.106.063531](https://doi.org/10.1103/PhysRevD.106.063531). arXiv: [2112.15126](https://arxiv.org/abs/2112.15126) [[astro-ph.CO](#)].
- [178] F. P. Silva and K. Koyama. “Self-Accelerating Universe in Galileon Cosmology”. In: *Phys. Rev. D* 80 (2009), p. 121301. DOI: [10.1103/PhysRevD.80.121301](https://doi.org/10.1103/PhysRevD.80.121301). arXiv: [0909.4538](https://arxiv.org/abs/0909.4538) [[astro-ph.CO](#)].
- [179] T. Kobayashi. “Cosmic expansion and growth histories in Galileon scalar-tensor models of dark energy”. In: *Phys. Rev. D* 81 (2010), p. 103533. DOI: [10.1103/PhysRevD.81.103533](https://doi.org/10.1103/PhysRevD.81.103533). arXiv: [1003.3281](https://arxiv.org/abs/1003.3281) [[astro-ph.CO](#)].
- [180] I. Quiros. “Selected topics in scalar-tensor theories and beyond”. In: *International Journal of Modern Physics D* 28.7, 1930012-156 (Jan. 2019), pp. 1930012–156. DOI: [10.1142/S021827181930012X](https://doi.org/10.1142/S021827181930012X). arXiv: [1901.08690](https://arxiv.org/abs/1901.08690) [[gr-qc](#)].
- [181] M. Ballardini et al. “Cosmological constraints on induced gravity dark energy models”. In: *JCAP* 05 (2016), p. 067. DOI: [10.1088/1475-7516/2016/05/067](https://doi.org/10.1088/1475-7516/2016/05/067). arXiv: [1601.03387](https://arxiv.org/abs/1601.03387) [[astro-ph.CO](#)].
- [182] A. Cerioni. “Cosmological perturbations in generalized theories of gravity”. PhD thesis. alma, Apr. 2011. URL: <http://amsdottorato.unibo.it/3562/>.
- [183] N. Chow and J. Khoury. “Galileon Cosmology”. In: *Phys. Rev. D* 80 (2009), p. 024037. DOI: [10.1103/PhysRevD.80.024037](https://doi.org/10.1103/PhysRevD.80.024037). arXiv: [0905.1325](https://arxiv.org/abs/0905.1325) [[hep-th](#)].

Bibliography

- [184] L. Amendola, D. Polarski, and S. Tsujikawa. “Are $f(R)$ dark energy models cosmologically viable ?” In: *Phys. Rev. Lett.* 98 (2007), p. 131302. DOI: [10.1103/PhysRevLett.98.131302](https://doi.org/10.1103/PhysRevLett.98.131302). arXiv: [astro-ph/0603703](https://arxiv.org/abs/astro-ph/0603703).
- [185] W. Hu and I. Sawicki. “Models of $f(R)$ Cosmic Acceleration that Evade Solar-System Tests”. In: *Phys. Rev. D* 76 (2007), p. 064004. DOI: [10.1103/PhysRevD.76.064004](https://doi.org/10.1103/PhysRevD.76.064004). arXiv: [0705.1158](https://arxiv.org/abs/0705.1158) [[astro-ph](#)].
- [186] S. Casas et al. “Euclid: Constraints on $f(R)$ cosmologies from the spectroscopic and photometric primary probes”. In: (June 2023). arXiv: [2306.11053](https://arxiv.org/abs/2306.11053) [[astro-ph.CO](#)].
- [187] E. Babichev, V. Mukhanov, and A. Vikman. “k-Essence, superluminal propagation, causality and emergent geometry”. In: *JHEP* 02 (2008), p. 101. DOI: [10.1088/1126-6708/2008/02/101](https://doi.org/10.1088/1126-6708/2008/02/101). arXiv: [0708.0561](https://arxiv.org/abs/0708.0561) [[hep-th](#)].
- [188] V. Gorini et al. “Gauge-invariant analysis of perturbations in Chaplygin gas unified models of dark matter and dark energy”. In: *JCAP* 02 (2008), p. 016. DOI: [10.1088/1475-7516/2008/02/016](https://doi.org/10.1088/1475-7516/2008/02/016). arXiv: [0711.4242](https://arxiv.org/abs/0711.4242) [[astro-ph](#)].
- [189] A. Adams et al. “Causality, analyticity and an IR obstruction to UV completion”. In: *JHEP* 10 (2006), p. 014. DOI: [10.1088/1126-6708/2006/10/014](https://doi.org/10.1088/1126-6708/2006/10/014). arXiv: [hep-th/0602178](https://arxiv.org/abs/hep-th/0602178).
- [190] C. Bonvin, C. Caprini, and R. Durrer. “A no-go theorem for k-essence dark energy”. In: *Phys. Rev. Lett.* 97 (2006), p. 081303. DOI: [10.1103/PhysRevLett.97.081303](https://doi.org/10.1103/PhysRevLett.97.081303). arXiv: [astro-ph/0606584](https://arxiv.org/abs/astro-ph/0606584).
- [191] G. Ellis, R. Maartens, and M. A. H. MacCallum. “Causality and the speed of sound”. In: *Gen. Rel. Grav.* 39 (2007), pp. 1651–1660. DOI: [10.1007/s10714-007-0479-2](https://doi.org/10.1007/s10714-007-0479-2). arXiv: [gr-qc/0703121](https://arxiv.org/abs/gr-qc/0703121).
- [192] T. Kobayashi, H. Tashiro, and D. Suzuki. “Evolution of linear cosmological perturbations and its observational implications in Galileon-type modified gravity”. In: *Phys. Rev. D* 81 (2010), p. 063513. DOI: [10.1103/PhysRevD.81.063513](https://doi.org/10.1103/PhysRevD.81.063513). arXiv: [0912.4641](https://arxiv.org/abs/0912.4641) [[astro-ph.CO](#)].
- [193] J. Renk, M. Zumalacarregui, and F. Montanari. “Gravity at the horizon: on relativistic effects, CMB-LSS correlations and ultra-large scales in Horndeski’s theory”. In: *JCAP* 07 (2016), p. 040. DOI: [10.1088/1475-7516/2016/07/040](https://doi.org/10.1088/1475-7516/2016/07/040). arXiv: [1604.03487](https://arxiv.org/abs/1604.03487) [[astro-ph.CO](#)].
- [194] R. Scaramella et al. “Euclid preparation - I. The Euclid Wide Survey”. In: *Astron. Astrophys.* 662 (2022), A112. DOI: [10.1051/0004-6361/202141938](https://doi.org/10.1051/0004-6361/202141938). arXiv: [2108.01201](https://arxiv.org/abs/2108.01201) [[astro-ph.CO](#)].
- [195] S. E. van Mierlo et al. “Euclid preparation - XXI. Intermediate-redshift contaminants in the search for $z > 6$ galaxies within the Euclid Deep Survey”. In: *Astron. Astrophys.* 666 (2022). [Erratum: *Astron. Astrophys.* 668, C3 (2022)], A200. DOI: [10.1051/0004-6361/202243950](https://doi.org/10.1051/0004-6361/202243950). arXiv: [2205.02871](https://arxiv.org/abs/2205.02871) [[astro-ph.GA](#)].
- [196] M. Schirmer et al. “Euclid preparation - XVIII. The NISP photometric system”. In: *Astron. Astrophys.* 662 (2022), A92. DOI: [10.1051/0004-6361/202142897](https://doi.org/10.1051/0004-6361/202142897). arXiv: [2203.01650](https://arxiv.org/abs/2203.01650) [[astro-ph.IM](#)].
- [197] A. Blanchard et al. “Euclid preparation: VII. Forecast validation for Euclid cosmological probes”. In: *Astron. Astrophys.* 642 (2020), A191. DOI: [10.1051/0004-6361/202038071](https://doi.org/10.1051/0004-6361/202038071). arXiv: [1910.09273](https://arxiv.org/abs/1910.09273) [[astro-ph.CO](#)].

Bibliography

- [198] W. Hu. “Power spectrum tomography with weak lensing”. In: *Astrophys. J. Lett.* 522 (1999), pp. L21–L24. DOI: [10.1086/312210](https://doi.org/10.1086/312210). arXiv: [astro-ph/9904153](https://arxiv.org/abs/astro-ph/9904153).
- [199] P. G. Castro, A. F. Heavens, and T. D. Kitching. “Weak lensing analysis in three dimensions”. In: *Phys. Rev. D* 72 (2005), p. 023516. DOI: [10.1103/PhysRevD.72.023516](https://doi.org/10.1103/PhysRevD.72.023516). arXiv: [astro-ph/0503479](https://arxiv.org/abs/astro-ph/0503479).
- [200] A. Spurio Mancini et al. “Testing (modified) gravity with 3D and tomographic cosmic shear”. In: *Mon. Not. Roy. Astron. Soc.* 480.3 (2018), pp. 3725–3738. DOI: [10.1093/mnras/sty2092](https://doi.org/10.1093/mnras/sty2092). arXiv: [1801.04251](https://arxiv.org/abs/1801.04251) [[astro-ph](https://arxiv.org/abs/astro-ph).[C0](https://arxiv.org/abs/C0)].
- [201] D. N. Limber. “The Analysis of Counts of the Extragalactic Nebulae in Terms of a Fluctuating Density Field.” In: *ApJ* 117 (Jan. 1953), p. 134. DOI: [10.1086/145672](https://doi.org/10.1086/145672).
- [202] N. Kaiser. “Weak gravitational lensing of distant galaxies”. In: *Astrophys. J.* 388 (1992), p. 272. DOI: [10.1086/171151](https://doi.org/10.1086/171151).
- [203] F. Schmidt, M. Liguori, and S. Dodelson. “Galaxy-CMB Cross-Correlation as a Probe of Alternative Models of Gravity”. In: *Phys. Rev. D* 76 (2007), p. 083518. DOI: [10.1103/PhysRevD.76.083518](https://doi.org/10.1103/PhysRevD.76.083518). arXiv: [0706.1775](https://arxiv.org/abs/0706.1775) [[astro-ph](https://arxiv.org/abs/astro-ph)].
- [204] S. Ilić et al. “Euclid preparation - XV. Forecasting cosmological constraints for the Euclid and CMB joint analysis”. In: *Astron. Astrophys.* 657 (2022), A91. DOI: [10.1051/0004-6361/202141556](https://doi.org/10.1051/0004-6361/202141556). arXiv: [2106.08346](https://arxiv.org/abs/2106.08346) [[astro-ph](https://arxiv.org/abs/astro-ph).[C0](https://arxiv.org/abs/C0)].
- [205] R. Laureijs et al. “Euclid Definition Study Report”. In: *arXiv e-prints*, arXiv:1110.3193 (Oct. 2011), arXiv:1110.3193. arXiv: [1110.3193](https://arxiv.org/abs/1110.3193) [[astro-ph](https://arxiv.org/abs/astro-ph).[C0](https://arxiv.org/abs/C0)].
- [206] I. Smail, R. S. Ellis, and M. J. Fitchett. “Gravitational lensing of distant field galaxies by rich clusters: I. - faint galaxy redshift distributions”. In: *Mon. Not. Roy. Astron. Soc.* 270 (1994), p. 245. DOI: [10.1093/mnras/270.2.245](https://doi.org/10.1093/mnras/270.2.245). arXiv: [astro-ph/9402048](https://arxiv.org/abs/astro-ph/9402048).
- [207] A. Pocino et al. “Euclid preparation - XII. Optimizing the photometric sample of the Euclid survey for galaxy clustering and galaxy-galaxy lensing analyses”. In: *Astron. Astrophys.* 655 (2021), A44. DOI: [10.1051/0004-6361/202141061](https://doi.org/10.1051/0004-6361/202141061). arXiv: [2104.05698](https://arxiv.org/abs/2104.05698) [[astro-ph](https://arxiv.org/abs/astro-ph).[C0](https://arxiv.org/abs/C0)].
- [208] D. J. Eisenstein, W. Hu, and M. Tegmark. “Cosmic complementarity: Joint parameter estimation from CMB experiments and redshift surveys”. In: *Astrophys. J.* 518 (1999), pp. 2–23. DOI: [10.1086/307261](https://doi.org/10.1086/307261). arXiv: [astro-ph/9807130](https://arxiv.org/abs/astro-ph/9807130).
- [209] A. Lewis and S. Bridle. “Cosmological parameters from CMB and other data: A Monte Carlo approach”. In: *Phys. Rev. D* 66 (2002), p. 103511. DOI: [10.1103/PhysRevD.66.103511](https://doi.org/10.1103/PhysRevD.66.103511). arXiv: [astro-ph/0205436](https://arxiv.org/abs/astro-ph/0205436).
- [210] A. Vallinotto. “The synergy between the Dark Energy Survey and the South Pole Telescope”. In: *Astrophys. J.* 778 (2013), p. 108. DOI: [10.1088/0004-637X/778/2/108](https://doi.org/10.1088/0004-637X/778/2/108). arXiv: [1304.3474](https://arxiv.org/abs/1304.3474) [[astro-ph](https://arxiv.org/abs/astro-ph).[C0](https://arxiv.org/abs/C0)].
- [211] R. Pearson and O. Zahn. “Cosmology from cross correlation of CMB lensing and galaxy surveys”. In: *Phys. Rev. D* 89.4 (2014), p. 043516. DOI: [10.1103/PhysRevD.89.043516](https://doi.org/10.1103/PhysRevD.89.043516). arXiv: [1311.0905](https://arxiv.org/abs/1311.0905) [[astro-ph](https://arxiv.org/abs/astro-ph).[C0](https://arxiv.org/abs/C0)].
- [212] P. M. Merkel and B. M. Schäfer. “Parameter constraints from weak-lensing tomography of galaxy shapes and cosmic microwave background fluctuations”. In:

Bibliography

- Mon. Not. Roy. Astron. Soc.* 469.3 (2017), pp. 2760–2770. DOI: [10.1093/mnras/stx1044](https://doi.org/10.1093/mnras/stx1044). arXiv: [1707.08153](https://arxiv.org/abs/1707.08153) [[astro-ph.CO](#)].
- [213] E. Schaaf et al. “Looking through the same lens: Shear calibration for LSST, Euclid, and WFIRST with stage 4 CMB lensing”. In: *Phys. Rev. D* 95.12 (2017), p. 123512. DOI: [10.1103/PhysRevD.95.123512](https://doi.org/10.1103/PhysRevD.95.123512). arXiv: [1607.01761](https://arxiv.org/abs/1607.01761) [[astro-ph.CO](#)].
- [214] Y. Omori et al. “Joint analysis of Dark Energy Survey Year 3 data and CMB lensing from SPT and Planck. I. Construction of CMB lensing maps and modeling choices”. In: *Phys. Rev. D* 107.2 (2023), p. 023529. DOI: [10.1103/PhysRevD.107.023529](https://doi.org/10.1103/PhysRevD.107.023529). arXiv: [2203.12439](https://arxiv.org/abs/2203.12439) [[astro-ph.CO](#)].
- [215] C. Chang et al. “Joint analysis of Dark Energy Survey Year 3 data and CMB lensing from SPT and Planck. II. Cross-correlation measurements and cosmological constraints”. In: *Phys. Rev. D* 107.2 (2023), p. 023530. DOI: [10.1103/PhysRevD.107.023530](https://doi.org/10.1103/PhysRevD.107.023530). arXiv: [2203.12440](https://arxiv.org/abs/2203.12440) [[astro-ph.CO](#)].
- [216] T. M. C. Abbott et al. “Joint analysis of Dark Energy Survey Year 3 data and CMB lensing from SPT and Planck. III. Combined cosmological constraints”. In: *Phys. Rev. D* 107.2 (2023), p. 023531. DOI: [10.1103/PhysRevD.107.023531](https://doi.org/10.1103/PhysRevD.107.023531). arXiv: [2206.10824](https://arxiv.org/abs/2206.10824) [[astro-ph.CO](#)].
- [217] J. R. Bermejo-Climent et al. “Cosmological parameter forecasts by a joint 2D tomographic approach to CMB and galaxy clustering”. In: *Phys. Rev. D* 103.10 (2021), p. 103502. DOI: [10.1103/PhysRevD.103.103502](https://doi.org/10.1103/PhysRevD.103.103502). arXiv: [2106.05267](https://arxiv.org/abs/2106.05267) [[astro-ph.CO](#)].
- [218] K. N. Abazajian et al. “CMB-S4 Science Book, First Edition”. In: (Oct. 2016). arXiv: [1610.02743](https://arxiv.org/abs/1610.02743) [[astro-ph.CO](#)].
- [219] P. A. R. Ade et al. “Planck 2015 results. XXI. The integrated Sachs-Wolfe effect”. In: *Astron. Astrophys.* 594 (2016), A21. DOI: [10.1051/0004-6361/201525831](https://doi.org/10.1051/0004-6361/201525831). arXiv: [1502.01595](https://arxiv.org/abs/1502.01595) [[astro-ph.CO](#)].
- [220] J. Carron, A. Lewis, and G. Fabbian. “Planck integrated Sachs-Wolfe-lensing likelihood and the CMB temperature”. In: *Phys. Rev. D* 106.10 (2022), p. 103507. DOI: [10.1103/PhysRevD.106.103507](https://doi.org/10.1103/PhysRevD.106.103507). arXiv: [2209.07395](https://arxiv.org/abs/2209.07395) [[astro-ph.CO](#)].
- [221] J. Carron, M. Mirmelstein, and A. Lewis. “CMB lensing from Planck PR4 maps”. In: *JCAP* 09 (2022), p. 039. DOI: [10.1088/1475-7516/2022/09/039](https://doi.org/10.1088/1475-7516/2022/09/039). arXiv: [2206.07773](https://arxiv.org/abs/2206.07773) [[astro-ph.CO](#)].
- [222] W. Hu. “Weak lensing of the CMB: A harmonic approach”. In: *Phys. Rev. D* 62 (2000), p. 043007. DOI: [10.1103/PhysRevD.62.043007](https://doi.org/10.1103/PhysRevD.62.043007). arXiv: [astro-ph/0001303](https://arxiv.org/abs/astro-ph/0001303).
- [223] B. D. Sherwin et al. “Two-season Atacama Cosmology Telescope polarimeter lensing power spectrum”. In: *Phys. Rev. D* 95.12 (2017), p. 123529. DOI: [10.1103/PhysRevD.95.123529](https://doi.org/10.1103/PhysRevD.95.123529). arXiv: [1611.09753](https://arxiv.org/abs/1611.09753) [[astro-ph.CO](#)].
- [224] K. T. Story et al. “A Measurement of the Cosmic Microwave Background Gravitational Lensing Potential from 100 Square Degrees of SPTpol Data”. In: *Astrophys. J.* 810.1 (2015), p. 50. DOI: [10.1088/0004-637X/810/1/50](https://doi.org/10.1088/0004-637X/810/1/50). arXiv: [1412.4760](https://arxiv.org/abs/1412.4760) [[astro-ph.CO](#)].
- [225] G. Simard et al. “Constraints on Cosmological Parameters from the Angular Power Spectrum of a Combined 2500 deg² SPT-SZ and Planck Gravitational

Bibliography

- Lensing Map”. In: *Astrophys. J.* 860.2 (2018), p. 137. DOI: [10.3847/1538-4357/aac264](https://doi.org/10.3847/1538-4357/aac264). arXiv: [1712.07541](https://arxiv.org/abs/1712.07541) [[astro-ph.CO](#)].
- [226] F. J. Qu et al. “The Atacama Cosmology Telescope: A Measurement of the DR6 CMB Lensing Power Spectrum and its Implications for Structure Growth”. In: (Apr. 2023). arXiv: [2304.05202](https://arxiv.org/abs/2304.05202) [[astro-ph.CO](#)].
- [227] J. Smidt et al. “The Impact of Secondary non-Gaussianities in the CMB on Cosmological Parameter Estimation”. In: *Phys. Rev. D* 81 (2010), p. 123528. DOI: [10.1103/PhysRevD.81.123528](https://doi.org/10.1103/PhysRevD.81.123528). arXiv: [0909.3515](https://arxiv.org/abs/0909.3515) [[astro-ph.CO](#)].
- [228] P. Ade et al. “The Simons Observatory: Science goals and forecasts”. In: *JCAP* 02 (2019), p. 056. DOI: [10.1088/1475-7516/2019/02/056](https://doi.org/10.1088/1475-7516/2019/02/056). arXiv: [1808.07445](https://arxiv.org/abs/1808.07445) [[astro-ph.CO](#)].
- [229] M. LoVerde, L. Hui, and E. Gaztanaga. “Magnification-Temperature Correlation: The Dark Side of ISW Measurements”. In: *Phys. Rev. D* 75 (2007), p. 043519. DOI: [10.1103/PhysRevD.75.043519](https://doi.org/10.1103/PhysRevD.75.043519). arXiv: [astro-ph/0611539](https://arxiv.org/abs/astro-ph/0611539).
- [230] T. Okamoto and W. Hu. “CMB lensing reconstruction on the full sky”. In: *Phys. Rev. D* 67 (2003), p. 083002. DOI: [10.1103/PhysRevD.67.083002](https://doi.org/10.1103/PhysRevD.67.083002). arXiv: [astro-ph/0301031](https://arxiv.org/abs/astro-ph/0301031).
- [231] P. A. R. Ade et al. “Planck 2013 results. XVII. Gravitational lensing by large-scale structure”. In: *Astron. Astrophys.* 571 (2014), A17. DOI: [10.1051/0004-6361/201321543](https://doi.org/10.1051/0004-6361/201321543). arXiv: [1303.5077](https://arxiv.org/abs/1303.5077) [[astro-ph.CO](#)].
- [232] “The Scientific programme of Planck”. In: (Apr. 2006). Ed. by J. Tauber et al. arXiv: [astro-ph/0604069](https://arxiv.org/abs/astro-ph/0604069).
- [233] W. Hu and T. Okamoto. “Mass reconstruction with cmb polarization”. In: *Astrophys. J.* 574 (2002), pp. 566–574. DOI: [10.1086/341110](https://doi.org/10.1086/341110). arXiv: [astro-ph/0111606](https://arxiv.org/abs/astro-ph/0111606).
- [234] P. A. R. Ade et al. “Planck 2015 results. XV. Gravitational lensing”. In: *Astron. Astrophys.* 594 (2016), A15. DOI: [10.1051/0004-6361/201525941](https://doi.org/10.1051/0004-6361/201525941). arXiv: [1502.01591](https://arxiv.org/abs/1502.01591) [[astro-ph.CO](#)].
- [235] W. Hu. “Angular trispectrum of the CMB”. In: *Phys. Rev. D* 64 (2001), p. 083005. DOI: [10.1103/PhysRevD.64.083005](https://doi.org/10.1103/PhysRevD.64.083005). arXiv: [astro-ph/0105117](https://arxiv.org/abs/astro-ph/0105117).
- [236] T. Namikawa, D. Hanson, and R. Takahashi. “Bias-Hardened CMB Lensing”. In: *Mon. Not. Roy. Astron. Soc.* 431 (2013), pp. 609–620. DOI: [10.1093/mnras/stt195](https://doi.org/10.1093/mnras/stt195). arXiv: [1209.0091](https://arxiv.org/abs/1209.0091) [[astro-ph.CO](#)].
- [237] M. H. Kesden, A. Cooray, and M. Kamionkowski. “Lensing reconstruction with CMB temperature and polarization”. In: *Phys. Rev. D* 67 (2003), p. 123507. DOI: [10.1103/PhysRevD.67.123507](https://doi.org/10.1103/PhysRevD.67.123507). arXiv: [astro-ph/0302536](https://arxiv.org/abs/astro-ph/0302536).
- [238] G. Fabbian, A. Lewis, and D. Beck. “CMB lensing reconstruction biases in cross-correlation with large-scale structure probes”. In: *JCAP* 10 (2019), p. 057. DOI: [10.1088/1475-7516/2019/10/057](https://doi.org/10.1088/1475-7516/2019/10/057). arXiv: [1906.08760](https://arxiv.org/abs/1906.08760) [[astro-ph.CO](#)].
- [239] M. Tegmark, A. Taylor, and A. Heavens. “Karhunen-Loeve eigenvalue problems in cosmology: How should we tackle large data sets?” In: *Astrophys. J.* 480 (1997), p. 22. DOI: [10.1086/303939](https://doi.org/10.1086/303939). arXiv: [astro-ph/9603021](https://arxiv.org/abs/astro-ph/9603021).

Bibliography

- [240] L. Amendola et al. “Cosmology and fundamental physics with the Euclid satellite”. In: *Living Rev. Rel.* 16 (2013), p. 6. DOI: [10.12942/lrr-2013-6](https://doi.org/10.12942/lrr-2013-6). arXiv: [1206.1225](https://arxiv.org/abs/1206.1225) [[astro-ph.CO](#)].
- [241] A. Alarcon, M. Eriksen, and E. Gaztañaga. “Cosmological constraints from multiple tracers in spectroscopic surveys”. In: *Mon. Not. Roy. Astron. Soc.* 473.2 (2018), pp. 1444–1460. DOI: [10.1093/mnras/stx2446](https://doi.org/10.1093/mnras/stx2446). arXiv: [1609.08510](https://arxiv.org/abs/1609.08510) [[astro-ph.CO](#)].
- [242] Planck Collaboration et al. “Planck 2015 results. I. Overview of products and scientific results”. In: *A&A* 594, A1 (Sept. 2016), A1. DOI: [10.1051/0004-6361/201527101](https://doi.org/10.1051/0004-6361/201527101). arXiv: [1502.01582](https://arxiv.org/abs/1502.01582) [[astro-ph.CO](#)].
- [243] D. Sciotti et al. “Euclid preparation. TBD. Forecast impact of super-sample covariance on 3x2pt analysis with Euclid”. In: (Oct. 2023). arXiv: [2310.15731](https://arxiv.org/abs/2310.15731) [[astro-ph.CO](#)].
- [244] M. Hazumi et al. “LiteBIRD: A Satellite for the Studies of B-Mode Polarization and Inflation from Cosmic Background Radiation Detection”. In: *J. Low Temp. Phys.* 194.5-6 (2019), pp. 443–452. DOI: [10.1007/s10909-019-02150-5](https://doi.org/10.1007/s10909-019-02150-5).
- [245] H. Sugai et al. “Updated Design of the CMB Polarization Experiment Satellite LiteBIRD”. In: *J. Low. Temp. Phys.* 199.3-4 (2020), pp. 1107–1117. DOI: [10.1007/s10909-019-02329-w](https://doi.org/10.1007/s10909-019-02329-w). arXiv: [2001.01724](https://arxiv.org/abs/2001.01724) [[astro-ph.IM](#)].
- [246] A. Heavens. “Statistical techniques in cosmology”. In: *arXiv e-prints*, arXiv:0906.0664 (June 2009), arXiv:0906.0664. DOI: [10.48550/arXiv.0906.0664](https://doi.org/10.48550/arXiv.0906.0664). arXiv: [0906.0664](https://arxiv.org/abs/0906.0664) [[astro-ph.CO](#)].
- [247] F. Leclercq, A. Pisani, and B. D. Wandelt. “Cosmology: from theory to data, from data to theory”. In: *Proc. Int. Sch. Phys. Fermi* 186 (2014). Ed. by A. Cooray et al., pp. 189–233. DOI: [10.3254/978-1-61499-476-3-189](https://doi.org/10.3254/978-1-61499-476-3-189). arXiv: [1403.1260](https://arxiv.org/abs/1403.1260) [[astro-ph.CO](#)].
- [248] N. Metropolis et al. “Equation of State Calculations by Fast Computing Machines”. In: *J. Chem. Phys.* 21.6 (June 1953), pp. 1087–1092. DOI: [10.1063/1.1699114](https://doi.org/10.1063/1.1699114).
- [249] W. K. Hastings. “Monte Carlo Sampling Methods using Markov Chains and their Applications”. In: *Biometrika* 57.1 (Apr. 1970), pp. 97–109. DOI: [10.1093/biomet/57.1.97](https://doi.org/10.1093/biomet/57.1.97).
- [250] V. Roy. “Convergence Diagnostics for Markov Chain Monte Carlo”. In: *Annual Review of Statistics and Its Application* 7.1 (Mar. 2020), pp. 387–412. DOI: [10.1146/annurev-statistics-031219-041300](https://doi.org/10.1146/annurev-statistics-031219-041300). arXiv: [1909.11827](https://arxiv.org/abs/1909.11827) [[stat.CO](#)].
- [251] A. Gelman et al. *Bayesian Data Analysis, Third Edition*. Chapman & Hall/CRC Texts in Statistical Science. Taylor & Francis, 2013. ISBN: 9781439840955. URL: <https://books.google.it/books?id=ZXL6AQAQBAJ>.
- [252] R. Trotta. “Bayesian Methods in Cosmology”. In: Jan. 2017. arXiv: [1701.01467](https://arxiv.org/abs/1701.01467) [[astro-ph.CO](#)].
- [253] D. Paoletti et al. “Isocurvature fluctuations in the effective Newton’s constant”. In: *Phys. Dark Univ.* 25 (2019), p. 100307. DOI: [10.1016/j.dark.2019.100307](https://doi.org/10.1016/j.dark.2019.100307). arXiv: [1809.03201](https://arxiv.org/abs/1809.03201) [[astro-ph.CO](#)].